ISSN 0916-7501
CODEN : TTEREB

TOYOTA Technical Review

2010/7 226



Prius

VOL.57 NO.1

Cover design:

The cover expresses the continued passion experienced in research and development of new technology. The Japanese character " 魁 " (sakigake), which means "vanguard," is used to vigorously convey the spirit of engineers creating a new future of motorization.

Contents

Preface

· Leading the Way into a New Era
Takeshi Uchiyamada, Executive Vice President 2

▷ Special Feature: Prius

Introduction: Evolution of the Third Generation Prius
Akihiko Otsuka/Takashi Yamazaki 4

· Hybrid Technologies in the Third Generation Prius
Hideaki Yaguchi/Takeshi Murakami/Ken Asakura/Tetsuro Kuzuya/Toshiya Hashimoto 10

· Aerodynamic Technologies Adopted in the Third Generation Prius
Hiroyuki Yamasaki/Yumiko Toki/Toshiyuki Murayama 18

· Development of the Third Generation Prius Focusing on Fuel Economy
Issaku Yamada/Junji Tokieda/Kunihiko Jinno/Tetsuya Takechi/Masakatsu Tsubouchi/Takato Ishihata 25

· Chassis Development for the Third Generation Prius
Masayuki Aso 31

· Solar Ventilation and Remote Air Conditioning Systems
Koji Ikeda/Takashi Ogawa/Takaaki Goto 35

· Design of the Prius as an Eco-Icon
Hideo Miwa 40

· Passive Safety Performance
Tsukasa Hayashizaki/Yasunari Sakai/Tomohiro Kimura/Yuji Nakane 50

▷ Technical Papers/Technical Articles

· Introduction of World's First Rear Seat Occupant Restraint System for Rear-End Collisions
Motonori Kitayama/Yoshio Mizuno/Michinori Kakumu 54

· Development of Front-Side Pre-Crash Safety System for Intersection Collisions
Tomoya Kawasaki/Jun Tsunekawa/Tomoaki Harada/Koji Suzuki 57

· Efficiency Improvement Study of High-Power Electric Power Steering System
Takeshi Goto/Masaharu Yamashita/Takatoshi Saito/Yoichi Fujinori/Hisashi Somada 61

· Logical Mediation Structures for Toyota's Driver Support Systems
Kazushi Kuroda 68

· Development of Fuel Consumption Estimation Technology Using VHDL-AMS
Kimitoshi Tsuji/Yasunari Kido/Junichi Ichihara 72

· Development of Hydraulic Pressure Servo Control Method for New Electronically Controlled Brake System -Adoption of Variable Differential Pressure Regulating Valve Control Method to Rapidly Varying Controlled Object-
Hiroshi Nakaoka/Tsukasa Fukasawa/Yoshito Tanaka/Mitsuo Fukuda 77

· Analysis of Sophisticated DPNR Catalyst -Focused on PM Particle Number Emissions-
Masamichi Kuwajima/Seiji Okawara/Shigehiro Matsuno/Masaaki Yamaguchi/Masato Tsuzuki 82

· Development of Double-Layered Three-Way Catalysts
Yuki Aoki/Takeru Yoshida/Toshitaka Tanabe/Masanori Shimizu 87

· Investigation of Novel Metal Plating Process Using Ozone Treatment
Hiroshi Yanagimoto/Takeshi Bessho 92

· Development of Power Diode for Hybrid Vehicles
Atsushi Tanida/Tetsuya Kanata/Katsuhiko Nishiwaki/Takahide Sugiyama 97

· Development of Electrode Structure for High Performance Fuel Cell Using CAE
Joji Tomiyasu/Takashi Harada/Makoto Fujiuchi/Takaji Inamuro/Shiaki Hyodo/Toshihisa Munekata 101

· Research on Fatigue Mechanism of High-Pressure Tank for Fuel Cell Vehicles
Riki Otsuka/Nobuyuki Ogami/Masayoshi Taki 106

▷ Technical Award News 112

▷ Award-Winning Patents 114

Leading the Way into a New Era



Takeshi Uchiyamada,
Executive Vice President

Twelve years have passed since the launch of the first generation Prius and sales of the latest third generation model are on the increase. I would like to take this timely opportunity to look back on my role in the birth of the first generation Prius, the world's first mass-produced hybrid vehicle.

It started with the G21 project that aimed to develop a vehicle for the 21st century and present it to the world. Its development concept was to provide solutions for the issues of a mobile society in the 21st century, while maintaining and enhancing the comfort and convenience of a conventional vehicle. After discussion, these issues were identified as energy and the environment.

At the time, Toyota was strenuously debating whether to introduce airbags and ABS as standard safety equipment, and the possibility was raised that customers might not want to buy a vehicle focused on energy and environmental concerns. However, realizing that these issues would be crucial in the future, the Prius project was given the go-ahead, and a hybrid system was developed and installed as the vehicle's power plant. The critical issues were identified and the necessary technical development for their resolution was given priority. In other words, we focused on developing the necessary technology to resolve the issues rather than on determining how to use existing technology.

Now, of course, we are standing in the middle of a battle to develop environmentally friendly technology. The competition to develop technology (including safety technology) and products will be an inescapable theme for the mobile society of the future. So, with an unavoidable, inevitable course ahead of us, we want to lead the way and drive forward with technology and products. However, it will not be enough simply to develop technology that meets the environmental and safety needs of the coming age. We want to boost technical development even further so that we can double the fundamental pleasure of driving. We have to develop technology that enhances aspects of perceived quality such as dynamic performance, driveability, stability and controllability, noise and vibration, and ergonomics, as well as aspects of convenience and comfort such as HVAC and ITS.

As we promote these elements of technical development, I want everyone, especially those in a position to guide young people in the workplace, to take the following points to heart.

1. Young engineers should get their hands dirty.
   Development itself is the crucible for education. We should set appropriate themes and help our young engineers develop by their own hands.

2. Managers should frequently engage in technical debate.
   While keeping an eye on the progress of these themes, managers and experienced people at the workplace should debate technical issues with the people in charge. We should set aside formal titles and debate equally as engineers. If we set an example like this, it will reinforce our image as engineers and help pass on our technical knowledge and thinking to the younger generation.

The technological competitive strength of our products cannot exceed our own ability. To create and maintain sustainable competitive power, continuing technical development is essential for the education of our future generations of engineers.

Evolution of the Third Generation Prius

Akihiko Otsuka*
Takashi Yamazaki*

1. Introduction

Making a model change of a successful product is said to be difficult. A car's model life is normally several years, and sales volume is initially high in the period after model release. Improvements of accessories and design changes are used from time to time to boost sales, but volumes normally decrease at the end of a car's model life. Sales volumes of the second generation Prius, however, increased steadily after its debut in September 2003, and even at the end of its model life, immediately before release of the third generation Prius, the model maintained strong sales. A global increase in the price of fuel and increased consumer awareness for ecological issues are considered to be factors for this, but the second generation Prius was consistently in the top 10 in the Japan market, excluding sales of mini vehicles. This resulted in an unusual debut for the third generation Prius. Through September 2009, the three generations of the Prius had achieved global sales of 1.55 million vehicles, and sales for 2008 in particular, surpassed 285,000. Thus, the Prius now competes with regular gasoline vehicles in terms of sales volume as well, and has become a representative Toyota vehicle (**Fig. 1**).

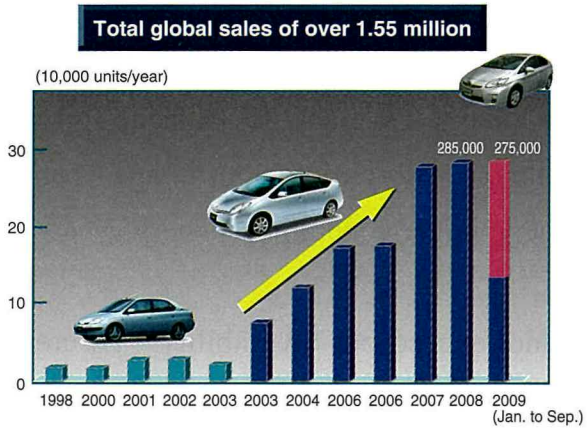


Fig. 1 Prius Sales Trend (Global)

2. A Car Named Prius

The word "Prius" means "preceding" in Latin. The original Prius used the unique and inventive Toyota Hybrid System (THS), which combined a planetary gear structure with drive power from a gasoline engine and an electric motor. Under the catch phrase "in time for the 21st century" (**Fig. 2**), sales of the world's first mass-produced hybrid vehicle began in 1997 (**Fig. 3**). The first generation Prius had fuel economy of 28.0 km/L (under Japan's 10·15 mode fuel economy regulations), or about double that of a gasoline-powered vehicle in the same class, and was accepted by the market as a remarkable vehicle.

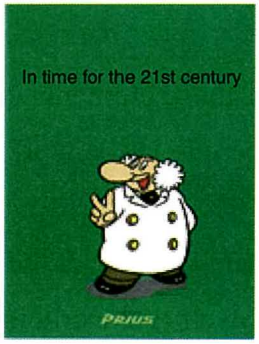


Fig. 2 First Generation Prius Catch Phrase



Fig. 3 First Generation Prius

In order to improve aerodynamic performance, the second generation Prius made a bold transformation from the sedan style of the first generation to a unique hatchback style (**Fig. 4**). The THS evolved into the THS II with changes such as advanced regenerative brake control, improved variable voltage control to increase the maximum motor control voltage to 500 V, higher motor output, and higher maximum rpm. Dynamic performance and fuel economy were both improved further.

In terms of features as well, advanced technology was applied without any reservations. The Smart Entry & Start System key could unlock the doors and start the system just by being carried near the vehicle, the shift-by-wire Electro Shift-matic system enabled changes in shift position with light force, Intelligent Parking Assist helped steering wheel operation when parking, EV Drive Mode enabled driving with the engine stopped and

* Toyota Passenger Vehicle Development Center 2

only the motor running, and electrical inverter air conditioning enabled operation of the air conditioning with the engine stopped. The second generation Prius was loaded with these and other features that had such an impact that they changed the concept of driving a car.



Fig. 4 Second Generation Prius

In this way the Prius, with its low fuel consumption and advanced features, created a new environmentally-conscious value, at a time when size and luxury were thought to determine a vehicle's status. Numerous Hollywood stars were sighted riding to the Academy Awards ceremonies not in luxurious limousines, but rather in the Prius. These sightings came to symbolize environmental consciousness and attracted lots of attention. In this way, the Prius was a representative car that established the "Toyota = hybrid vehicles" image.

3. Development of Third Generation Prius

For the development of the third generation Prius, large targets were set to increase the brand value that already existed and reinforce the "Toyota = hybrid vehicles" image, while also expanding the customer base with an entry model hybrid car.

In order to achieve these targets, the following four-pillar approach was taken.

- Overwhelming hybrid performance
- Progressive style with a functional form
- Progressive features ahead of their time
- Advancing the fundamental performance of the original car

These items are discussed below.

3.1 Overwhelming hybrid performance

The hybrid system was newly developed with engine displacement increased to 1.8 liters. The effects of the synergy of the system combined with fuel consumption reduction items in other areas of the vehicle, achieved reductions in total energy consumption for the vehicle.

The hybrid system was made more powerful, lighter, more compact, and lower cost. As a result, performance in each of the four hybrid qualities (**Fig. 5**) was vastly improved. The four hybrid qualities refer to the four criteria used to express the strengths of Toyota hybrid cars, fuel economy, driving performance, the environment, and quietness.

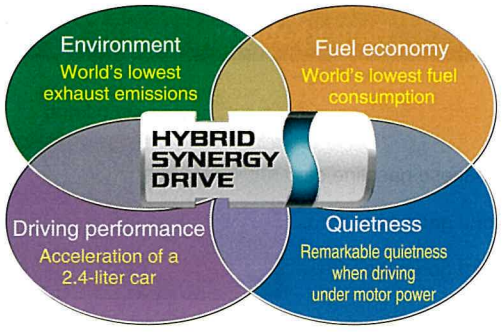


Fig. 5 The Four Hybrid Qualities

- Fuel economy

In Japan, the catalog fuel economy in 10·15 mode testing was improved from the previous 35.5 km/L to 38.0 km/L. For actual fuel economy, which simulates real driving conditions, a fuel economy increase of about 10% was achieved.

- Driving performance

Output was increased for both the engine and hybrid battery, resulting in system output of 100 kW. Acceleration feeling similar to that of a 2.4-liter vehicle was achieved (**Fig. 6**).

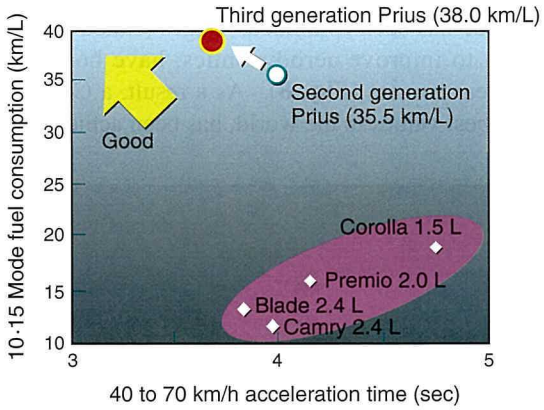


Fig. 6 Advances in Acceleration Feeling and Fuel Economy

- Environment

Exhaust emissions were reduced, and emissions regulations in various countries have been cleared. The Prius is compliant with California AT-PZEV in the U.S. and with Euro 5 in Europe. In Japan it has acquired SU-LEV status, which means that exhaust emissions are 75% reduced from 2005 levels.

- Quietness

In low speed ranges, the THS can completely stop the engine and drive with only the motor, thereby providing overwhelming quietness. Moreover, due to greater engine displacement, engine speed is lower when driving in the high speed range, and the locations of noise insulation materials have been optimized, resulting in a high degree of quietness (**Fig. 7**).

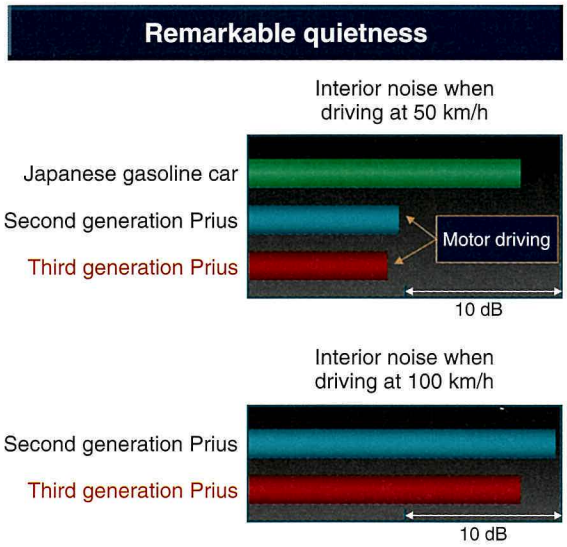


Fig. 7 Comparison of Quietness Performance

3.2 Progressive style with a functional form

The exterior design was developed with an "eco management" theme, and achieves a beautiful form while also giving priority to aerodynamic performance. The unique triangular silhouette view from the side has been continued. Edges (called "aero corners"), which aim to improve aerodynamics, have been used for the front and rear corners (**Fig. 8**). As a result, a Cd value of 0.25, one of the best values in the world, has been achieved.



Fig. 8 Exterior with Aero Corners

The interior design was created around the keyword "human-tech," and the instrument panel area consists of two zones (**Fig. 9**) to give maximum priority to ease of operation and ease of view. Moreover, organic shapes and texture in the motif of leaf veins were added to the instrument panel surface, which achieves a space that gently engulfs vehicle occupants. The shift knob takes advantage of its electronic characteristics and is positioned as if floating on the center cluster. This achieves a unique design while also improving operation.

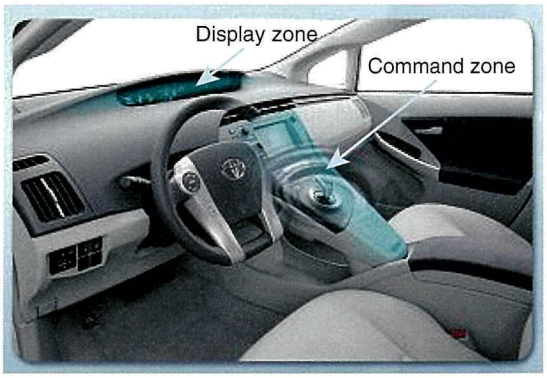


Fig. 9 Command and Display Zones

3.3 Progressive features ahead of their time

As stated above, the Prius cannot simply be categorized as a hybrid car, and sophisticated features that are ahead of their time have been applied without reservation. The third generation is equipped with advanced features as shown below.

3.3.1 Solar ventilation system & remote air conditioning system

The solar panel (**Fig. 10**) provides clean energy recovered from solar energy. The solar ventilation system uses energy generated from the solar panel installed on the roof to drive the air conditioning blower motor, which circulates air when the vehicle is parked. It is also equipped with a remote air conditioning system that takes advantage of the ample power of the hybrid battery. With this system, the user presses a wireless key to operate the air conditioning system before the vehicle is entered. These features reduce the heat inside the cabin, for example, when entering the car on hot summer days.



Fig. 10 Solar Panel Installed on Roof

3.3.2 Touch tracer display

In order to improve the operability of features such as the audio and air conditioning, it has become common to use switches on the steering wheel. One drawback however, is that

the driver's focal point must move drastically to look at these switches to operate them while driving. The touch tracer display (**Fig. 11**) was developed to overcome this problem by displaying the locations of the hand switches on the center meter, to enable operation while looking at this display. Two types of sensors, pressure-sensitive and contact, are built into the switches on the steering wheel. Lightly touching a pressure-sensitive sensor displays a switch arrangement screen on the meter to show which switch is being touched. Pushing a switch in further while it is being displayed and touching the contact sensor will cause the system to perform the desired operation. As a result, switches can be operated with less movement of the driver's focal point.



Fig. 11 Touch Tracer Display

3.3.3 LED headlamps

LEDs light up quickly, have a long life, and consume low levels of energy. LEDs are used on the Prius headlamp low beams, a first for the Toyota brand (**Fig. 12**). Three LEDs are located on each side, two projector type and one reflector type, to achieve both light volume and light distribution performance. As a result, energy consumption when driving at night is reduced.



Fig. 12 LED Headlamp

3.3.4 Three Drive Modes

With the THS II, the powerful motor can assist the engine, and the system can also run with just the motor. In addition to normal driving mode, this unique characteristic allows the Prius to have three other drive modes for different driving conditions (**Fig. 13**).

(1) EV drive mode

In this mode, the car can be driven with just the motor, without starting the engine. The drive feel of an electric vehicle can be experienced, and no exhaust gasses are emitted while driving in this mode.

(2) ECO mode

In this mode, drive power in response to pressing the accelerator pedal and operating the air conditioning are moderated to achieve even lower fuel consumption. Thus the Prius can help drivers reduce fuel consumption, in accordance with their environmental consciousness.

(3) PWR mode

In power mode, when the accelerator pedal is pressed, drive power response is much sharper. This enables sporty driving, for example, up hills and on mountain roads.



Fig. 13 Drive Mode Change Switch (From Right: EV Drive Mode, ECO Mode, and PWR Mode)

3.3.5 ECO drive monitor

Fuel consumption is one aspect of vehicle performance, and it changes considerably depending on driving style. There are large differences in individual driving styles, and to actually implement environmentally responsible driving, it is difficult to maintain the correct depression of the accelerator and brake pedals. The Prius is equipped with an ECO drive monitor, which supports environmentally responsible driving by enabling visual confirmation of how these pedals are pushed.

The ECO drive monitor consists of three screens: the hybrid system indicator, energy monitor, and fuel consumption history. These are displayed to the side of the meter in the multi-display. By operating the "DISP" button on the steering wheel, the display can be toggled among these views.

(1) Hybrid system indicator

This indicator supports environmentally responsible driving by demonstrating how the pedals are being pushed (**Fig. 14**). Depending on how far the accelerator pedal and brake pedal are pushed, the bar on the indicator moves left and right. The charge area (CHG) indicates energy regeneration levels when the brake

is pushed. Regeneration increases as the bar extends further to the left, and this indicates that the amount of energy recovered at the hybrid battery is large.

The wide bar in the center shows the "ECO area." Operating the accelerator pedal within this area indicates that the vehicle is being driven in an efficient range, and the ECO drive indicator lamp also illuminates. When there is a bar in the power area on the right side (PWR), it indicates that the system is performing powerful driving outside of the ECO driving range. Displaying the movements of these bars can give the driver an estimate of how much the accelerator pedal and brake pedal are being operated, in order to drive with low fuel consumption.



Fig. 14 Hybrid System Indicator

(2) Energy monitor

This indicator shows, at a glance, the THS II operation state (**Fig. 15**). The operation states of the engine and motor and their power and energy flows are shown by the movement of arrows. As a result, it is possible to know if the current driving state is using motor or engine power, and if electric energy from the battery is being used or if energy is being regenerated from the motor.

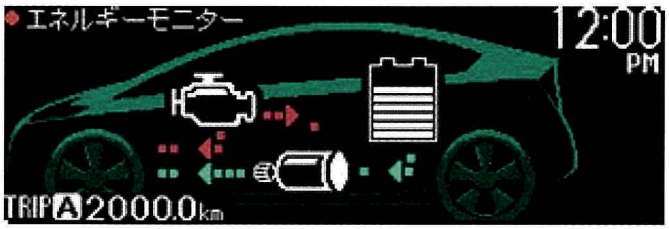


Fig. 15 Energy Monitor

(3) Fuel consumption history

While the previous two screens show the current state, the three displays of the fuel consumption history show previous results. Fuel consumption history (**Fig. 16**) shows fuel consumption for the distance driven, five-minute consumption (**Fig. 17**) shows fuel consumption in five-minute intervals, and one-minute consumption allows fuel consumption to be checked at even shorter intervals.

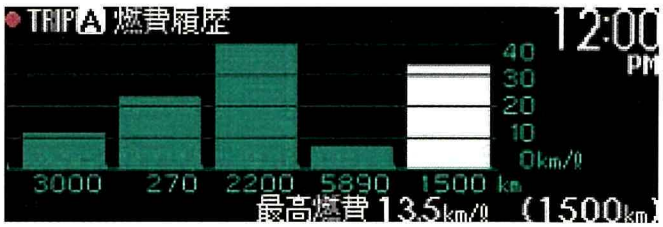


Fig. 16 Fuel Consumption History

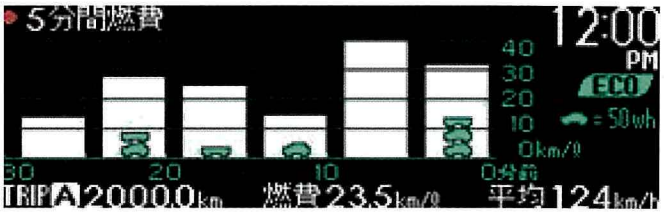


Fig. 17 Five-Minute Consumption

3.4 Advancing the fundamental performance of the original car

In the third generation Prius, the platform has been updated, suspension geometry has been revised, and steering stability and ride comfort—the fundamental qualities that make a car appealing—have been improved (**Fig. 18**).

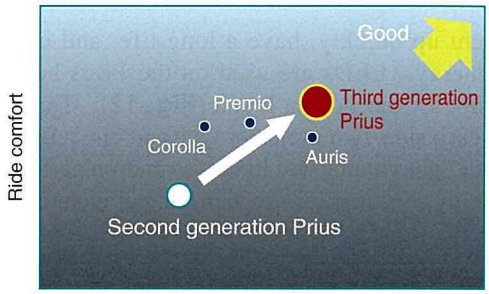


Fig. 18 Advances in Steering Stability and Ride Comfort

In terms of the package design, the vehicle size is similar to that of the second generation Prius, but the interior space and luggage capacity have been expanded (**Fig. 19**).

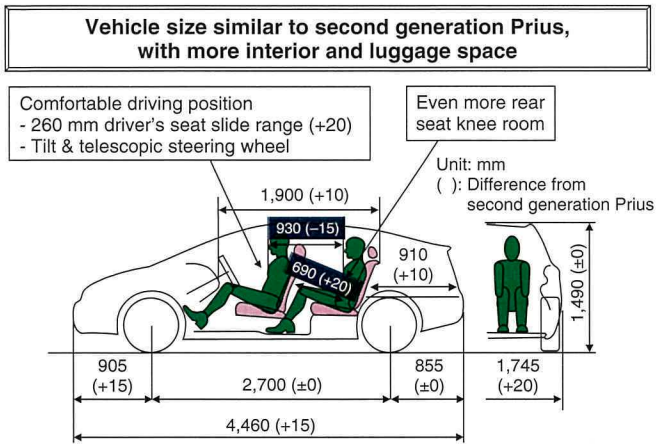


Fig. 19 Package Design of Third Generation Prius

The hybrid battery is the same as in the second generation Prius, but improvements such as a more compact cooling system have increased luggage volume to 446 liters (VDA measurement method), which enables the loading of three golf bags.

Also, the peak of the roof, when viewed from the side, has been moved rearward. While the vehicle's silhouette is more relaxed, headroom and ease of entry in the rear seats are improved, and use of a thin seatback for the front seats gives the rear seats more legroom (**Fig. 20**).

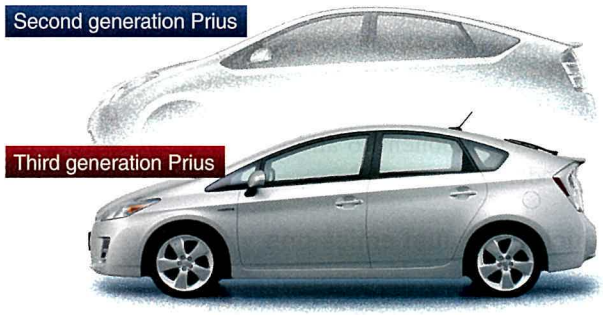


Fig. 20 Comparison of Second and Third Generation Prius Side Silhouettes

4. Environmental Performance

4.1 Saving resources and recycling more

Environmentally responsible plastic, which saves petroleum resources and reduces CO_2 emissions, was developed as a reusable plant-derived resource, and is used in parts such as the cowl side trim, finish plate, and scuff plate. Toyota Super Olefin Polymer (TSOP), a highly recyclable thermoplastic resin, is used for interior and exterior parts such as the bumper and pillar garnish.

Furthermore, a system for recovering all of the hybrid batteries has been established, and in order to make disassembly of recyclable parts more efficient, marks to make disassembly easier have been added to large parts.

4.2 Life cycle assessment (LCA)

For the Prius, an LCA was performed to evaluate the total environmental impact of materials, parts, vehicle production, driving, maintenance, and disposal (**Fig. 21**). Emissions of CO_2 and other atmospheric pollutants have been reduced, not just during the usage period, but also for the entire life cycle from production to disposal.

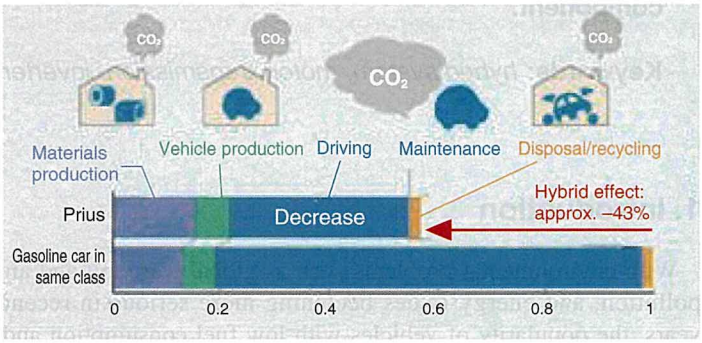


Fig. 21 Prius LCA Evaluation (Example of CO_2)

5. Conclusion

Since its release, sales of the third generation Prius have been boosted in many countries by tax reductions for environmentally sound vehicles and scrapping incentives, and the vehicle has recorded strong sales well in excess of targets. Clearly, from this point on, cars will be expected to have even better environmental performance.

In the future, it will be important to make efforts to use various fuels and energy sources in order to adapt to alternative fuels, contribute to CO_2 reduction, and protect the atmosphere. Against this background, hybrid technology has a wide range of applicability, to which all types of engine and powertrain technology can be adapted. The Prius will continue to serve to further advance the THS as a key technology of the future.

Authors


A. OTSUKA


T. YAMAZAKI

Hybrid Technologies in the Third Generation Prius

Hideaki Yaguchi*
Takeshi Murakami**
Ken Asakura***
Tetsuro Kuzuya****
Toshiya Hashimoto*

Abstract
This article describes the hybrid system installed in the third generation Prius. The system structure is based on the THS II developed for the previous generation, and each component has been newly designed to further improve fuel economy. In addition to basic fuel economy, the development improved actual fuel economy in winter and at high speeds, and reduced the size and weight of the system to allow application to a wide variety of models. The sections below detail the performance of the hybrid system and the new technologies used in each component.

Keywords: *hybrid system, motor, transmission, inverter, engine*

1. Introduction

With environmental problems such as global warming and air pollution, and energy issues becoming more serious in recent years, the popularity of vehicles with low fuel consumption and low emissions such as hybrid vehicles is expected to increase.

The system efficiency of the third-generation Prius that was launched in May 2009 was maximized to improve actual fuel economy in winter and at high speeds, as well as basic fuel economy. Furthermore, to encourage as many customers as possible to choose hybrid vehicles, the size and weight of the hybrid system was reduced to allow its application to a wide variety of models. This article describes the new hybrid system technologies used in the third-generation Prius.

2. Development Aims

2.1 Improving fuel economy

The fuel economy improvement of hybrid vehicles during city driving is achieved by the following basic features: i) idle stop, ii) regenerative braking, and iii) EV mode operation during low-load driving. However, it has been pointed out that the fuel economy in winter and at high speeds is not as good as that achieved during city driving. This is because items i) and iii), which are basic features of hybrid vehicles, are not effective at high speeds, and the opportunity to make use of item ii) is reduced. Furthermore, items i) and iii) are restricted in winter by the energy demand from the heater, which uses the engine coolant as its heat source. In developing the latest system, the objective was to improve the fuel economy in winter and at high speeds, in addition to further improving the basic fuel economy during city driving.

2.2 Improving system applicability

Replacing conventional vehicles with hybrid vehicles with better environmental performance would help reduce emissions of CO_2 and other exhaust gases in urban areas. Therefore, one aim in developing the new system was to reduce the size and weight of each component to allow its application to a wide variety of models.

2.3 Reducing exhaust emissions

Reducing the exhaust emissions of current automobiles is a requirement for lowering air pollution in urban areas. The new system was developed to satisfy the strictest exhaust emissions standards in the world. Another aim was to reduce emissions (CO_2) on actual roads by keeping the air-fuel ratio in the engine in the stoichiometric region at all times.

3. System Configuration

Fig. 1 and **Table 1** show the system configuration and system specifications, respectively. Using the boost system adopted in the previous model as the base, both the engine displacement and system voltage were increased, and a motor reduction device was adopted.

* Hybrid Vehicle Management System Development Div.
** Engine Engineering Div. 2
*** Hybrid Vehicle Power Train Development Div.
**** Drivetrain Engineering Div. 3

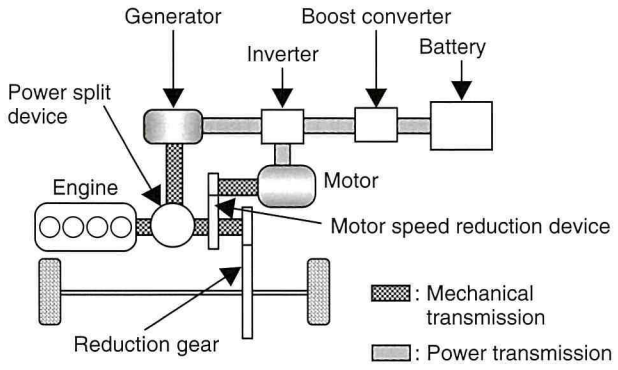


Fig. 1 THS II System Configuration

Table 1 HV unit specifications

		New	Old
Engine	Displacement	1.8 L	1.5 L
	Maximum power	73 kW	57 kW
	Maximum torque	142 Nm	115 Nm
Motor	Maximum power	60 kW	50 kW
	Maximum torque	207 Nm	400 Nm
	Maximum rpm	13,500 rpm	6,400 rpm
	Maximum voltage	650 V	500 V
	Reduction gear ratio	2.636	—
Battery	Type	Nickel-metal hydride	
System power	Maximum power	100 kW	82 kW

The engine displacement was increased from 1.5 to 1.8 liters. The efficiency of the engine itself increases as the S/V ratio is reduced by a larger displacement. Generally speaking, fuel economy worsens as the displacement is increased, but this is because previously, the engine had to be used even during light-load periods when efficiency was poor. In contrast, the THS II can stop the engine when the load is light, enabling EV mode operation. Therefore, the engine is used only when its efficiency is high, leading to improved fuel economy.

A reduction device was used for the motor to reduce the system size and weight. Details are described in Section **5.1** below.

The maximum system voltage was increased from 500 V to 650 V. Increasing the voltage makes it possible to reduce the motor size while increasing power. Furthermore, since this also allows the motor drive current to be decreased, heat dissipation from the inverter and device size are reduced, with the result that the inverter itself can also be made more compact.

These steps were adopted to improve the efficiency of the system and reduce its size and weight, while simultaneously improving power from 82 kW to 100 kW. Consequently, the system can also be applied to vehicles heavier than the Prius. As a result, the powertrain performance of the Prius improved to a level equivalent to that of a 2.4-liter gasoline-powered vehicle.

4. Engine

Fig. 2 shows the fuel consumption rate. The 2ZR-FXE engine installed in the third-generation Prius achieves lower fuel consumption over a wider operational range, owing primarily to the adoption of the following items.

- Atkinson cycle
- Coordinated control between the cooled exhaust gas recirculation (EGR) and variable valve timing-intelligent (VVT-i) systems
- Friction reduction in the electric water pump

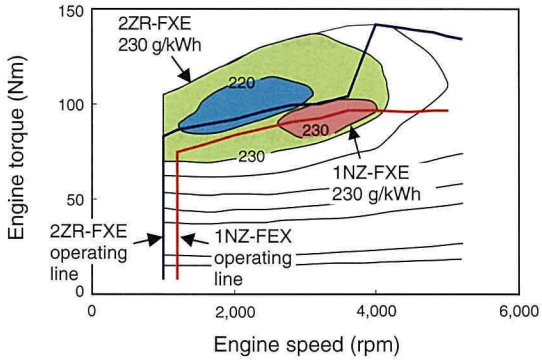


Fig. 2 Fuel Consumption Rate Map

4.1 Increasing displacement

Because engine speed increases during high-speed operation, a 1.5-liter engine will operate outside the minimum fuel consumption region shown in **Fig. 2**. Therefore, the engine displacement was increased to 1.8 liters to lower the rpm and expand the vehicle speed range that operates in the minimum fuel consumption region. This improved fuel economy at high speeds.

4.2 Atkinson cycle

In order to improve thermal efficiency, the same high expansion ratio cycle was adopted as in engines for previous hybrid vehicles. Setting the mechanical compression ratio to 13.0 and delaying the timing for closing the intake valve lowered the effective compression ratio, thereby avoiding knocking and improving the thermal efficiency.

Fig. 3 shows the effects of the Atkinson cycle at typical points in city driving. An improvement of 8.5% in fuel economy was achieved over the base 2ZR-FE.

Furthermore, the use of the newly adopted cooled EGR system improved the fuel economy by an additional 1.7% over the use of the Atkinson cycle alone.

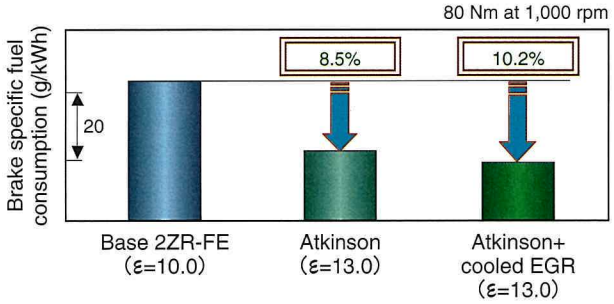


Fig. 3 Effects of Atkinson Cycle and Cooled EGR System

4.3 Coordinated control between cooled EGR and VVT-i systems

Fig. 4 shows an external view of the cooled EGR system. It was possible to advance the spark timing by significantly cooling the gas in the EGR system, thereby further improving fuel economy. In hybrid engines, which utilize the high-load region, the intake air temperature can be prevented from rising by cooling the gas in the EGR system. This expands the knocking threshold, improves power, and lowers the exhaust temperature.

Furthermore, in this engine the fuel economy improvement effect was maximized in accordance with driving conditions by coordinating VVT with the EGR system.

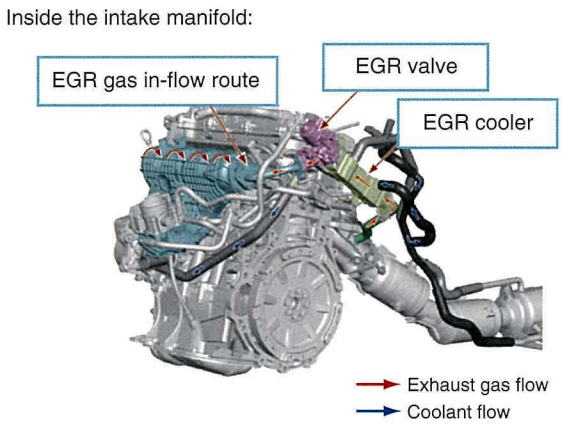


Fig. 4 Cooled EGR System

Fig. 5 shows the relationship of the fuel consumption rate and pumping loss with the EGR rate and the VVT advance angle in the low-load region. At low-load, the effect of pumping loss is significant. Therefore, greater fuel economy can be achieved by maximizing the pumping loss reduction effect by retarding the VVT angle to introduce a large volume of exhaust gas rather than increasing the actual compression ratio by advancing the VVT angle.

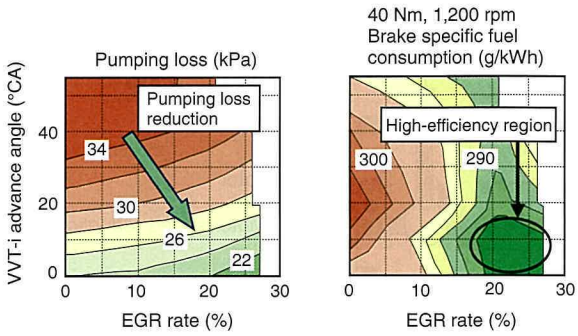


Fig. 5 Effect of EGR System and VVT

Fig. 6 shows the relationship of the fuel consumption rate and spark timing with the EGR rate and VVT advance angle in the high-load region. The combustion temperature was lowered by introducing the cooled EGR system, and the fuel economy was improved by advancing the spark angle.

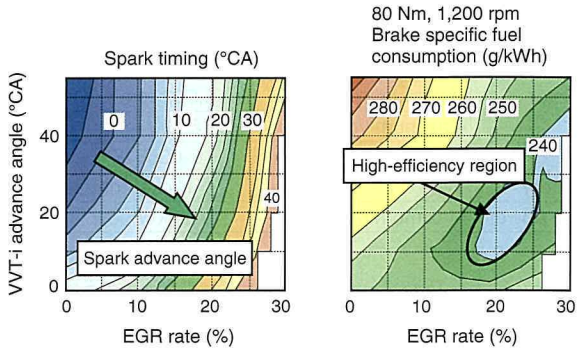


Fig. 6 Effect of EGR System and VVT

This engine achieved the minimum fuel consumption over a wider operational range by coordinating the pumping loss reduction due to the EGR system in the low-load region with the actual compression ratio improvement created by VVT in the high-load region.

4.4 Electric water pump

In order to improve fuel economy by increasing the efficiency of the cooling system, an electric water pump and heat recovery unit were adopted. **Fig. 7** shows the cooling system.

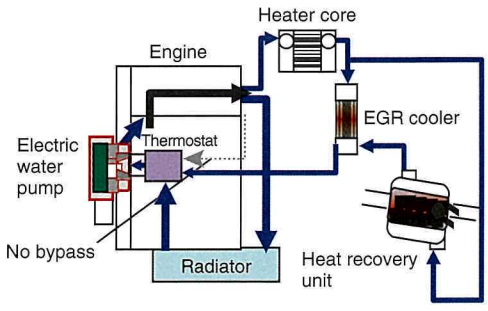


Fig. 7 Cooling System

The electric water pump provides the following six primary benefits:

- Reduced friction by eliminating the accessory drive belts.
- Reduced water pump power requirement by optimizing the discharge volume.
- Improved heating performance by optimizing the heater flow rate.
- Improved fuel economy in the low/medium-load region and suppressed knocking in the high-load region.
- Shorter warm-up period by reducing the volume of coolant circulated following a low-temperature startup.
- Eliminated maintenance by eliminating the accessory drive belts.

Steps such as the optimization of tubing reduced the flow rate by 60% compared to a conventional water pump.

4.5 Friction reduction

Fig. 8 shows the breakdown of engine friction reduction compared to a conventional engine. The switch to the electric water pump allowed the elimination of the accessory drive belts, which led to a significant friction reduction.

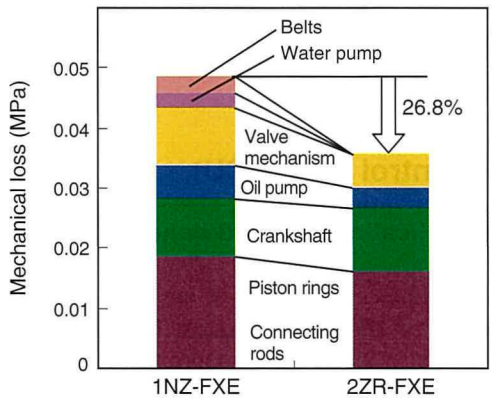


Fig. 8 Friction Reduction Breakdown

4.6 Engine summary

Fuel efficiency was improved over the conventional 1.5-liter gasoline engine while improving power performance and reducing emissions.

5. Hybrid Transmission

A new hybrid transmission was developed for use in compact-class vehicles. The newly adopted motor reduction device increases power and torque while shortening the overall length of the motor. Additionally, placing the compound gear on the outside of the motor reduction device and power split device enables a 3-axis structure and reduces size.

Fig. 9 shows a sectional diagram of the transmission.

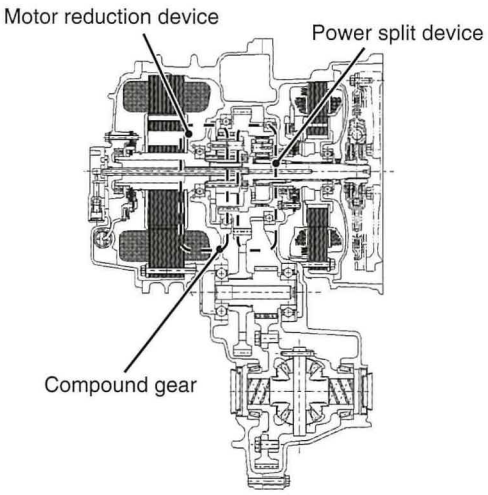


Fig. 9 Sectional Diagram of Transmission

5.1 Motor reduction device

The number of teeth on each gear of the motor reduction device is 22 for the sun gear, 18 for the pinion gear, and 58 for the ring gear, with the reduction rate set to 2.636. As a result, the motor torque is amplified 2.636 times by the ring gear (compound gear).

The motor reduction device supports high rotation speed, low-torque specifications for the motor as shown in **Fig. 10**. Since motor size is nearly proportional to total torque, the motor reduction device also enabled the motor size to be reduced.

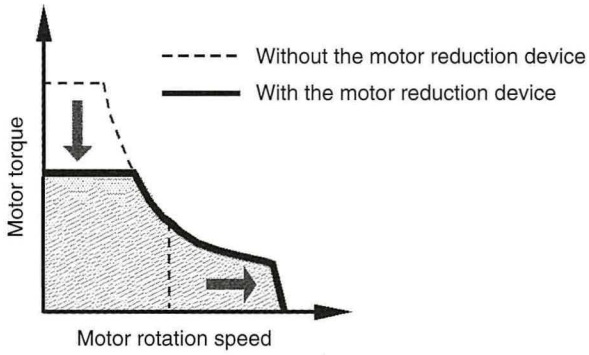


Fig. 10 Motor Size Reduction by Motor Reduction Device

5.2 Compound gear

The compound gear consists of two ring gears, a counter drive gear, and a parking gear, resulting in a compact size. Furthermore, since the bearing that supports the compound gear was placed on the outside of the planetary gear, there was no need to increase the total length of the transmission to accommodate the bearing. In contrast, however, the bearing for supporting the counter drive gear increased in diameter. This resulted in a higher circumferential speed and its durability had to be improved.

Because the compound gear has a large-diameter cylindrical shape, which in turn consists of four gears, difficulties in machining and distortions from heat treatments were expected. The necessary precision and strength were achieved by improving the processing method and heat treatment method.

5.3 Motor size reduction

A new drive motor was developed by combining a stator with a 3-phase, AC, 8-pole, 48-slot distributed winding with an embedded magnet-type rotor. The use of a high-energy magnet for the rotor reduced the motor body size and mass. For the stator, new compression molding technologies, including a new coil wire winding method and a pre-processing method, were developed to shorten the length of the coil end by 20%. The drive motor was reduced by 35% in weight, 40% in volume, and 30% in total length.

For the motor generator, a stator with a 3-phase, AC, 8-pole, 12-slot concentrated winding was developed. The length of the coil end was reduced by 30% through measures such as modularization of the winding cassette coil, modularization of the terminal to reduce the size of the terminal processing area, and the use of resin molding to strengthen the cooling performance.

As a result, the newly developed motor is 20% lighter and 10 mm shorter than the previous version.

5.4 Low fuel consumption

Through improvements in the motor, the newly developed transmission simultaneously achieved compact size, high power, and low loss. The items adopted in order to reduce motor loss are described below.

Fig. 11 shows the distribution of motor operating points during city driving. It indicates that the motor operation frequency is high in the low-load region.

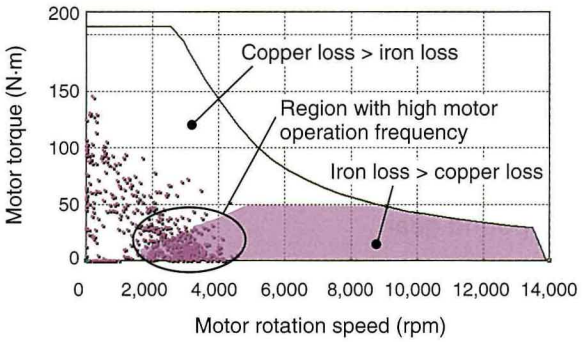


Fig. 11 Distribution of Motor Operating Points During City Driving

However, in terms of the motor loss in the low-load region with high operating frequency, iron loss, which is a form of energy loss that occurs in the iron core, is greater than copper loss, which is Joule heat produced in the coil. Therefore, addressing iron loss is important for improving fuel economy.

Fig. 12 shows the rotor magnet positioning on the rotor. In the newly developed product, the reluctance torque was significantly improved by optimally positioning the permanent magnets in a V shape, thus reducing iron loss during low load. Additionally, since iron loss increases roughly proportionally to the square of the frequency, high-frequency components were reduced by providing dips on the perimeter of the rotor core. This also contributed significantly to reducing iron loss.

In terms of strength, providing ribs in the center of the magnets and securing the magnets using molded resin made high-speed rotation possible.

With respect to materials, 0.3 mm electromagnetic steel plates were used instead of the conventional 0.35 mm electromagnetic steel plates, achieving a significant loss reduction.

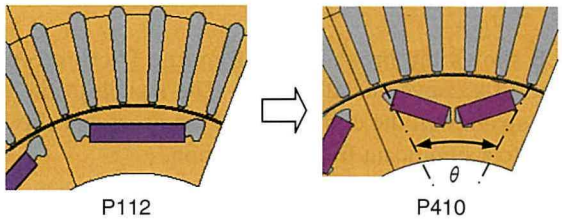


Fig. 12 Permanent Magnet Positioning on Rotor

6. Power Control Unit (PCU)

6.1 Main specifications of third-generation PCU

Fig. 13 shows the configuration of the third-generation PCU. As the power of the HV system increased, the maximum power of the PCU was also increased by approximately 10%. On the other hand, it was possible to reduce the rated current of the inverter for the motor from 230 Arms to 170 Arms by adopting a high-voltage, high-speed motor, thus reducing the size and losses in the power semiconductor devices.

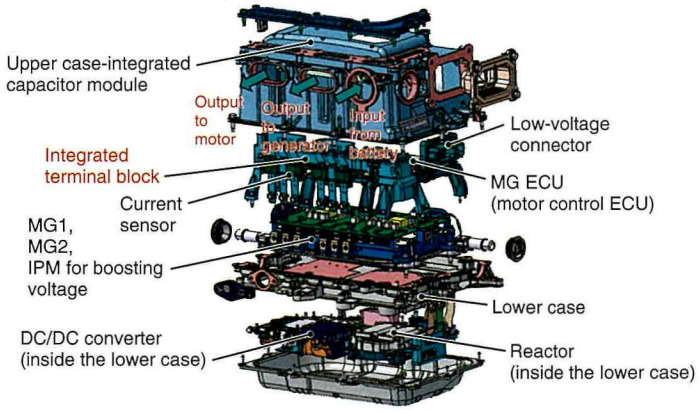


Fig. 13 Configuration of Third-Generation PCU

To reduce both the size and weight of the PCU, a direct cooling structure was used for the IPM, a thinner-film capacitor was adopted, the DC/DC converter power density was improved, and the space utilization efficiency was increased. As a result, the third-generation PCU is 37% smaller in volume and 36% lighter than the second-generation version (**Fig. 14**).

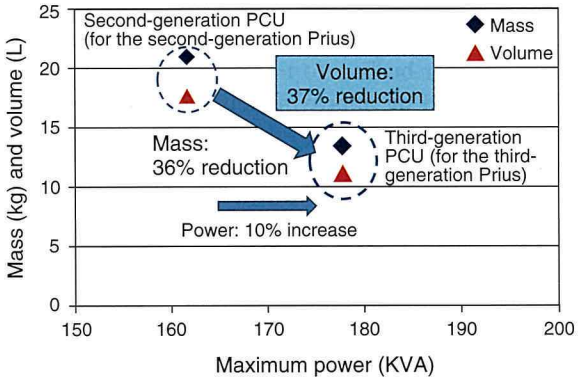


Fig. 14 Reductions in Mass and Volume of PCU

6.2 Intelligent power module (IPM)

For the third-generation IPM, a direct-cooling structure was developed in which an insulating board with mounted devices is brazed directly onto a cooling unit. This structure simultaneously achieves a significant improvement in cooling efficiency through the elimination of heat dissipation grease. It also established a new technique for preserving heat cycling performance without the use of copper alloy heat-dissipation plates. **Fig. 15** shows the direct-cooling structure.

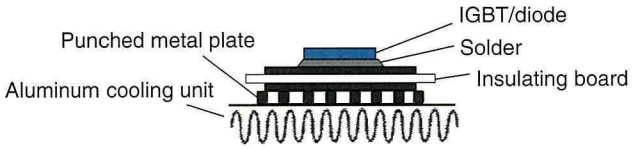


Fig. 15 Sectional Diagram of Third-Generation IPM

One problem with the direct cooling structure was the fact that the thermal stress in the cooling unit (made of aluminum), which has a large coefficient of linear expansion, was applied directly to the insulating board, deteriorating the heat cycling performance. Therefore, a structure was adopted in which the insulating board was brazed to the cooling unit via a punched metal (aluminum) plate to absorb thermal distortion. The punched metal plate is optimally provided with multiple holes. As a result, it was possible to significantly reduce thermal distortion during heat cycling based on the distortion of these holes while minimizing deterioration in thermal resistance. Consequently, a level of heat cycling performance equivalent to the conventional structure was maintained and cooling efficiency was improved by 30% compared to the second-generation IPM.

Furthermore, the third-generation PCU also features an integrated IPM for boosting voltage that is equivalent in size to the IPM for the second-generation motor/generator. This helped reduce the PCU size. Additionally, by eliminating the copper-alloy heat-dissipation plates, both weight and cost were reduced. **Fig. 16** shows the third-generation IPM.

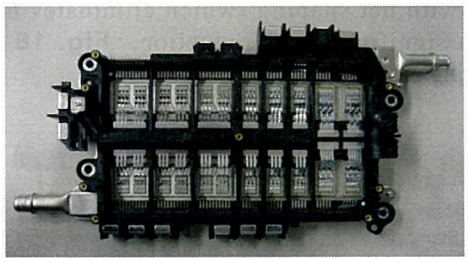


Fig. 16 Third-Generation IPM

6.3 Insulated gate bipolar transistor (IGBT)

To reduce the size of the third-generation PCU while increasing power and efficiency, a trench-type gate and thin-film technology was adopted in the IGBTs (**Fig. 17**) for the motor and the generator. Normally, the withstand voltage of a device and its steady-stage loss have a tradeoff relationship. However, by utilizing a technique to reduce the Si substrate region, which acts only as a resistance element, the device thickness was reduced by 60% compared to a conventional device. This reduced the steady-state loss by 25% and improved the withstand voltage by 50%. The improvement in the withstand voltage increased the IGBT switching speed, helping reduce switching losses.

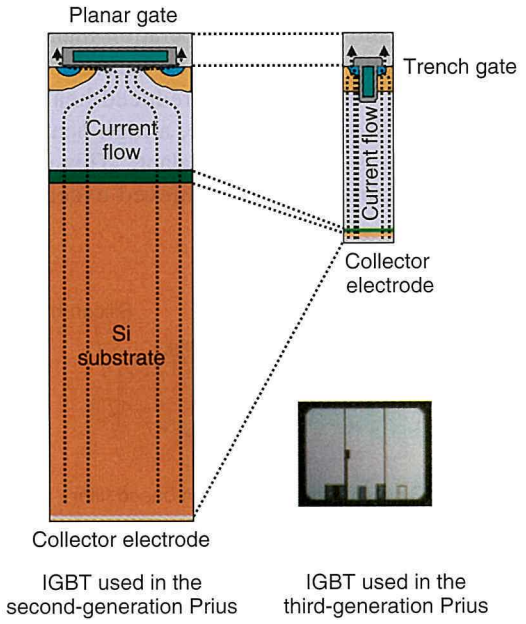


Fig. 17 Sectional Diagram of IGBT

6.4 Reactor

For the reactor, a new high-density magnetic composite (HDMC) core was developed. This core was formed from iron powder with an insulating layer and maintained the same performance level as the conventional electromagnetic steel plates it replaced. Simplification of the manufacturing process combined with net shaping (which eliminates machining) resulted in significant cost reduction. **Fig. 18** shows the manufacturing process.

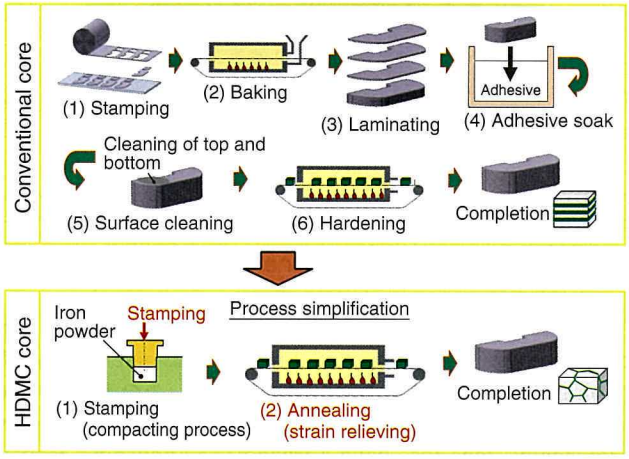


Fig. 18 Comparison of Core Manufacture Processes

Since an HDMC core has larger magnetostriction than a conventional core, external magnetic field fluctuations can cause large vibrations, making noise a problem. In other words, developing a low-vibration structure became a major issue. For the new reactor, a core with a floating structure was used instead of one secured to the case, thereby preventing the transmission of vibrations and achieving quieter operation than the existing model. **Fig. 19** shows the floating, low-vibration propagation structure. To allay concerns about reduced heat dissipation performance of the floating structure, a high-heat-conducting silicon-based resin was used as the sealant. This improved the heat dissipation performance and achieved excellent thermal performance.

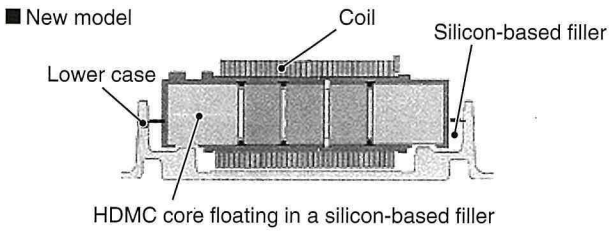


Fig. 19 Sectional Diagram of Third-Generation Reactor

6.5 Capacitor module

The capacitor module consists of a smoothing capacitor for smoothing the voltage for controlling the motor and a filtering capacitor for smoothing the voltage of the high-voltage rechargeable battery. A newly developed thin film was adopted, which was individually optimized for each of the capacitors. In addition, the number of capacitors was reduced by increasing their size, and space efficiency was improved by thinning the copper busbar (to t=0.8). As a result, volume and mass were reduced by approximately 33% and approximately 40%, respectively, compared to the second-generation capacitor module (**Fig. 20**).

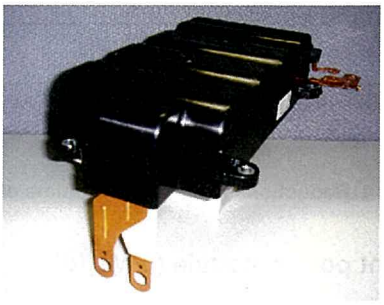


Fig. 20 Third-Generation Capacitor Module

6.6 DC/DC converter

For the third-generation Prius DC/DC converter, the circuit method was changed from the conventional full-bridge method to the boost half bridge (BHB) method. This reduced the number of power devices, simplified the converter control circuit, and reduced power device loss. As a result, size reduction and efficiency improvement were achieved in the normal operating region. The volume was reduced by approximately 30% while improving the maximum power by 20%.

7. Vehicle Performance

Table 2 shows the fuel economy of the third-generation Prius in various modes. Fuel economy improvements of between 7% and 14% were achieved in Japan, the U.S., and Europe.

Table 2 Fuel Economy

	Third-generation Prius	Second-generation Prius
10·15 mode (Japan)	38 km/L	35.5 km/L
U.S. combined	50 mpg	46 mpg
EC mode (Europe)	89 g/km*	104 g/km

*CO_2 emissions

Additionally, **Fig. 21** shows the fuel economy at high speeds and in winter. Fuel economy improvements of between 11% and 19% were achieved over the second-generation Prius. The fuel economy at high speeds is superior to that of conventional diesel-powered vehicles with a manual transmission in terms of both CO_2 emissions (g/km) and mileage (km/L).

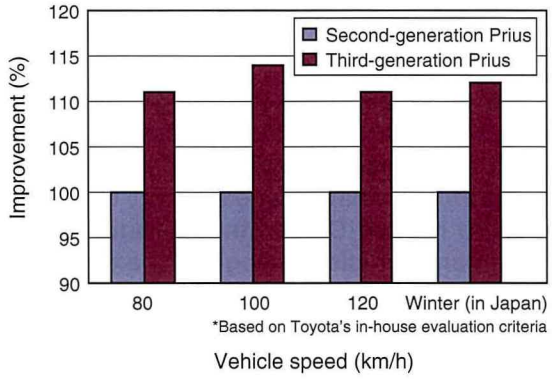


Fig. 21 Fuel Economy at High Speeds and In Winter

To enhance applicability to other models, the drive power margin as a hybrid system was increased. Consequently, dynamic performance was improved by between 14% and 20% compared to the second-generation Prius. As shown in **Fig. 22**, equivalent dynamic performance as a vehicle equipped with a 2.4-liter engine was achieved, contributing to an improvement in commercial appeal.

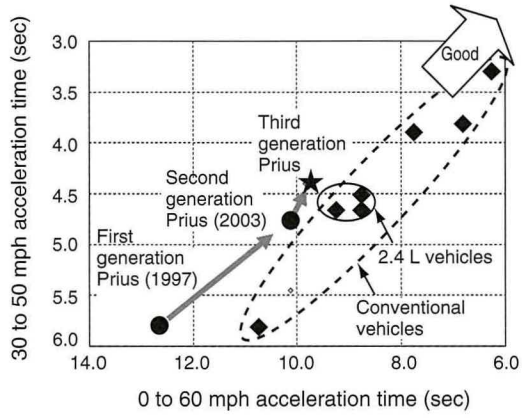


Fig. 22 Dynamic Performance

In addition, following on from the previous generation, the third generation Prius also satisfies emissions regulations such as AT-PZEV in the U.S., Step 5 in Europe, and J-SULEV in Japan.

References

(1) T. Hashimoto et al. "Development of New Hybrid System for Compact Class Vehicles." *JSAE Annual Congress (Spring)* (2009).
(2) T. Matsubara, Yaguchi, Takaoka, Jinno. "Development of New Hybrid System for Compact Class Vehicles." *SAE Paper* 2009-01-1332 (2009).

Authors


H. YAGUCHI


T. MURAKAMI


K. ASAKURA


T. KUZUYA


T. HASHIMOTO

Aerodynamic Technologies Adopted in the Third Generation Prius

Hiroyuki Yamasaki*
Yumiko Toki*
Toshiyuki Murayama*

Abstract
Some of the most important factors supporting the fuel economy performance of the third generation Prius are its technologies for reducing aerodynamic drag. The third generation Prius has a coefficient of drag (C_D) of 0.25, which is among the best in the world. Three concepts were applied to improve aerodynamic performance: (1) smooth convergence of airflow behind the vehicle, (2) adoption of optimized shapes at each part of the vehicle, and (3) the achievement of total aerodynamics. Various proposals to reduce C_D continually and over a wide range were made at each stage of the development process from primary vehicle packaging to exterior styling, parts designing, and manufacturing.

Keywords: *aerodynamic performance, environment, fuel economy, packaging, exterior styling, CO_2*

1. Introduction

The Kyoto Protocol ratified in 1997 contained a proposal to reduce the emissions of greenhouse gases, including CO_2. Since the transportation sector accounts for approximately 1/4 of total CO_2 emissions, reducing emissions from cars is an important and urgent issue.

In developing the latest, third-generation Prius, the aim was to reduce the C_D compared to the second-generation Prius to help achieve a substantial improvement in fuel economy. This article details the technologies employed to improve the aerodynamic performance of the third-generation Prius.

2. Importance of Reducing Coefficient of Drag and Aims of Development

Decreasing running resistance is vital for improving fuel economy. Factors that add to running resistance include resistance to acceleration, which is affected by the vehicle weight, the rolling resistance of the tires, driving resistance when the engine's drive force is transmitted, slope resistance from gradients in the road, and aerodynamic drag (**Fig. 1**).

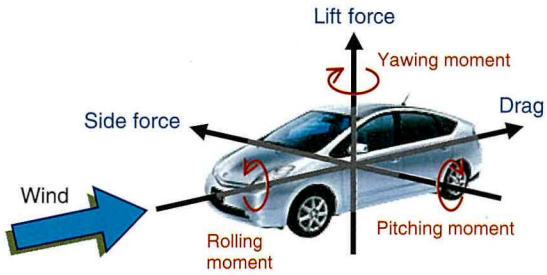


Fig. 1 Six Components of Aerodynamic Force

The amount of work (W_{aero}) performed against the aerodynamic drag can be expressed using Equation 1.

$$W_{aero} = \int_{t0}^{tf} F_{D(t)} \cdot V_{(t)}\, dt \quad (1)$$

$$F_{D(t)} = \frac{1}{2} \rho V_{(t)}^2 \cdot C_D \cdot A \quad (2)$$

where,

F_D: force in front-rear axle direction (N)
ρ: air density (kg/m^3)
V: vehicle speed (m/s)
A: frontal area (m^2)
t: time (sec)

As can be seen from these equations, since C_D is proportional to the cube of the speed (while aerodynamic drag is proportional to the square of the speed), the greater the speed, the greater the impact of the aerodynamic drag.

* Vehicle Evaluation & Engineering Div. 1

Fig. 2 shows the relationship between the vehicle speed and running resistance in the Prius. At a constant speed of 120 km/h, the aerodynamic drag accounts for approximately 80% of the running resistance, representing a significant impact on the vehicle's fuel economy.

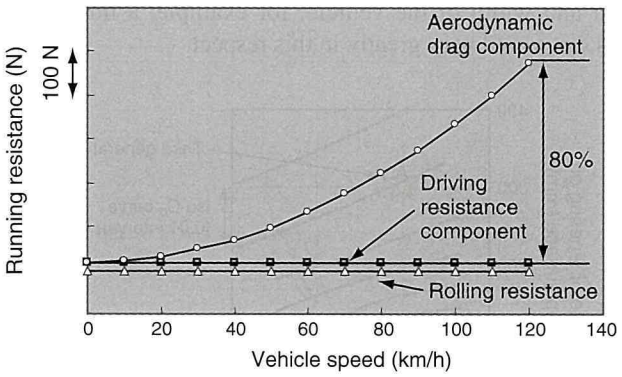


Fig. 2 Vehicle Speed and Running Resistance

Historically, developments in aerodynamic technologies have improved the C_D of passenger cars year after year as shown in **Fig. 3**. Technical developments spurred by the oil shocks resulted in cars that broke through the C_D barrier of 0.30, a value considered the limit in the 1980s but now commonplace with even large-size sedans. In 2000, Toyota achieved a C_D value of 0.25 in the Lexus LS. More recently, however, the reduction rate seems to have slowed or even hit bottom.

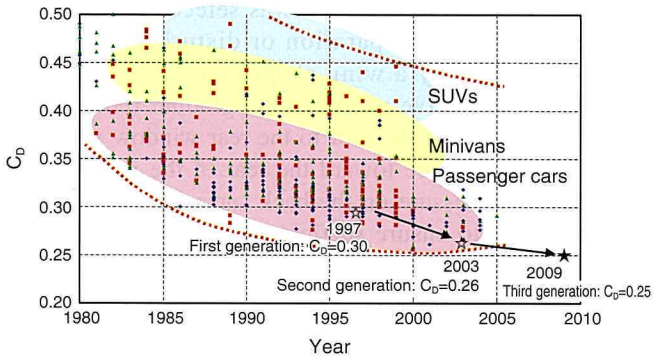


Fig. 3 C_D Trends

The aerodynamic drag (C_D) of the Prius was improved from 0.30 for the first generation to 0.26 for the second generation. The first-generation Prius established Toyota's direction for compact car packaging, with the implementation of various measures such as improved aerodynamic characteristics of the vehicle platform, a flattened floor, and spats installed in front of the tires.

In the second generation, Toyota adopted the so-called "triangle silhouette," which became one of the defining features of the Prius, creating an external shape that conveyed excellent aerodynamic and environmental performance. Furthermore, by adding an aerodynamic undercover to the floor, Toyota further flattened the floor, achieving the highest aerodynamic performance in its class.

With the third-generation Prius, Toyota set out to reduce the aerodynamic drag by approximately 5%, with the goal of achieving a C_D of 0.25, one of the lowest in the world.

To achieve this goal, the Prius development incorporated the technologies described below into the vehicle.

3. Aerodynamic Development Concept for the Third Generation Prius

More than 90% of the aerodynamic drag of a blunt-nosed object such as an automobile consists of pressure drag. However, frictional drag, which is the main issue with sharp-nosed airplanes and bullet trains, accounts for less than 10% of the total drag of an automobile because of differences in size and speed. Thus, to reduce an automobile's aerodynamic drag, it is more effective to focus on the areas with greater pressure drag. The key is improving the rear end, which causes most of the pressure drag in a blunt-nosed vehicle, and restoring the pressure as quickly as possible behind the vehicle.

One of the unique aerodynamic characteristics of an automobile is the fact that its body moves close to the ground. Unlike an airplane traveling through a vast space, less air flows under the automobile, resulting in asymmetrical air flows at the top and bottom behind the body (**Fig. 4**). As a result, the side air flows also converge downward, and therefore it is important to align the air flows on the three surfaces, which have different flow speeds, in order to promote pressure recovery behind the vehicle (**Fig. 5**).

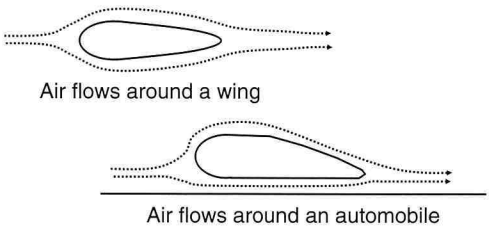


Fig. 4 Air Flows Around Objects

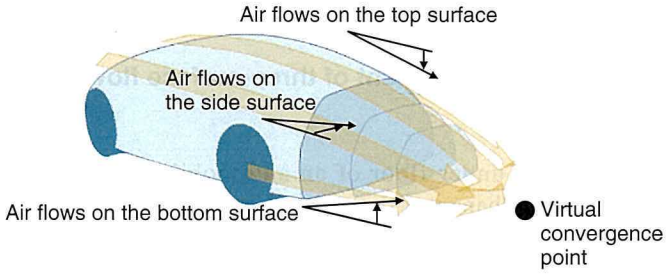


Fig. 5 Convergence of Air Flows from Three Surfaces

The following three aerodynamic development goals were set for the Prius.

(1) To consider a balanced air-flow division that will promote the best pressure recovery upon the convergence of the three air flows behind the vehicle.
(2) To achieve the best possible pressure recovery and smoothing of the three air flows on the three surfaces of the vehicle.
(3) To achieve total aerodynamics (both kinetic performance and driving/riding comfort).

Since the process of achieving these goals would be closely related to the overall vehicle concept, styling, and performance, it was crucial to achieve a balance between aerodynamic performance and other requirements beginning at the packaging development phase in the planning department. Furthermore, since air flows are nonlinear and can change drastically once a certain threshold is exceeded, the robustness of the air flows was also an important area of focus during the development.

The development items and the measures implemented are summarized below (**Fig. 6**).

(1) Overall:
Managing the convergence of the flows on the three surfaces
(2) Smoothing the flow on the top surface and recovering the pressure:
Shape leading from the roof to the rear spoiler (optimizing the triangle silhouette)
(3) Smoothing the flow on the side surfaces:
Front bumper shape, wheel shape, front pillar shape, combination tail light shape, and rear bumper shape
(4) Smoothing the flow on the bottom surface:
Managing the distance of parts from the ground
Optimizing the shapes of parts such as covers and spats
(5) Optimizing the cooling flow inside the engine room
Details of the measures implemented for each development item are described below.

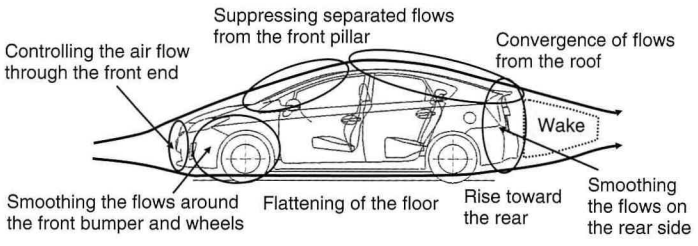


Fig. 6 Aerodynamic Development Items in the Prius

3.1 Overall: management of three-surface flow convergence

Because the under floor of an automobile is close to the ground, a wing shape that is convex on the top is the ideal shape, and the slower bottom flow must be smoothly merged with the flows from the top and side surfaces behind the vehicle. **Fig. 7** shows the relationship between C_D and the degree of tapering on the top and side surfaces on a vehicle the size of the Prius. It can be seen that tapering on the top surface is more effective than on the side surfaces. As described below in the optimization of the top-surface flow, recovering the pressure on the top surface and reducing the flow velocity can suppress the generation of eddy currents during the convergence with the flows on the other two surfaces. Note that the iso-C_D curve differs depending on the height and width of the vehicle; for example, a minivan and a sports car would vary greatly in this respect.

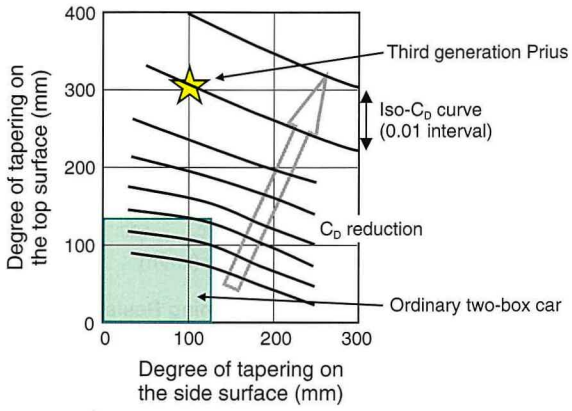


Fig. 7 Relationship between C_D and Degree of Tapering on Top and Side Surfaces

3.2 Top surface flow smoothing and pressure recovery (triangle silhouette optimization)

The triangle silhouette is one of the defining appearance characteristics of the Prius. It was selected to achieve both air flows with little separation or disturbance (which can be accomplished by a wing shape) and a cabin space that comfortably seats five people. The gradual reduction in the vehicle's height from the roof to the rear window was designed to recover the pressure toward the rear of the vehicle, in order to increase the pressure on the back surface of the vehicle. At the same time, to ensure sufficient headroom for the vehicle occupants, it was important to recover the pressure within an extremely short distance.

Figs. 9 and **10** show the roof sloping angles and the flows around the body using the bluff body shown in **Fig. 8**. When the roof sloping angle is 15 degrees, the flow from the roof follows along the downward-sloping surface. In contrast, when the roof sloping angle is 22.5 degrees, the flow does not easily follow the downward-sloping surface.

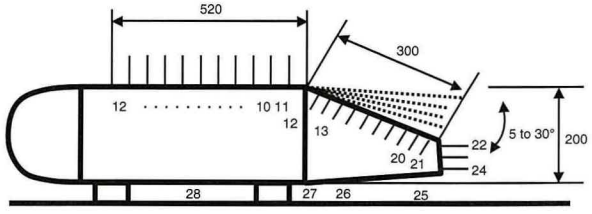


Fig. 8 Bluff Body



Fig. 9 Stream Line (Sloping Angle of 15 Degrees)

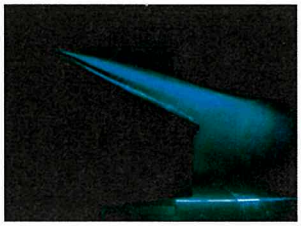


Fig. 10 Stream Line (Sloping Angle of 22.5 Degrees)

Fig. 11 shows the changes in the pressure on the rooftop at various sloping angles. When the sloping angle is between 5 and 20 degrees, the pressure on the downward-sloping surface of the roof recovers, and the greater the angle, the greater the pressure on the back surface. However, since the flow can no longer follow the downward-sloping surface of the roof beginning at 22.5 degrees, the pressure on the roof top surface increases, with no pressure recovery beyond that point.

Utilizing this observation in the actual development, the development worked to optimize the roof shape while preserving the cabin space and maximizing pressure recovery.

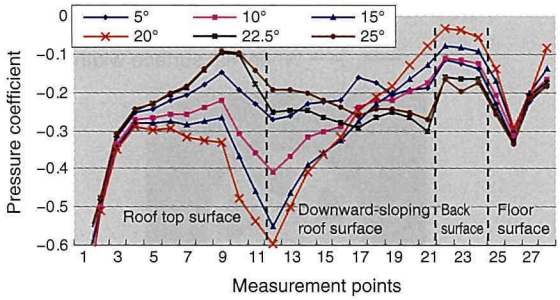


Fig. 11 Bluff Body Surface Pressure

Furthermore, to ensure both sufficient cabin space and pressure recovery, the development of the third generation Prius focused on the position of the vertex of the triangle silhouette, during the development. **Figs. 12**, **13**, **14**, and **15** show the changes in the vehicle back-surface pressure coefficient and the pressure distribution when the roof vertex was moved by 300 mm forward or backward from its position in the second-generation Prius. When the roof vertex is moved backward, it is presumed that there is not sufficient distance to recover the pressure, increasing the negative pressure on the back surface and the C_D.

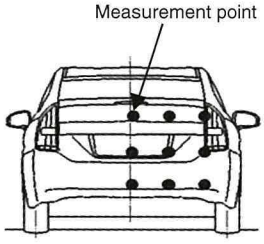


Fig. 12 Pressure Measurement Positions

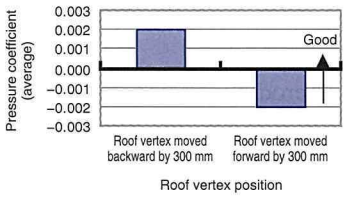
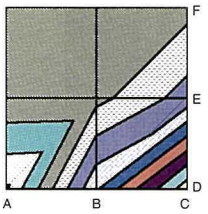


Fig. 13 Changes in Back-Surface Pressure



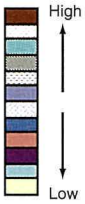


Fig. 14 Back-Surface Pressure (Roof Vertex Moved Forward by 300 mm)

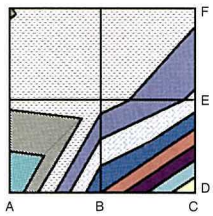


Fig. 15 Back-Surface Pressure (Roof Vertex Moved Backward by 300 mm)

This problem was resolved by focusing on the shape of the rear spoiler. **Figs. 16**, **17**, and **18** show changes in the rear spoiler angle and rear window surface pressure. The rear window pressure recovers by setting the rear spoiler angle in the direction that receives the flow on the top surface. However, since increasing the rear spoiler angle can also increase the back surface area, there is a limit to how much the angle can be increased. Therefore, the optimum spoiler angle was studied.

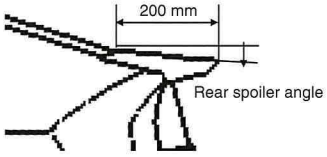


Fig. 16 Rear Spoiler Angle

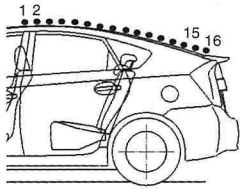


Fig. 17 Pressure Measurement Positions

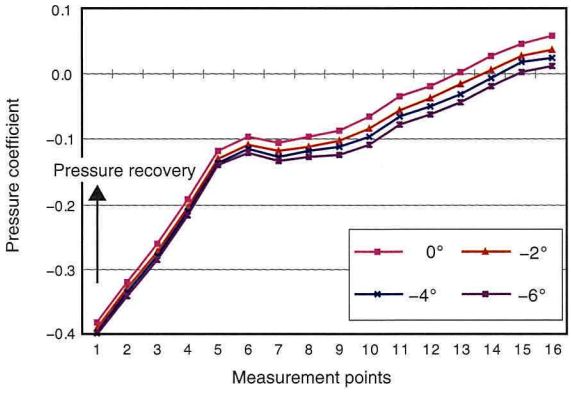


Fig. 18 Rear Spoiler Angle and Rear Window Surface Pressure

Ultimately, a roof vertex position and spoiler angle were selected that both recover back-surface pressure and increase cabin space. The roof vertex was moved in the new packaging by 300 mm from its position in the second-generation Prius (**Figs. 19**, **20**, **21**, and **22**).

Furthermore, decreasing the spoiler angle also reduces the rear lift coefficient (CLr), thus improving driving stability at high speeds. Therefore, the third generation Prius can be seen as an example in which the total aerodynamic performance has been improved.

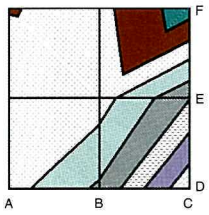




Fig. 19 Back-Surface Pressure (No Rear Spoiler)

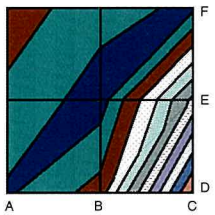


Fig. 20 Back-Surface Pressure (Rear Spoiler: –2 degrees)

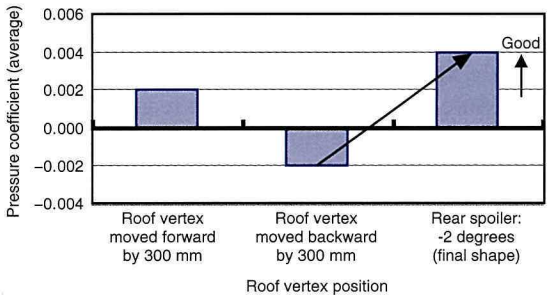


Fig. 21 Changes in Back-Surface Pressure (Final)

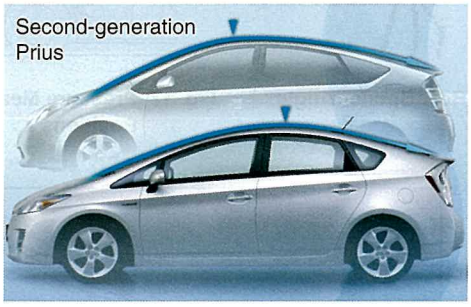


Fig. 22 Roof Vertex Position

3.3 Side surface flow smoothing

Generally, air flows from the gaps between the tires and the fenders in the front wheel housing. As shown in **Fig. 23**, the air surrounding the tire is sucked into the wheel housing from the rear side by the rotation of the tire, and discharged from the front side of the wheel housing. This out flow not only acts as resistance in this location, but also adversely affects the flow convergence behind the vehicle.

To suppress this flow on the Prius, a surface parallel to the tire was provided on the side surface of the front bumper, thereby reducing the disturbance caused by the tire housing. Turn signals and other styling features were incorporated into the bumper, but rounded shapes and low steps were used in order to prevent flow separation (**Fig. 24**). Additionally, a fender liner shape that reduces eddy flow was adopted, along with a flat surface for the wheel (**Figs. 25** and **26**), thereby achieving a smooth side flow.

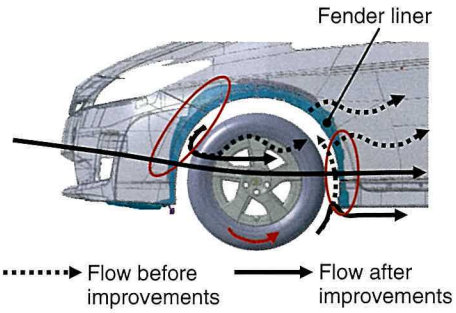


Fig. 23 Flows Around Tire



Fig. 24 Bumper Shape

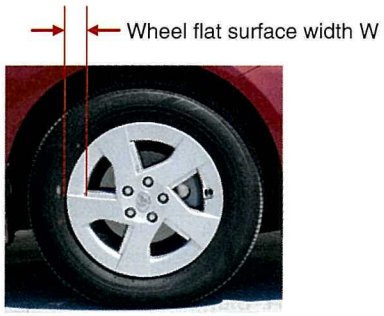


Fig. 25 Aluminum Wheel (15-Inch)

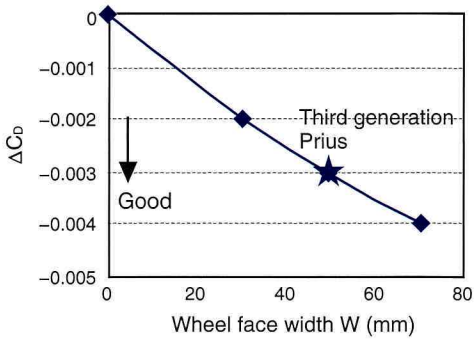


Fig. 26 C_D-Reduction Effect of Wheel Shape

Aerodynamic consideration was also given to the front pillar step. Because the front pillar step causes a large separated flow on the side glass surface, this step was made as small as possible, thereby reducing the C_D (**Figs. 27** and **28**). This change also greatly helped reduce the wind noise generated by the area surrounding the front pillar.

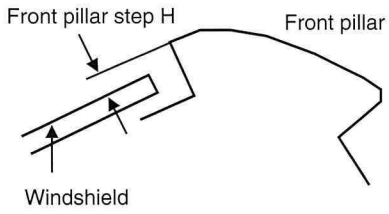


Fig. 27 Front Pillar Step

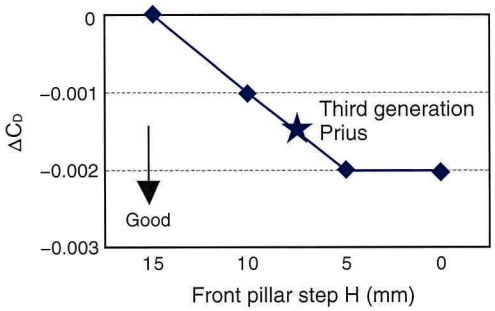


Fig. 28 Reducing C_D by Reducing Step Height

In addition, rear fender and combination tail light shapes that prevent the flow from the front of the vehicle from turning into an eddy current behind the vehicle were adopted. A large radius of curvature in this area would generate an eddy current on the vehicle's back surface, reducing the back-surface pressure. Therefore, the side surfaces of the combination tail light and rear bumper were extended toward the back of the vehicle, and the radius of curvature was shortened (**Fig. 29**).

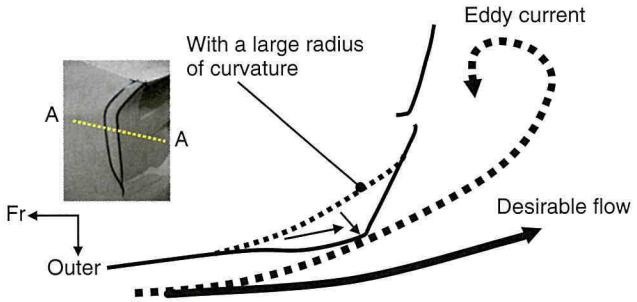


Fig. 29 Aerodynamic Measures Surrounding Rear Side (Section A-A)

3.4 Bottom surface flow smoothing

The basic approach to smoothing the flow under the floor is to allow the flow that enters to exit behind the vehicle without any loss of energy and to let it recover its pressure. However, a wide variety of structures and parts are used under the floor of the vehicle, and the flow is disturbed when it strikes these parts or eddies up into the gaps between them. To resolve this problem, the first step was to control the distances of the under-floor structures and parts from the ground, and then to expand the flat area on the bottom of the floor with the use of covers.

3.4.1 Managing part distance from ground using standard line of aerodynamics

The distance from the ground of the parts and structures under the floor was re-assessed from the viewpoint of aerodynamic performance and a standard line was established (called the "standard line of aerodynamics"). Specifically, by increasing the height of the fuel tank, raising the rear suspension higher than the tank, and raising the spare tire housing surface even higher, lines were established that rise toward the back of the vehicle. The rising line between the wheelbase was set to approximately 0.5 degrees, while the rising line for the rear floor was set to approximately 7 degrees. In this way, under-floor pressure recovery was maximized while accommodating packaging requirements (**Fig. 30**).

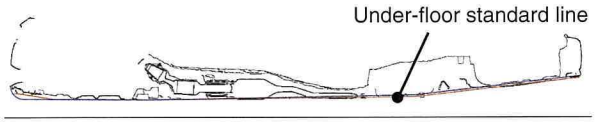


Fig. 30 Standard Line of Aerodynamics (Section of Vehicle Center)

3.4.2 Installing aerodynamic covers

Aerodynamic covers were installed to expand the flat surface areas (**Fig. 31**). For example, the size of the engine undercover and floor covers was increased.

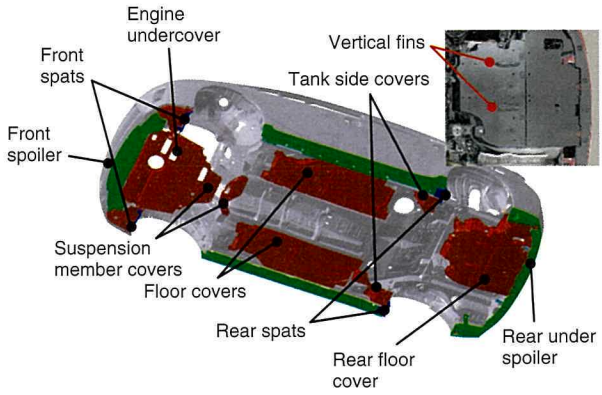


Fig. 31 Aerodynamic Covers

Of course, these measures for smoothing the under-floor flow are also effective in reducing the out flow from the engine room and the out flow to the side surfaces, and therefore contributed greatly to reduce the C_D. The size of the spats in front of the tires was increased and optimized to further smooth the flows surrounding the tires. A large cover was used for the rear floor and vertical fins were added to increase the flow-smoothing effect, thereby reducing the C_D and improving driving stability at high speeds.

3.5 Optimizing cooling flow inside engine room

The air entering the engine room through the openings in the front bumper acts as a flow-through resistance, and moreover adversely impacts the airflow over the entire vehicle. With the third generation Prius, the volume of the incoming air was reduced by decreasing the area of the openings, and installing flow-smoothing plates inside the openings to ensure that the air reaches only the cooling devices such as the radiator. This reduced the flow-through resistance (**Figs. 32** and **33**).

With regard to the air exiting the engine room, a cover was installed behind the front suspension member to ensure that exiting air would converge smoothly and not cause the under-floor flow to eddy up behind the vehicle.

These measures to optimize the cooling flow inside the engine room reduced the C_D, improved the engine cooling performance, and also helped improve driving stability by reducing the front lift coefficient (CLf).

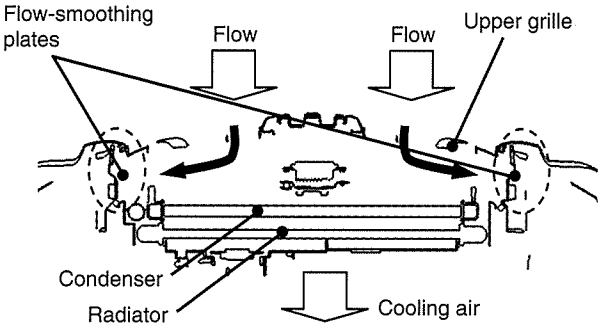


Fig. 32 Smoothing Plates on Front of Radiator (Plane View)

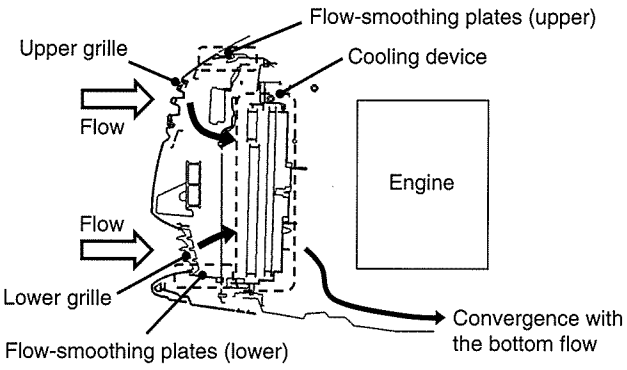


Fig. 33 Smoothing Plates on Front of Radiator (Side View)

4. Achieving Total Aerodynamic Performance

The above sections have discussed the management of air flows on the top surface, side surfaces, bottom surfaces, and in the engine room. At the same time, the development also tried to achieve balance with dynamic performance, wind noise, engine cooling, brake cooling, and performance in special operation environments (**Fig. 34**).

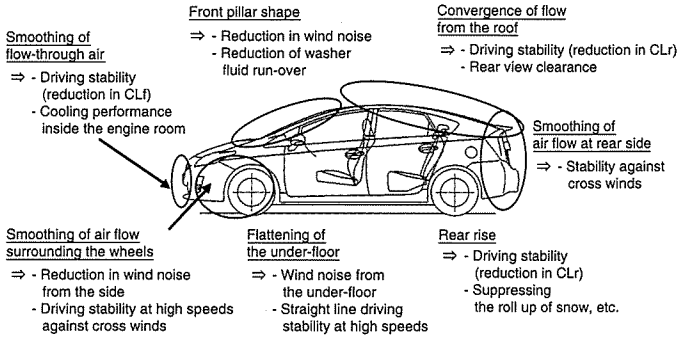


Fig. 34 Total Aerodynamic Performance

In the third generation Prius, all related performance factors were considered as a whole in the development of optimum air flows for the vehicle. As a result, it was possible to reduce the C_D and improve other performance factors at the same time, thereby achieving total aerodynamic performance (**Fig. 35**).

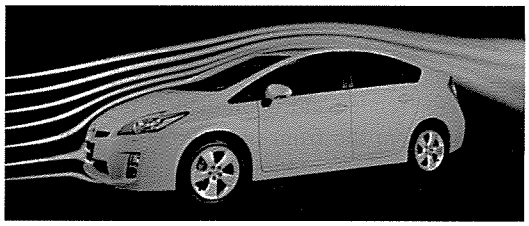


Fig. 35 Overall Stream Lines

5. Conclusion

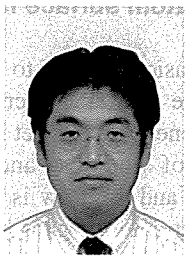
The aim of third generation Prius was to improve aerodynamic performance. To achieve this goal, a wide range of measures were implemented based on the designers' understanding of the vehicle concept, the vehicle packaging, and the overall air flows in and around the vehicle. As a result it was possible to achieve a C_D of 0.25.

In the future, it is hoped to expand the scope of the development based on new perspectives and to continue to make technical improvements and advances toward the next-generation of vehicles.

Authors


H. YAMASAKI


Y. TOKI


T. MURAYAMA

Development of the Third Generation Prius Focusing on Fuel Economy

Issaku Yamada*
Junji Tokieda*
Kunihiko Jinno*
Tetsuya Takechi**
Masakatsu Tsubouchi***
Takato Ishihata***

Abstract
Launched in 1997 and installed with the Toyota Hybrid System (THS), the Prius was the world's first mass production hybrid vehicle. True to its name, the Prius ("to go before" in Latin) has achieved impressive and leading environmental performance. Since its launch, issues such as global warming and soaring oil prices have increased expectations for fuel-efficient hybrid vehicles and particularly the Prius. In addition to mode fuel economy, the third generation Prius has been developed with cutting edge technology to improve fuel economy in practical conditions (actual fuel economy) and to assist fuel-efficient driving.

Keywords: *hybrid, Prius, Fuel economy, Toyota, Environment*

1. Introduction

In 1997, the first-generation Prius, equipped with the Toyota Hybrid System (THS), was launched as the world's first mass-production hybrid vehicle. The second-generation Prius, equipped with the THS II and introduced in 2003, featured enhanced powertrain performance along with a further improvement in fuel economy, and was received positively in the market (**Fig. 1**). However, as oil prices have soared worldwide and people's awareness about the environment has increased, the market is demanding even greater improvements in fuel economy.

Responding to this need, Toyota has employed cutting-edge technologies in the third-generation Prius and achieved a significant improvement in fuel economy by thoroughly reducing loss and effectively utilizing energy.

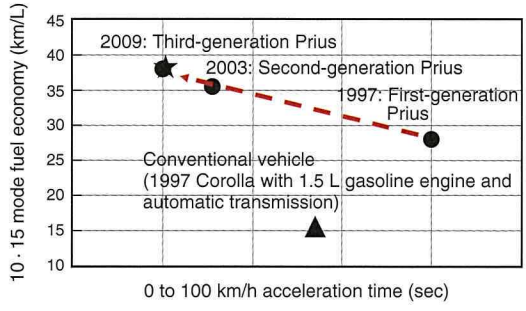


Fig. 1 Mode Fuel Economy and Powertrain Performance (in Japan)

2. Mode Fuel Economy

The first-generation Prius was launched with astonishingly high fuel economy compared to conventional vehicles - approximately 1.8 times that of the 1997 Corolla with a 1.5 L gasoline engine and automatic transmission (**Fig. 2**). The THS, which was installed in the Prius for the first time, adopted many new technologies including idle stop, EV drive, regenerative braking, and an Atkinson cycle engine.

The second-generation Prius was enhanced with further improvements in fuel economy and powertrain performance, solidly establishing the Prius as the leading environment-friendly vehicle.

With the third-generation Prius, Toyota took steps to thoroughly reduce loss in all components and control functions that could impact fuel economy (**Fig. 3**), successfully achieving a further improvement in fuel economy (**Table 1**).

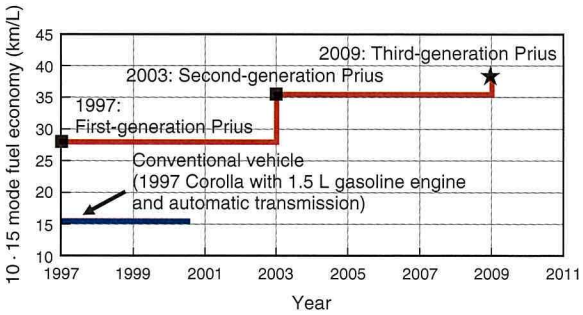


Fig. 2 10·15 Mode Fuel Economy (in Japan)

* Vehicle Evaluation & Engineering Management Div.
** Denso Corporation
*** Under Body Design Div.

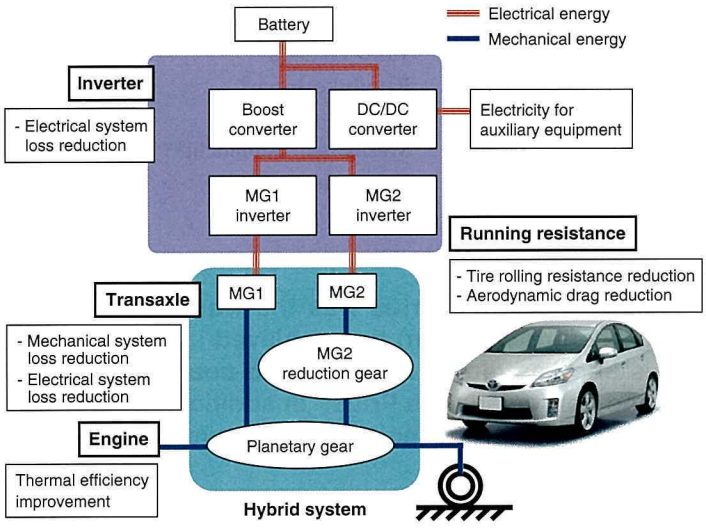


Fig. 3 Hybrid System and Running Resistance

Table 1 Fuel economy performance

	Third generation	Second generation
10 · 15 mode (Japan)	38 km/L	35.5 km/L
U.S. combined	50 mpg	46 mpg
EC mode (Europe)	89 g/km*	104 g/km

* CO_2 emissions

The hybrid system has adopted a cooled EGR system and a motorized water pump in the engine, reduced both electrical and mechanical loss in the transaxle, improved various control systems including the hybrid control system, improved the regenerative efficiency, and reduced the power used by auxiliary equipment.

In addition, Toyota has thoroughly pursued the issue of running resistance to reduce loss in all factors affecting fuel economy, including reducing the aerodynamic drag (to a Cd of 0.25), reducing the rolling resistance of the tires, and reducing the braking loss (**Fig. 4**).

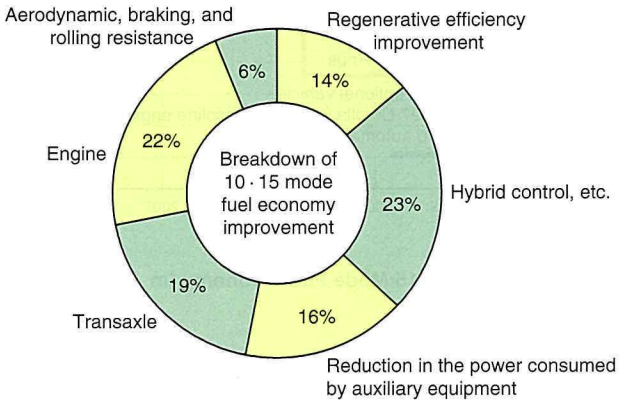


Fig. 4 Breakdown of 10 · 15 Mode Fuel Economy Improvement

3. Actual Fuel Economy

3.1 Purpose of improving actual fuel economy

It has been pointed out that the fuel economy of a vehicle equipped with the THS in an actual usage environment (actual fuel economy), especially at high speeds, in winter, and in summer, does not represent as much of an improvement over conventional vehicles as mode fuel economy. This is because at high speeds, EV driving, one of the basic features of a hybrid vehicle, is not effective, in addition to the fact that the opportunity to make use of regenerative braking is reduced. Meanwhile, EV driving in winter is limited by the energy demand from the heater, and by the energy required for the air conditioner in summer.

The third-generation Prius has been developed with a focus on improving fuel economy at high speeds, in winter and in summer, in addition to mode fuel economy. Furthermore, the eco drive mode and hybrid system indicator were developed. These support fuel efficient driving, reduce unnecessary engine starts and rpm fluctuations, and reduce the energy demand for climate control (heating and cooling), to achieve even more fuel-efficient driving (**Fig. 5**).

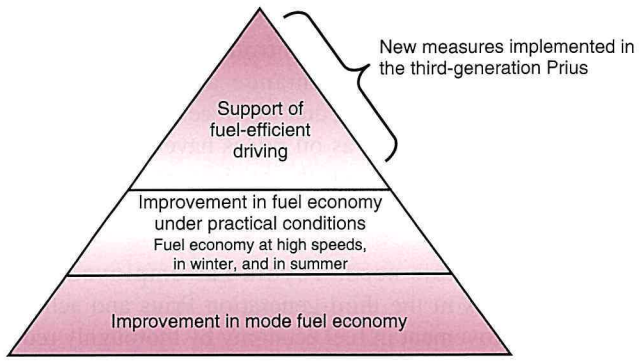


Fig. 5 Measures Implemented to Improve Fuel Economy of the Prius

3.2 Fuel economy at high speeds

In addition to making improvements to the THS II developed for the second-generation Prius, fuel economy at high speeds was improved by increasing the engine displacement from 1.5 to 1.8 liters so that the engine could be operated in a lower-rpm region with high efficiency. Furthermore, the third-generation Prius achieved a fuel economy improvement of approximately 10% over the second-generation Prius through such measures as aerodynamic drag reduction (to a Cd of 0.25) to reduce the running resistance (**Figs. 6** and **7**).

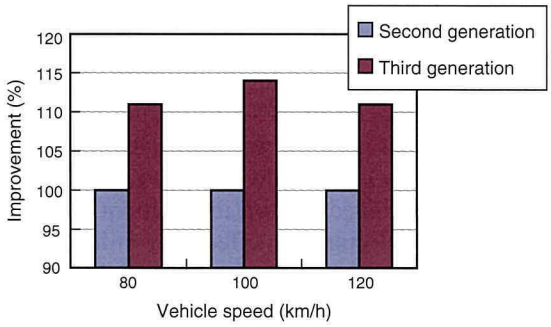


Fig. 6 Fuel Economy at High Speeds

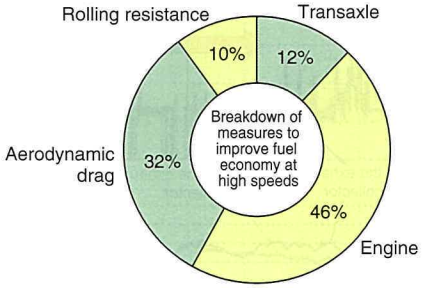


Fig. 7 Breakdown of Measures to Improve Fuel Economy at High Speeds

3.3 Actual fuel economy in winter

The actual fuel economy in winter is significantly affected by the heating requirements for the cabin and engine warm-up immediately after start-up. While reducing powertrain loss and running resistance can improve mode fuel economy, doing so also reduces the engine heat loss. This means that the engine warm-up is delayed in winter, delaying the timing at which EV drive is enabled. Consequently, the actual fuel economy improvement is not as good as in mode fuel economy. Therefore, the development worked to secure a sufficient amount of thermal energy.

For the second-generation Prius, the actual winter fuel economy target Toyota established internally was 1.6 times that of a conventional vehicle. In contrast, the third-generation Prius achieved an actual winter fuel economy of 1.8 times that of a conventional vehicle through various measures including improving the engine warm-up performance using an EHR system, better control of the engine during the warm-up process, and completely reassessing the battery recharging control (**Figs. 8** and **9**).

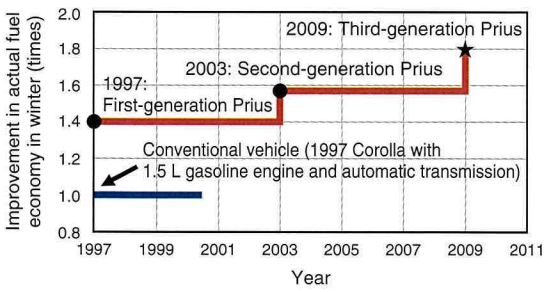


Fig. 8 Actual Fuel Economy in Winter (Internal Evaluation Criteria)

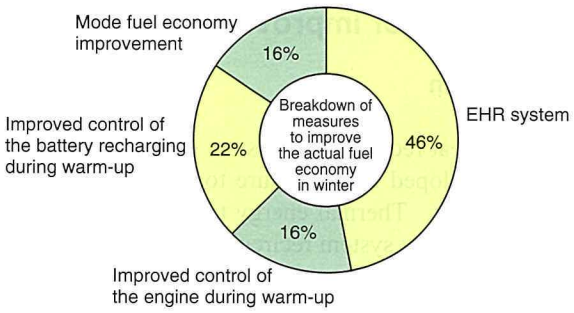


Fig. 9 Breakdown of Measures to Improve Actual Fuel Economy in Winter

3.4 Actual fuel economy in summer

To improve the actual fuel economy in summer, it was necessary to reduce the energy requirement from the air conditioner. In the first-generation Prius, the engine could not be stopped when the air conditioner compressor was activated, and the actual summer fuel economy target established internally was only 1.4 times that of a conventional vehicle.

The second-generation Prius achieved an actual summer fuel economy of 1.8 times that of a conventional vehicle through various measures including the adoption of a motorized compressor, IR-cut glass, and body insulation materials.

In contrast, the third-generation Prius achieved an actual summer fuel economy of 2.0 times that of a conventional vehicle through measures that included improving air-conditioning efficiency using an ejector cycle system (ECS) evaporator in a passenger car for the first time in the world, improving the compressor, and reducing the heat loss in the tubing (**Figs. 10** and **11**).

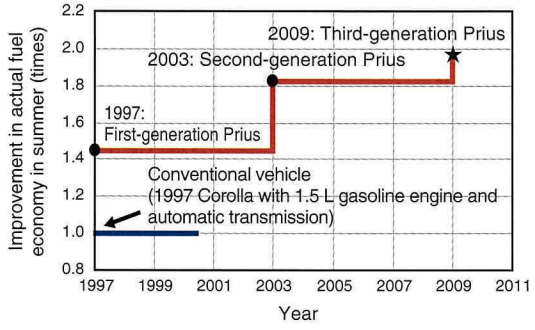


Fig. 10 Actual Fuel Economy in Summer (Internal Evaluation Criteria)

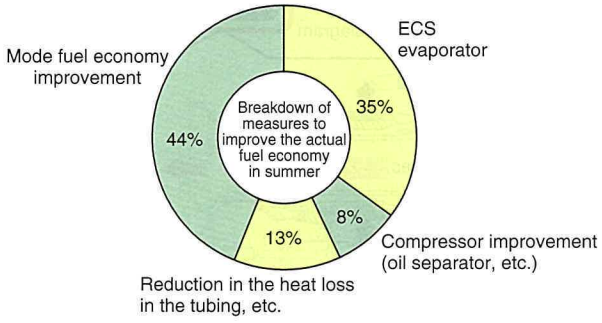


Fig. 11 Breakdown of Measures to Improve Actual Fuel Economy in Summer

4. Major Items for Improving Fuel Economy

4.1 EHR system

The exhaust heat recirculation system for recirculating thermal energy was developed as a measure to improve the actual fuel economy in winter. Thermal energy tends to be in short supply in the winter, and this system recirculates it from the exhaust gas to the engine coolant.

In hybrid vehicles, this EHR system helps promote engine warm-up, allowing engine stop to occur earlier or more frequently, which leads to improved fuel economy in winter.

In the EHR system adopted in the third-generation Prius, an exhaust heat collector is positioned immediately after the catalytic converter to allow heat to be recovered directly from the high-temperature gas that has been reacted in the catalytic converter (**Fig. 12**).

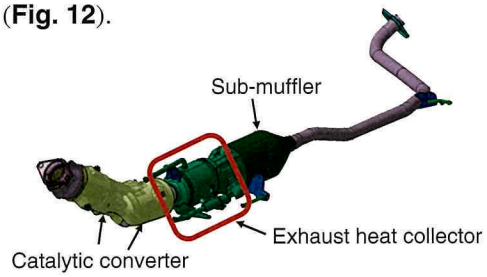


Fig. 12 EHR System

Fig. 13 shows a system diagram of the EHR system and the structure of the exhaust heat collector. The valve opens and closes according to the coolant temperature or the difference in the pressure before and after the valve. The figure shows the heat-exchange state in which the valve is closed. The collector was designed to have a double-layered structure, with a longer internal layer. The exhaust gas is reciprocally passed through the space between the two layers to ensure efficient contact.

To ensure early engine stop after startup, reducing the heat mass is also important, and therefore the size of the collector and the wall thickness of the innermost tube were reduced.

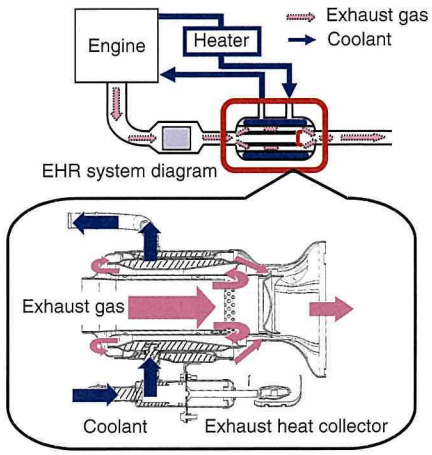


Fig. 13 EHR System Diagram and Exhaust Heat Collector

Fig. 14 compares the engine coolant temperature characteristics, both with and without the use of the exhaust heat collector, during city driving in the following cases: when the ambient air temperature is –5°C, during a cold start, and when the cabin heater is on. It was confirmed that installing the exhaust heat collector enabled the engine to stop early, and also that the engine continued to stop intermittently thereafter. It became clear that collecting and effectively utilizing the exhaust heat prevented unnecessary fuel consumption and increased the EV driving frequency in winter.

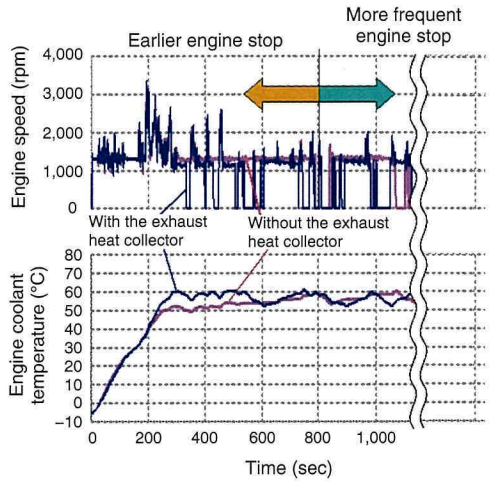


Fig. 14 Comparison of Engine Coolant Temperature Characteristics

These results show that the actual fuel economy in winter improved by approximately 9%. Furthermore, as can be seen from the temperature transition shown in **Fig. 14**, fuel economy can be improved even more by assessing the thermal environment during the first 300 seconds following start-up and making further improvements to the heat-exchanging performance of the exhaust heat collector.

Further improvements in thermal efficiency will likely eliminate heat loss from the engine coolant in the form of waste heat, and therefore the EHR system is essential for both improving the actual fuel economy and ensuring high cabin heating performance.

4.2 ECS evaporator

To improve the actual fuel economy in summer, it was necessary to significantly reduce the energy requirements of the air conditioner. Various improvement ideas were examined, including those related to the refrigeration cycle and control. In the process, however, the limits of conventional technologies were identified and it was decided to adopt the ejector cycle.

In a conventional refrigeration cycle, an expansion valve reduces the pressure of the refrigerant to cool the air in an evaporator, with expansion loss due to the vortex that occurs. Therefore, it was decided to recover the expansion energy that increases the refrigerant pressure in the ejector cycle and utilize

it as power. The refrigerant is ejected from the ejector nozzle, to be reduced in pressure and increased in flow speed, and a suction flow utilizing the high-speed flow acts as a pump and assists the compressor, which accounts for the majority of the energy requirement of an air conditioner, in compressing the refrigerant (**Fig. 15**).

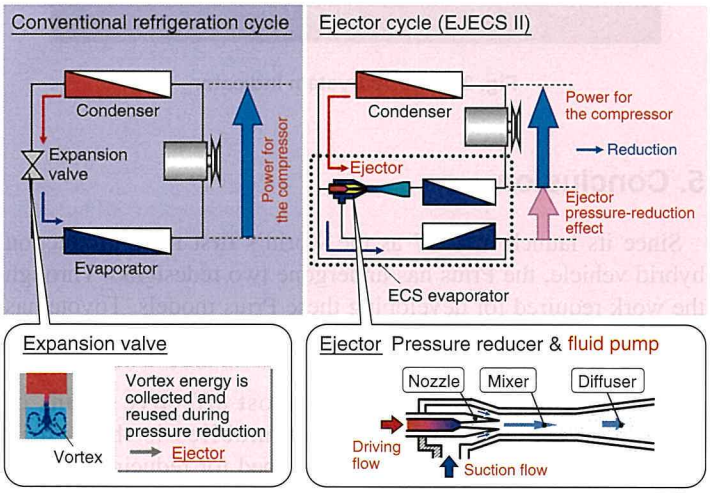


Fig. 15 Overview of Ejector Cycle

Fig. 16 shows examples of utilizing the ejector effect to reduce the power requirements for the compressor, assuming the same air conditioning capacity.

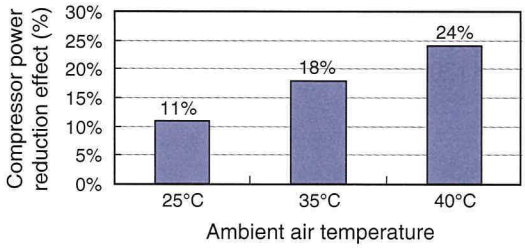


Fig. 16 Ejector Effect Examples

Although the ejector cycle had been commercialized for chillers in refrigerated trucks, it required a massive structure that could not be easily adapted to car air conditioners.

Therefore, the world's first ECS evaporator that condenses the change points of the ejector cycle into a heat exchanger was developed. The ejector was successfully embedded into the limited space inside the evaporator tank, thereby achieving the ejector cycle within the same amount of space required previously (**Fig. 17**).

This ECS evaporator made it possible to adapt the ejector cycle to a car air conditioner, and can therefore be considered an important technology for improving efficiency further in the future.

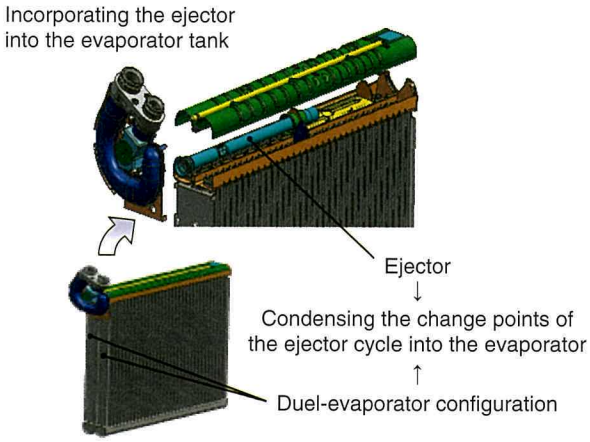


Fig. 17 ECS Evaporator

4.3 Support for fuel-efficient driving

4.3.1 Aim

For the third-generation Prius, technologies were developed to support fuel-efficient driving, in addition to the aforementioned fuel economy improvement technologies. Specifically, the ECO mode switch was developed (**Fig. 18**), which allows the driver to select fuel-efficient drive control and climate control, as well as the hybrid system indicator, which graphically advises the driver on how to drive more efficiently.



Fig. 18 ECO Mode Switch

4.3.2 ECO mode switch

When the ECO mode switch is selected, the drive control and climate control change to the more fuel-efficient economy drive mode. In drive control, the accelerator characteristics become nonlinear, widening the accelerator opening range in which only the electric motor is used (effect A). Additionally, when the accelerator pedal is depressed, the engine speed is kept

lower than in normal mode (effect B). These effects together make the engine more likely to operate in the region with higher combustion efficiency, leading to more fuel-efficient driving (**Figs. 19** and **20**).

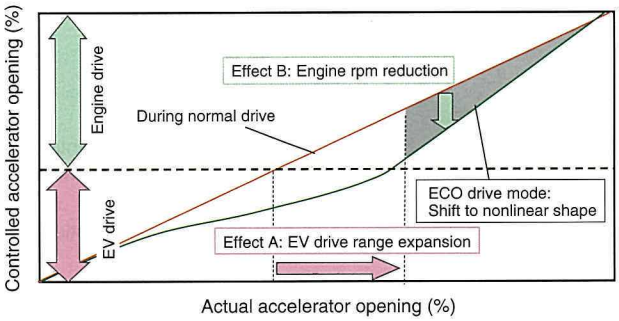


Fig. 19 Nonlinear Accelerator Map and Power Control

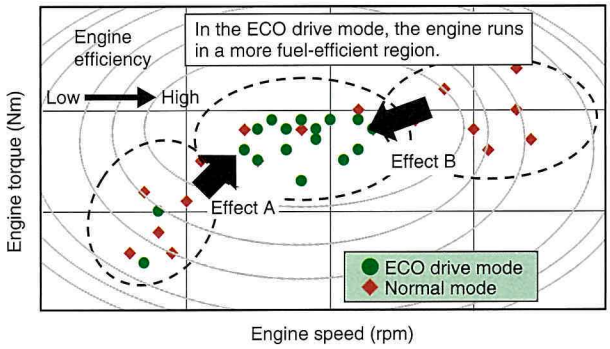


Fig. 20 Comparison of Engine Operation Points

4.3.3 Hybrid system indicator

In the hybrid system indicator of the third-generation Prius, the so-called normal power meters are divided and displayed in the following four areas: (1) regenerative braking area, (2) EV drive-enabled area, (3) area in which both the motor and the engine are used, and (4) area in which the engine is used because of high load (**Fig. 21**). In area (4), if the driver is driving inefficiently, the ECO lamp, which indicates fuel-efficient driving, is turned off to encourage the driver to practice more fuel-efficient driving techniques.

Furthermore, displaying the EV drive-enabled area in (2) is intended to help the driver experience the key feature of a hybrid vehicle and also to suppress unnecessary engine starts, thereby supporting fuel-efficient driving. Using EV drive too often, however, will draw down the battery and cause the engine to remain on in order to charge the battery, resulting in decreased fuel economy rather than increased. For this reason, an icon that shows the remaining battery charge was included inside the same screen. These steps led to the development of the hybrid system indicator, which supports fuel-efficient driving in the third-generation Prius.

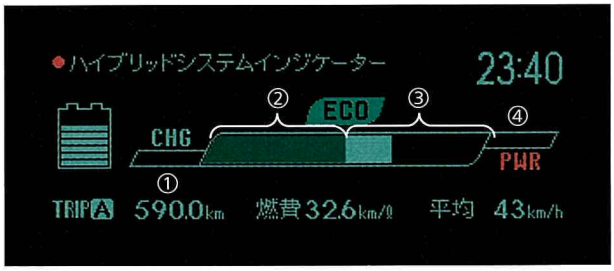


Fig. 21 Hybrid System Indicator

5. Conclusion

Since its launch in 1997 as the world's first mass-production hybrid vehicle, the Prius has undergone two redesigns. Through the work required for developing these Prius models, Toyota has succeeded in achieving successively higher fuel efficiency and power performance.

Toyota believes that one of the most effective means of reducing CO_2 emissions from automobiles is the hybrid vehicle. Using the technologies developed for reducing running resistance, the THS, EHR system, ECS evaporator, and fuel-efficient drive support as a basis, Toyota will strive to continue providing even more efficient and attractive hybrid vehicles.

References

(1) T. Matsubara et al. "Development of New Hybrid System for Compact Class Vehicles." *SAE Paper* 2009-01-1332 (2009).
(2) T. Nakagawa et al. "Exhaust Heat Recirculation System for Actual Fuel Economy." *Review of Automotive Engineering* 20084978 (2008).

Authors


I. YAMADA


J. TOKIEDA


K. JINNO


T. TAKECHI


M. TSUBOUCHI


T. ISHIHATA

Chassis Development for the Third Generation Prius

Masayuki Aso*

Abstract

This article summarizes the development of chassis components used in the third generation Prius, which was launched in May 2009. The Prius uses a new platform developed for the Auris and features better stability and controllability than the previous generation. Efforts have also been made to improve ride comfort. Furthermore, the weight of the chassis has been substantially reduced to help achieve the world's best environmental performance.

Keywords: *Prius, new platform, stability and controllability, ride comfort, mass reduction*

1. Introduction

The third generation Prius went on sale in Japan in May 2009 ahead of the rest of the world. To a background of increasing global environmental consciousness, the development of the third generation Prius aimed to achieve high stability and controllability performance in addition to environmental friendliness. This article describes an outline of the development of chassis components designed for the third generation Prius (**Fig. 1**).

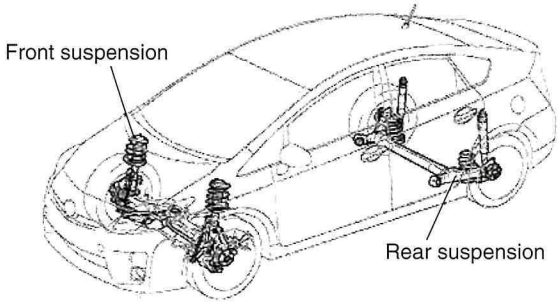


Fig. 1 Developed Chassis Components

2. Development Outline

2.1 Aims of development

The following three aims were set for the development of the third generation Prius (**Fig. 2**).

1) To improve items pointed out by users in the second generation Prius
2) To achieve an appropriate level of ride comfort for the Prius
3) To reduce mass to help achieve world-leading environmental performance

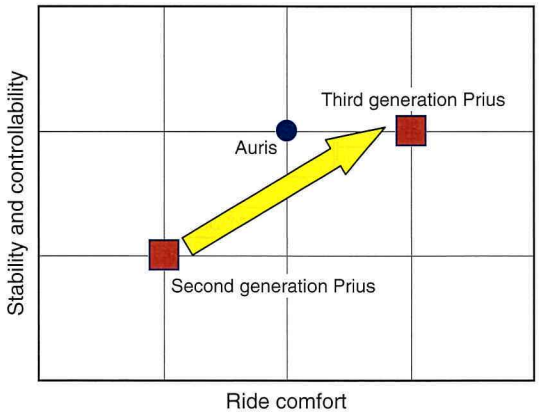


Fig. 2 Image of Performance Development

To achieve these goals, the suspension system of the second generation Prius (front: MacPherson strut, rear: torsion beam) was kept, but the new platform developed for the Auris was further improved and lightened to achieve high stability and controllability performance and flat ride comfort.

2.2 Basic specifications

Adopting the new platform allowed the alignment of the vehicle to be modified (**Fig. 3**). Although the wheelbase was kept unchanged from the second generation Prius, the tread was widened to help improve stability and controllability. The caster angle was almost doubled from that in the second generation, and this improved straight line stability and steering feedback (**Table 1**).

* Chassis Engineering Div. 2

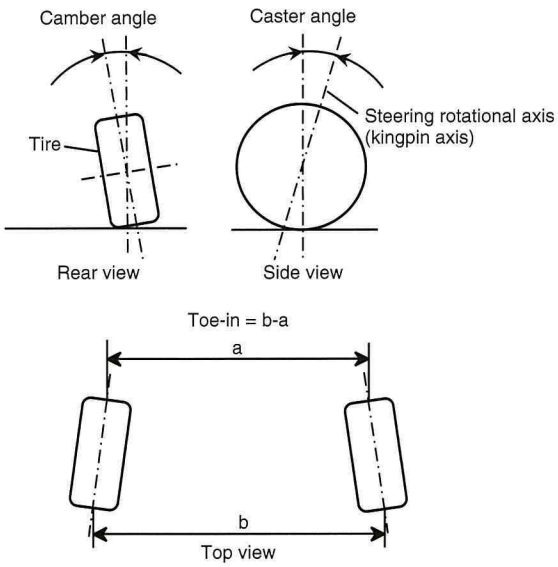


Fig. 3 Alignment

Table 1 Alignment Comparison

		Third generation	Second generation
Wheelbase (mm)		2,700	2,700
Tread	Front (mm)	1,524	1,505
	Rear (mm)	1,520	1,480
Alignment			
Front	Toe-in (mm)	2	0
	Camber angle	−0° 15'	−0° 35'
	Caster angle	5° 55'	3° 10'
Rear	Toe-in (mm)	2	3
	Camber angle	−1° 30'	−1° 30'

2.3 Front suspension

The geometry of the front suspension (**Fig. 4**) was optimized by adopting the new platform. This gives the third generation Prius better steering feedback while maintaining controllability and straight line stability. A highly efficient stabilizer arrangement also enabled high roll stiffness.

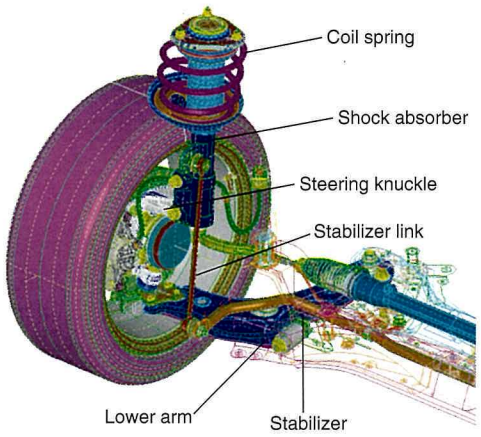


Fig. 4 Front Suspension

2.3.1 Separate input construction type upper support

Some grades of the Prius have a new separate input construction type upper support to improve ride comfort. In comparison, a conventional structure uses a combined input construction type, in which input from the shock absorber and input from the coil spring are assimilated and passed to the body through the rubber portion of the upper support (**Fig. 5**).

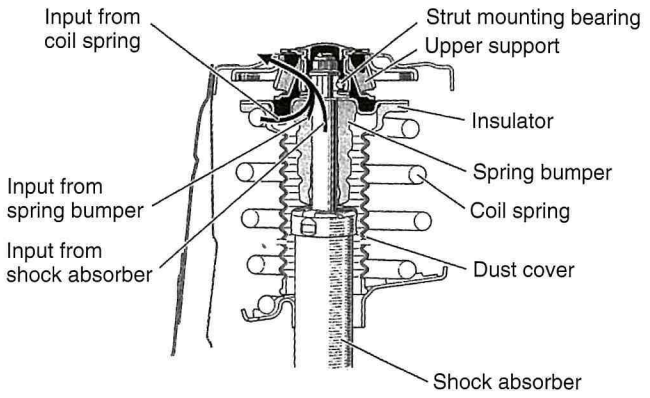


Fig. 5 Combined Input Construction Type Upper Support

This structure is simple, but the softness of the upper support rubber has limitations, which restricts the adjustment range for ride comfort, vibration, stability, and controllability.

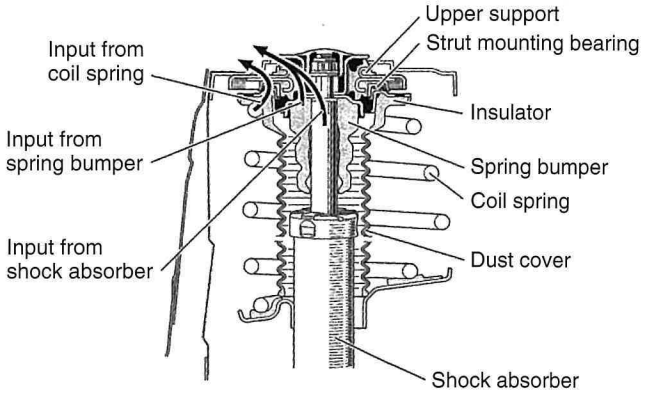


Fig. 6 Separate Input Construction Type Upper Support

In comparison, the separate input construction type (**Fig. 6**) separates the input from the shock absorber and coil spring. This increases the design freedom of the upper support rubber and allows excellent ride comfort and quietness to be achieved.

2.3.2 Stabilizer bush

The shape of the stabilizer bush was modified to improve ride comfort. As shown in **Fig. 7**, the contact surface with the stabilizer was given a dimpled shape to reduce sliding resistance and achieve smooth ride comfort.

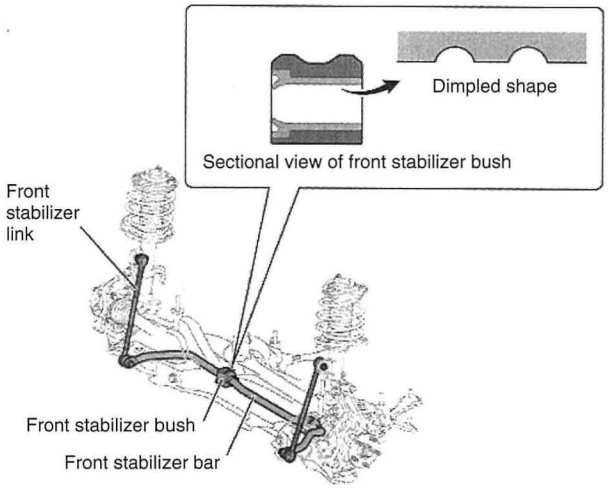


Fig. 7 Stabilizer Bush

2.4 Rear suspension

As with the front suspension, the rear suspension (**Fig. 8**) adopts the format of the new platform, in this case, a torsion beam.

In addition to a stabilizing function, a pipe formed beam was adopted to reduce mass and increase stiffness. This gives the suspension high roll, steer, and camber stiffness.

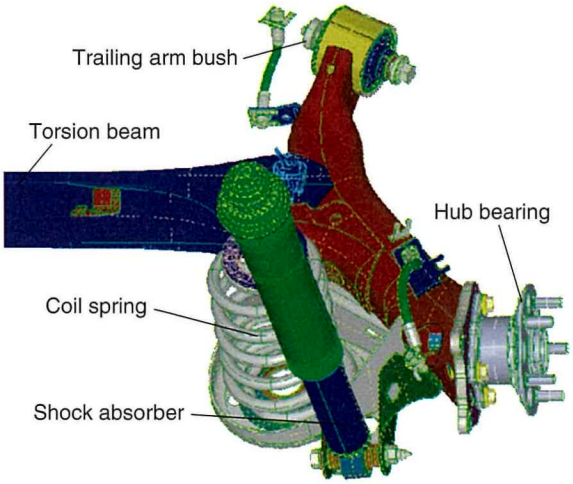


Fig. 8 Rear Suspension

In addition, the trailing arm bush was arranged at an angle. This allows high stability and controllability with a conventional bush shape by allowing correct steer to the toe-in side from the longitudinal and lateral force generated on the bush when cornering.

In addition, the separate arrangement configuration of the coil spring and shock absorber also increase the space of the luggage compartment. Furthermore, the trailing arm bush characteristics were revised to improve ride comfort.

2.5 Steering system

The column-assist type EPS steering system developed for the Auris was also adopted on the third generation Prius (**Fig. 9**).

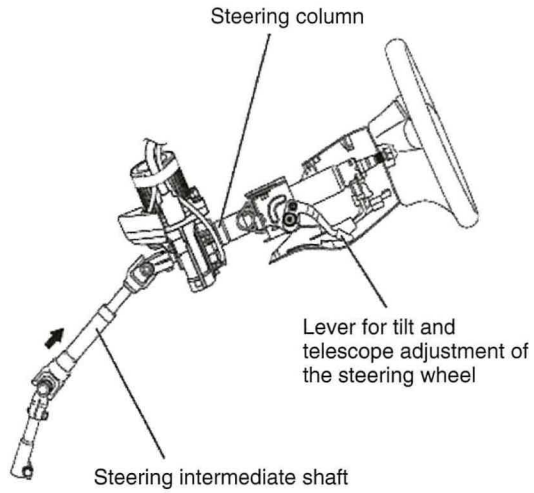


Fig. 9 Steering Column

As is the case with the second generation Prius, some grades use a high-power brushless motor system in place of the usual motor with brush. This system allows quick handling at a large gear ratio (**Table 2**) as well as a natural steering feel by improving the smoothness of control.

Table 2 Overall Gear Ratio

	Overall gear ratio
With brush	17.8
Brushless	14.6

All vehicle grades have the telescopic adjustment function, which allows the driver to select the optimum driving position.

The steering gear is attached directly to the front suspension member without passing through an elastic body. This maintains steering stiffness and allows linear steering characteristics.

2.6 Tires

The tires used by the third generation Prius have a reduced rolling resistance coefficient with a larger μ.

Table 3 Tire Sizes

	Tire size
L grade	185/65R15
S and G grades	195/65R15
S and G grades (touring package)	215/45R17

3. Mass Reduction

Mass reduction was a vital part of achieving the world's best environmental performance. In the third generation Prius, many of the parts in the base Auris suspension were re-designed to reduce mass by 8% (**Fig. 10**).

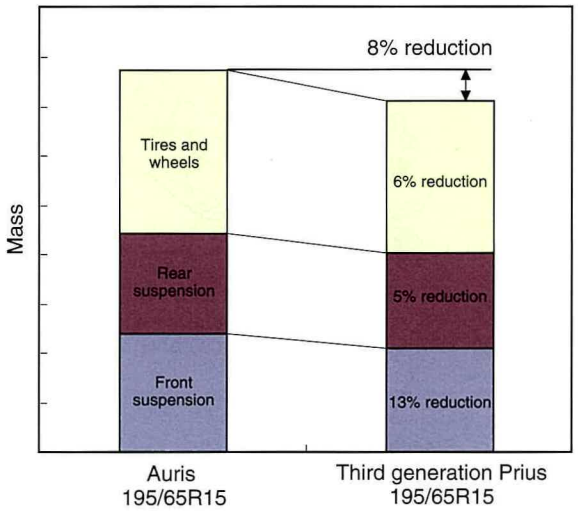


Fig. 10 Mass Reduction

Some of the main mass reduction measures are as follows: the steel steering knuckle and stabilizer links were changed to aluminum castings (**Fig. 11**); the thickness of the lower arm was reduced and its section made smaller; the PCD of the hub bearing was reduced (**Fig. 12**); the size of the lower ball joint was reduced; the stabilizers were made thinner; and the material of the trailing arm bush bulge was changed to plastic.

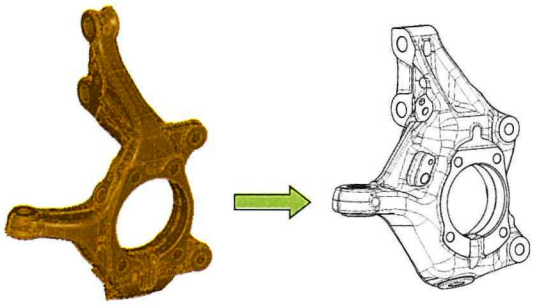


Fig. 11 Introduction of Aluminum Casting Knuckle

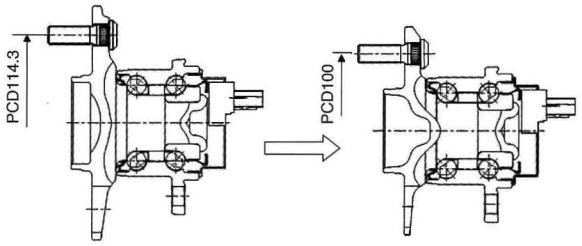


Fig. 12 PCD Change of Rear Hub Bearing

4. Conclusion

This article has outlined the chassis technology adopted in the third generation Prius. It has described the details of the development of each component and their contribution to stability, controllability, and ride comfort. It also detailed the main development items that enabled substantial mass reduction. In the future, Toyota will continue listening to the voices of our customers and using their suggestions to further improve the Prius.

Author



M. ASO

Solar Ventilation and Remote Air Conditioning Systems

Koji Ikeda*
Takashi Ogawa*
Takaaki Goto*

Abstract
The importance of air conditioning for improving interior comfort has grown steadily in recent years and customer needs have become more diverse. As a result, in addition to basic cooling and heating performance, air cleaning and other technologies have been developed to create a more refined interior space. However, discomfort caused by the transition period until the effect of the air conditioning can be felt is one area of improvement that has yet to be addressed satisfactorily. Focusing on the discomfort felt by users after entering a vehicle that has been parked under a hot sun, this article describes the solar ventilation and remote air conditioning systems that were developed to help resolve this issue.

Keywords: *comfort, remote air conditioning system, solar, ventilation system, pre-air conditioning*

1. Introduction

Automatic air conditioning technology has been improved and technologies such as pollen removal have been developed in response to diverse customer needs, resulting in a refined and comfortable interior space. Furthermore, air purification technology to remove matter that is difficult to sense, such as bacteria and mold, has been developed in response to an increase in health consciousness. In this way, maintaining air conditioning comfort has become an important element of vehicle marketability.

However, even though air conditioning technology has advanced and become more diverse, the technology is still not adequate to resolve, in particular, the unpleasant feeling of extreme heat or cold during the period immediately after entering the vehicle before the air conditioning has an effect. Technology such as reducing thermal load by changing interior materials is being developed, but the current state is not sufficient and further improvements are still needed. With conventional air conditioning systems, there is no way to address these issues, because the air conditioning cannot be used without the engine running, making it difficult to maintain power while parked.

This article describes the solar ventilation and remote air conditioning systems that were developed to resolve these issues with a focus on summer heat. These systems are installed on the third generation Prius, which is the most suitable vehicle for advanced technology of this nature.

* Interior Design Div.

2. Solar Ventilation and Remote Air Conditioning Systems

The interior temperature of a vehicle that has been parked in the hot summer sun for a long time varies depending on sunlight levels and ambient temperatures, but can rise to nearly 80°C. The instrument panel and seat temperatures increase at the same time, and the unpleasant feeling of entering a hot vehicle is something everyone has experienced.

The solar ventilation system uses power generated from the solar panel installed on the roof, as shown in **Fig. 1**. The air conditioning blower motor is operated to ventilate the interior air of the vehicle parked in direct sunlight. Outside air is drawn in and hot air is blown out, which has a controlling effect on the increase in interior temperature and also contributes to controlling the surface temperature of the instrument panel and seats. However, the system relies on external air, and therefore the occupant compartment temperature cannot be reduced below the external temperature.

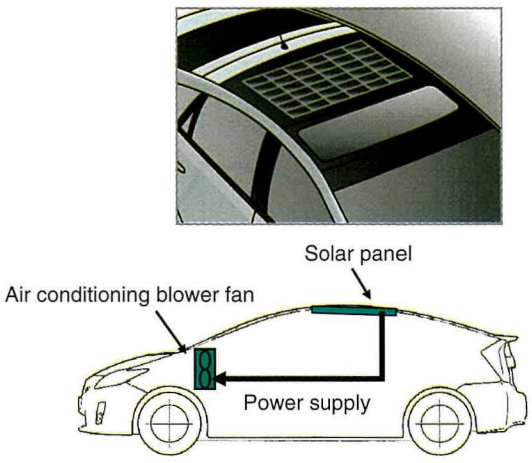


Fig. 1 Diagram of Solar Ventilation System

In addition, the remote air conditioning system is enabled by the electric compressor air conditioning system used on this hybrid vehicle. It is capable of cooling the vehicle interior without starting the engine. As shown in **Fig. 2**, using electricity stored in the hybrid battery, the electric compressor is driven by remote operation to enable air conditioning before the vehicle is entered, and this has a large effect of reducing the occupant compartment temperature and the temperature from the outlet vents. However, since its operation period is shorter than the solar ventilation system, the temperature of parts such as the instrument panel and seats will not drop as much.

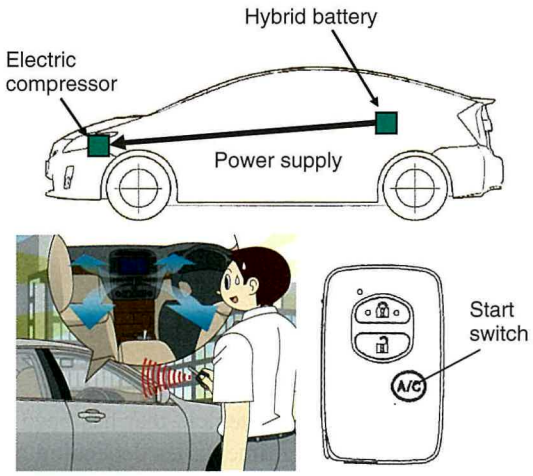


Fig. 2 Diagram of Remote Air Conditioning System

Accordingly, these two systems can be combined to reduce the occupant compartment temperature, outlet vent temperature, and interior surface temperature, with the aim of reducing heat and discomfort when entering a vehicle parked in the sun. Moreover, in addition to the comfort felt immediately after entering the vehicle, the user can expect the length of time before the vehicle is sufficiently cool to be shorter. In this way, contributions to air conditioning performance can be made with a different perspective than the conventional aims of improving the performance of individual air conditioning parts. **Fig. 3** shows a diagram of the effect of the combined systems on vehicle interior temperature.

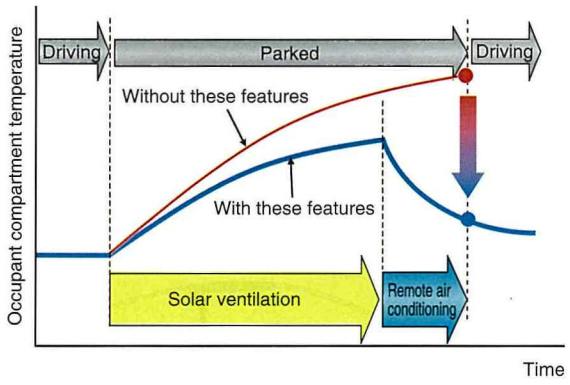


Fig. 3 Effect Diagram

3. Solar Ventilation System

3.1 System configuration

The configuration of the solar ventilation system is shown in **Fig. 4**. The solar panel, the part that symbolizes the entire system, generates power from solar radiation with the aim of supplying electricity to the system. This electricity source is independent from the existing electrical system.

A dedicated solar ventilation electronic control unit (ECU) is installed for this system and performs overall control based on required information such as the solar radiation level and outside temperature. On the other hand, the existing air conditioning ECU has a support role, such as for changing the outlet vents, and is not involved when ventilation control is performed. The air conditioning blower fan, which serves to draw in outside air and blow it into the vehicle, is shared with the normal air conditioning system and automatically changes between normal air conditioning and the ventilation system in accordance with vehicle conditions.

Finally, the ventilator switch that triggers operation of this system requires explanation. The system gives maximum priority to the user's intention, and the system can be turned ON or OFF manually. For example, if the air quality outside of the car is poor and the user does not want air to ventilate, the system can be switched to OFF so that it will not run even if there is enough solar radiation.

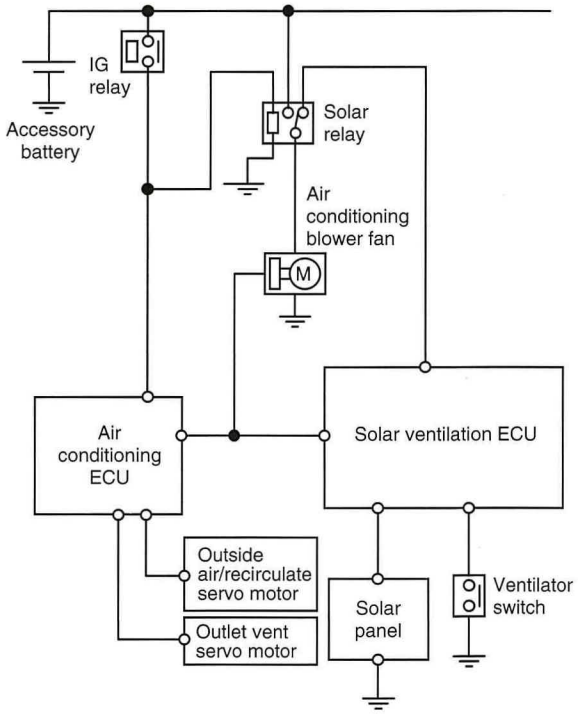


Fig. 4 Solar Ventilation Diagram

3.2 Start control

An outline of operation is shown in **Fig. 5**. First, in order to secure a path for ventilation, the air conditioning blower fan is switched to outside air mode, and the outlet vents are changed to face mode. This change is detected at the air conditioning ECU while the ventilator switch is ON. Each servo motor change is performed about one minute after the vehicle power is switched OFF.

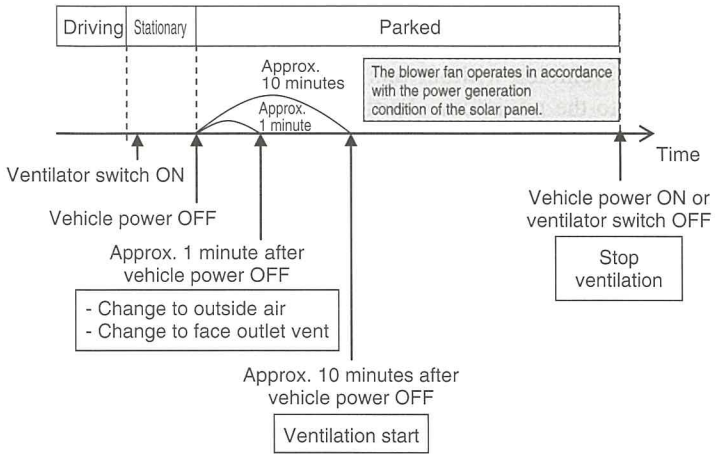


Fig. 5 Solar Ventilation Operation Diagram

Next, the solar ventilation ECU determines if air ventilation is necessary. For this judgment, the ECU must determine the type of environment in which the vehicle is parked, and a solar panel V-I curve like the one is **Fig. 6** is used. The characteristics of the solar panel are such that electricity is generated on the curve, and the energy that can be generated is the product of the voltage at the operation point and the current. The open circuit voltage is the voltage that can be obtained when the solar panel output terminal is open, and the short circuit current is the current that can be obtained when the load resistance is zero ohms. As shown in **Fig. 7** and **Fig. 8**, the amount of electricity generated by the solar panel varies with the solar radiation level and temperature. The short circuit current and solar radiation level have a proportional relationship, and the open circuit voltage decrease as temperature rises. The ambient temperature and solar radiation level in the area where the vehicle is parked can be estimated using these characteristics by detecting voltage and current. Finally, operation control starts when air ventilation is determined to be necessary.

In addition, air ventilation does not begin immediately after parking. A timer delay of about 10 minutes is set so that cool air remaining from the air conditioning during driving will not be blown out of the vehicle immediately.

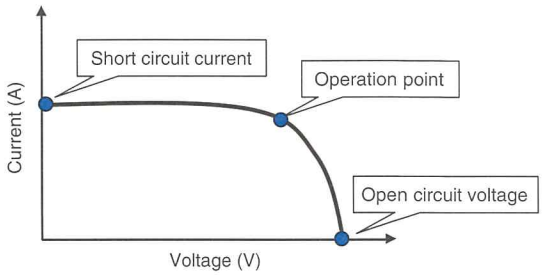


Fig. 6 V-I Curve

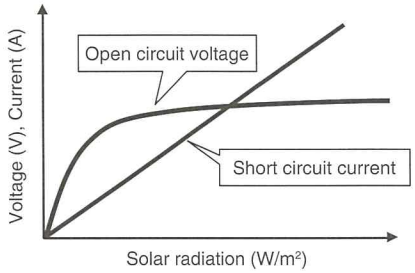


Fig. 7 Solar Radiation Level × Open Circuit Voltage and Short Circuit Current

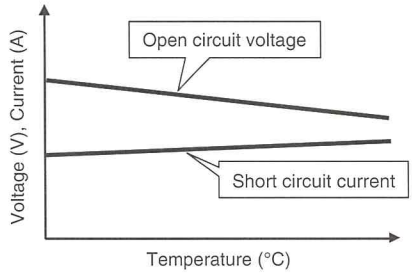


Fig. 8 Temperature × Open Circuit Voltage and Short Circuit Current

3.3 Operation control

As stated in the section above, the solar panel generates electricity on the V-I curve, and therefore a control target point is determined so that the system will operate in the high output (power) area to start air ventilation. Depending on weather conditions and the parking environment, because the input solar radiation level changes by the second, the operating speed of the air conditioning blower fan is constantly adjusted while the system is in continuous operation. Additionally, air ventilation sometimes stops due to sudden changes in solar radiation level from, for example, the shadow of a building or clouds. After a certain period of time, the system is restarted in accordance with the solar radiation levels at that time. If the ventilator switch is turned OFF or the vehicle power is turned ON during this time, air ventilation stops.

3.4 Solar panel

The solar panel consists of 36 155 mm × 75 mm solar cells connected in series, as shown in **Fig. 9**. Average output is 56 W when solar radiation is at 1,000 W/m^2 and cell temperature is at 25°C. This output performance is determined in accordance with the target air ventilation volume. If the air ventilation volume is extremely low, then warm air will be simply mixed up within the vehicle, and there is no temperature reduction effect in the interior and on the seat surfaces. The air ventilation volume is established for this reason.

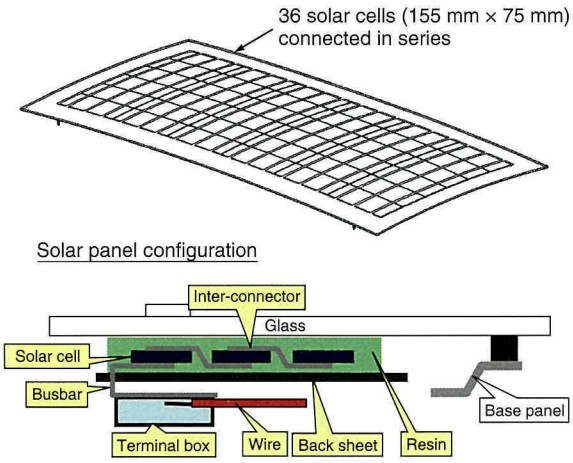


Fig. 9 Solar Panel Configuration

3.5 High durability blower motor

The solar ventilation system will operate constantly if the conditions for operation, such as solar radiation level, are satisfied, while the vehicle is parked. As a result, compared to the air conditioning blower fan in a conventional system, the frequency of use is much higher for this blower fan. While it varies with the weather conditions in different regions, the blower fan durability requirement is about ten times higher. Therefore, a blower fan with greatly improved durability is used. For example, the bearing has been changed from an oil-impregnated sintered bearing to one with ball bearings.

4. Remote Air Conditioning System

4.1 System configuration

The configuration of the remote air conditioning system is shown in **Fig. 10**. In response to operation by the user, the wireless switch emits a remote air conditioning start or stop signal, and outputs information to the main body ECU through the smart key computer assembly.

The main body ECU performs functions such as overall control of system starting and stopping, confirmation of vehicle state, and requesting power ON to the power management ECU. Vehicle conditions such as hybrid system operation and the hybrid battery charge level are confirmed at the power management ECU.

Based on commands from the main body ECU, the air conditioning ECU makes decisions to drive the cooler and control the air conditioning. In this way, the various ECUs are coordinated through communication, and detailed control is necessary.

As much as possible, the component parts are common with parts in vehicles without this system, and changes have been limited to the minimum. Furthermore, in order to minimize the need for user input and also to perform optimum control, the temperature setting is set by the user. Then, based on that value, air conditioning settings such as the outlet vent temperature, the outlet vent to be used, the intake source, and the air volume are all controlled automatically.

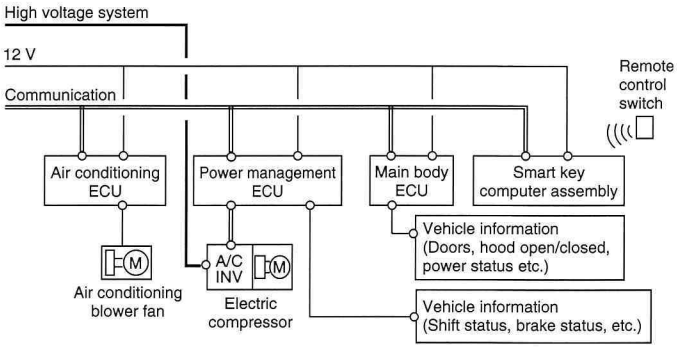


Fig. 10 Remote Air Conditioning System Diagram

4.2 Start control

As shown in **Fig. 11**, this system is started when the user operates the remote control switch. Because most starts are remote starts, a vehicle status check is always performed before the system starts. Check items include, for example, whether vehicle power is OFF and the doors and hood are closed, and the shift status. After checking, door lock operation is performed to confirm that the doors are locked. If any of the conditions are not satisfied, the system will not begin operation control. Also, a special power mode exclusive to the remote air conditioning system is used for the power source condition, which is different from the power ON condition during normal driving. In this power mode, items such as the wireless door lock and smart key, which are not directly related to the air conditioning, are controlled to operate as when the vehicle is parked normally. Additionally, the main body ECU performs overall control of this system because it has most of the vehicle information required for these control functions.

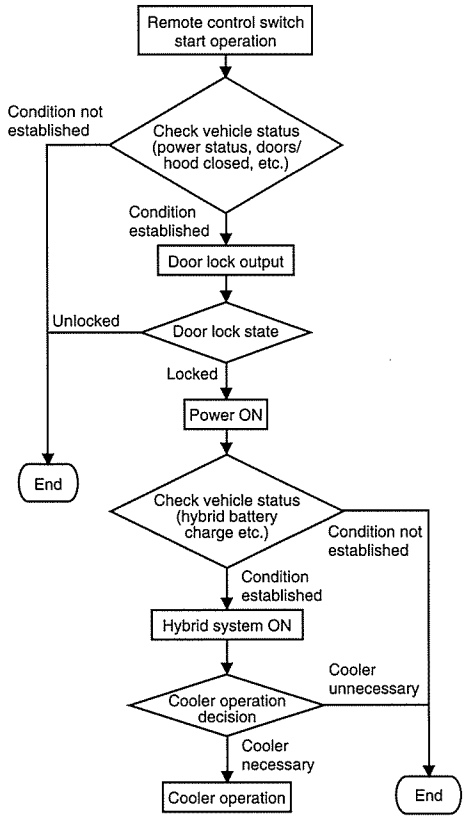


Fig. 11 Remote Air Conditioning Start Control

4.3 Operation control

After the completion of start control, the system begins operation control. For this, the main body ECU starts the air conditioning system by issuing a power ON request to the power management ECU. At this time, the air conditioning ECU, in response to the set air conditioning temperature, determines whether or not cooled air is necessary and stops the system if it is not. The decision to cool is the same as with conventional air conditioning, and is performed in response to inputs from various sensors with information such as outside air temperature, solar radiation level, and vehicle interior temperature.

Moreover, with this system, because the hybrid battery is the power source, measures such as establishing usage limits in accordance with the battery charge are taken to ensure compatibility with the hybrid system.

4.4 Stop control

Fig. 12 is a flow chart for the stop control. In addition to stopping when the vehicle conditions that are confirmed during start and operation control are not satisfied, the system also stops after a maximum operation time of three minutes. Stop control was determined after visualizing the use scenarios of customers with the system and considering the following overall factors: (1) usage immediately before entering the vehicle, (2) detection range for the wireless remote control, and (3) range of use of the hybrid battery. If battery performance is improved or other changes are made to the vehicle system to expand the range of possible use of the remote air conditioning system, then the maximum operation period is likely to be extended.

The system also stops when the user performs a remote stop operation.

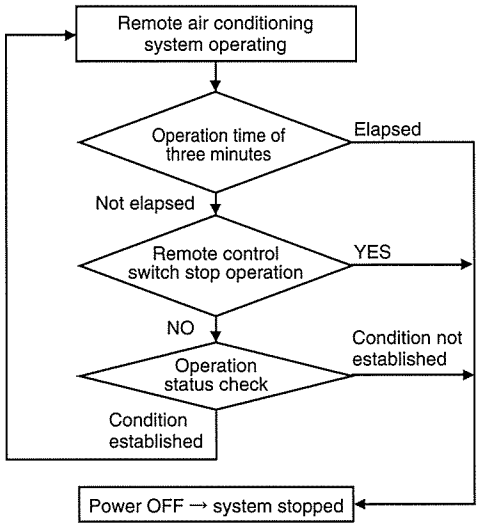


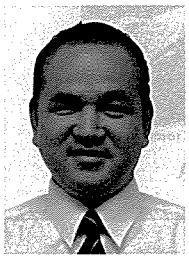
Fig. 12 Remote Air Conditioning Stop Control

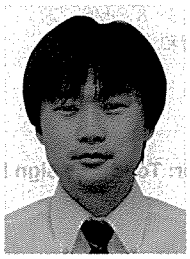
5. Conclusion

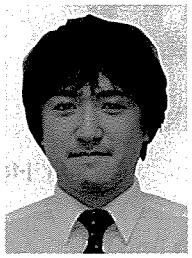
This article has introduced the solar ventilation and remote air conditioning systems, which successfully reduce heat and discomfort immediately after entering a vehicle. This problem had been difficult to address with conventional methods, and it is hoped that the system will positive evaluations in the market.

Finally, this article has introduced a system that uses energy from a solar panel to ventilate air while the vehicle is parked, but the applications of this system are still limited. It has various possibilities other than air ventilation, such as charging the battery. Development of solar panel technology is still in its early phases, and in the future when batteries with even higher output, thinner profiles, and lighter weight are developed, there will be no limit to the range of possible applications. Toyota will strive to continue improving comfort and making efficient use of natural energy.

Authors


K. IKEDA


T. OGAWA


T. GOTO

Design of the Prius as an Eco-Icon

Hideo Miwa*

Abstract

As one of the first vehicles to address global environmental and energy issues, the original Prius was launched in 1997 with the aim of helping to achieve a low carbon society. Through innovative packaging evocative of a new era, the Prius appealed to customers with futuristic styling that set it apart as a hybrid vehicle different from conventional small sedans. As such, it was promoted using the catchphrase, "In time for the 21st century". The second generation Prius was launched in 2003 with improved dynamic performance and interior space. In line with these advances, an aerodynamic 5-door hatchback design (called a triangular silhouette) was introduced to help improve fuel efficiency. Since then, the Prius has built up a leading position among HVs and has become synonymous with hybrid technology. This article describes the styling of the new third generation Prius, featuring elements that have continued on and evolved from the second generation.

Keywords: *j-factor, Vibrant Clarity, air management, eco-icon, triangular silhouette, glazed ceramic*

1. Introduction

Before discussing the design of the third generation Prius, I would like to discuss the Toyota design philosophy. We call the DNA of Toyota design the "j-factor" (**Fig. 1**). This quality can be seen in the value perceptions and beauty esthetics that are intrinsic to Japan. For example, as shown in **Fig. 2**, given one value A in the orange box on the left and another completely different value B in the white circle on the right, there is neither conflict nor compromise. On the contrary, they are harmonized without losing either of their respective values. This harmony is simplified to create a completely new value. I think that the contrast of these opposing values results in synergy, giving rise to intrinsic Japanese dynamism and elegance.



Fig. 1 j-factor: Toyota Design DNA

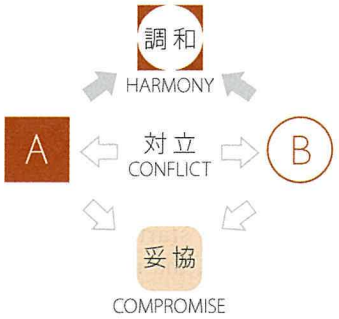


Fig. 2 The j-factor Concept

There has been a preference for this method in Japan from the past to the present. For example, consider the assimilation of East and West in mentai (fish roe) spaghetti, or the letters of the Japanese kana syllabary, which are simplified Chinese characters that have lost their meanings (**Fig. 3**). We define this method as the j-factor, and it has been established as the common DNA in Toyota and Lexus design.

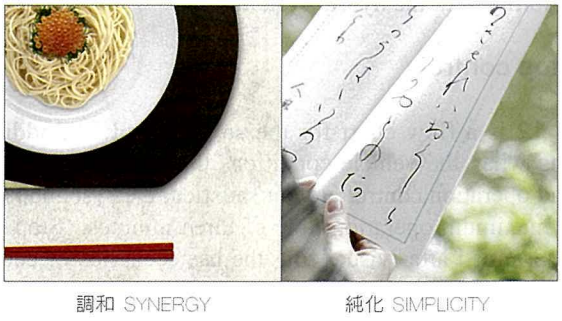


Fig. 3 The Creation of New Values

* Toyota Design Div.

Additionally, we implemented Vibrant Clarity as the design philosophy for the Toyota brand. The conflicting design elements of an exciting "vibrancy" are harmonized with a refreshing "clarity" that anyone can appreciate. This stimulates a high degree of emotion and rationality, leading to the birth of new values (**Fig. 4**). This philosophy consists of the following three design elements.

(1) Perfect imbalance
(2) Integrated component architecture
(3) Freeform geometrics

These elements (**Fig. 5**) are also based in the j-factor, and are combinations of contradictory words.



Fig. 4 Vibrant Clarity



Fig. 5 Three Elements of Vibrant Clarity

This philosophy had already been adopted when the second generation Prius was developed, and now this DNA is the design foundation for all Toyota vehicles. The Vibrant Clarity concept also applies to the third generation Prius, which aims to physically embody a beauty of design that is only possible with a hybrid car. It combines the fun of driving with advanced aerodynamic performance that further improves fuel economy.

The next section describes the exterior style in terms of the three design elements that make up the Toyota's Vibrant Clarity design philosophy.

2. "Eco-Icon" as a Development Theme

2.1 Succession and evolution of idea that hybrid = Prius

Looking at the current state of new car sales, while partially due to the effect of tax incentive measures, the top rankings are dominated by environmentally responsible cars. This was forecasted when the third Prius started development. However, the Prius has not become lost in a sea of such "eco" cars, and has maintained and evolved the hybrid = Prius image that it established by being the first hybrid car. We thought that there was a need to respond to the expectations of a new generation of people. These are customers with increased environmental awareness and overlapping priorities such as health concerns, social assertiveness (the statement value in **Fig. 6**), and self-assurance (the personal value).

For this reason, we believed that the mission of the third generation Prius was to establish a benchmark to which all future eco cars will be compared. Therefore, we established the "Eco-icon" design development theme (**Fig. 6**). While people and the environment were at the center of the concept, it started with the proportions (triangular silhouette) carried over from the previous generation. In order to improve aerodynamic performance and achieve beautiful styling, design expressions were woven into all aspects of the Prius with a focus on air management based on aerodynamic theory.

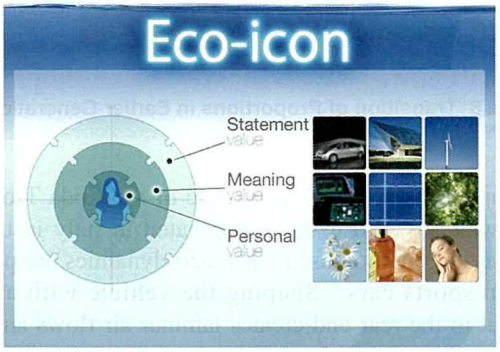


Fig. 6 Eco-Icon

2.2 Transition of proportions

The first generation Prius that was released in 1997 had a three-box style developed with consideration given to the so-called 5-number size classification in the Japan market. However, the proportions were the result of a new package researched with steady focus on the 21st century, and were different from the proportions of a conventional three-box sedan.

In addition to expanding the vehicle height and wheelbase, changes such as setting the hip point of occupants as much as 100 mm higher and bringing the cowl forward created a new riding posture and large interior space. Moreover, although the length was reduced for a minimalist intent, the proportions had

strong characteristics of a big cabin and a mono-form feeling (**Fig. 7**), even at the concept stage. These characteristics gave the Prius innovative qualities firmly focused on the 21st century, and the resulting sedan style drew lots of attention.

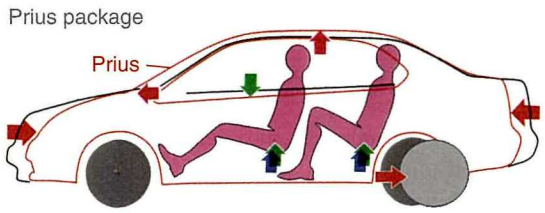


Fig. 7 Image of First Generation Prius Package

The second generation Prius, which was released in 2003, targeted power performance improvement for the North American market and further improvement of fuel economy. Improvements in aerodynamic performance were also expected for the exterior design.

This resulted in the birth of the five-door hatchback triangular silhouette (**Fig. 8**).

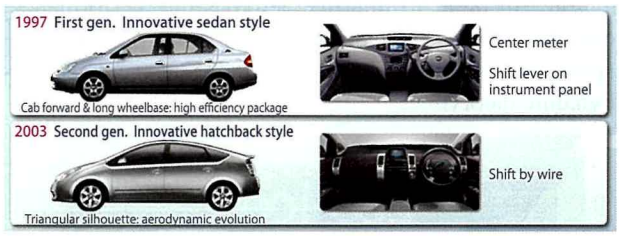
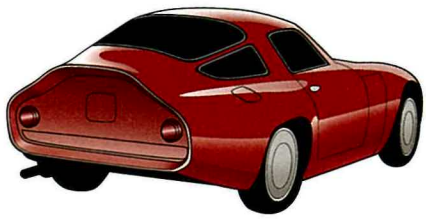


Fig. 8 Transition of Proportions in Earlier Generations

The proportions are similar to those of the Coda Tronca (**Fig. 9**) style, which is said to have originated in Italy in the 1960s. This is a styling method used when aerodynamics are prioritized, such as in sports cars. Shaping the vehicle with an abrupt, vertical cut to the rear end creates laminar air flows and reduces weight by making the body shorter.



Coda Tronca: Alfa Romeo Giulia TZ (1963)

Fig. 9 Alfa Romeo Giulia "Coda Tronca"

The triangular silhouette of the second generation Prius consists of a solid formed by connecting the front and rear wheels and the center of the cabin interior space, and it further improved interior comfort. Moreover, a simple and clean image fitting for an eco car was given to the surfaces.

The refreshing and futuristic proportions stirred and moved the hearts of people who saw the vehicle. The clear and refreshing design had styling appropriate for Vibrant Clarity, and it caught on throughout the world as the Prius style image.

Then, the third generation Prius has maintained and further advanced the evolution of the triangular silhouette.

3. Achieving Both Aerodynamic Performance and Unique Beauty

3.1 Evolution of the triangular silhouette

The proportions of the second generation Prius were continued as the triangular silhouette and they evolved further to really embody the expression of perfect imbalance. While the second generation Prius expressed its futuristic environmentally responsible image through clean and simple styling, development of the third generation Prius called for improved dynamic vehicle performance. Then, in order to appeal to more customers worldwide, it also required a clean, advanced feel with energetic and emotional styling.

Specifically, in order to apply dynamism with an advanced feel to the entire body, the base of the cabin front pillar was moved forward 25 mm to emphasize the line that starts at the edge of the head lamp and connects to the front pillar (**Fig. 10**).



Fig. 10 Front Pillar Moved Forward

In addition, locating the peak of the cabin (more specifically, the peak of the triangular side window graphic) towards the rear gave the vehicle the impression of sharp movement. As a result, headroom clearance for rear seat passengers is approximately 12 mm greater than in the second generation, which also has the effect of improving interior comfort (**Fig. 11**).

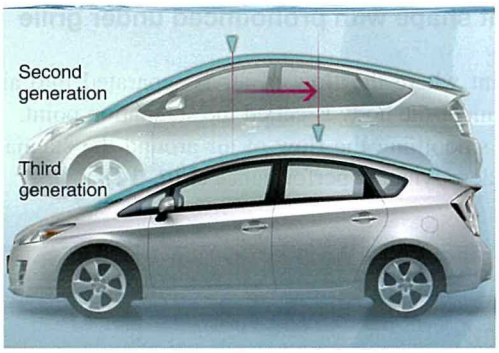


Fig. 11 Cabin Peak Moved Rearward

However, the proportions of this new triangular silhouette, in terms of aerodynamic performance, created a silhouette with a contradictory aerodynamic function. Normally, with an aerodynamically effective silhouette similar to Coda Tronca or an artillery shell, the position of the cabin peak is moved forward to create a long roof line extending rearward from the peak, and the wind follows the roof. This results in laminar air flow and improves the aerodynamic C_D value.

For the third generation Prius, it was boldly decided that an advanced silhouette and comfortable interior would be given priority. This required innovations such as moving the cabin peak rearward, making the rear spoiler longer as a means of extending the length of the shortened rear roof and optimizing height and angle.

Through the use of air management, which is discussed in the next section, the challenge of solving conflicting requirements was performed in all areas of the vehicle. This next explanation is where we can see perfect imbalance.

3.2 Harmony through air management

It goes without saying that the reason the Prius exists is to improve fuel economy and reduce CO_2 emissions. Therefore, it is largely assumed that the vehicle must have improved aerodynamic performance. The second generation Prius achieved a C_D value of 0.26, the best for passenger vehicles of this size. For the third generation Prius, the target C_D value was set even lower. Thus, the primary design condition for exterior styling was improved aerodynamics.

To this end, close cooperation was performed with the aerodynamic testing division from the sketch phase, and air management was taken into consideration while shaping the forms. This was carried out while giving consideration to the maintenance of an original, innovative design true to the philosophies of Vibrant Clarity and integrated component architecture. The design stimulated the harmonization of aerodynamic requirements with beautiful styling.

Looking back at cars that have been made with priority given to aerodynamics, as a result of prioritizing wind flow, most have an aerodynamic test vehicle style that sacrifices interior space. The style of a test vehicle is not sufficient in order to gain the approval of a large number of customers who might ride in the vehicle. Hence, a design that is both beautiful and practical is an absolute necessity.

The elements of air management design are introduced in detail here. First, the volumetric composition (architecture) is introduced.

The initial idea sketches (**Fig. 12**) express this clearly, but the large discus shape that makes up the cabin appears to be blended with a trapezoid shaped to minimize wind flow. Thus we started with a remarkably simple and dynamic theme. The idea sketches show the influence of the image of the discus cutting through the wind and the trapezoid creating laminar air flow.

The image of the cross-section of a discus was maintained in the wedged, sharp side character of the third generation Prius. This, when combined with the triangular silhouette side view, become the iconic character that makes the third generation Prius unique.

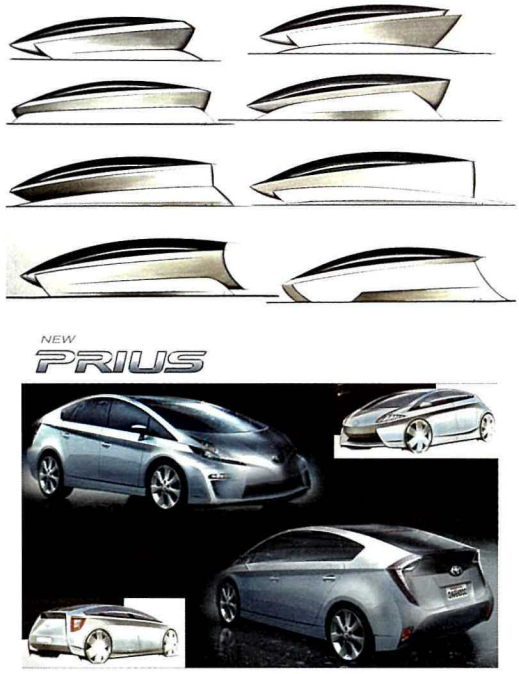


Fig. 12 Initial Idea Sketches

One other unique architecture of the third generation Prius is the use of aero corners. These were implemented to create laminar flow from the wind that comes from the front corners, passes over the door sides, and exits past the rear end (**Fig. 13**). Securing a flat surface with a minimum area on each of the tire front and rear overhang sections smoothes out the flow of wind that is disrupted by the wheel arches.

However, simply expressing the dimensions required for aerodynamics gives the corners a heavy weight and poor balance of style. At this point, an idea was necessary to achieve both aerodynamics and a beautiful, stylish appearance.

The idea was to boldly add a sharp edge to the bumper corner. The flat surface, considered a necessity, on the contrary, stands

out conspicuously as a result of the sharp edge and creates a nice contrast of form. The architecture that was born as a result went beyond the stereotypical assumption that bumper corners are round.

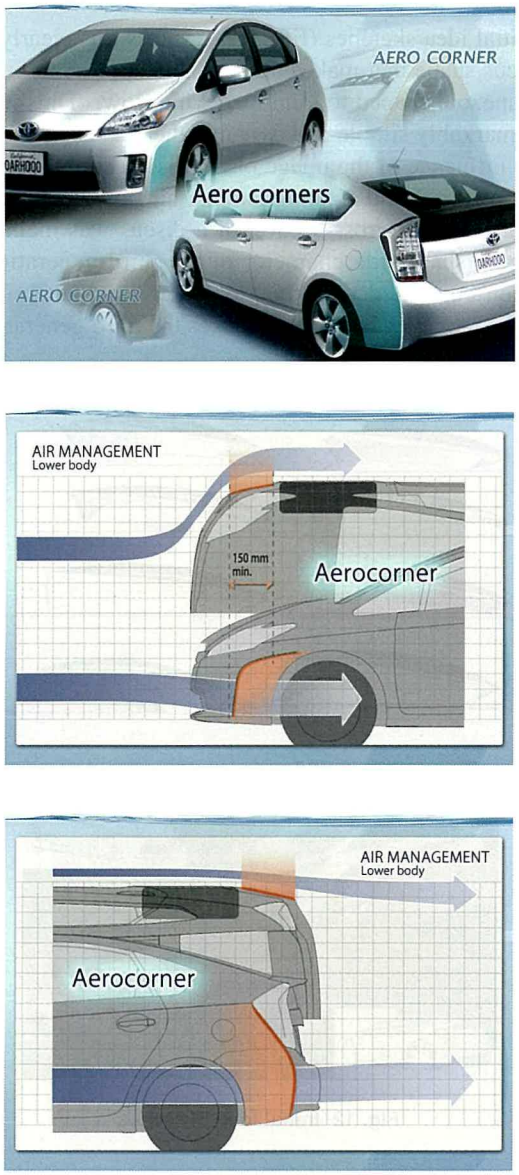


Fig. 13 Aero Corners

A sharp edge on the aero corners was needed, as far back as possible, to prevent wind from being pulled into the rear surface from the side. There is an edge line that runs diagonally across the exterior panel surface of the rear corner, and an additional sharp edge was added even further behind the edge line, on the lens surface of the rear combination lamp. The sharp edge is actually further rearward that it appears to be, and this measure enabled achievement of both design qualities and the necessary functionality.

3.3 Front shape with pronounced under grille

The point where the flow of air is separated into air flowing over and under the body is called the stagnation point. Generally speaking, smoothing the flow of air around the stagnation point improves aerodynamic performance (**Fig. 14**).

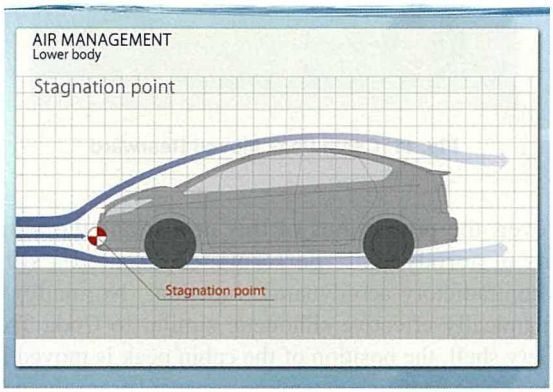


Fig. 14 Stagnation Point

The opening of the upper grille was made small, and the opening of the under grille was made large. These openings reduce wind resistance and also can be expected to efficiently cool the radiator (**Fig. 15**).

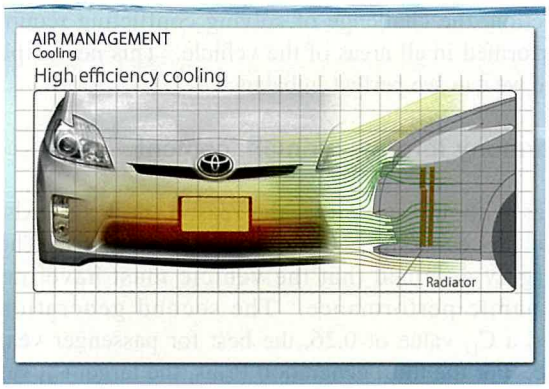


Fig. 15 Reduced Wind Resistance and Efficient Cooling

Additionally, the recession on the lower edge of the bumper, also has a protective effect in a collision involving a pedestrian (**Fig. 16**). These improvements to aerodynamics, cooling, and the protection of pedestrians were the basis of the under grille, and the unique front shape that was created by the prominent under grille was called "under priority" (**Fig. 17**). When combined with the previously explained aero corners, this expresses a unique front mask. Under priority is being considered as a common front shape for the Toyota brand (**Fig. 18**).

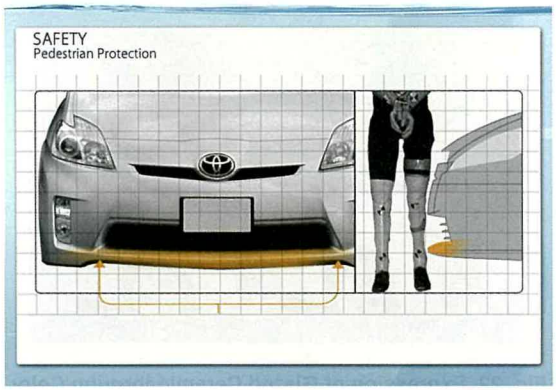


Fig. 16 Pedestrian protection

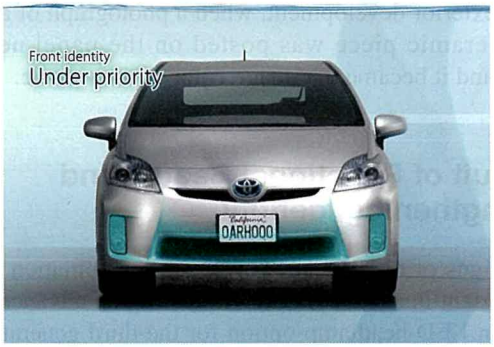


Fig. 17 Under Priority

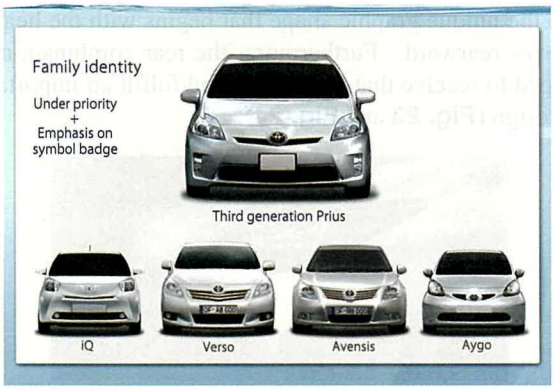


Fig. 18 Toyota Brand Common Front Shape

3.4 Effect of air management

As stated above, we proceeded with shaping of the vehicle while striving for harmony between the aerodynamic requirements and the design ideals necessary for beautiful style. Additionally, the rocker cross-section was brought outward, the height of the rear bumper lower edge and the angle of its lower surface were adjusted, the curved taper of the planar side panel surfaces was optimized, the under floor was made flat, and the wheels were given a new design to improve aerodynamics. Air management changes such as these were made throughout the vehicle to achieve a C_D value of 0.25, better than that of the second generation Prius and at the top level of aerodynamic performance (**Fig. 19**).

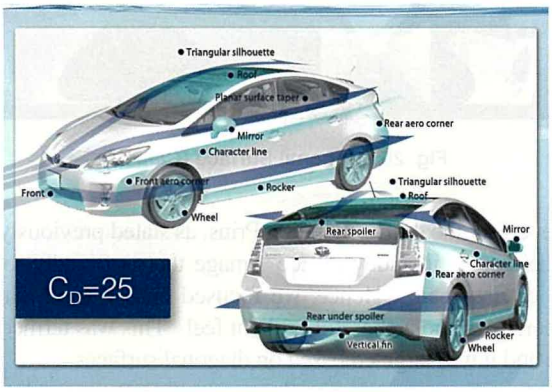


Fig. 19 C_D 0.25: Air Management

4. Clean and People-Friendly Surfaces

4.1 Advance qualities and glazed ceramic

The second generation Prius was designed with a simple and clean shape, and the style maintained its eco image. This image made it the style leader for all hybrid cars, and customers appreciate that the Prius is friendly to both people and the environment. We thought that the third generation Prius should maintain the clean image that was carved out for hybrids by its predecessors.

Surface development proceeded under the philosophy of freeform geometrics under Vibrant Clarity, and while the Prius was given a clean and athletic outline, it also has cheerful charm and surfaces with smooth transitions that contrast with sharp edges. Thus, we were able to create surfaces suitable for the next generation hybrid.

The basis for these surfaces was the diagonal surface expression used for the iQ. Diagonal surface refers to mathematical models for expressing shape, first created by mathematicians at the end of the 19th century and used to express curved surfaces with formulas. The volumetric shapes were photographed and expressed with light and shadow, and had minimalist, simple, and emotional tastes (**Fig. 20**). Development of the iQ focused on diagonal surfaces, and the model was visualized with computer graphics. CAD and NC machining were used to create a physical model to improve the image, and these motifs were expressed throughout the surfaces of the iQ. Surfaces based on these diagonal surfaces are used throughout the third generation Prius as well.

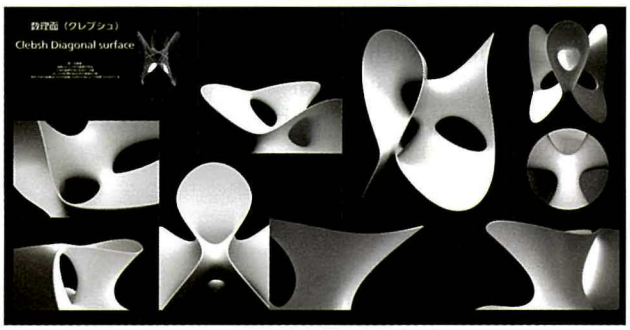


Fig. 20 Diagonal Surface (Clebsh)

However, for the third generation Prius, as stated previously, it was also necessary to include an "eco" image that is friendly to people and the environment. Hence, we focused on a warmth similar to that of ceramics and a cheerful brilliant feel. This was termed glazed ceramic and it was targeted based on diagonal surfaces.

As a specific example, in the case of pottery such as blue porcelain, the porcelain comes out of the kiln hardened and has a deep, brilliant finish that is the result of glaze. The result is warm to the touch and has a smooth demeanor. By giving this quality to surfaces with relief and sharp edges throughout the car, such as to the aero corners, bumper surfaces, and door cross sections, the ideas of cleanliness and the warmth of a person's hand were both achieved. Thus, a unique hybrid feel was expressed (**Fig. 21**). We think that this warmth is actually more necessary on an advanced car such as the Prius.

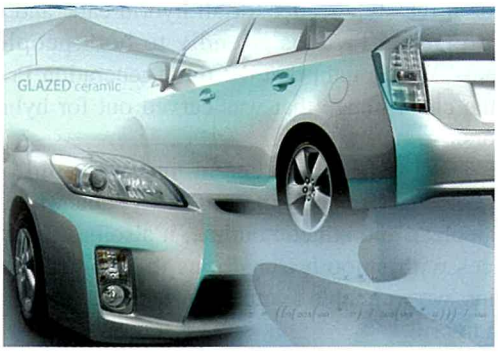


Fig. 21 Expression of Glazed Ceramic

4.2 Glazed ceramic through color

Two new colors were added exclusively for the Japan market; aqua blue metallic and iceberg silver mica metallic. Under the "human-tech" theme, both of these aim to give a feel of intelligence and human warmth. Due to the multiplying effect of the exterior glazed ceramic, they express a hardness and feeling of elegance.

More specifically, aqua blue metallic expresses transparency, a feeling of depth, and a refreshing hybrid quality. Iceberg silver mica metallic has a cheerful, brilliant expression with a powerful impact (**Fig. 22**).

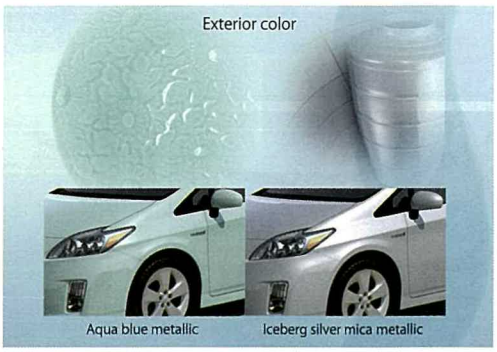


Fig. 22 Expression of Glazed Ceramic through Color

Aqua blue metallic in particular, was used from the initial stages of exterior development, when a photograph of a similarly colored ceramic piece was posted on the panel next to the sketches, and it became the image color of the vehicle.

5. Pursuit of Functional Beauty and Strengthening Identity

The designs of the headlamps and rear combination lamps are very important items in terms of expressing an advanced quality. There is an LED headlamp option for the third generation Prius, and the shape of these advanced headlamps not only fulfills a role in advanced functionality, but also forms the edge of the triangular silhouette style theme. The headlamps also help express the unique graphic shape that begins with the headlamps and moves rearward. Furthermore, the rear combination lamps are shaped to receive that movement and fulfill an important role in the design (**Fig. 23** and **Fig. 24**).



Fig. 23 LED Headlamps (Option)

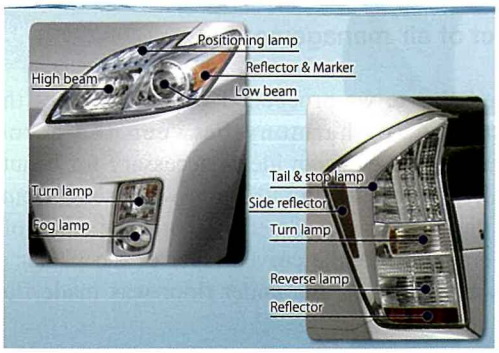


Fig. 24 Headlamp and Rear Combination Lamp

Other functional items include a solar ventilation system, a Toyota-first that generates electricity at a solar panel to circulate air through the vehicle (**Fig. 25**). The solar battery can be seen through the roof glass and is an appealing point of the styling; it is an expression of the advanced qualities of a hybrid car.

Furthermore, in order to distinguish the vehicle as a hybrid car, the front and rear Toyota symbol marks use a color called hybrid synergy blue. The same thought went into lamps and other items throughout the vehicle to contribute to and strengthen the hybrid identity of the Prius (**Fig. 26**).



Fig. 25 Solar Ventilation System

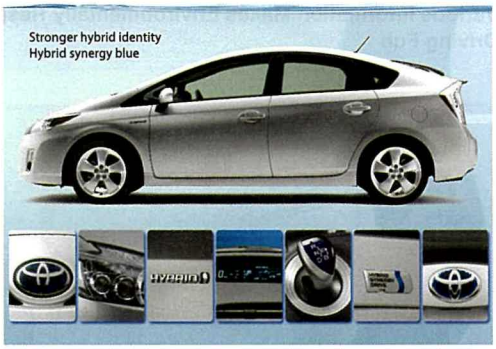


Fig. 26 Hybrid Synergy Blue

6. Interior Built Around People

"Human-tech" was also the development theme of the interior design as well as for the color design. We strove for an interior design that combined advanced qualities with warmth, as is possible with a hybrid car, so that it would be built around people.

At the same time, we needed an interior design that would reflect the emotional driving made possible by improvements to power performance in the third generation Prius. The interior is introduced with the same Vibrant Clarity theme used for the exterior.

First, perfect imbalance is achieved with the lower instrument panel's feeling of stability due to a lateral motif and the instrument panel upper, which joins the lower with an organic overlap. These are combined with the bridge-shaped center cluster to result in a composition that is asymmetrical left to right. This combination expresses the unique beauty of a shape with a unique imbalance. The overall width of the instrument panel is 60 mm greater than that of the second generation Prius, and increasing the size of the triangular windows creates a feeling of openness. At the same time, the cluster designed for ease of use provides an appropriate feeling of enclosure (**Fig. 27**).



Fig. 27 Interior Built Around People

The concepts of integrated component architecture are clearly separated into a command zone with controls centered on the touch panel at the hands, and a display zone where information is shown. This separation makes it easier for the driver to see and operate the controls (**Fig. 28**). As a result of this layout, human perception is the reference point, and overall harmony is achieved with both emotional qualities and functionality.



Fig. 28 Display and Command Zones

Shift-by-wire technology made it possible to locate the symbolic bridge shaped cluster with the shift lever in a position where it is easiest for the driver to operate. There is no sense of confinement in leg space, which results in a clean design, and some of the lower space has been used to create storage compartments.

Moreover, the shift lever represents the center of ripples of concentric circles that spread out across the layout, and the positioning of the touch panel and switches makes operation of the controls natural for the driver (**Fig. 29**).



Fig. 29 Ripples Spreading Across the Switch Layout

The displays are concentrated in the forward center meter. Because the focal point is farther from the driver, shifts in focus have been reduced. Additionally, the driver does not have to change focus to his or her hands to operate the switches. This is because the locations of the steering wheel switches touched by the driver's hands are displayed on the center meter. Hence, the Prius is equipped with the world's first touch tracer display (**Fig. 30**).



Fig. 30 Touch Tracer Display

Furthermore, the hybrid system indicator helps facilitate driving with minimal environmental impact, the energy monitor clarifies at a glance, if drive power is coming from the motor or engine, and there is also a screen that introduces fuel consumption history. In this way, the Prius is equipped with functions that facilitate environmentally responsible driving but that are also fun (**Fig. 31**).

As an expression of freeform geometrics, line segments with agile movement are used across the entire instrument panel and throughout the finer details of the steering wheel and trim ornaments. This rich texture expression achieves ecological and warm emotion combined with technological innovation.

Additionally, on the top of the instrument panel upper, a leaf vein grain that blends natural leaves with a geometric pattern is used to create a soft, refined feel (**Fig. 32**).

For the interior as well, an aqua color with an advanced feel was used with the aim of achieving an image of both intelligence and crispness. This color emphasizes the refined qualities of the covering materials and a calm, smooth feel (**Fig. 33**).

The use of a thin seat back made possible by a new seat frame increases knee room in the rear seat by 20 mm compared with the second generation Prius. As a result, the seat achieves both design and function (**Fig. 34**).

Revisions to trim cross-sections and the positioning of the battery cooling system increased luggage space from 415 liters in the second generation Prius to 446 liters, so that the Prius can now carry three golf bags (**Fig. 35**). Thus, interior comfort and function were both improved.



Fig. 31 Various Information Makes Environmentally Responsible Driving Fun



Fig. 32 Instrument Panel Grain in the Image of Leaf Veins



Fig. 33 Aqua Has an Intelligent and Crisp Image

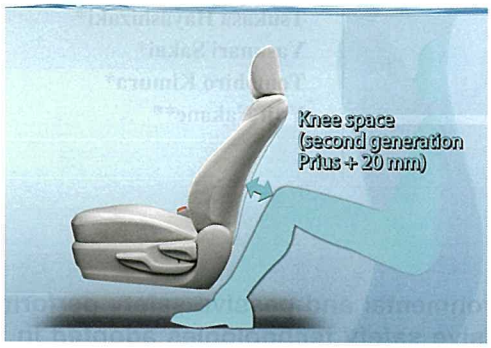


Fig. 34 New Frame Enables Thin Seat Back

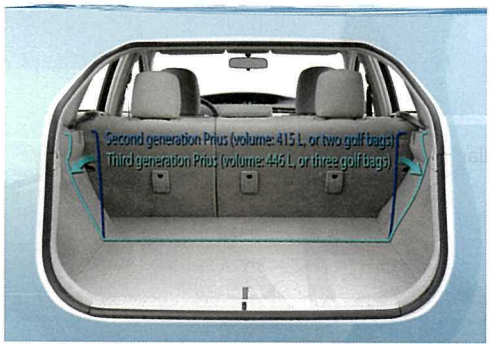


Fig. 35 Expanded Luggage Space

7. Conclusion

This article has introduced the design of the third generation Prius. In the future, we anticipate continued development of a plug-in hybrid vehicle but many other environmentally responsible vehicles such as electric and fuel cell cars. This development will take place at a fast pace and with an eye on technological innovation. Moreover, infrastructure is expected to advance in step with these technological advances. Against this background, the hybrid car needs to continue to combine "eco" with "fun" in order to appeal to a wide range of customer needs. The styling of the third generation Prius is based on the Eco-icon motif and symbolizes the all environmentally responsible vehicles. I am certain that this styling will tow many future cars behind it.

Author



H. MIWA

Passive Safety Performance

Tsukasa Hayashizaki*
Yasunari Sakai*
Tomohiro Kimura*
Yuji Nakane**

Abstract
The third generation Prius has achieved the same excellent environmental and passive safety performance as the previous generations. This article describes the various passive safety technologies adopted in the third generation Prius to realize the level of collision safety required by a mobile society.

Keyword: *passive safety*

1. Introduction

The development of the third generation Prius focused on achieving both excellent environmental and safety performance. In the same way as the second generation, the body of the third generation Prius was developed with advanced safety technology to achieve performance that meets the world's toughest passive safety targets of Toyota's Global Outstanding Assessment (GOA). At the same time, the body incorporated a wide range of mass reduction measures to help reduce environmental load and achieve the ecological performance demanded of a hybrid vehicle.

2. Passive Safety

2.1 Frontal collision performance

GOA requires a high level of both cabin and occupant protection performance. It simulates real-world accidents and includes offset impacts that cause heavy damage to the occupant compartment and full-lap impacts that apply strong forces to the occupants.

The front body of the third generation Prius has a dual level structure consisting of front side members and under members that use high strength steel sheets. This structure increases impact-absorbance in a frontal collision.

In addition, intrusion into the occupant compartment is kept to a minimum by actively dispersing input loads from the front to the strongly reinforced structural members of the cabin (i.e., the rockers, pillars, and door reinforcements in **Fig. 1**).

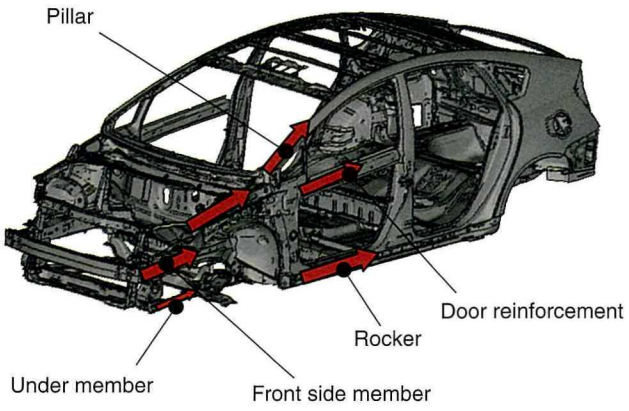


Fig. 1 Transmission of Load in Frontal Collision

Occupant protection devices in the event of a frontal collision include driver and passenger side SRS airbags (**Fig. 2**) and seatbelts equipped with pretensioners and force limiters as standard equipment. These help to alleviate impacts to the head and chest of occupants in combination with an impact-absorbing steering column.



Fig. 2 Driver and Passenger Side SRS Airbags

Additionally, impact-absorbing foam was arranged at the feet of the occupants to help absorb impacts from the floor surface in the event of a collision (**Fig. 3**). The structure of the foot

* Toyota Auto Body Co., Ltd.
** Vehicle Evaluation & Engineering Div. 2

and parking brake includes a mechanism to prevent these pedals from being forced back into the compartment, thereby helping to alleviate lower limb injury.

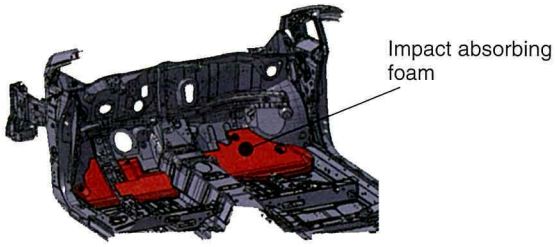


Fig. 3 Floor Surface Impact Absorbing Foam

2.2 Side impact collision performance

Development of the third generation Prius focused on improving side impact performance and reducing mass. Side impact input load is mainly absorbed by the B pillar and door beam and dispersed efficiently to the cross members and rocker. This structure, which uses high strength steel sheets, helps reduce deformation of the occupant compartment (**Fig. 4**).

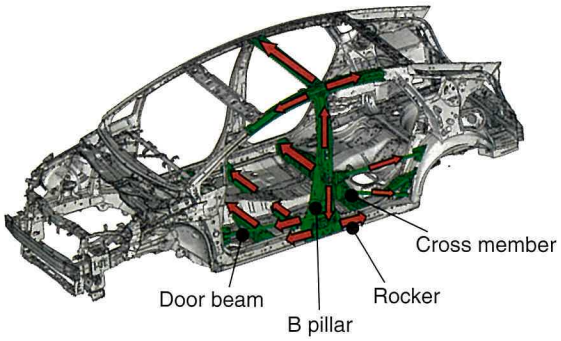


Fig. 4 Transmission of Load in Side Impact Collision

In addition, the third generation Prius also has a structure that uses the seat frames to efficiently absorb lateral input in the event of a side impact collision (**Fig. 5**).

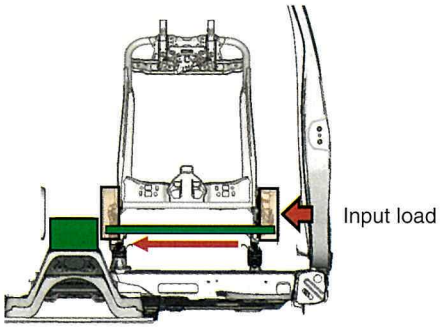


Fig. 5 Transmission of Load to Seat Frame

Occupant protection devices in the event of a side impact collision include SRS side airbags and SRS curtain shield airbags to protect the heads of occupants as standard equipment (**Fig. 6**). These help to alleviate input force to the occupants in combination with impact-absorbing pads provided in the doors.

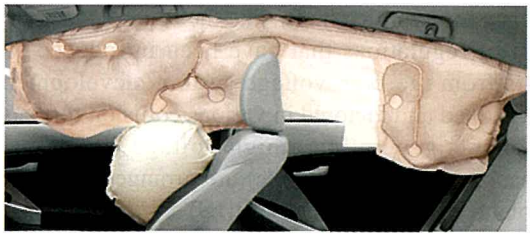


Fig. 6 SRS Side Airbags and SRS Curtain Shield Airbags

2.3 Rear end collision performance

The rear side members were straightened and the reinforcement members were optimized to help prevent damage to the occupant compartment and fuel system in the event of a rear end collision (**Fig. 7**).

The front seats are also equipped with active head restraints that help alleviate impact to the necks of the occupants when a rear end collision occurs.

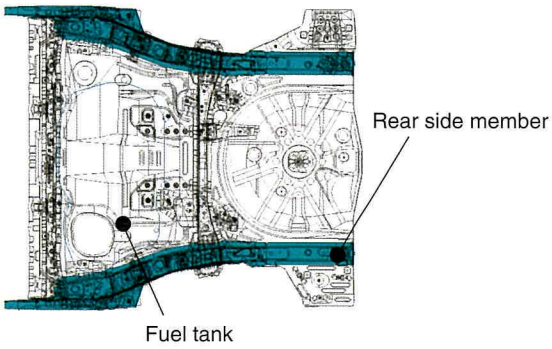


Fig. 7 Vehicle Rear Structure

2.4 All-direction compatibility

The concept of compatibility in GOA aims to protect the vehicle in a crash with other vehicles of different types and heights. The third generation Prius was developed to satisfy these requirements. The development assumed frontal, side, and rear end impacts with heavier passenger vehicles and taller SUVs (**Fig. 8**) to achieve the highest level of passive safety in the world.

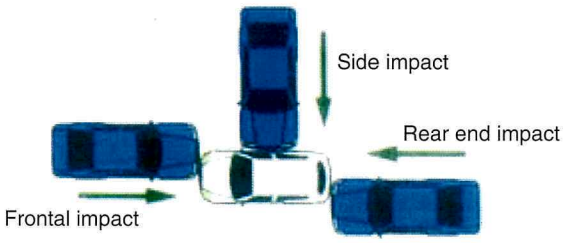


Fig. 8 All-Direction Compatibility

2.5 Passive safety of hybrid vehicles

Protecting the high voltage system as well as the conventional fuel system is a critical issue for securing adequate passive safety performance for hybrid vehicles like the Prius.

In light of regulations that have been introduced to protect occupants from the high voltage system, development of the Prius envisioned and factored in various collision formats.

Components generating a high voltage (the high voltage battery pack, cables, and the like) are arranged in positions less susceptible to collision damage (**Fig. 9**)

In the event of a collision, the airbag operation signal triggers operation of the system main relay (SMR) automatic shut-off mechanism on the battery pack side. This shuts off the supply of high voltage to the electric converter.

Furthermore, care has been taken so that occupants and emergency rescue personnel do not come into direct contact with high voltage parts after an accident occurs.

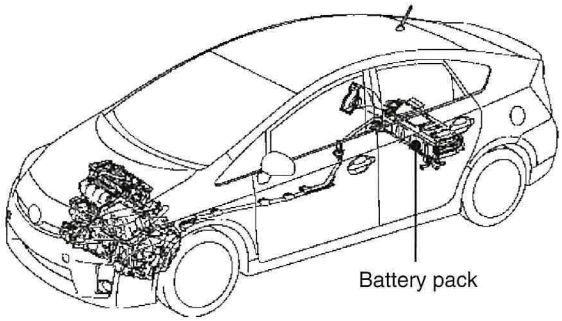


Fig. 9 High-Voltage System Outline

3. Pedestrian Protection Performance

The third generation Prius is equipped with the latest pedestrian protection technology and a wide range of mass reduction measures have been adopted, assuming a collision with a person.

3.1 Head protection

Aluminum was adopted for the hood to reduce its mass, but with a different structure to a conventional steel hood. It was discovered in tests with a head impactor that the material characteristics of aluminum caused an adverse affect on initial energy absorbance compared to a steel hood (**Fig. 10**).

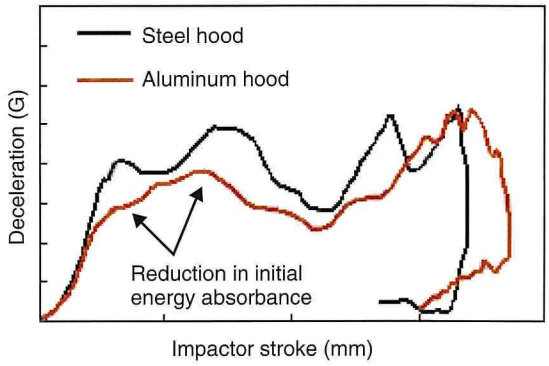


Fig. 10 Energy Absorbing Characteristics

Since a deterioration in initial energy absorbance worsens head injury criteria, an optimal balance was found with mass reduction by optimizing the structure.

A longitudinal wave form bead type hood inner was adopted and the stiffness balance with the hood look reinforcement was optimized. This improved the energy absorbance characteristics and helped reduce injury criteria (**Figs. 11** and **12**).

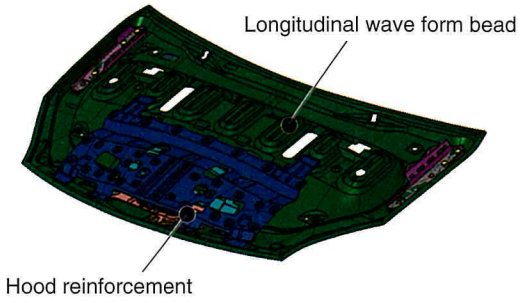


Fig. 11 Hood Structure

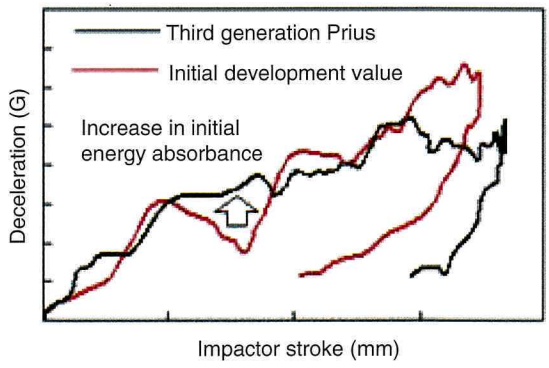


Fig. 12 Improvement of Hood Energy Absorbance

A space was also provided between the body frame and the fender panel as a measure to help alleviate impacts between pedestrians and the fender. This was achieved by installing a fender attachment bracket with an impact-absorbing structure. Since the fender must be stiff in normal use conditions and provide pedestrian protection performance, the development assumed various cases of impact load and direction. As a result, the bracket was given a structure that is strong in the lateral direction and easily-collapsible in the vertical direction (**Figs. 13** and **14**).

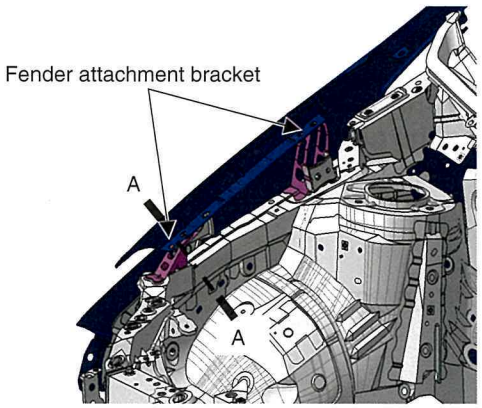


Fig. 13 Provision of Fender Attachment Bracket

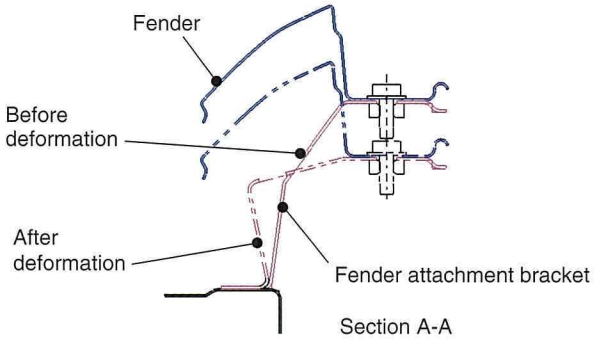


Fig. 14 Sectional Deformation Diagram of Fender Attachment Bracket

3.2 Leg protection

An impact-absorbing structure was set in front of the front bumper reinforcement and at the lower portion of the radiator support. These help alleviate injury by preventing the leg of a pedestrian sliding under the vehicle in a collision.

Development of the third generation Prius optimized the input load to the front bumper reinforcement and at the lower portion of the radiator support. The license plate holder was also given a collapsible structure (**Fig. 15**).

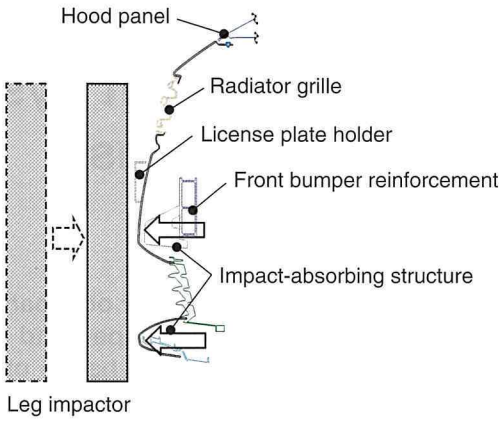


Fig. 15 Layout Diagram of Leg Impact-Absorbing Structure

4. Conclusion

The third generation Prius is a vehicle driven by the needs of society and various new technologies were incorporated in its development. Some complex issues were encountered, but the developers overcame them to provide the safest possible car for our customers.

The experience gained and the technologies developed in this process will form the inspiration for future vehicle development.

Authors


T. HAYASHIZAKI


Y. SAKAI


T. KIMURA


Y. NAKANE

Introduction of World's First Rear Seat Occupant Restraint System for Rear-End Collisions

Motonori Kitayama*
Yoshio Mizuno**
Michinori Kakumu***

Abstract

For vehicles where the heads of occupants sitting in the rear seats are positioned very close to the rear window or rear door, Toyota has developed and mass-produced the world's first SRS rear window curtain shield airbag (RWCSA) to help to protect the heads of rear seat occupants in the event of a rear-end collision. The RWCSA deploys after a collision is detected by the airbag satellite accelerometers and the accelerometer in the ECU. The system consists of an airbag and an inflator. Normally, the RWCSA is stored in a folded state behind the head lining at the rear of the vehicle, and it deploys downward along the glass surface of the rear window from between the rear end of the head lining and the vehicle body. The deployed airbag covers the rear end of the vehicle body beyond the head lining and the glass surface of the rear window around the head restraints. It was confirmed that a deployed RWCSA helps to reduce injury criteria.

Keywords: *passive safety, rear-end collision, rear seats, occupant restraint system*

1. Introduction

Exhaustive efforts are being made to reduce the number of people killed and injured in traffic accidents and alleviate the seriousness of injuries by enhancing the safety equipment in vehicles and developing new devices. In recent years, the focus has begun to shift toward developing safety devices for rear-end collisions that are capable of further reducing the number of casualties in various types of traffic accidents. As shown in **Fig. 1**, rear-end collisions account for the largest proportion of injury-causing accidents by direction, and the head is the most frequently injured part of the body (**Fig. 2**).

The heads of occupants in the rear seats of some three-row and compact hatchback type vehicles are very close to the rear window or rear door. For this reason, Toyota has developed and mass-produced the world's first SRS rear window curtain shield airbag (RWCSA) with the aim of protecting the heads of rear seat occupants in the event of a rear-end collision.

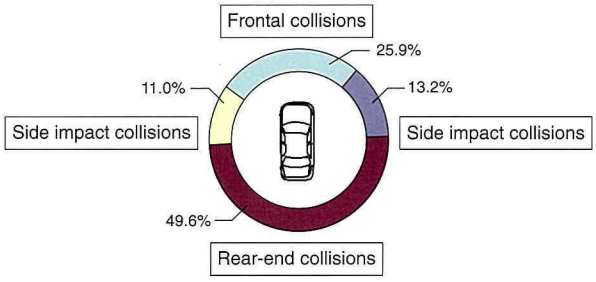


Fig. 1 Types of Injury-Causing Accidents

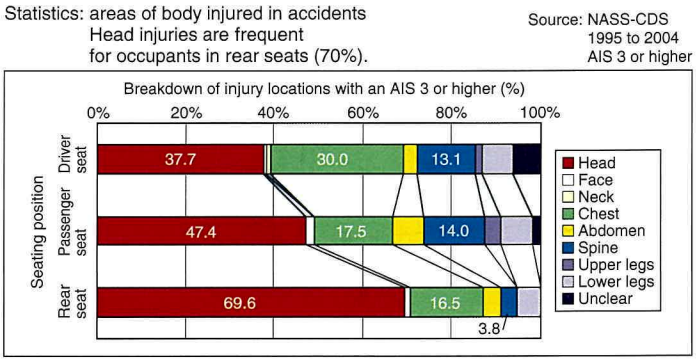


Fig. 2 Locations of Injury

2. Aims of Development

The heads of rear seat occupants are protected by head restraints that reduce rearward movement of the head and alleviate whiplash injury to the neck. However, as a result of the impact force or floor deformation, the head may strike the vehicle body at the rear glass or head lining, or even the impacting vehicle.

This newly developed RWCSA is a restraint device for rear-end collisions that aims to protect the heads of rear seat occupants from the two standpoints described below. The protection area of the RWCSA has main two sections shown by (1) and (2) in **Fig. 3**.

Standpoint (1): Alleviation of secondary impacts between head and vehicle interior (head lining, header trim, and glass)

Standpoint (2): Alleviation of secondary impacts between head and impacting vehicle or objects

* Toyoda Gosei Co., Ltd.
** Daihatsu Motor Co., Ltd.
*** Seat Design Dept., Interior Design Div.

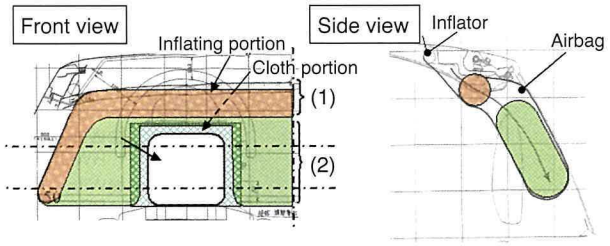
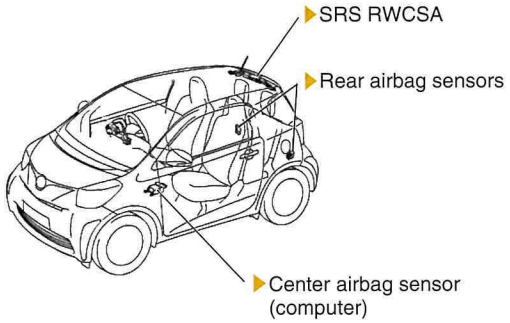


Fig. 3 Areas Protected by Airbag

3. Outline of System

The RWCSA is deployed when judged necessary by the airbag ECU after a collision is detected by the airbag satellite accelerometers and the accelerometer in the ECU (**Fig. 4**).

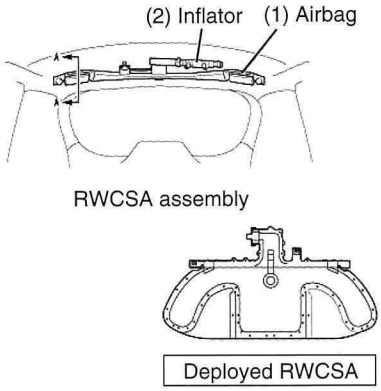


Taken from explanation of SRS rear airbag in online TMC manual for electronic components in new models

Fig. 4 Airbag System

4. Structure of RWCSA and Surrounding Area

As shown in **Fig. 5**, the RWCSA consists of (1) an airbag and (2) an inflator (a gas generation device) for deploying the airbag.



Taken from explanation of SRS rear airbag in online TMC manual for electronic components in new models

Fig. 5 Airbag Structure

Normally, the RWCSA is stored in a folded state behind the head lining at the rear of the vehicle. **Figs. 6** and **7** show the RWCSA in its stored state. The head lining is fixed in two locations by plastic clips to prevent sagging caused by the mass of the airbag. These clips have been designed with a new split structure that separates from the head lining without scattering when the airbag deploys (**Fig. 8**).

Additionally, since the head lining has been designed with a notched portion, the airbag folds downward at the same position each time, increasing the stability of its deployment behavior.



Fig. 6 RWCSA Installation State 1

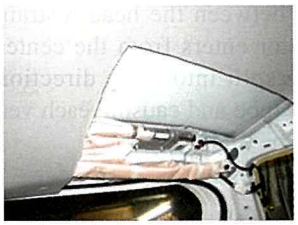


Fig. 7 RWCSA Installation State 2

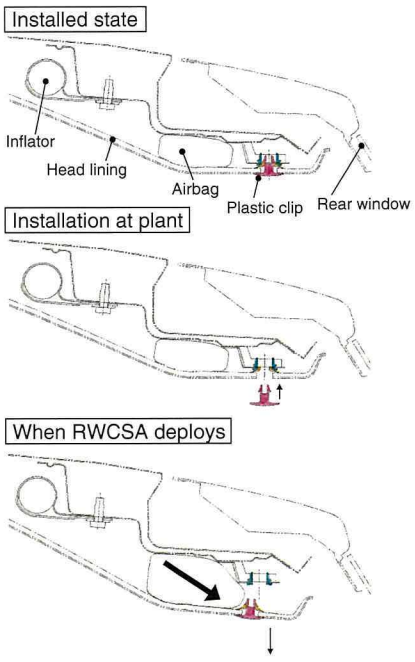


Fig. 8 Surrounding Area of RWCSA

5. Principle of Deployment

The airbag deploys downward along the glass surface of the rear window from between the rear end of the head lining and the vehicle body. The deployed airbag covers the rear end of the vehicle body beyond the head lining in addition to the glass surface of the rear window around the head restraints (**Fig. 9**).

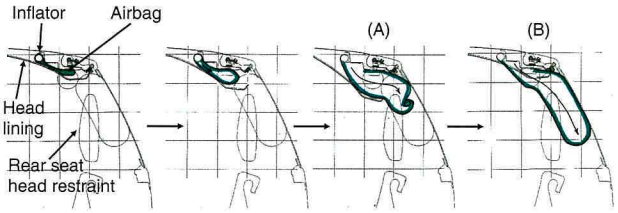


Fig. 9 RWCSA Deployment

Fig. 10 shows the gas flow inside the airbag. The shape of the airbag is divided into portions that cover the rear end of the vehicle body beyond the head lining (horizontal cells) and portions that connect to the horizontal cells and cover the areas to the outside and between the head restraints (vertical cells). Gas from the inflator enters from the center of the horizontal cells, before being split into three directions (left, right, and center) by the inner tube and causing each vertical cell to deploy downward at the same time.

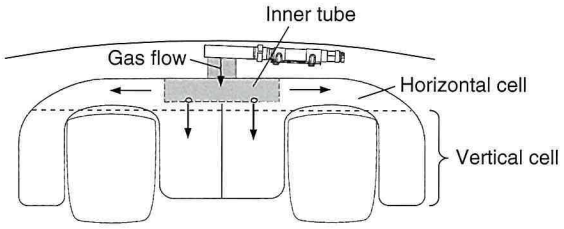


Fig. 10 Gas Flow Inside RWCSA

6. Effect

Fig. 11 compares the effect on head injury indices with and without the RWCSA. With RWCSA deployment in a rear-end collision, head injury is reduced by approximately half as defined by the head injury criterion (HIC), and by approximately two-thirds as defined by 3 m/s head acceleration.

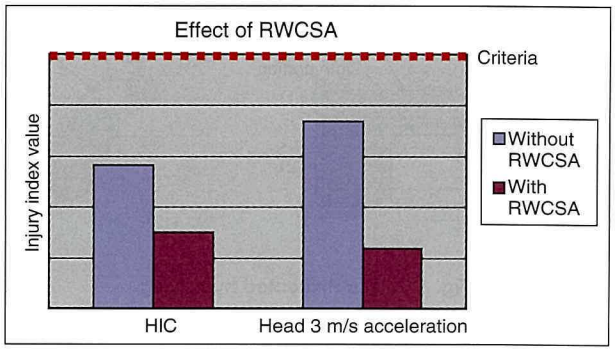


Fig. 11 Effect of RWCSA on Head Injury Indices

7. Conclusion

The RWCSA was installed for the first time in the world in Toyota's iQ city car. It represents the next phase in the ongoing efforts to enhance and develop vehicle safety equipment to further reduce the number of people killed and injured in rear-end collisions.

The authors would like to express their gratitude to Toyoda Gosei Co., Ltd. and everyone inside and outside Toyota for their cooperation in developing and mass-producing the RWCSA.

Reference

(1) Y. Mizuno, Kitayama, Kakumu. "SRS Rear Window Curtain Shield Airbag (iQ)" (in Japanese). *Automotive Engineering Extra Edition: New Technology of the Year 2008-'09* Vol. 58 pp. 102-106.

Authors


M. KITAYAMA


Y. MIZUNO


M. KAKUMU

Development of Front-Side Pre-Crash Safety System for Intersection Collisions

Tomoya Kawasaki*
Jun Tsunekawa**
Tomoaki Harada**
Koji Suzuki*

Abstract
This research has developed a front-side pre-crash safety system that broadens the scope of control of such systems to include collisions at intersections with good visibility and collisions with oncoming vehicles intruding into the path of the drives' vehicle. To detect objects in this expanded range, short-range millimeter wave radars with enhanced distance resolution capabilities and a high level of sensitivity were used. The crash prediction algorithm was also set to a higher speed than conventional algorithms in accordance with the circumstances of the target accidents. Also, based on an algorithm that estimates which part of the drives' vehicle will receive the impact, a function was added that prepares the appropriate side airbags for activation upon impact if there is a high possibility of a side-impact collision. Combined with conventional systems, this new system enhances the damage-mitigation effect when an accident occurs.

Keywords: *pre-crash safety, radar, intersection collision, side impact collision, airbag*

1. Introduction

In recent years, advanced active safety technologies that fill the gap between passive and active safety systems have gathered attention as ways of achieving the ultimate aim of reducing traffic accidents, injuries, and fatalities to zero. In February 2003, Toyota Motor Corporation commercialized the world's first pre-crash safety system. This uses millimeter wave radar to detect and judge the potential for collision with objects directly in front of the driver's vehicle in the direction of travel and then operates collision damage mitigating devices before a collision occurs.(1) Subsequently, the development of new technologies has progressed rapidly, and the following enhancements were achieved. Firstly, in addition to objects already detected by the millimeter wave radar such as vehicles or guardrails, the incorporation of a stereo camera to create a sensor fusion system made it possible to address accidents involving pedestrians.(1) Secondly, a rear pre-crash safety system was developed to help alleviate damage caused by rear-end collisions by expanding the range of the system to cover the rear of the vehicle.(1)

However, categorized results of traffic accidents in Japan in 2007 show that intersection collisions between vehicles going straight on (called intersection collisions below) account for the largest percentage of fatalities and serious injuries, at 28% (see **Fig. 1**). Conventional systems are unable to detect this type of accident. The same analysis shows that head-on collisions are responsible for a high proportion of fatal accidents, but conventional systems are only capable of detecting half of such accidents.

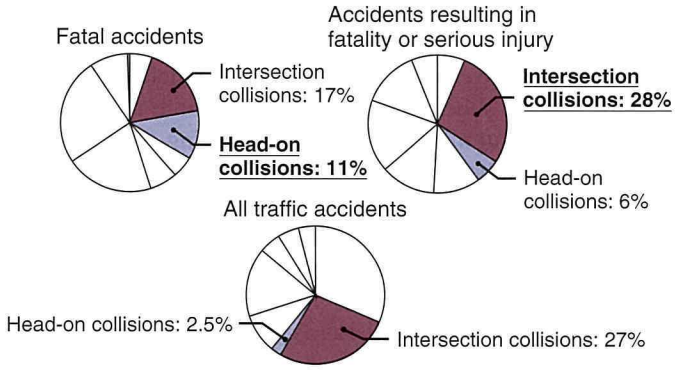


Fig. 1 Proportions of Categorized 2007 Accidents in Japan
Source: 2007 Status of Traffic Accidents **(in Japanese). Traffic Bureau of the National Police Agency**

To further reduce traffic accident fatalities and injuries, it is therefore critical to expand the scope of system controls to cover the following types of accidents: i) intersection collisions and ii) frontal collisions with approaching objects located diagonally in front of the driver's vehicle (called "oblique collisions" below), such as oncoming vehicles intruding into the path of the driver's vehicle. For this reason, a new front-side pre-crash safety system has been developed that uses short-range millimeter wave radars to monitor objects diagonally in front of the driver's vehicle and judge the possibility of collisions at intersections with good visibility and oblique collisions. This article describes the configuration and functions of this new system and its key pre-crash sensor technology. Note that this system was installed and released in the Crown Majesta in March 2009.

* Electronics Development Div. 2
** Vehicle Control System Development Div.

2. System Configuration

Fig. 2 shows the configuration of the front-side pre-crash safety system. The system consists of a pre-crash sensor that predicts crashes and collision damage mitigating devices. The pre-crash sensor is comprised of millimeter wave radars and other types of sensors, and a pre-crash safety electronic control unit (ECU). The new system has been achieved based on the format of the conventional systems. Specifically, short-range millimeter wave radars (SRR) have been added to the pre-crash sensor, and a side-impact airbag control function has been added to the collision damage mitigating devices. The pre-crash sensor detects vehicles approaching the driver's vehicle. It then calculates their respective positions and speeds, estimates the likely trajectory of each vehicle, and judges the probability of a collision occurring. Based on prescribed levels of probability, it then sends instructions to operate the collision damage mitigating devices. Summaries of the functions of these devices are described below (see **Fig. 3**).

I. Collision warning
Informs the driver of the possibility of a collision by means of a buzzer and meter indicator, and encourages avoidance maneuvers by operation of the steering wheel and brakes.

II. Pre-crash brake assist system and suspension controls
Supplements hydraulic pressure according to brake pedal effort to improve response and reduce vehicle speed, while adjusting the shock absorber damping force to control the brake dive resulting from emergency braking.

III. Pre-crash seat belt system
Retracts the seat belts with motors to speed up restraint of the vehicle occupants and enhance occupant safety performance in the event of a collision.

IV. Side-airbag control
When a side-impact collision is judged to be unavoidable, this control prepares operation of the side-airbags, curtain shield airbags, and the like.

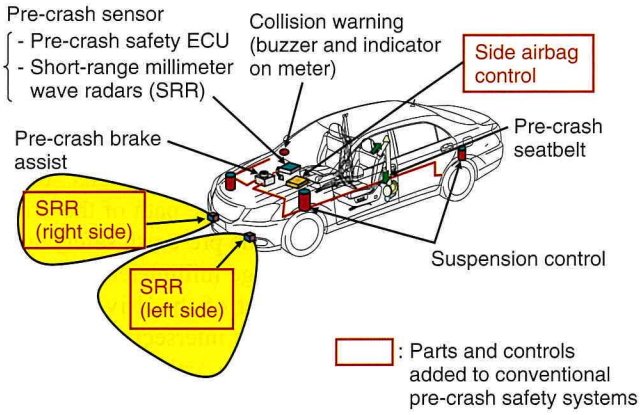


Fig. 2 Configuration of Front-Side Pre-Crash Safety System

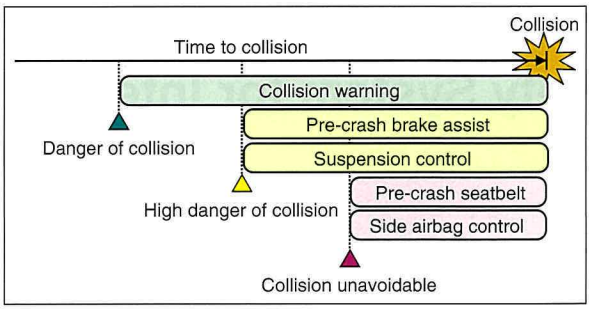


Fig. 3 Front-Side Pre-Crash Safety System Functions

3. Pre-Crash Sensor

3.1 SRR

The SRR are required to monitor the areas diagonally in front of the driver's vehicle and detect vehicles approaching at right angles to the direction of travel. However, two major issues had to be resolved to accomplish this. First, in the case of an intersection collision, although the SRR pick up reflective waves from the corner of approaching vehicles, these waves are approximately 10 dB weaker than those from an object directly ahead (see **Fig. 4**). Second, these weaker reflective waves were being cancelled out by the greater reflective strength of guardrails, reducing the detection rate of approaching vehicles.

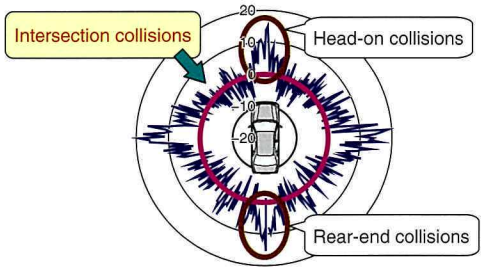


Fig. 4 Vehicle Reflection Characteristics

To counter these issues, reception sensitivity was increased to allow the detection of weak reflective waves. Next, the distance resolution capabilities of the system were improved by increasing the radar modulation bandwidth. This countermeasure improved the ability of the system to discriminate between approaching vehicles and guardrails, and reduced the potential for reflective waves from these objects to overlap. In addition, the phase monopulse method was adopted for directional calculation due to its relatively low processing load. This speeded up the recognition cycle of the system and reduced the continuous overlapping frequency of reflections from approaching vehicles and guardrails. **Table 1** and **Fig. 5** show the specifications and an external view of the developed SRR, respectively.

Table 1 SRR Specifications

Item		Specification
Radar system		- FM-CW - 3-channel phase monopulse
Center frequency		76.5 GHz
Detection performance	Range	2 to 50 m (@10 dBsm)
	Relative speed	0 to 180 m
	Field of view	52 deg
	Calculation cycle	29 ms
Size		W: 108 mm, H: 90 mm, D: 76 mm



Fig. 5 External View of SRR

As described above, the SRR must detect weak reflective waves. For this reason, factors that might attenuate the radio waves had to be minimized. As a result, the SRR were installed behind the brake ducts of the front bumper, which are unpainted and have good radio wave permeability. This installation position allowed both good styling and performance to be achieved (**Fig. 6**).

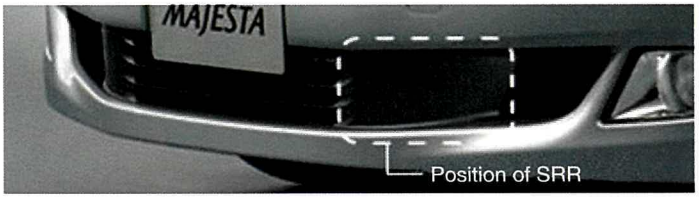


Fig. 6 Installation Position of SRR

3.2 Crash prediction algorithm

Conventional systems predict collisions with objects directly in front of the driver's vehicle in the direction of travel.[2] However, this new system must also predict collisions with objects in other areas, which means that the required performance of the two types of systems differs greatly. To meet the requirements of the new system, its crash prediction algorithm was completely re-developed. This algorithm is summarized as follows (see **Fig. 7**).

i) Prediction of trajectories of approaching vehicle and driver's vehicle
The distance, direction, and relative speed of an approaching vehicle detected by the SRR are determined to predict its subsequent trajectory. Information from the wheel speed sensors, yaw rate sensor, and steering sensor is used to predict the subsequent trajectory of the driver's vehicle.

ii) Calculation of collision probabilities
If the estimated vehicle trajectories intersect, the system assumes that the vehicles will crash. The time remaining before the driver's vehicle reaches the point of collision is then calculated, and which parts of the vehicle might receive the impact are predicted from the estimated positions of the vehicles. Collision probabilities are calculated for each time distributed impact position.

iii) Device operation judgment
Conditions such as a high probability of collision and a short time to collision (TTC) are comprehensively integrated to judge the possibility of a collision. Based on this judgment, appropriate operation instructions are sent to the collision damage mitigating devices.

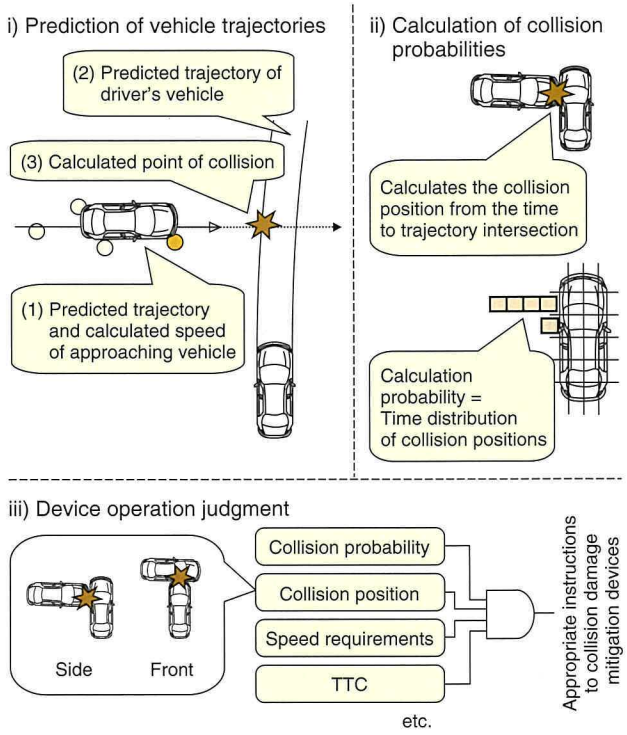


Fig. 7 Outline of Collision Prediction Algorithm

A major issue in this development was shortening the calculation time for crash prediction. In intersection and oblique collisions, the inevitability of a collision is strongly dependent on timing, and crash prediction cannot be performed until immediately before the collision. Additionally, many intersection collisions in Japan occur at intersections with impaired visibility, which means that the approaching vehicle cannot be seen until immediately before the collision. Consequently, to obtain a damage mitigating effect in an intersection or oblique collision, the crash prediction must be performed within a shorter time than in a conventional system, and sufficient time must be secured for operation of the collision damage mitigating devices. For this reason, the time required by the new algorithm to make crash prediction has been reduced to 1/3 of the time of the conventional algorithm. A trade-off of

reducing the crash prediction time is an increase in the frequency of unnecessary operation of the collision damage mitigating devices. The following countermeasure was developed to resolve this issue. The developed crash prediction algorithm calculates the part of the driver's vehicle that will receive the impact. The system uses this time distribution information to discriminate between situations that will and will not result in collision. In other words, when the time distributed impact position has a wide variation, the system judges that a collision will not occur. In contrast, when the time distributed impact position is concentrated at a set point, the system judges that a collision is likely. In addition, to shorten the crash prediction time, the SRR recognition algorithm was also modified. In particular, the algorithm was calibrated to enhance response with respect to the lateral movement of approaching vehicles while eliminating the effect of roadside objects such as guardrails. This algorithm was optimized using data obtained from over 100 crash tests carried out under various conditions and from over 50,000 km of real world driving, achieving a highly efficient performance in judging collisions.

4. Side Airbag Control

Conventional systems only determine whether a collision is unavoidable, but as described above, the new system also judges where the collision is most likely to occur. To take advantage of this feature, a new function utilizing pre-crash safety technology was added to the conventional airbag system. This function operates as follows. As a means of securing high reliability and safety, airbag systems use two accelerometers (a main sensor and a safing sensor) to detect an impact caused by a collision. The side airbag control of the front-side pre-crash safety system releases the safing sensor to the ON position when a side-impact collision with the driver's vehicle is judged to be unavoidable. The aim of this control is to speed up the general deployment response of the airbag after the side-impact collision. The reliability of the airbag system after this modification was secured by adding a function that enables the system to be monitored mutually by both the airbag ECU and the pre-crash safety ECU.

5. Conclusion

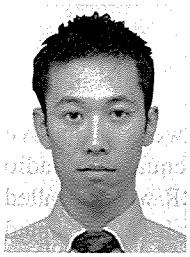
Conventionally, the development of pre-crash safety systems has focused on addressing frontal collisions and pedestrian accidents, which account for high fatality rates, and rear-end collisions, which account for over half of accidents involving injury in Japan. However, to further increase the effect of these systems in reducing fatalities and injuries caused by traffic accidents, a front-side pre-crash safety system was developed that is capable of detecting collision types such as intersection and oblique collisions. Technological development will be continued with the aims of expanding the detection area to all directions and expanding the collision damage mitigation effect of the system. It is hoped that this will contribute to achieving a safe and comfortable mobile society.

Finally, the authors would like to extend their gratitude to everyone at Fujitsu Ten Ltd. for their indispensable cooperation in the development of this front-side pre-crash safety system.

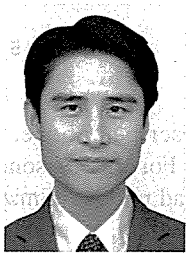
References

(1) T. Kawasaki. "Pre-Crash Safety –Autonomous Integrated Safety Technology–." *Toyota Technical Review* Vol. 56 No. 2 (2009) pp. 50-56.
(2) S. Tokoro et al. "Pre-Crash Sensor for Pre-Crash Safety." *18th ESV Conference Paper* No. 545 (2003).

Authors


T. KAWASAKI


J. TSUNEKAWA


T. HARADA


K. SUZUKI

Efficiency Improvement Study of High-Power Electric Power Steering System

Takeshi Goto*
Masaharu Yamashita*
Takatoshi Saito**
Yoichi Fujinori*
Hisashi Somada*

Abstract

This article describes an energy consumption simulation for an electric power steering (EPS) system comprising an EPS model portion and a tire frictional force estimation portion. It also details the results of studies for optimizing the installation locations of electrical parts and for evaluating system robustness. Although tire frictional force at low speeds (up to 30 km/h) cannot be estimated from lateral acceleration, this simulation estimates it simply from the rack axial force ratio map for each steering wheel angle using the stationary tire frictional force as a reference. The effectiveness of this new method was verified through actual vehicle tests in parking and mountain road driving conditions. An installation study of the electrical parts of the EPS enabled optimization of the location of the ECU and the separate type DC/DC converter. This resulted in a robust system capable of withstanding drops in power supply voltage and increases in wiring resistance. In combination with greater mechanical efficiency of its component parts, the efficiency of the EPS system was increased by 25%.

Keywords: *steering system, EPS, high efficiency, simulation, energy consumption*

1. Introduction

EPS was first used in a mini vehicle in 1988 with the aim of improving fuel economy. Since that time, the number of vehicle models, primarily small and medium vehicles, equipped with EPS has expanded rapidly.[1]

As global CO_2 emissions regulations have become more stringent, there is increasing demand for high-power EPS systems that can be used in large vehicles.[2][3] However, EPS consumes more energy as power output is increased, and in order to reduce the amount of energy consumed, it is critical to optimize component part locations to minimize energy loss from electronic parts. In this article, EPS energy consumption specifically refers to the consumption of battery power for motor assist force, which is generated in response to tire frictional force that occurs when the driver turns the steering wheel.

The following two critical evaluation indices are adopted in efficiency improvement studies related to energy consumption. (i) Maximum energy consumption, as a means of improving steering responsiveness when stationary and when performing sudden maneuvering required for emergency avoidance. Maximum energy consumption affects decisions related to alternator and battery size. (ii) Average energy consumption for normal driving in all vehicle speed ranges (extremely low speeds to medium and high speeds). This affects the vehicle's actual fuel economy, and sensitivity is several %/100 W when compared with vehicle fuel economy.

During the planning stages, these indices are absolute requirements for a highly accurate study of energy consumption. Previously, there have been examples of calculations of vehicle fuel economy using calculation models for power systems,[4] and examples that studied EPS energy consumption using maximum energy consumption. However, there are almost no examples of studies in which tire frictional force during driving is estimated and EPS average energy consumption is calculated for obtaining the optimal location of electronic parts.

This article describes the unique characteristics of a newly proposed EPS energy consumption simulation. In addition, as an example of highly efficient design for a vehicle system to which this simulation was applied, it also describes investigations into the optimal locations of electronic parts in the vehicle and system robustness.

* Chassis Development Div.
** Chassis System Engineering Div.

2. EPS Energy Consumption Simulation

Fig. 1 shows a configuration diagram of a steering system.

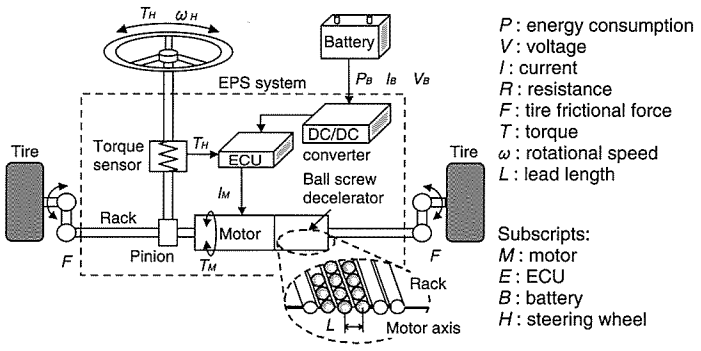


Fig. 1 Steering System Configuration Diagram

The EPS system uses a boost pressure method to reduce energy loss, and consists of a motor driven at 42 V,[5][6] an ECU (inverter), a DC/DC converter (pressure boost/reduction circuit) to convert to 42 V, and a torque sensor. EPS system power is supplied by the vehicle battery. The system is structured such that, when the driver operates the steering wheel, the motor generates assist force in response to the torque on the steering wheel in order to turn the tires.

In previous studies of maximum energy consumption, it was sufficient to use vehicle lateral acceleration to estimate tire frictional force only when stationary and when driving at medium to high speeds. In contrast, to estimate average energy consumption, tire frictional force estimates are required at all ranges of vehicle speeds. However, in extremely low to moderately low speed ranges, vehicle lateral acceleration also becomes very low, thereby making precise estimates impossible. Moreover, tire frictional force varies greatly depending on the driving situation and suspension type. Therefore, studies must be completed by inputting test measurements from an actual vehicle, which is a problem in terms of development efficiency. For this reason, a method was needed that would allow precise and efficient estimation of average energy consumption at the initial stages of development without driving on normal roads. This method should also allow these estimates to be reflected in optimized design of electronic parts. This section describes the derivation of energy consumption P_B, which is necessary for a high efficiency study of an EPS system.

2.1 EPS system modeling

Fig. 2 shows a block diagram of the energy consumption simulation. Item (2) is an estimation block for tire frictional force, the result of which is input into the EPS system (1). This process creates a structure for calculating energy consumption.

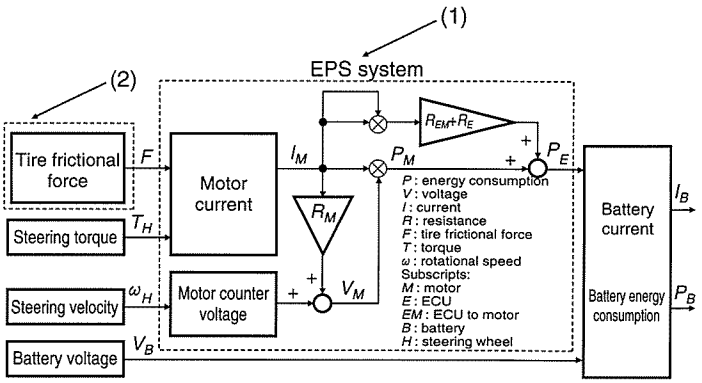


Fig. 2 Block Diagram of Battery Energy Consumption Estimation

2.1.1 EPS system section[7]

The energy consumption level at the battery is calculated as described below.

Motor input power P_M is described as follows.

$$P_M = V_M \times I_M = (R_M I_M + K\omega_H Sr/L) \times I_M \quad (1)$$

Tire frictional force F is the sum of assist force and steering effort, and is expressed as follows.

$$F = \frac{2\pi\eta_{BS} T_M}{L} + \frac{2\pi\eta_{RP} T_H}{Sr} \quad (2)$$

Motor current I_M is:

$$I_M = \frac{T_M}{K} = \frac{(F - 2\pi\eta_{RP} T_H / Sr) \times L}{2\pi\eta_{BS} K} \quad (3)$$

In contrast, the consumed energy P_B is:

$$P_B = V_B \times I_B = P_E + R_{BE} I_B^2 \quad (4)$$

I_B is calculated as follows.

$$I_B = \frac{V_B - \sqrt{V_B^2 - 4R_{BE} P_E}}{2R_{BE}} \quad (5)$$

ECU input power P_E is:

$$P_E = P_M + (R_{EM} + R_E) I_M^2 \quad (6)$$

Accordingly, applying input values for F, ω_H, T_H, and V_B to Equations 4 and 5 enables the calculation of P_B and I_B.

The symbols in the above equations have the following meaning. η: efficiency, K: constant, L: ball screw lead length, and Sr: rack stroke ratio. The subscript letters are BE: battery to ECU, BS: ball screw decelerator, and RP: rack and pinion gear.

2.1.2 Tire frictional force estimation block

This block estimates tire frictional force, which is load on the motor. Motor load has a direct effect on energy consumption, and therefore must be accurately predicted.

Fig. 3 shows actual measurement values of maximum tire frictional force plotted at different vehicle speeds (thin line) after driving approximately 1,500 km on normal roads. It also includes maximum values from estimation results (thick line) taken from the vehicle lateral acceleration method (LA), in which tire frictional force is calculated using the conventional method of vehicle lateral acceleration (LA).

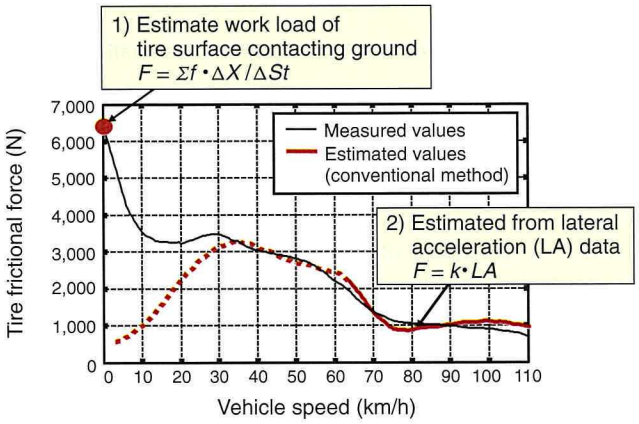


Fig. 3 Comparison of Conventional Estimation Results and Actual Measurements of Tire Frictional Force

These results show that at vehicle speeds of 30 km/h or lower, the actual values are very different from the estimation values. The reason for this is thought to be that in the low speed range vehicle lateral acceleration (LA) is low, and tire frictional force cannot be accurately estimated. Moreover, this driving data was organized by frequency at each vehicle speed. The results show that driving at speeds of 30 km/h or lower takes up about 45% of the total energy consumption. Therefore, it is necessary to improve the estimation accuracy for tire frictional force in this speed range. The estimation method at 30 km/h is discussed below.

1) Structural factors of tire frictional force

The structural factors of force generation for estimating tire frictional force were studied. The results are shown in **Fig. 4**. This graph shows tire frictional force, organized by each steering velocity, for driving at a constant vehicle speed of 5 km/h. Among the tire frictional forces are tire friction caused by the steering operation component $K \cdot X$, the jack up torque component F_J, the component identified by lateral acceleration F_{LA}, and the drive force component F_t. When these elements are analyzed in detail, $K \cdot X$, which is generated in proportion to the steering velocity, is the largest and most dominant factor in tire frictional force. This force is similar to the tire frictional force.

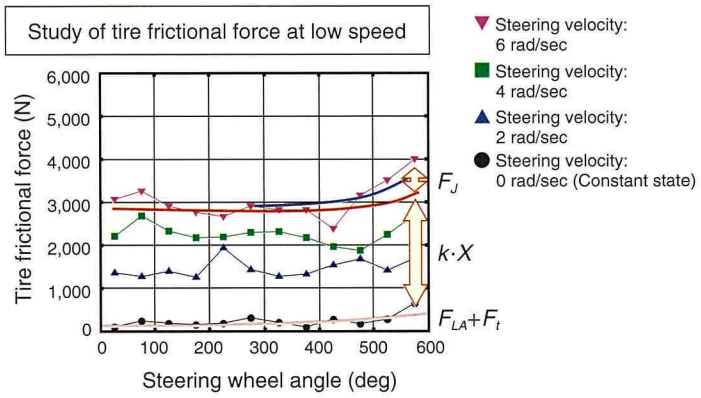


Fig. 4 Tire Frictional Force at Different Steering Velocities (Low-Speed Driving)

2) Estimation of tire frictional force when driving at low speeds

The drag force integration method was newly proposed as an accurate method of estimating stationary tire frictional force. In this method, the tire surface in contact with the ground is divided into a grid, and the drag force of each minute division ΔS of the grid is integrated.

However, tire frictional force at low speeds could not be estimated with this method without modification because the contact surface conditions and drag conditions underwent dynamic and drastic changes. Therefore, by combining static, stationary data with actual driving data, a method of estimating dynamic changes to tire frictional force was investigated.

Frictional force F during driving, when simply defined as the sum of forces from each minute division ΔS when the tire is flexed, is expressed as follows.

$$F = \Sigma k \cdot \Delta x / \Delta S = k \cdot \Sigma \Delta x / \Delta S \quad (7)$$

Also, stationary tire frictional force F_0 is calculated from the drag integration method by the following equation.

$$F_0 = \Sigma \mu W \cdot \Delta x_0 / \Delta S = \mu W \cdot \Sigma \Delta x_0 / \Delta S \quad (8)$$

where, k: tire elasticity coefficient, μ: friction coefficient, and W: pushing load.

Under quasi-static driving conditions where lateral acceleration is small and there is no roll, the distance traveled Δx and the total surface area in contact with the ground S are assumed to be the same as when stationary. The quasi-static tire frictional force F_{QST} can be calculated in geometrical terms based on the suspension specifications as follows,

$$F_{QST} \propto F_0 \cdot (k / \mu W) \quad (9)$$

Next, existing vehicle A (which was used for actual measurements) and target vehicle B (for which data is required) were assumed to be driven on the same course. Because the longitudinal and lateral accelerations are the same, the degree of load change on the tire $K(t)$ can be assumed to be the same, and dynamic tire frictional force F_{DYN} has the relationship shown in Equation 10.

$$F_{DYN} = K(t) \cdot F_{QST} \propto K(t) \cdot F_0 \cdot (k / \mu W) \quad (10)$$

From the relationship between tire frictional force from vehicle A (existing vehicle) $F^{A}_{DYN}=K'(t)\cdot F^{A}_{0}\cdot(k/\mu W)$ and tire frictional force B (target vehicle) $F^{B}_{DYN}=K'(t)\cdot F^{B}_{0}\cdot(k/\mu W)$, the value of F^{B}_{DYN} is as shown below.

$$F^{B}_{DYN}=(F^{A}_{DYN}/F^{A}_{0})\cdot F^{B}_{0}=(F^{B}_{0}/F^{A}_{0})\cdot F^{A}_{DYN} \quad (11)$$

Accordingly, comparing and mapping tire frictional force when stationary against each steering wheel angle registered in the existing vehicle database, results in a proportional coefficient called the "rack axial force ratio map (F^{B}_{0}/F^{A}_{0})" (**Fig. 5**), which enables the calculation of tire frictional force during driving. **Fig. 6** shows an example of the actual tire frictional force from the registered vehicle database, multiplied by the rack axial force ratio map.

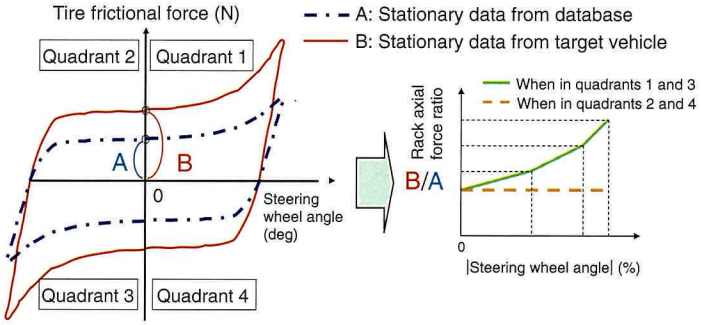


Fig. 5 Stationary Tire Frictional Force and Rack Axial Force Ratio Map

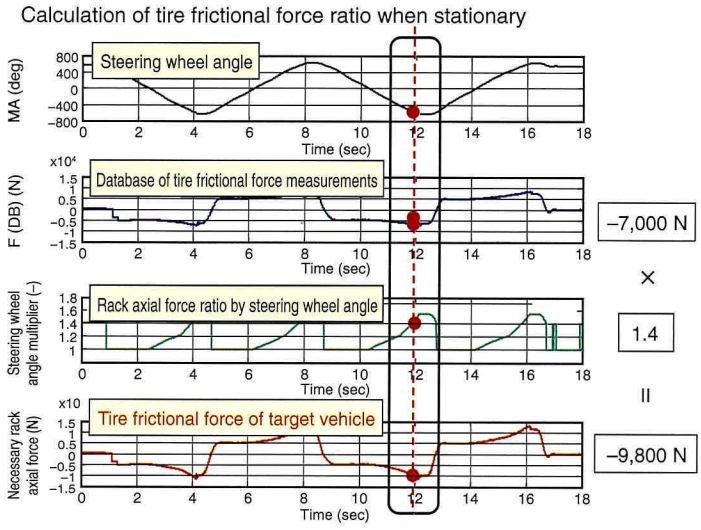


Fig. 6 Calculation Example of Tire Frictional Force Using Rack Axial Force Ratio

Fig. 7 shows a summary of the overall development method. Input consists of the results of calculations for stationary tire frictional force data for the vehicle being investigated, and output is the tire frictional force estimate, when assuming the vehicle is driven on normal roads. The database for this block was formed from actual data of tire frictional force, measured during driving on normal roads in the past.

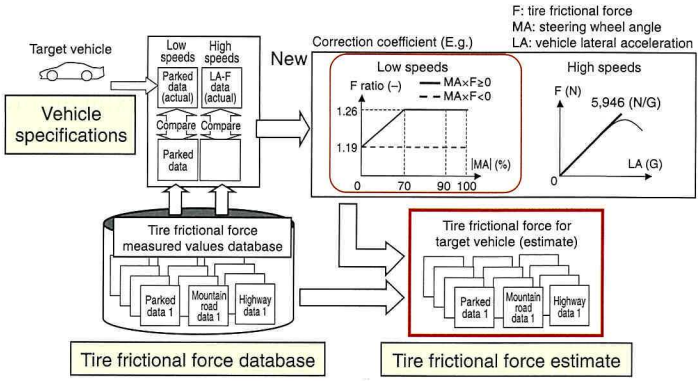


Fig. 7 Summary of Tire Frictional Force Estimation Method

By comparing the [steering wheel angle when stationary - tire frictional force] data from the database against the calculated data for the target vehicle when stationary, the rack axial force ratio for each steering wheel angle can be derived. By multiplying the rack axial force ratios to the tire frictional force values (measured values) from the database of driving on normal roads, it is possible to estimate tire frictional force that simulates driving the target vehicle on normal roads.

2.2 Verification results

Measurement results from actual driving on normal roads (thin line) and results calculated using this estimation method (thick line) are compared in **Fig. 8**. By using the drag force integration method when the vehicle is stationary, the method using the rack axial force ratio map for each steering wheel angle at speeds from 0 to 30 km/h, and the lateral acceleration method (LA) for speeds of 30 km/h and higher, tire frictional force was accurately estimated from stationary to high speed ranges.

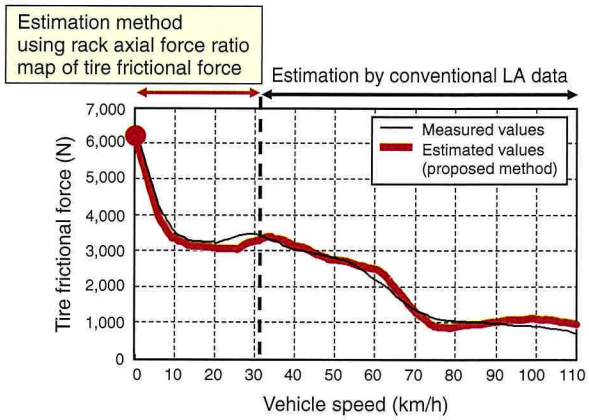


Fig. 8 Calculation Results for Tire Frictional Force Estimates in All Vehicle Speed Ranges

Fig. 9 compares the measured and simulation values of average energy consumption when driving at low speed (0 to

15 km/h) while making a right turn in a multi-story parking structure.

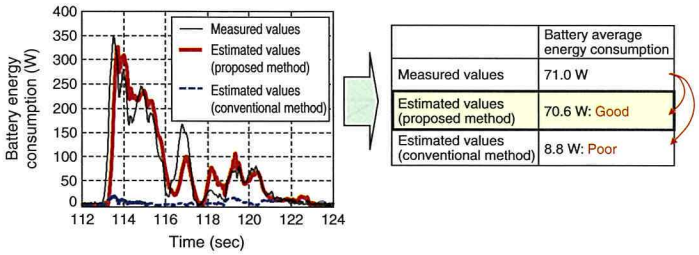


Fig. 9 Comparison of Measured and Calculated Average Energy Consumption Values (When Driving at 0 to 15 km/h in Parking Structure)

With the conventional lateral acceleration (LA) method (dashed line), there is almost no energy consumption shown. By comparison, estimating the rack axial force ratio map for each steering wheel angle (thick line) has made it possible to estimate within a margin of error of 3% with respect to actual measurements of average energy consumption (thin line).

In the same way, it was confirmed that accurate estimates are possible for other speed ranges. As a result, from the planning stages of vehicle development, predicting EPS energy consumption has become possible, without driving on normal roads.

3. Study of System Optimization for High Power

In order to optimize the EPS system, it is necessary to optimize installation locations on the vehicle and to efficiently design units such as the motor and ball screw decelerator. This section describes installation location, which is an important vehicle requirement. Using the design of a rack coaxial type EPS system with output of 15,000 N as an example,[8] an optimized design method that uses the energy consumption simulation developed here, is discussed.

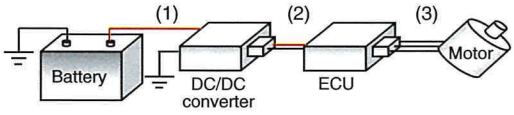
3.1 Study to reduce energy loss due to installation location in vehicle

Vehicle fuel economy can be expressed in values using, for example, 10-15 Mode or JC08 Mode fuel economy testing, but these modes do not express the fuel economy impact of EPS activation caused by operation of the steering wheel. By calculating average energy consumption, it is possible to understand this impact.

Energy consumption is calculated as a weighted average that emphasizes certain driving patterns such as city and highway driving. Actual driving features a high ratio of city and highway driving that involves keeping the steering wheel in a turned position, which leads to worse average energy consumption. This is because the current between the ECU and motor increases. The most common solution is to position the ECU as close as possible to the motor. On the other hand, in terms of maximum energy consumption, in order to reduce current loss between the battery and ECU, it is best to position these as close as possible.

Here, optimal vehicle installation locations for the power source, the DC/DC converter, the ECU, and the motor are investigated, assuming the use of a pressure boost circuit with separate construction and a large degree of flexibility for ECU location. However, the installation locations of the motor and battery are basically determined by vehicle requirements. Therefore, as assumed conditions for the optimization investigation, the distance between the 12 V battery and motor was 4,000 mm, and that between the 280 V battery and motor was 8,000 mm. Given these assumptions, the positioning of the DC/DC converter and ECU were investigated. An example with the studied parameters is shown in **Table 1**. In this table, a length of 0 mm in column (2) indicates that the pressure boost circuit is housed internally, and a length of 2,000 mm indicates that it is separate from the ECU.

Table 1 Energy Consumption Investigation Parameters (Battery Voltage and Wire Length Specifications)



System No.	Battery voltage (V)	Wire length (mm)		
		Portion (1)	Portion (2)	Portion (3)
System 1	12	3,000	0	1,000
System 2	12	1,000	0	3,000
System 3	12	1,000	2,000	1,000
System 4	280	7,000	0	1,000
System 5	280	5,000	2,000	1,000

When using the EPS simulation described in Section 2, and assuming output to be constant, the calculation results of battery energy consumption are as shown in **Fig. 10**. The solid lines are limit lines when the pressure boost circuit and ECU are separated, and the dashed lines are limit lines when the pressure circuit is housed inside the ECU. The separated type was shown to have a maximum of a 14% improvement over the internally housed (black circles) type.

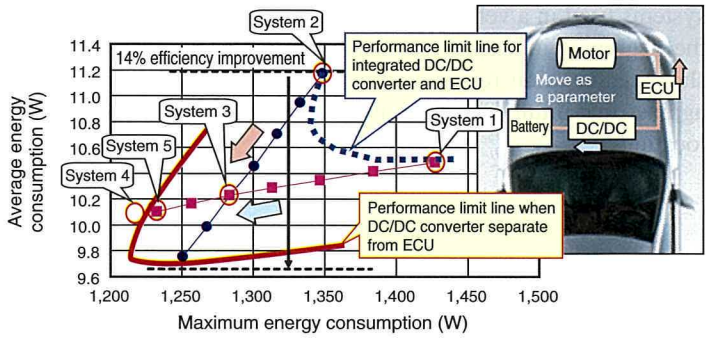


Fig. 10 Calculation Results for Energy Consumption

Next, the optimization of location in the vehicle for a separate-type DC/DC converter was studied, while considering constraining conditions for installation. The ECU has installation constraints, for example, for water immersion and engine exhaust heat, and therefore it is necessary to consider the location relationships between the DC/DC converter and fuse box. These results are shown in **Fig. 11**. Ultimately, after taking wire diameter into consideration, the energy loss as a result of installation on the vehicle was reduced 10% or more. Moreover, when combined with a 15% efficiency improvement for component parts such as the motor and ball screw decelerator,[10] the efficiency of the overall EPS system was improved by 25%.

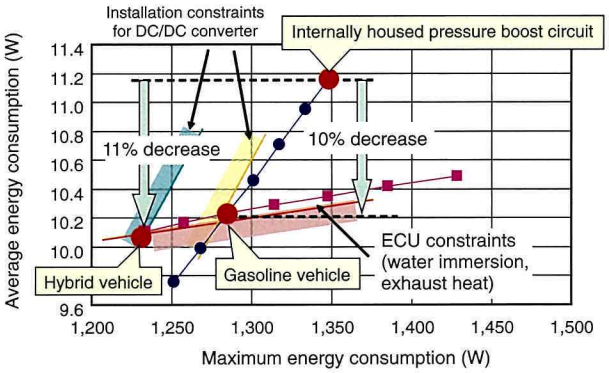


Fig. 11 Relationship Between Wire Length and Energy Consumption (Calculation Results)

3.2 Study of system robustness and maximum energy consumption

There is a limit to the energy that can be used in a 12 V power source, and it is important to accurately estimate the maximum energy from the planning stages. Furthermore, in order to withstand the influence of fluctuations in battery power and system resistance, it is also necessary to consider the robustness of these items.

3.2.1 Influence when battery power is reduced

In accordance with the increase in the number of electronic systems used in a vehicle, it has become necessary to think about the degree of influence of changes in battery voltage. **Fig. 12** shows calculation results comparing changes in battery voltage against maximum energy consumption at different installation locations.

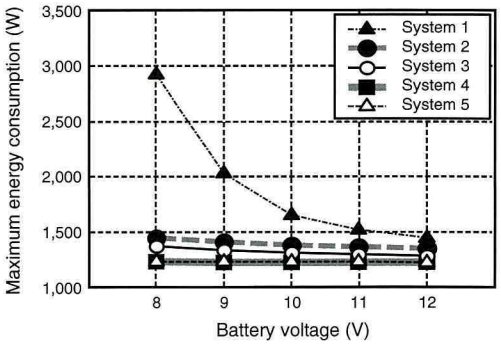


Fig. 12 Calculation Results Comparing Maximum Energy Consumption at Different Installation Locations Against Changes in Battery Voltage

Here, systems 4 and 5, which are 280 V systems, are compared side-by-side with 12 V systems, with the horizontal axis scaled at a ratio of 12 V/280 V.

As a result, it can be seen that system 1 has inferior robustness against reductions in voltage. It is thought that, as the voltage decreases, a large amount of current flows in order to supply the same power, and energy loss ($\propto$current^2) increases. Accordingly, the low voltage distance between the battery and DC/DC converter must be designed to be as short as possible.

3.2.2 Influence when wire resistance increases

Because a large amount of current flows through high power systems, energy loss due to wire resistance is high. Additionally, depending on change over time, the resistance value might increase, increasing the influence of resistance even more. **Fig. 13** shows how changes in maximum energy consumption vary with changes in wiring resistance. The wiring resistance ratio is 1 when new, and this investigation was performed up to a resistance ratio of 4.

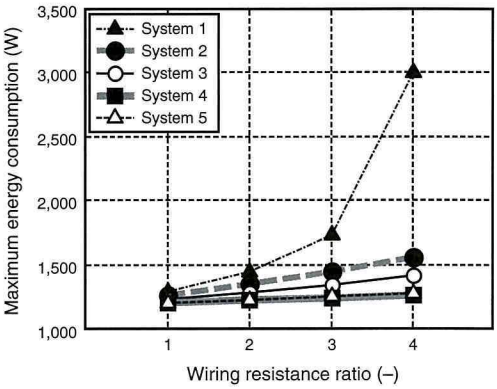


Fig. 13 Calculation Results of Maximum Energy Consumption with Changes in Wiring Resistance

As a result, it is clear that, even in this investigation, the robustness of system 1 is extremely poor. The cause is the same as when battery power is low. There is large energy loss in the 12 V line between the battery and DC/DC converter. In this case as well, the same design considerations as stated above must be made.

4. Summary

The following conclusions can be drawn from this efficiency study.

(1) A simulation that can accurately calculate the energy consumption of an EPS system from a stationary state to high speeds was developed.

(2) The investigation of the EPS installation location in a vehicle with a 12 V battery concluded that the DC/DC converter should be positioned as close as possible to the battery, and the ECU should be as close as possible to the motor.

(3) It was possible to reduce EPS energy consumption by 10% or more (compared to 2003 levels) by optimizing the locations of the ECU and DC/DC converter and by reducing energy loss in wires.

In the future, overall vehicle systems will be studied for further efficiency improvements, and these studies will include efficiency investigations of variable gear ratio steering systems.

References

(1) J. Fukuda. "Improvements in Steering Technology Contributing to Advances in the Automobile" (in Japanese). *Tribology* No. 242 (2007) pp. 40-43.

(2) Y. Nagahashi, Kawakubo, Tsujimoto, Kagei, Hasegawa, et al. "Development of High Power Column Type Electric Power Steering System" (in Japanese). *JTEKT Engineering Journal* No. 1003 (2007) pp. 35-39.

(3) T. Sakaguchi, Endo. "Development of a High-Output Brushless DC Motor for EPS" (in Japanese. *NSK Technical Journal* No. 682 (2007) pp. 33-41.

(4) T. Fukada, Ogawa, Fujita, Nishimura. "Effect of Vehicle Power Supply on Fuel Efficiency when Driving" (in Japanese). *Proceedings of the International Conference on Electrical Engineering* Vol. 2008 No. 4 (2008) p. 332.

(5) H. Eki, Teratani, Iwasaki. "Power Consumption and Conversion of EPS System." *The Fourth Power Conversion Conference (PCC) Nagoya* (2007).

(6) T. Chikada. "Research into Standardization of High Voltage Automotive Electrical Systems: 2005 Investigative Report" (in Japanese). *New Energy and Industrial Technology Development Organization* (2006) pp. 21-25.

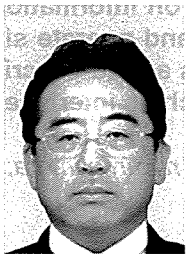
(7) K. Izutani, Shimizu. "Development of EPS Energy Consumption Estimation Method" (in Japanese). *JTEKT Engineering Journal* No. 1007 (2009) pp. 44-47.

(8) K. Fukumura. "IFS-Integrated EPS for Lexus LS" *Passenger Car Steering Systems - Preparation for the Technology of Tomorrow* (2007).

(9) H. Kutsuzawa, Ishihara. "DC-DC Converter for Electronic Power Steering" (in Japanese). *Toyota Industries Technical Review* No. 56 (2008) pp. 21-24.

(10) T. Takahashi, Suzuki, Nakayama, Fujiyama, Yamaguchi et al. "Application Technology of High-Power Electric Power Steering System" (in Japanese). *JTEKT Engineering Journal* No. 1006 (2009) pp. 49-54.

Authors


T. GOTO


M. YAMASHITA


T. SAITO


Y. FUJINORI


H. SOMADA

Logical Mediation Structures for Toyota's Driver Support Systems

Kazushi Kuroda*

Abstract

The driver support system (DSS) ECU is the computer responsible for controlling multiple systems such as adaptive cruise control (ACC), pre-crash safety (PCS), and lane-keeping assist (LKA). The DSS ECU makes requests to various activators based on information from peripheral sensors such as radars and cameras. To enable such systems to share parts and operate simultaneously, it is important to make sure that the systems do not interfere with each other. This article describes the logical mediation structures applied in the design of diagnostics, controls, and human-machine interfaces (HMI) to prevent such interference.

Keywords: *driver support, active safety, radar, camera, HMI, interference*

1. Introduction

Driver support systems (DSS) such as ACC, PCS, and LKA that aim to reduce driver workload and mitigate crash damage have evolved in accordance with improvements in radar and camera recognition technology.

Such systems use parts in common and are also activated simultaneously. In addition, the control states of each system are displayed on the combination meter in front of the driver. As a result, the design and development of these systems must make thorough consideration of various types of interference that may occur between systems.

This article describes the logical mediation structures applied in the design of diagnostics, controls, and HMI to prevent such interference.

2. Driver Support Systems

ACC systems use forward radar and control the vehicle-to-vehicle distance. Systems that control the vehicle at high speeds (approximately 40 km/h or more) are referred to as AC- below and systems that also use a forward stereo camera and controls the vehicle from high speed cruising to start/stop driving in congestion is referred to as AC+.[1]

PCS systems can be categorized into forward, rear, and front-side types. Forward PCS uses information obtained from a forward radar and camera (stereo or monocular), as well as a camera that monitors the driver. These systems control the seatbelts, engine, brakes, adaptive variable suspension (AVS), buzzer, and variable gear ratio steering (VGRS) depending on the degree of collision risk.[2]-[6] Rear PCS uses information from rear radar to flash the hazard lights to warn the driver of a vehicle approaching from behind if the risk of a rear-end collision is judged to be high. It also automatically moves the head restraints to a position behind the head to mitigate whiplash.[7] Front-side PCS uses front-side radar to perform brake assist, to control the seatbelts, AVS, and buzzer, and to increase the response of the side airbags.

LKA systems consist of lane departure warning (LDW) and lane keeping (LK) functions that utilize information from a forward camera. The former detects the possibility of lane departure and prompts the driver to return to the lane using buzzer alerts and short-term control of the electric power steering (EPS). The latter is activated during ACC operation and uses EPS control to help the driver maintain the vehicle in the center of the lane.[8]

As described above, DSS have evolved through the use of radars and cameras. These systems are controlled by the DSS ECU. **Fig. 1** shows the flow of DSS information and **Fig. 2** shows the main component parts in the systems.

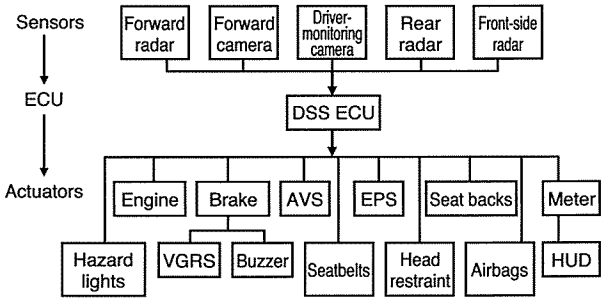


Fig. 1 Information Flow of DSS

* Electronics Development Div. 2

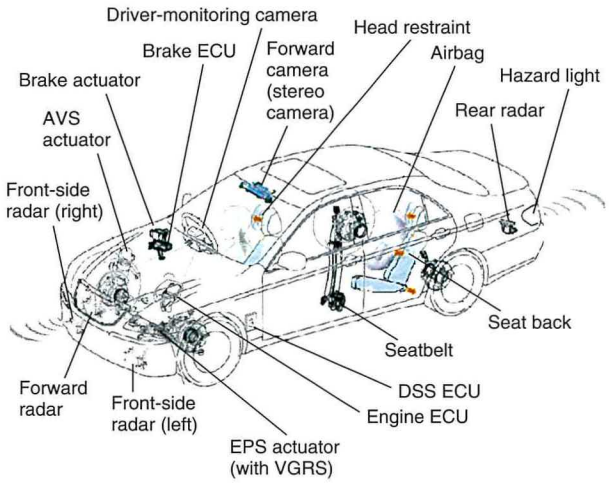


Fig. 2 Configuration of DSS Parts

3. Concept of Coordination Design

3.1 Relationship between DSS

The relationship between DSS is determined based on three types of coordination (diagnostics, control, and HMI) in consideration of the overlapping regions (1) to (4) shown in **Fig. 3**.

In the following discussion, "ACC" refers to cruise control systems, which generally include functions such as a steady speed driving mode. However, this section describes only ACC to simplify the explanation.

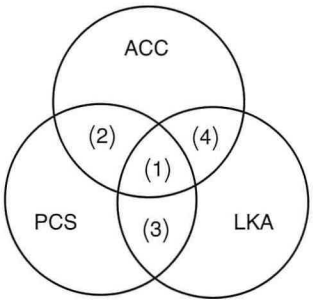


Fig. 3 Relationship between DSS

3.2 Diagnostic coordination

DSS use sensors and actuators in common. If, for example, a shared part suddenly becomes inoperable, each system switches to fail-safe processing and the driver is informed of each control state on the combination meter. In this event, coordination design must consider the differences in diagnostics and control displays between each system.

3.3 Control coordination

In addition to the priority order of control of each DSS, behavior if another control such as vehicle stability control (VSC) is in operation must be determined in advance based on the priority order of overall vehicle behavior. The priority order for brake system control is shown below. In this case, the brake control within PCS, which comprises the pre-crash brake (PB) and pre-crash alert brake (PAB), is adapted.

VSC > PCS > ACC > LKA

3.4 HMI coordination

HMI coordination refers to the combination meter, head up display (HUD), and buzzer. This article describes the display on the combination meter as a typical example of coordination.

The combination meter of a vehicle installed with DSS generally contains a multi-information area. This area shows messages to the driver in accordance with a pre-determined order of priority. The main types of messages are those related to diagnostics and those that provide general information. The former has a higher priority than the latter and are displayed immediately after a system error occurs. If the problem continues, these messages are displayed cyclically in an alternating fashion with other messages. However, PB warnings have a high priority and are included in this type as an exception. General information messages are displayed immediately after the vehicle state changes, but some are not displayed again unless a further change occurs. Displays related to the outside temperature, fuel efficiency, and the control state of DSS are included in this type. It is particularly important to carefully consider the display of control states since messages for multiple DSS may have to be displayed at the same time.

4. Coordination Design

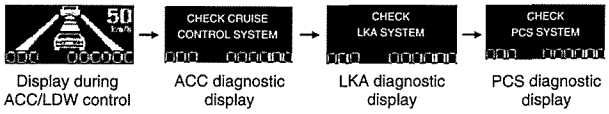
4.1 Diagnostic design

In the event that a part shared between DSS becomes inoperative, behavior differs depending on the system. For example, in the case of a buzzer failure, a diagnostic display is performed for all systems and control is stopped. In contrast, the ACC and PCS systems also stop if the forward radar becomes inoperative, but a diagnostic message for the LKA system is not shown and only LK is automatically cancelled. This is because the radar is only used by the LKA system as an auxiliary sensor and does not have a fundamental effect on LKA control. **Table 1** shows the result when only diagnostic messages are required as in the first case above (A) and when mixed diagnostic and control state messages are required as in the second case (B). **Fig. 4** shows typical meter displays for cases (A) and (B).

Table 1 Diagnostic Coordination Matrix (Excerpt)

	(A)	(B)
(1)	AC+ AC– Yaw rate communication error Buzzer failure Forward camera communication error Forward camera failure	AC+ AC– Forward radar communication error Forward radar failure Forward camera overheat
(4)	AC+/AC– Stop switch failure Brake communication error	AC+/AC– Dirty forward radar Wiper operation

Note: (1) and (4) in the table are equivalent to (1) and (4) in **Fig. 3**.



(A) Transition when only diagnostic message display is required (buzzer failure)



(B) Transition when mixed display of diagnostic and control state messages is required (during wiper operation)

Fig. 4 Diagnostic Coordination Meter Display Transitions

The display priority in case **(A)** is ACC > LKA > PCS. Since PCS does not activate under normal driving conditions, it has the lowest priority. The time used to determine whether these systems are inoperative in the event of an identical failure is set to a common fixed time. Therefore, the DSS ECU mediates the priority order and transmits the diagnostic information in sequence to the combination meter to enable display as shown in **Fig. 4 (A)**. The diagnostic design for **Fig. 4 (B)** factors in the control cancel time and diagnostic judgment time to prevent the display from flashing

4.2 Control design

Fig. 5 shows the flow of control cancel signals based on the priority order of control inside and outside the DSS. This is achieved by a configuration that includes the brake ECU in addition to the DSS ECU. **Table 2** shows the results of control mediation. When VSC is in operation, control of all DSS stops in accordance with the priority order.

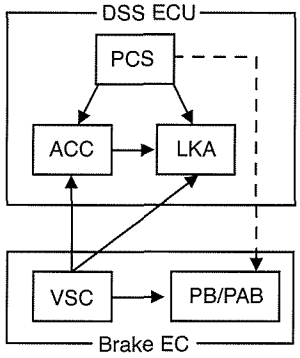


Fig. 5 Flow of Control Cancel Signals

Table 2 Control Coordination Matrix (Excerpt)

No	Coordination item	AC+	AC-	LK	LDW	PB
(1)	Fusion PB	r	r	r	r	–
(4)	Switch A operation	r	r	r	r	o
	Switch B operation	r	r	r	o	o
Other	VSC	r	r	r	r	r

1) (1) and (4) in the table are equivalent to (1) and (4) in **Fig. 3**.
2) Fusion PB: pre-crash braking performed by fusion of radar and camera information
3) r: function removed, o: normal operation, –: not applicable
4) Switch A: Brake switch, wiper high mode switch
5) Switch B: main cruise control switch, cruise control cancel switch

4.3 HMI design

DSS-related displays on the combination meter include states of the control during operation, alerts, and non-control states. **Fig. 6** shows examples of these displays.

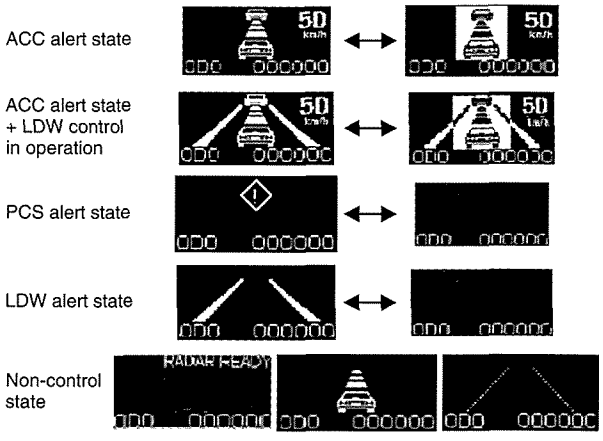


Fig. 6 Control State Displays of DSS

In principle, alerts are displayed by blinking the display at a frequency of 1 Hz. When LDW control is superimposed over an ACC alert, a portion of the white lines is shown in black.

Table 3 shows the control state mediation procedure for these systems. **Table 4** shows specific examples of mediation.

Table 3 Method of Control State Mediation

Procedure	Mediation method	Mediation portion
1	Priority order output (within DSS)	A
2	Simultaneous display (within meter)	B-1
3	Priority order display (within meter)	B-2
4	Blinking synchronization (within meter)	B-3

Table 4 Specific Examples of Control Display Mediation

Mediation portion	Examples
A	ACC/PCS alerts generated simultaneously ⇒ Output of PCS alert set to OFF
B-1	ACC non-control display + LDW control display ⇒ Simultaneous display (no display interference)
B-2	ACC non-control display + PCS alert display ⇒ PCS alert display only
B-3	ACC/LK alerts generated simultaneously ⇒ Blinking mediated

Fig. 7 shows a specific example of the blinking synchronization described in B-3. Synchronization is performed to prevent driver annoyance and is achieved by delaying simultaneous display.

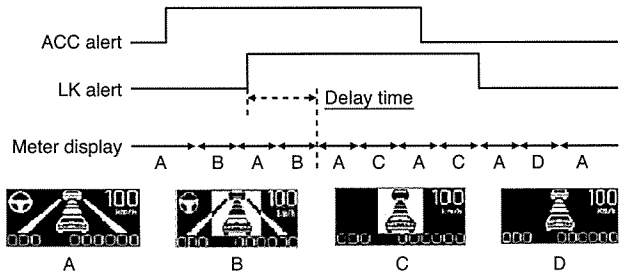


Fig. 7 Synchronization of Display Blinking

Table 5 shows the results of DSS system display mediation based on this procedure. All display combinations are determined by the mediation portion in advance.

Table 5 Meter Display Coordination Matrix (Excerpt)

	System			Mediation portion			
	ACC	PCS	LKA	A	B-1	B-2	B-3
(1)	Non-control	Alert	LDW control		○	○	
(2)	Non-control/control	Alert	–		○	○	
	Alert	Alert	–	○			
(3)	–	Alert	LDW control		○		
	–	Alert	LDW alert		○		○
(4)	Alert	–	LDW control		○		
	Alert	–	LDW alert		○		○

5. Conclusion

This article has described the logical mediation structures for Toyota's DSS. The following points are considered for mediation.

(1) The optimum location for mediation should be determined in advance.
(2) The correct amount of information should be conveyed to the driver without creating a sense of incongruity.

It is predicted that in the future, the driver will be exposed to growing amounts of information, including from systems other than DSS (for example, visual assistance systems). Therefore, an order of priority must be applied to all information to be conveyed to the driver as an overall system. The mediation method described in this article should be considered for adoption in these future systems.

References

(1) M. Morita et al. "Introduction to Radar Cruise Control System with Full-Speed Following Function." *Toyota Technical Review* Vol. 55 No. 1 (2007) pp. 58-63.
(2) K. Fujita et al. "Development of Pre-Crash Safety System." *18th ESV Conference* (2003) Paper No. 544-W.
(3) S. Tokoro et al. "Pre-Crash Sensor for Pre-Crash Safety." *18th ESV Conference* (2003) Paper No. 545-W.
(4) K. Ohue et al. "Development of a New Pre-Crash Safety System." *SAE Paper* No. 2006-01-1461 (2006).
(5) M. Usami et al. "Stereo Vision System for Advanced Vehicle Safety System." *SAE Paper* No. 2007-01-0405 (2007).
(6) M. Shimizu, Usami, Fujinami. "Development of Collision-Avoidance System." *14th World Congress on Intelligent Transport Systems* (2007).
(7) K. Matsubayashi et al. "Development of Rear Pre-Crash Safety System for Rear-End Collisions." *Toyota Technical Review* Vol. 55 No. 1 (2007) pp. 82-87.
(8) S. Kawakami et al. "Introduction to Lane-Keeping Assist." *Toyota Technical Review* Vol. 55 No. 1 (2007) pp. 52-57.

Author



K. KURODA

Development of Fuel Consumption Estimation Technology Using VHDL-AMS

Kimitoshi Tsuji*
Yasunari Kido**
Junichi Ichihara***

Abstract

CO_2 reduction is becoming one of the primary responsibilities for manufacturers. For vehicle manufacturers in particular, there is an urgent requirement to meet the conflicting demands of fuel economy and dynamic performance in product development. To meet this demand, energy analysis of the whole vehicle is becoming indispensable. In the research described in this article, multi-domain simulation using IEEE standardized simulation modeling was applied to a whole vehicle model and validated. The results showed that estimating fuel economy at the planning stage enables quantitative discussions about the conflicting aspects of performance, as well as discussions about transient fuel economy such as during the warming up process. IEEE1076.1 is being promoted by the AK30 working group of the VDA and by an SAE committee. In Japan a similar activity has also been launched by the Institute of Electrical Engineers of Japan (IEEJ). Greater use of this standard is expected to provide better coordination and development efficiency between OEMs and suppliers.

Keywords: *multi-domain simulation, IEEE1076.1, VHDL-AMS, SILS*

1. Introduction

CO_2 reduction is becoming one of the most vital initiatives and responsibilities of corporations, in particular automobile manufacturers, as they strive to curb global warming. Product development that meets the conflicting demands for high levels of performance, comfort, and fuel economy has become an urgent requirement.

As is well known, the production of CO_2 is the result of various types of energy being consumed. In order to reduce the consumption of energy in an automobile, it is necessary to optimize the overall flow of energy and create an efficient system. This can be accomplished through such measures as reducing the amount of electricity that is consumed, reducing the vehicle mass, drag, and running resistance so that it requires less energy to move, and through heat management related to the performance of the air-conditioner and more efficient transmission of drive power from the engine, especially the reduction of engine friction at low temperatures. It is also vital to comprehensively examine the mutual interactions between these different types of energy.

As this suggests, it is necessary to simultaneously analyze multiple technical areas (i.e., a multi-domain) such as electricity, movement, and heat. The most effective method of doing this is thought to be simulation. However, the analysis conducted up until now has been focused on detailed, so called partially optimized simulations for the purpose of developing systems and units. Consequently, a new technology that can broadly analyze the whole vehicle has become necessary.

In response, the IEEE1076.1 (VHDL-AMS) standard treats various physical quantities as if they correspond to the concepts of "through quantity" and "across quantity" used in Kirchhoff's Current Law, as shown in **Fig. 1**, which results from the law of the conservation of energy. As shown in **Table 1**, IEEE1076.1 (VHDL-AMS)[1]-[6] is thought to be the most effective method of analyzing the synergistic effects between the multi-domain of thermal, electrical, and kinetic energy of the whole vehicle. Therefore, research into whole-vehicle modeling has been promoted based on this standard.

This article introduces a comprehensive vehicle simulation technology for thermal, electrical, and kinetic energy that was developed by applying the worldwide standard IEEE modeling technology to a pioneering whole-vehicle simulation model.

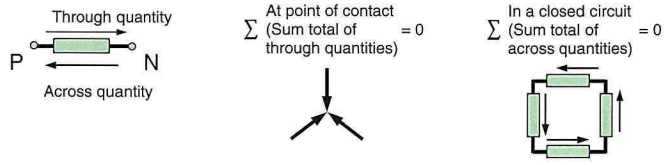


Fig. 1 Outline of Kirchhoff's Law

Table 1 Application of Kirchhoff's Law

	Electrical	Mechanical		Thermal
		Rotating system	Translational system	
Across quantity	Voltage (V)	Rotational speed (rad/sec)	Speed (m/sec)	Temperature (K)
Through quantity	Current (A)	Torque (Nm)	Force (N)	Thermal flow (W)

* Advanced Vehicle Control System Development Div.
** Vehicle Control System Development Div.
*** Daiichi System Engineering Co., Ltd.

2. Vehicle Model

2.1 Vehicle model concepts

1) The vehicle model should have a configuration that allows for common analysis of both traditional vehicles (vehicles that are not HV, EV, or FC vehicles, hereinafter referred to as conventional vehicles) and also hybrid vehicles (HV). The model configuration should also allow for the simultaneous analysis of power performance.
2) It should be possible to generate plans with integrated control due to the configuration of the control software, which allows it to be installed.
3) The model configuration should be able to simultaneously analyze the relationships between thermal, electrical, and kinetic energy that are closely linked to fuel efficiency and power performance.
4) A driver model should be adopted and the model configuration should allow verification of differences in fuel economy that result from differences in how the accelerator is operated.
5) The expression level (detailed model, simplified modeling of the characteristic graph, etc.) of each model should be able to be changed as necessary.
6) The model should be able to make use of electrical component models and other models that are widely used in Europe and other regions[7] in accordance with IEEE standards.
7) The interior of the model should have a black box (nondisclosure) function in order to make it easy to insert and remove the model and also to make it possible for affiliated companies to conduct cooperative work.

2.2 Basic model and database

In order to broadly grasp the whole vehicle, detailed physical models have been avoided as much as possible and simple model formulas and characteristics (characteristic diagrams) are used as the basis. By intervening in these characteristic diagrams, detailed simulations and test results, such as for the engine and drive system, can also be coordinated.

In addition, as a trial run conducted simultaneously in connection with suppliers, models for parts such as the lead battery, alternator, starter, air-conditioning unit, and wiring harness were jointly developed with suppliers. As a result models identified with product-equivalent values were introduced.

2.3 Conventional vehicle model

A conventional vehicle model is shown in **Fig. 2**. Values for the general vehicle specifications, such as drag, vehicle mass, tire radius, and running resistance are shown in the upper left of the same figure. The model has been configured so that parameters can be studied easily by entering values into the specification sheet.

As shown in the same figure, the model has also been configured so that the actual vehicle parts correspond with their images in the model. Along each of the respective connecting lines for the physical quantities that are used in the model, the mechanical rate, quantity of electricity, and quantity of heat are calculated with the same physical quantities as the actual vehicle. Consequently, it has become easier for the engineers to grasp the characteristics of the vehicle.

Furthermore, the model also gives consideration to the temperature characteristics of items in the main components, including areas such as the engine, transmission, and battery. This is because these characteristics are thought to have a large influence on fuel economy performance depending on the temperature. As a result, it became possible to analyze fuel economy characteristics during the warming up process and the performance of parts that receive thermal restriction under high load.

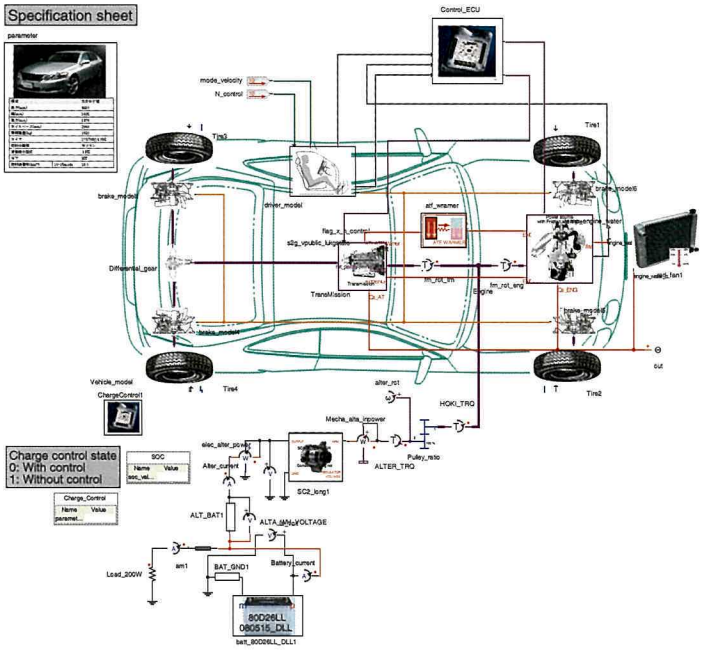


Fig. 2 Conventional Vehicle Model

2.4 HV vehicle model

An HV vehicle model is shown in **Fig. 3**. Fundamentally, this model is configured with the same concepts as a conventional vehicle model. However, the power train on an HV vehicle is different from that on a conventional vehicle. It consists of a unit with an integrated electric motor and a high-voltage battery that drives that motor, a boost converter, and a DC-DC converter that provides electric power to accessories.

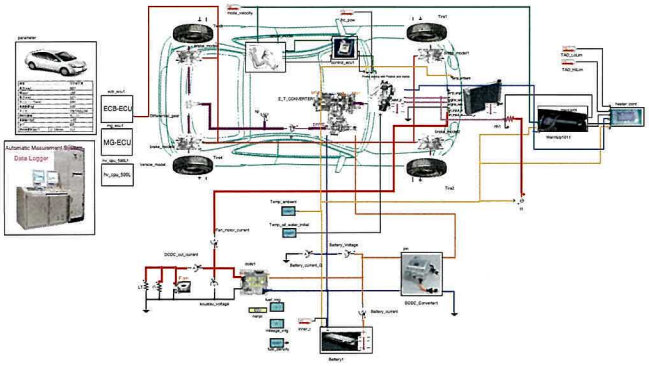


Fig. 3 HV Vehicle Model

2.5 Main unit models

An example of an engine unit model is shown in **Fig. 4** and an example of an AT model is shown in **Fig. 5** as examples of main unit models.

The torque characteristics, friction characteristics, and thermal model are integrated into the engine model. In addition, the engine model uses the relationship provided by the temperature change of the friction to define the relationship between the friction loss at low temperature and the temperature of the coolant in the engine.

The AT model is composed of the torque converter performance curve and temperature characteristics for the torque converter transfer efficiency, thermal capacity, thermal conductivity, oil pump performance curve, ATF warmer thermal conductivity, variable speed gear ratio, gear ratio loss characteristics, gear speed line, lock-up line, flex lock-up line, and so on.

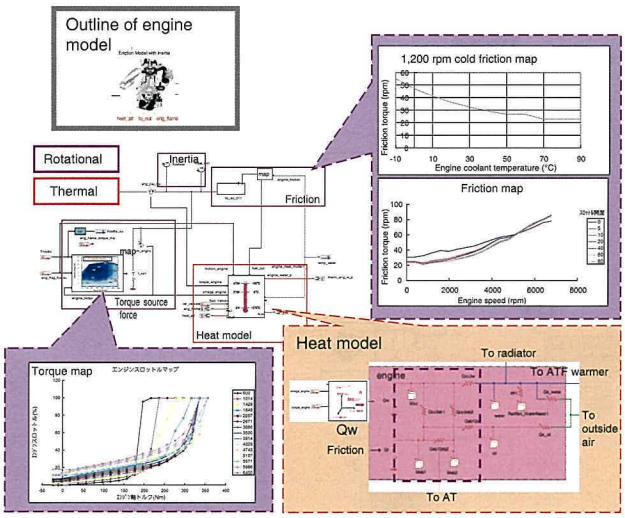


Fig. 4 Outline of Engine Model

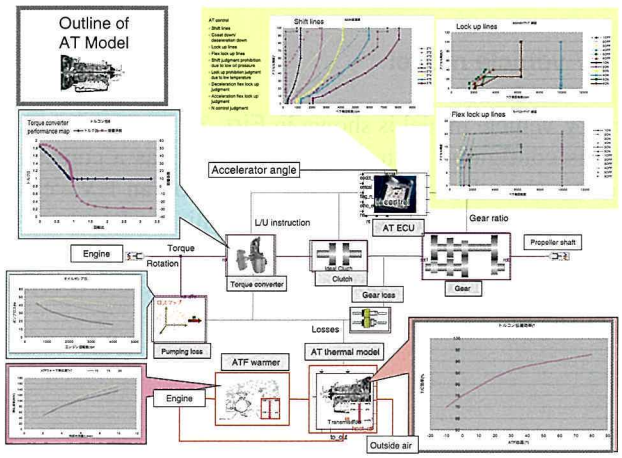


Fig. 5 Outline of AT Model

3. Verification Results from Simulation

The following are provided as verification examples: a conventional vehicle driven through LA#4 (a U.S. certified driving pattern) and an HV vehicle driven through a Japanese test driving pattern that approximates practical driving conditions.

3.1 Fuel economy of conventional vehicle model under cold conditions

A fuel economy evaluation vehicle was used and driven through the LA#4 pattern to conduct a fuel economy verification under cold conditions (25°C at time of engine start). Example results are shown in **Figs. 6a** to **6c**. The results showed an actual vehicle fuel economy of 10.3 km/L and a simulation-estimated fuel economy of 10.19 km/L, for an error of 1.1%.

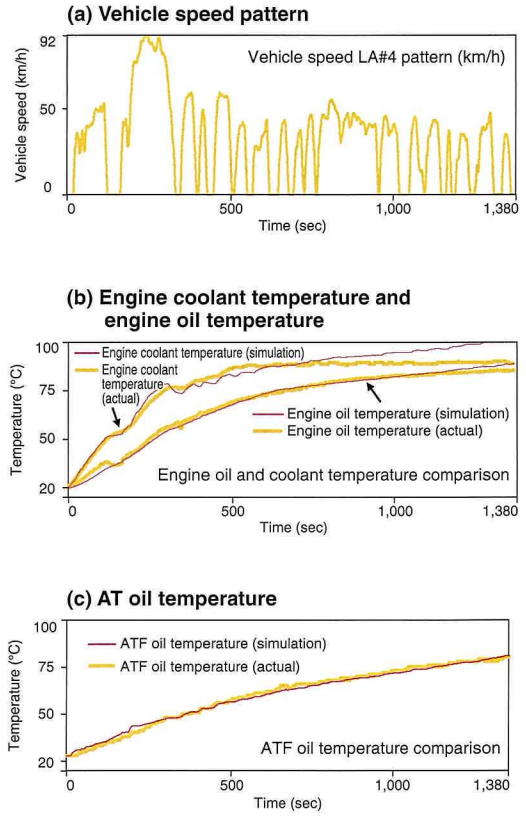
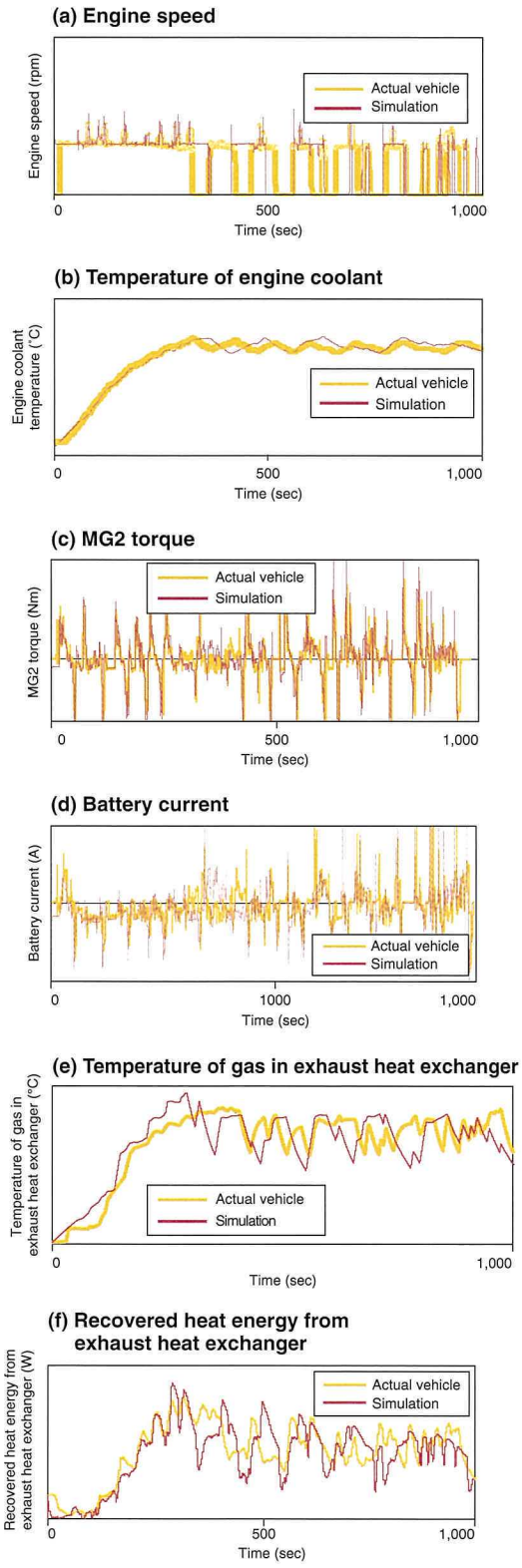


Fig. 6 Verification Results on Conventional Vehicle

3.2 Cold start fuel economy of HV vehicle model

Figs. 7a to **7h** show the main results from driving an HV vehicle (Prius) after a cold start. From these same results it became clear that it was possible to simultaneously analyze the thermal, electrical, and kinetic energies.



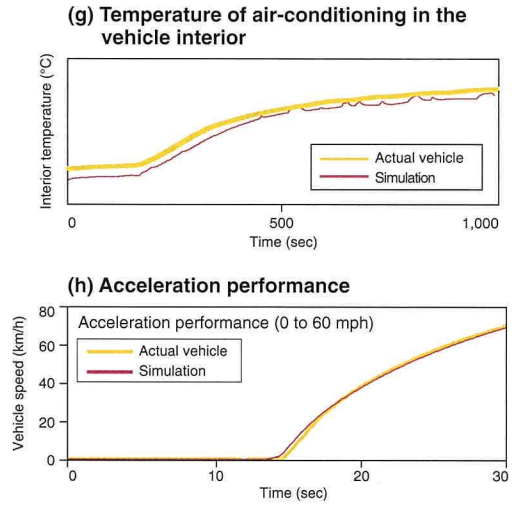


Fig. 7 Verification Results on HV Vehicle

The margin of error for fuel economy in the above test patterns was 3.1%. Similarly, the results from the LA#4 (25°C at engine start) mode were 21.7 km/L for the actual vehicle and 22.0 km/L for the simulation, an error of 1.4%.

4. Summary

The world's first practical vehicle fuel economy simulation technology was developed through the use of VHDL-AMS multi-domain simulation.

The fuel economy results demonstrated that VHDL-AMS is suitable for multi-domain simulation because it was precise and the simulated results were kept to an error of approximately 3% or less compared to the actual vehicle results. It also became clear that many other related results (for example, electrical power to drive the MG, recovered exhaust heat energy, interior temperature, and acceleration performance) corresponded precisely to those found on the actual vehicle. Analytic results for thermal, electrical, and kinetic energy are vital to the development of practical vehicle fuel economy. Furthermore, these results showed that estimating fuel economy at the planning stage enables quantitative discussions about the conflicting aspects of performance, as well as discussions about transient fuel economy, such as during the warming up process.

This IEEE1076.1 standard is being promoted strongly for automobile electrical components in Europe by the AK30 working group (Audi, BMW, Daimler, Ford, Porsche, VW, Conti Temic, Delphi, Hella, Siemens/VDO, Yazaki, and the like) of the German Automobile Manufacturers Association (VDA). It has also been taken up for discussion by the Society of Automotive Engineers (SAE) in the U.S. and by the automobile-related committee (Toyota, Nissan, Honda, Isuzu, Denso, Hitachi, Panasonic Storage Battery, Furukawa Electric, Sumitomo Wiring Systems, and Yazaki Corporation, etc.) within the Institute of Electrical Engineers of Japan (IEEJ). As explained above,

IEEE1076.1 takes into account the law of the conservation of energy, it is easy to understand since the models can express physical phenomena in the same form, it is easy to insert and remove the models, and because it possesses a nondisclosure function that protects the interior of the model, cooperative work between different corporations is also possible. The AK30 working group mentioned above is using these functions and has started to determine model interface specifications for vehicle-mounted parts in order to promote better coordination between OEMs and suppliers.(7)

As explained above, because the models conform to international standards, they can be used with a variety of different software and should make it easy for corporations to coordinate work between themselves. Therefore, it is sincerely hoped that this modeling will continue to spread and become widely used in the future.

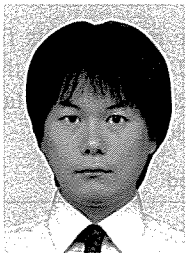
The authors would also like to take this opportunity to express their sincere thanks to all those people at affiliated companies (Denso, Panasonic Storage Battery, Yazaki Corporation, and the like) who kindly cooperated with us in the joint development and trials, as well as to all those who generously participated in the data collection and joint evaluations.

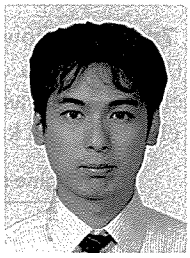
References

(1) *1076 IEEE Standard VHDL Language Reference Manual*. IEEE Std 1076-2002, ISBN: 0-7381-3247-0 (2002).
(2) *IEEE Standard VHDL Analog and Mixed-Signal Extensions*. IEEE Std 1076.1-2007, ISBN: 0-7381-5627-2 (2007).
(3) "Management Technology of Automotive Electric Power Supply Systems." *IEEJ Technical Report* No. 1121 (2008) pp. 28-32.
(4) T. Kato. "Modeling Power Electronic Systems with VHDL-AMS and their Simulations." *2004 IEEJ Industrial Application Division Conference* Vol. 1 No. S11-3 (2004) pp. 75-80.
(5) K. Tsuji, Kataoka, Kusaka, Teratani, Abe. "EPS System Analysis Using Multi Domain Simulation for Power Network Design in a Vehicle." *The Fourth Power Conversion Conference Nagoya* LS5-4-2 (2007) pp. 1340-1345.
(6) "IEEJ Journal Special Issue: Research Frontiers in Analysis and Design of Motor Driving Systems." *Institute of Electrical Engineers of Japan* Vol. 129 No. 6 (2009) pp. 344-359.
(7) *Materials Related to FAT-AK30*. The German Association of the Automotive Industry (VDA). http://fat-ak30.eas.iis.fraunhofer.de/index_en.html

Authors


K. TSUJI


Y. KIDO


J. ICHIHARA

Development of Hydraulic Pressure Servo Control Method for New Electronically Controlled Brake System

–Adoption of Variable Differential Pressure Regulating Valve Control Method to Rapidly Varying Controlled Object–

Hiroshi Nakaoka*
Tsukasa Fukasawa**
Yoshito Tanaka*
Mitsuo Fukuda***

Abstract

The regeneration of energy during deceleration is an important way of improving the fuel efficiency of hybrid vehicles. To accomplish this, an electronically controlled brake (ECB) system is used to maximize the amount of power generated by the motor, thereby enabling a high deceleration energy recovery rate. A mechanical automatic pressure adjustment function (called the variable differential pressure regulating valve control method) that acts effectively with respect to rapid variations in the controlled object has been developed for the hydraulic pressure control of the ECB. Adopting this control method has allowed the development of a compact, low weight, and highly versatile new ECB system with the optimum configuration for realizing the required functions. This article describes this new control technology.

Keywords: *hydraulic pressure servo, hydraulic pressure control, differential pressure regulating valve, linear valve, ABS, ECB, regenerative-friction brake coordination, brake assist*

1. Introduction

1.1 Details of ECB development

In recent years, technologies such as ABS, VSC, and regenerative-friction brake coordination on hybrid vehicles have advanced electronic hydraulic pressure control and increased the functionality of brakes. In 2001, Toyota adopted the world's first electronically controlled brake system (hereinafter referred to as ECB) in the Estima Hybrid and since then has steadily increased the number of vehicle models equipped with ECB each year. However, in order to further popularize hybrid vehicles, it has become necessary to develop a more versatile ECB.

1.2 Basic configuration of ECB

The ECB system electronically controls the hydraulic pressure in the brakes (**Fig. 1**).

The amount that the brake pedal is depressed by the driver is sent to the ECU via an electric signal. Based on this value, the ECU then controls the current of the high hydraulic pressure source (power supply), which comprises components such as the accumulator, and of the linear valves (the pressure boosting linear valve (SLA) and pressure reducing linear valve (SLR)) that are positioned downstream from the power supply. The purpose of this control is to adjust the hydraulic pressure of the wheel cylinders. The right side of **Fig. 1** shows the basic hydraulic pressure circuit of the ECB.

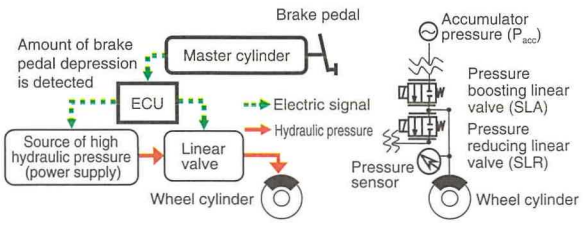


Fig. 1 Basic Configuration and Basic Hydraulic Pressure Circuit of ECB

1.3 Hydraulic pressure servo

The hydraulic pressure servo is the function in the ECB that manages the hydraulic pressure control. **Fig. 2** shows the control block diagram and control model. The hydraulic pressure servo software possesses a function that outputs the current (I) of the linear valve so that the controlled pressure (P_{fr}) tracks the target pressure. The target pressure is created based on the brake pedal input. The current is determined at that time by adding together each of the following relationships as models: the relationship between the current of the linear valve and the flow rate (Q) (the I-Q characteristic), the integral relationship

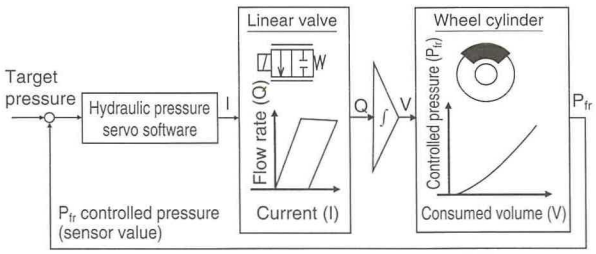


Fig. 2 Hydraulic Pressure Servo Block Diagram and Control Model

* Production Engineering Development Div.
** Chassis Development Div.
*** Toyota Motor Engineering & Manufacturing North America, Inc.

between the flow rate and the consumed volume (V) (the Q-V characteristic), and the relationship between the consumed volume going to the wheel cylinder and the hydraulic pressure (P_{fr}) (the V-P characteristic).[2] The result of the adjusted controlled pressure is expressed as vehicle behavior. Therefore, the hydraulic pressure servo has an extremely important function that is related to controlling the dynamic characteristics of the vehicle.

2. New ECB

2.1 Configuration of new ECB and its control functions

The new ECB is shown in **Fig. 3**. In the new ECB, a pair of linear valves (SLA and SLR) and a single pressure sensor are used to carry out functions such as regenerative-friction brake coordination and brake assist. In addition, ON-OFF valves are positioned at each wheel (ABS holding valve and ABS pressure reducing valve, hereinafter referred to as the "ABS valves") to carry out functions such as VSC, ABS, and traction control. This new configuration has reduced the size and weight of the new ECB.

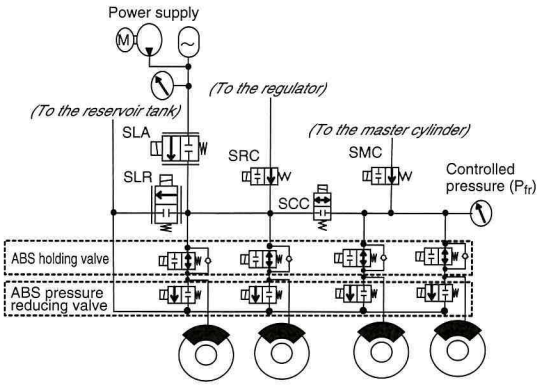


Fig. 3 Simplified Diagram of New ECB Hydraulic Pressure Circuit

In the configuration shown in **Fig. 3**, when all four wheels are controlled with the same pressure, such as during regenerative-friction brake coordination, then the ABS valves do not operate and the controlled pressure is adjusted by the linear valves based on the value from the pressure sensor (P_{fr}) as shown in **Fig. 4**.

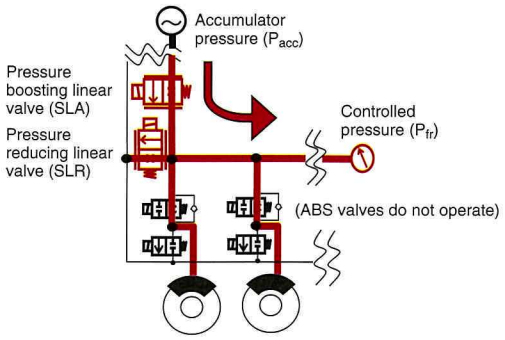


Fig. 4 Control during Regenerative-Friction Brake Coordination

Furthermore, during normal activation of the ABS, the linear valves do not operate and the ABS is activated by the introduction of regulator pressure (introduction of pressure from the SRC valve shown in **Fig. 3**) and the individual operation of the ABS valves. This process can be handled by current control technology.

However, when the ABS operates during brake assist, or the VSC or traction control functions are activated, linear valve control is performed based on the pressure sensor. Simultaneously and independently, ABS valve control at each wheel is performed based on the wheel speed sensors. This is shown in **Fig. 5**.

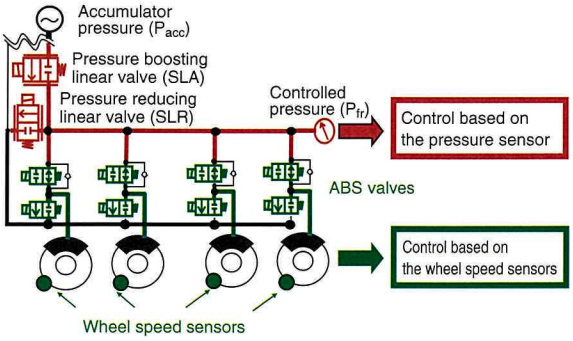


Fig. 5 Control when ABS is Activated during Brake Assist

At that time, the wheel cylinder pressure of each wheel is independently increased or decreased by the operation of each ABS valve. This is shown in the lower graph of **Fig. 6**. Consequently, the controlled pressure that is located upstream from the ABS valves is influenced by this fluctuation as shown by the upper graph in **Fig. 6**.

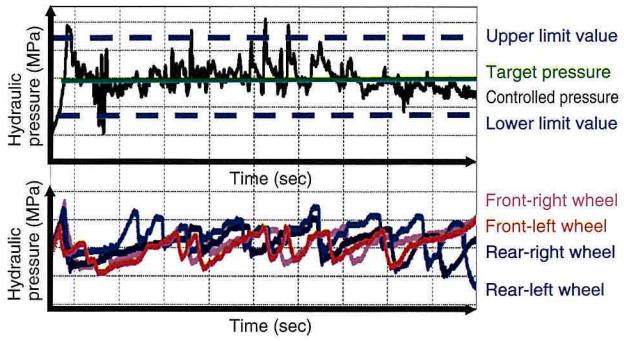


Fig. 6 Controlled Pressure (Upper Graph) and Fluctuation of Hydraulic Pressure at Each Wheel (Lower Graph) during ABS Activation

The controlled pressure must track the target pressure within a fixed range between the upper limit and lower limit, particularly when the ABS is activated during brake assist. This is important from the standpoint of maintaining the pressure-increase performance at each wheel and reflecting the brake pedal operation of the driver. In order to satisfy this demand a new hydraulic pressure control technology was necessary.

3. Variable Differential Pressure Regulating Valve Control Method

3.1 Difficulty of control

There are two issues related to the hydraulic pressure servo when ABS is activated during brake assist.

3.1.1 Inadequate electrical feedback tracking capability

The hydraulic pressure fluctuation band f_{ABS} (Hz) when ABS is activated (see **Fig. 6**) with respect to the electrical feedback cutoff frequency f_{SOFT} (Hz), which is generated by the hydraulic pressure servo software shown in **Fig. 2**,[1] is $f_{SOFT} << f_{ABS}$. This shows that the electrical feedback tracking capability is inadequate when ABS is activated.

3.1.2 Difficulty of determining linear valve current

When the ABS valves are not operating, such as during regenerative-friction brake coordination, the wheel cylinder characteristics are such that the controlled pressure (P_{fr}) corresponds to a certain value with respect to the total supplied consumed volume (V). This can be expressed as shown in Equation 1.

$$P_{fr} = \phi(V) \tag{1}$$

However, when ABS is activated, due to the sudden increase and decrease of pressure in each of the wheel cylinders, factors such as the time component (t) and state of each wheel cylinder (X) contribute to the controlled pressure, which fluctuates as the complicated system shown in Equation 2.

$$P_{fr} = \phi(V, t, X) \tag{2}$$

The difference in these pressure characteristics is shown in **Fig. 7**.

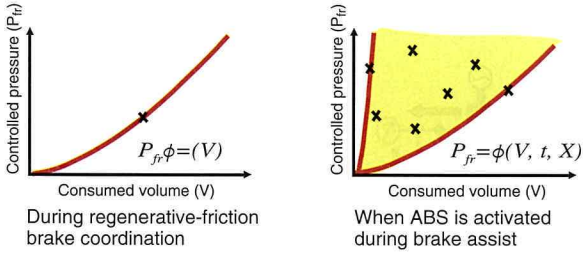


Fig. 7 Difference in Pressure Characteristics with Respect to Consumed Volume

Previously, the current of the linear valves was calculated using Equation 1. However, when the ABS is activated the wheel cylinder characteristics fluctuate as shown in Equation 2. Therefore a method of determining the current for the linear valves that takes this fluctuation into consideration is important for the hydraulic pressure servo.

3.2 Differential pressure regulating valve characteristics of linear valves

Consequently, development focused on the linear valve function as a differential pressure regulating valve. The left side of **Fig. 8** shows the forces in balance, where the differential pressure is ΔP, the spring constant is k, and the current applied to the valve is I_0. If the force from differential pressure is $F_{\Delta P}$, the electromagnetic attractive force is F_{I_o}, and the spring restoring force is kx, then Equation 3 is realized when the forces are in balance.

$$F_{I_o} + F_{\Delta p} = kx \tag{3}$$

When the differential pressure changes from the balanced state of ΔP to $\Delta P'$ ($<\Delta P$) due to the operation of the ABS, then the valves open mechanically and fluid flows in, as shown on the right side of **Fig. 8**. The equation changes to that shown in Equation 4.

$$F_{I_o} + F_{\Delta p'} > kx \tag{4}$$

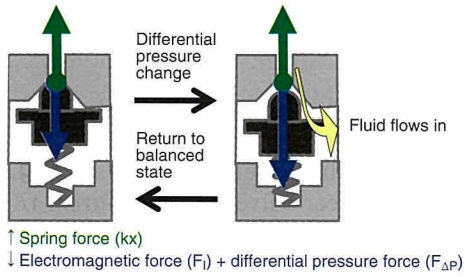


Fig. 8 Movement of Linear Valves when Balanced (Left) and during Change in Differential Pressure (Right)

Subsequently, the entry of fluid causes the differential pressure to change to a direction that will cancel out the change in differential pressure, and the valves will close, as shown in the balanced state on the left side of **Fig. 8**. Therefore, the development focused on the differential pressure regulating value characteristics and pressure regulating function of the linear valves.

3.3 Reasons for focus

There were two reasons for focusing on the linear valve function as a differential pressure regulating valve: mechanical response characteristics and the characteristic that the open valve differential pressure of each linear valve is determined as a unique value by the current.

3.3.1 Mechanical response characteristic of linear valves

The mechanical response characteristic of the linear valves when functioning as differential pressure regulating valves was examined as follows. The frequency response of the system model (mass–spring–attenuation) was investigated with the mass of the linear valve shaft defined as M and the attenuation coefficient defined as c.

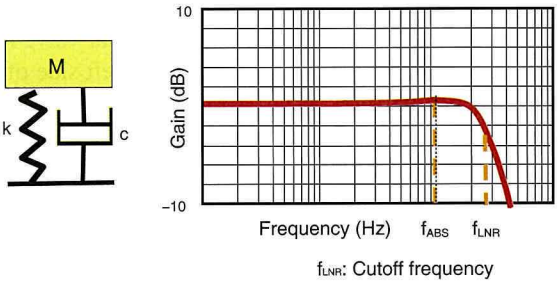


Fig. 9 Linear Valve System Model (Mass–Attenuation–Spring) and Gain Diagram

According to the gain diagram in **Fig. 9**, $f_{ABS} < f_{LNR}$, so the mechanical response characteristic of the linear valves has a response band with respect to the fluctuation in pressure that occurs when ABS is activated.

3.3.2 Open valve differential pressure characteristic due to current

The pressure boosting linear valve has a function g that uniquely determines the open valve differential pressure (P_{SLA}) from the pressure in the accumulator (P_{acc} in **Fig. 5**) located upstream from the linear valve, and the current (I_{SLR}). In the same way, the pressure reducing linear valve has a function h that determines the open valve differential pressure (P_{SLA}) from the current (I_{SLR}).

$$P_{SLA} = g(P_{acc}, I_{SLA}) \tag{5}$$

$$P_{SLR} = h(I_{SLR}) \tag{6}$$

Using Equations 5 and 6, it is possible to adjust the controlled pressure (P_{fr}) by controlling each of the open valve differential pressures that are generated due to the current flowing to each linear valve. This is expressed in Equation 7 using the function L.

$$P_{fr} = L(g(P_{acc}, I_{SLA}), h(I_{SLR})) \tag{7}$$

Equation 7 is not dependent on the change in wheel cylinder characteristics due to ABS that is expressed in Equation 2. It shows that it is possible to adjust the controlled pressure by determining the current of the linear valves.

3.4 Control flow

Fig. 10 shows a block diagram of a hydraulic pressure servo control system that incorporates the characteristic changes in the control object due to ABS activation and the mechanical pressure adjustment function (variable differential pressure regulating valve control method).

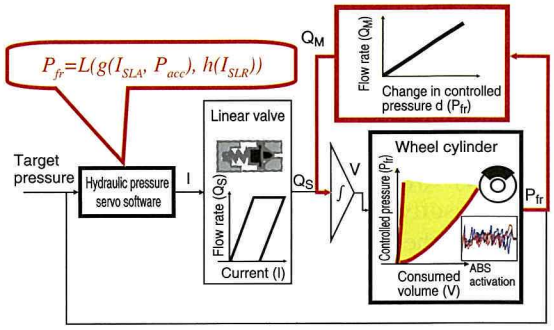


Fig. 10 Outline Diagram of Flow of Variable Differential Pressure Regulating Valve Control Method

Without adding any new mechanical components, the variable differential pressure regulating valve control method that uses Equation 7 realizes a control system in which a mechanical pressure adjustment function operates in response to sudden changes in the controlled pressure due to the operation of the ABS valves, without requiring input from the hydraulic pressure servo software.

3.5 Pressure adjustment mechanism

The pressure adjustment function of the variable differential pressure regulating valve control method is shown in **Fig. 11** with the pressure boosting side divided into steps (1) to (5).

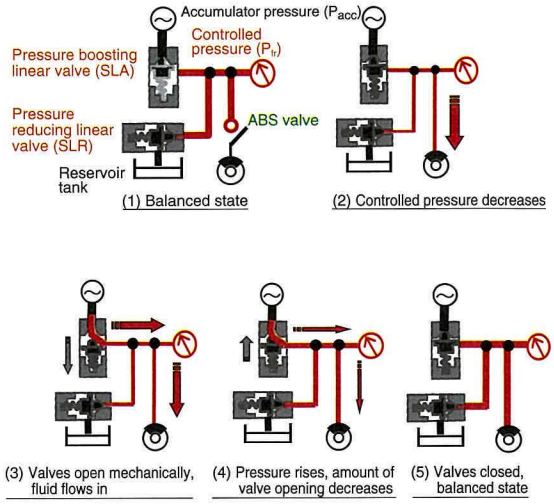


Fig. 11 Pressure Adjustment Mechanism of Variable Differential Pressure Regulating Valve Control Method (Pressure Boost)

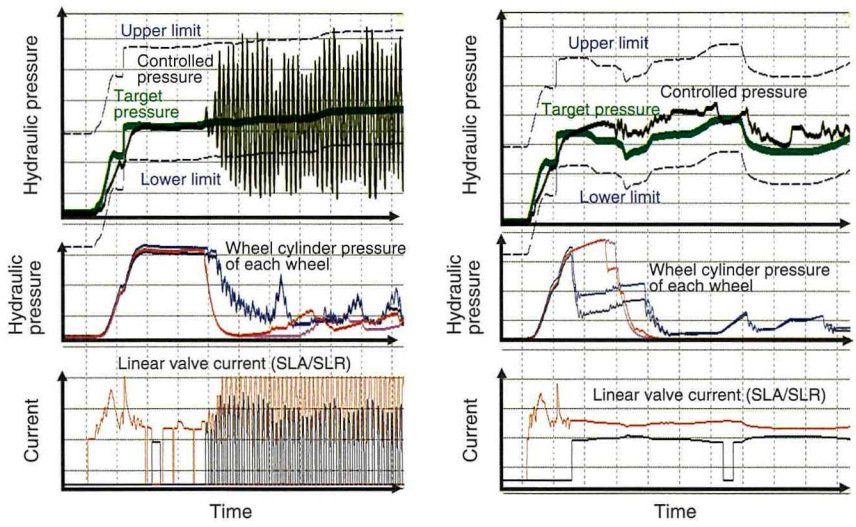


Fig. 12 Vehicle Data when ABS Activated during Brake Assist
(Left: Normal Control, Right: Variable Differential Pressure Regulating Valve Control Method)

4. Vehicle Evaluation

The left side of **Fig. 12** shows vehicle data for the new ECB in a case where the same control is executed as during regenerative-friction brake coordination (normal control) when the ABS is activated during brake assist. The right side of the figure shows vehicle data for a case where the variable differential pressure regulating valve control method is executed as explained in this article. Furthermore, for each set of data, the lower graph shows the current of the linear valves, the middle graph shows the wheel cylinder pressure of each wheel, and the upper graph shows the controlled pressure, target pressure, and upper and lower limit pressures.

The changes in the controlled pressure in the upper graph show that compared to normal control, the variable differential pressure regulating valve control method suppresses vibrations and improves the target pressure tracking performance of the controlled pressure. In addition, the controlled pressure is adjusted within the upper and lower limits, and both pressure boost performance and driver pedal operation reflection requirements are satisfied.

5. Conclusion

Through the application of the control method described in this article, the required functions were realized and a compact, low weight, and highly versatile new ECB system has been developed. A special characteristic of this control method is the combination of a mechanical pressure adjustment function for electrical feedback control with useful control technology that handles systems in which the control object fluctuates in a very short amount of time.

References

(1) Y. Tanaka et al. "Development of Hydraulic Pressure Servo for ECB" (in Japanese). *Proceedings of the Toyota Engineering Society* 1-1 (2001) pp. 1-4.
(2) M. Okubo et al. "Development of Hydraulic Pressure Servo for ECB2" (in Japanese). *Proceedings of the Toyota Engineering Society* 1-7 pp. 25-28.

Authors


H. NAKAOKA


T. FUKASAWA


Y. TANAKA


M. FUKUDA

Analysis of Sophisticated DPNR Catalyst –Focus on PM Particle Number Emissions–

Masamichi Kuwajima*
Seiji Okawara*
Shigehiro Matsuno**
Masaaki Yamaguchi**
Masato Tsuzuki***

Abstract
The diesel particulate and NOx reduction system (DPNR) is an effective diesel engine after-treatment technology capable of simultaneously reducing PM and NOx. However, whereas conventional development for treating PM has concentrated on reducing exhaust weight, in the future it will be necessary to focus on PM particle number emissions. This study clarified the relationship between the pore structure of the DPNR catalyst and PM particle trapping by evaluating a cordierite diesel particulate filter (DPF) with high porosity and an average pore size of 20 μm or more. As a result, a pore structure capable of efficiently trapping PM particles was identified, which can be controlled using the coating amount. It may be possible that this sophisticated DPNR catalyst can play a role in meeting future regulation values for PM particle number emissions.

Keywords: *DPNR catalyst, DPF, emissions, PM particle number, pore structure*

1. Background

Diesel engines with good fuel economy are an effective means of reducing CO_2 emissions and are recognized as an important technology for helping to control global warming. On the other hand, emissions regulations for vehicles are becoming more stringent year after year and regions all around the world are demanding further decreases in particulate matter (PM) and nitrogen oxides (NOx). In reaction to these trends, Toyota Motor Corporation developed the diesel particulate and NOx reduction system (DPNR) that is capable of reducing PM and NOx simultaneously through a combination of a NOx storage reduction (NSR) catalyst and engine control technology (**Fig. 1**).[1]

Fig. 2 shows an outline of emissions treatment by the DPNR catalyst. It consists of a NSR catalyst coated onto a diesel particulate filter (DPF). The DPF uses a cordierite substrate that is closed off at alternating ends in order to trap emitted PM in pores provided on the internal walls of the DPF. Since the cordierite DPF used here is coated with the NSR catalyst, the average diameter of the pores on the walls has to be increased to at least 20 μm, which is larger than a conventional SiC DPF.[1] The action of the NSR catalyst coated on the DPF wall surfaces and the surfaces of the pores on the walls oxidizes PM. Additionally, fuel is added to create a rich atmosphere, which enables NOx stored in the NSR catalyst to be reduced to N_2.

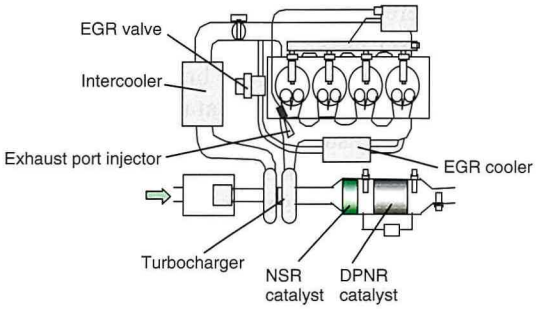


Fig. 1 Diagram of DPNR System

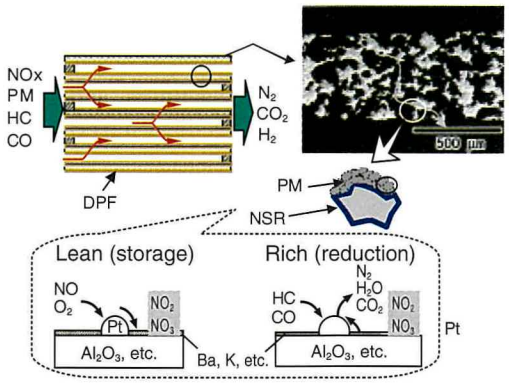


Fig. 2 Outline of DPNR Catalyst

The DPNR catalyst has been optimized over time to reduce the amount of emissions, but with the emissions regulations in Europe becoming more stringent, it is now important to also focus on the number of exhaust particles. As shown in **Fig. 3**,

* Power Train Material Engineering Div.
** Engine Engineering Div.1
*** Engine Management System Development Div.

PM with a diameter in the order of several nanometers is capable of passing through the DPNR catalyst. Therefore, lowering the PM particle number emissions using the DPNR catalyst with a pore diameter in the order of several micrometers is a difficult technical issue.

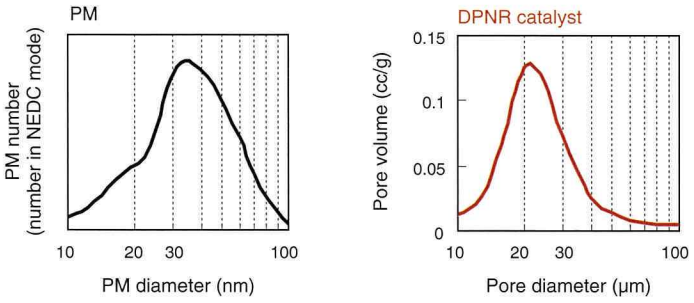


Fig. 3 PM Particle Size and DPNR Catalyst Pore Size Distributions

In this study, the relationship between the catalyst pore structure and the trapping of PM was identified using a DPNR catalyst comprised of a cordierite DPF with a conventional porosity of 65% and an average pore diameter of 20 μm or greater. This article discusses the effect on lowering PM particle number emissions.

2. Experiment

2.1 Test samples

Various cordierite substrates capable of being manufactured by existing processes (average pore diameter: 20, 25, 30 μm, 2-liter) were adopted for the DPF. A NSR catalyst was used as the coating material (coating amounts: ±10 and 33% of reference value A).

2.2 Experimental method

2.2.1 Measurement of PM particle number emissions in NEDC mode

The PM particle number emissions in the new European driving cycle (NEDC) mode of a passenger vehicle equipped with a 2.2-liter diesel engine were measured by UN-authorized instrumentation (PMP proposal method) after treatment under the prescribed preconditions.(2)

2.2.2 Analysis of catalyst structure

The pore distribution of the DPNR catalyst was measured by a mercury porosimeter and consists of an average of six points from the DPNR catalyst. The two- and three- dimensional structures of the pores on the walls were measured by a scanning electron microscope (SEM) and X-ray CT, respectively.

3. Experimental Results and Remarks

3.1 Analysis of catalyst pore structure

Fig. 4 shows the measurement results for PM particle number emissions in the NEDC mode using DPNR catalysts with DPFs with an average pore diameter of 20, 25, and 30 μm, and NSR catalyst coating amounts of reference value A±10% (g/L). The diagram indicates that the PM particle number emissions decreased when a smaller DPF average pore size and less coating was used. This result is the opposite of previous results where the PM particle number emissions were lowered by making the pores smaller and increasing the coating amount. These results confirm that catalyst pores affect 1/1,000-mm order PM particles, and it was presumed that an optimal catalyst pore structure should be able to lower the PM particle number emissions.

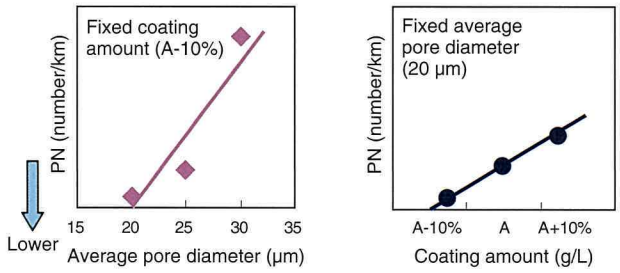


Fig. 4 Influence of DPNR Catalyst on PM Particle Number (PN)

Therefore, to investigate the effective pore diameter for lowering the PM particle number emissions, a mercury porosimeter was used to measure the pore distribution of DPNR catalysts with the specifications described above (**Fig. 5**) and the pore volume of each section (<10 μm, 10 to 20 μm, and the like) was calculated. **Table 1** summarizes the relationship between the pore volume of each section and PM particle number emissions for each sample. As a result, it was found that the correlation coefficients (R2) of 10 to 20 μm and >30 μm pores for PM particle number emissions were much higher than other pores.

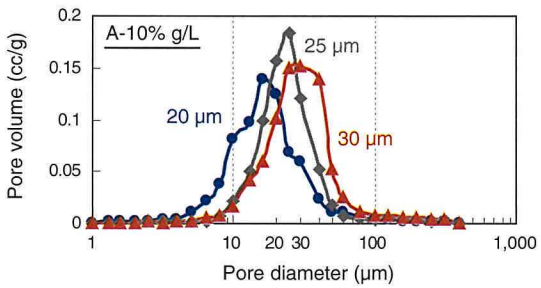


Fig. 5 Influence of DPNR Catalyst on Pore Distribution

Table 1 Influence of Pore Volume (DPNR Catalyst)

Sample	PN (number/km)	Pore volume (cc/g)					
		<10 μm	10-20	20-30	30-40	40-50	50<
1	***	0.15	0.29	0.18	0.05	0.02	0.05
2	***	0.09	0.18	0.28	0.08	0.03	0.07
3	***	0.08	0.11	0.26	0.21	0.14	0.11
R^2		0.26	0.61	0.01	0.77	0.84	0.73
					0.80		

Fig. 6 shows the relationship between pore volumes of 10 to 20 μm and >30 μm, which were found to have an effect in **Table 1**, and PM particle number emissions. No effect was found with pores below 10 μm and between 20 and 30 μm (see **Table 1**), but the PM particle number emissions became lower as the pore volume with a diameter of 30 μm or greater became smaller (**Fig. 6a**). The PM particle number emissions also lowered as the volume of pores with a diameter between 10 and 20 μm became larger (**Fig. 6b**).

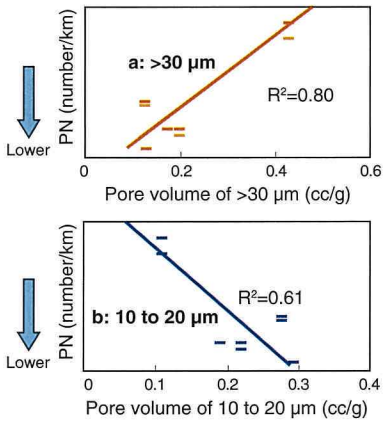


Fig. 6 Influence of Pore Size on Lowering PN (a: Pore Diameter >30 μm, b: 10 to 20 μm)

The next step was to identify the reason why nano-order PM particles were influenced by a DPNR catalyst with a micro-order pore structure. It is already known that, in general terms, particles with a diameter of less than 100 nm are diffused by Brownian motion.[3] Therefore, the PM trap mechanism was analyzed focusing on the relationship between the moving distance of the particles due to Brownian motion and the pore diameter of the DPNR catalyst. Equation 1 shows Einstein's relational expression for the Brownian motion of particles,[3] in which the parameters are temperature, moving time (velocity), and particle diameter. The moving distance of the PM particles in NEDC mode was calculated by the following procedure. Firstly, the temperature of the engine exhaust gases (T_E) and the amount of air intake (Ga, g/sec) were extracted from the engine data in representative steady state conditions in NEDC mode. T_E was used as T in Equation 1. Next, Ga was used to calculate the time to pass through the wall of the DPF as t in Equation 1. Finally, a particle diameter of 30 nm was assumed as a in Equation 1. **Fig. 7** shows the relationship between vehicle speed in NEDC mode and the moving distance of PM particles. These calculated results show that nano-order particles have a moving distance of 1 to 20 μm due to Brownian motion.

Equation 1 shows Einstein's relational expression for particle Brownian motion.

$$\langle \hat{x}(t) \rangle^2 = 2Dt \ , \ D = \frac{RT}{N_A} \frac{1}{6\pi\eta a} \qquad (1)$$

where,

$\langle \hat{x}(t) \rangle^2$: expectation value for moving distance
D: coefficient of diffusion, t: moving time
R: gas constant, T: absolute temperature
N_A: Avogadro's number,
η: coefficient of viscosity, a: particle radius

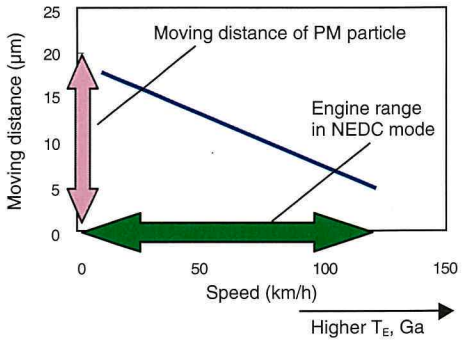


Fig. 7 Relationship Between Vehicle Speed and Moving Distance of PM Due to Brownian Motion in NEDC Mode

Fig. 6 shows that the larger the volume of 10 to 20 μm pores, the lower the PM particle number emissions became. This was probably due to an increase in the trap efficiency when PM particles diffused by Brownian motion collided with the pore walls of the DPNR catalyst. However, PM particles did not collide with the walls of larger diameter pores (>30 μm) because the size of these pores exceeded the moving distance of Brownian motion. This increased the amount of PM passing through the filter, thereby worsening the trap efficiency (**Fig. 8**). Based on the PM moving distance, PM trap efficiency should improve as the pore diameter decreases, but the experimental results in **Table 1** indicate that the correlation coefficients of pores less than 10 μm was low. This is due to pores becoming too small and the gas flow being maldistributed to larger pores or being inhibited altogether, thereby worsening the exhaust gas flow performance.

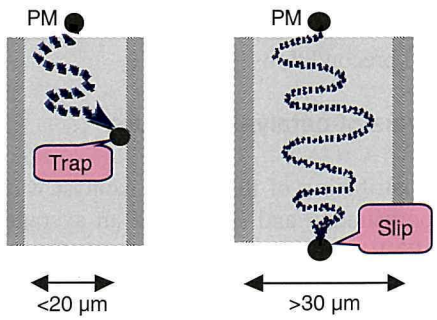


Fig. 8 PM Trap Mechanism by Brownian Motion

3.2 Effect of coating amount

The effect of the coating amount on the catalyst pore structure was examined. DPNR catalysts were prepared using a DPF with an average pore diameter of 25 μm, and coating amounts of ±10% and ±33% of reference value A (g/L). These DPNR catalysts were also used to measure the PM particle number emissions in NEDC mode. **Fig. 9** shows the relationship between the coating amount and the PM particle number emissions. At A+33% to A-10%, the PM particle number emissions became lower in accordance with the decrease in coating amount. In addition, the pore distribution was then measured. As shown in **Fig. 10**, this was due to the increase in the volume of high trap efficiency pores with a diameter of 10 to 20 μm as the coating amount decreased. However, up to A-33%, the PM particle number emissions increased as the coating amount decreased. Focusing on the pore diameter of 40 to 50 μm shown in **Fig. 10**, the A-33% sample had a larger pore volume than the A-10% sample. Therefore, if the coating amount is too little, it is thought that capillary action causes the coating material to first selectively cover the pores with a diameter of less than 10 μm, thus inhibiting the coating of larger diameter pores and making it easier for PM particles to pass through.

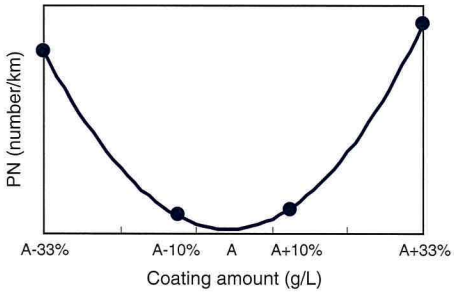


Fig. 9 Influence of Coating amount on PN

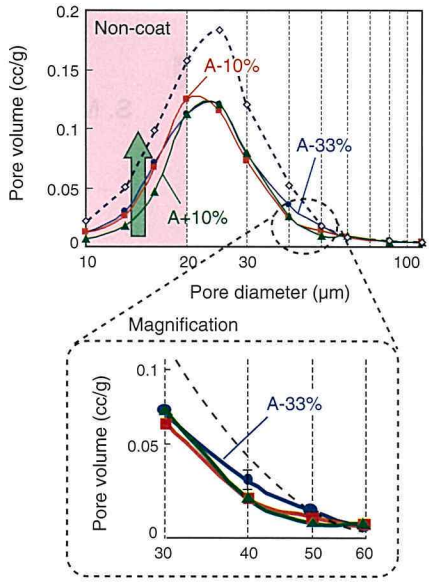


Fig. 10 Pore Distribution with Different Coating amounts

To confirm this presumption, pore wall sections from the A-10% and A-33% samples were observed by SEM (**Fig. 11**). The SEM images show that the coating amount on the A-33% sample was too low to cover the larger pores. The existence of the portions where PM particles can pass through could be confirmed by two-dimensional observations. Therefore, it was concluded that the presumption was correct.

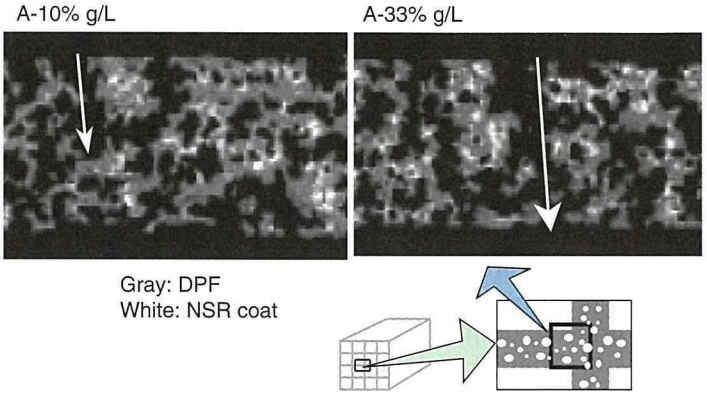


Fig. 11 SEM Images of DPNR Catalyst (Cross Section)

The catalyst pore structure was analyzed in three dimensions by X-ray CT to investigate the influence of the coating amount on the proportion of continual pores that the PM particle can pass through. **Fig. 12** shows 3D images of different coating amounts (the gray portions indicate the continual pores). After calculating the proportion of continual pores by image processing, it was confirmed that the A-33% sample had 16% more continual pores than the A-10% sample.

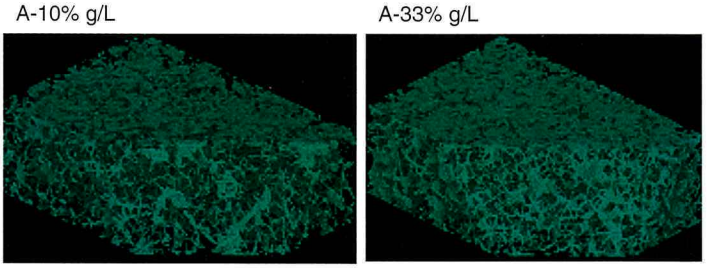


Fig. 12 3D Images of DPNR Catalysts

Fig. 13 shows a summary of these study results. Although the absolute value for the coating amount on both the A-33% and A+33% samples was different, it was verified that the pore volume of 30 μm or greater was larger than the pore volume of 10 to 20 μm. As a result, the gas flow was maldistributed to larger pores with low PM trap efficiency and the PM particle number emissions increased. Therefore, this clarifies how it is possible to lower the PM particle number emissions by optimally controlling the coating amount.

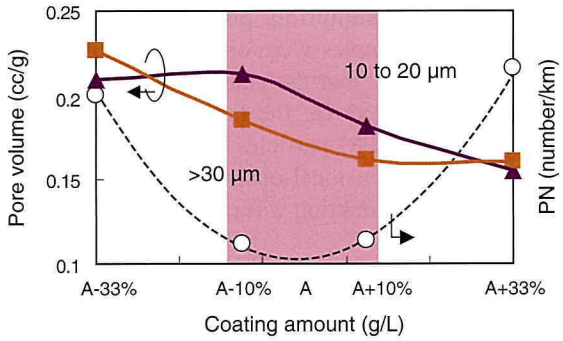


Fig. 13 Influence of Coating amount on PN and Pore Structure

To show the influence of the coating amount and the average pore diameter on the PM particle emissions concurrently, the initial pressure drop of each catalyst is explained from the viewpoint of resistance against gas pass-through. The initial pressure drop of all the DPNR catalysts studied (i.e., those with different coating amounts and average pore sizes described above) was measured and the relationship between the initial pressure drop and PM particle number emissions was analyzed. **Fig. 14** shows the results. The analysis showed that the PM particle number emissions are a quadratic function of the initial pressure drop. When the initial pressure drop was below 0.62 kPa or above 0.7 kPa, the PM particle number emissions increased substantially. In the former range, it shows that PM particles passed through the large pores (two-dimensional continual pores) that were created by an insufficient coating amount or by using a DPF with over-sized average pore diameters. In the latter range, a surplus coating amount resulted in the selective blockage of small pores due to capillary action. Thereby, gas flow was maldistributed to larger pores and PM particles passed through the pores of the DPNR catalyst.

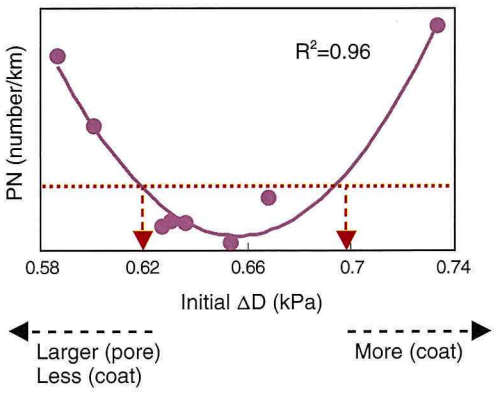


Fig. 14 Influence of Initial ΔD of DPNR Catalyst on PN

4. Conclusion

This study identified the relationship between the pore structure of the DPNR catalyst and the trapping of PM particles, and showed clearly that it is possible to lower the PM particle number emissions by optimally controlling the coating amount of the conventional cordierite DPF. As a result, this sophisticated DPNR catalyst should be able to play a part in meeting future regulation values for PM particle number emissions.

In addition, to further lower the PM particle number emissions, it will be necessary to improve the conventional DPF. This study indicates the direction for future development. New DPF development based on these technical studies (i.e., increasing the volume of 10 to 20 μm pores while lowering that over 30 μm) is making progress.

This research was performed in cooperation with Denso Corporation, and the authors would like to offer their sincere gratitude to everyone involved.

References

(1) T. Mizuno et al. *SAE Paper* No. 010578 (2004).
(2) T. Yamashita et al. "Automotive PM Particle Number Emissions Measured by PMP Method" (in Japanese). *Proceedings of the Society of Automotive Engineers of Japan* No. 34-08, 20085332 (2008).
(3) P. Atkins. *Physical Chemistry*. Tokyo Kagaku Dozin Co., Ltd. (1993).

Authors


M. KUWAJIMA


S. OKAWARA


S. MATSUNO


M. YAMAGUCHI


M. TSUZUKI

Development of Double-Layered Three-Way Catalysts

Yuki Aoki*
Takeru Yoshida**
Toshitaka Tanabe***
Masanori Shimizu****

Abstract

As emissions regulations around the world become ever more stringent, there is an urgent need to develop high performance automotive catalysts for reducing exhaust emissions. In a conventional single-layered three-way catalyst containing Pt and Rh catalytic material on the same coating layer, alloying of Pt and Rh by high temperature exhaust gas causes catalytic performance to deteriorate. However, this study found that a double-layered three-way catalyst loaded with Pt and Rh on separate catalyst layers suppresses the alloying of noble metals, thereby improving catalytic performance. In addition, although the adoption of a double-layered structure tends to adversely affect OSC performance, this was overcome by the development of a new Rh support and analysis of the optimum Pt loading amount. As a result, a high performance three-way catalyst was developed that requires approximately 40% less noble metals than conventional catalysts.

Keywords: *three-way catalyst, double-layered catalyst, CeO_2-ZrO_2, OSC, XAFS, Pt sintering*

1. Introduction

Exhaust emissions regulations of various regions around the world will become stricter in the near future, for example due to the introduction of Euro 5 in Europe and PZEV in the United States. In order to cope with stricter regulations, there is an urgent need to develop technologies to lower exhaust emissions, beginning with exhaust treatment catalysts. As issues for more effective exhaust treatment catalysts include the scarcity of resources and soaring cost of materials, there is a demand for the development of a three-way catalyst that can enhance catalyst performance while dramatically lowering the amount of noble metals used.

2. Current Issues and Development Aims

Fig. 1 shows a pattern diagram of a three-way catalyst. The catalyst is composed of the noble metals Pt and Rh, and Pt and Rh support materials. The Rh support uses ZrO_2 compound oxides and the Pt support uses a CeO_2-ZrO_2 type. The Pt support has an oxygen storage capacity (OSC) performance derived from CeO_2. Loading the different noble metals on different support materials optimizes catalytic activity by loading each noble metal on the best support.(1)

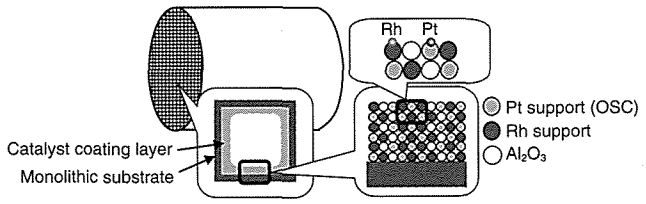


Fig. 1 Three-Way Catalyst Pattern Diagram

To clarify the current problems of catalysts, the previously mentioned catalyst was submitted to a 1,000°C floor temperature durability test using the exhaust of an actual engine, and the noble metal grains were observed under a transmission electron microscope (TEM). **Fig. 2** shows the results. After the durability test, Pt and Rh grains loaded on the supports were detected in the form of Pt-Rh alloy grains. This indicates that the noble metals are diffused on mutual support materials during the durability test. **Fig. 3** shows the results of a study of the effect of alloying on catalytic activity by a model gas evaluation. The NOx conversion performance diminished as alloying progresses in rich conditions. Because the NOx conversion performance of Rh is originally superior in rich conditions, Rh characteristics are most probably degraded by alloying. This is probably due to the fact that noble metal grains diffuse easily as oxides because Pt and Rh are stable as oxides under high temperatures and because vapor pressure is higher for oxides than for metals. Because the catalysts are exposed to strong oxidizing conditions under exhaust from actual engines due to factors such as fuel cuts, alloying is thought to originate from the aggregation of noble metal grains in the high oxidation state of vapor pressure.(2)

* Power Train Material Engineering Div.
** Toyota Motor Engineering & Manufacturing North America
*** Toyota Central R & D Labs., Inc.
**** Cataler Corporation

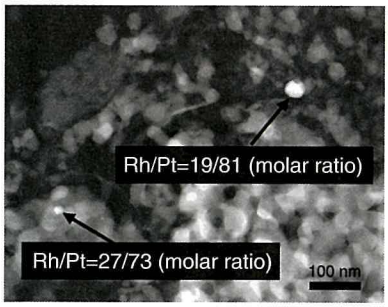


Fig. 2 TEM Image after Durability Test

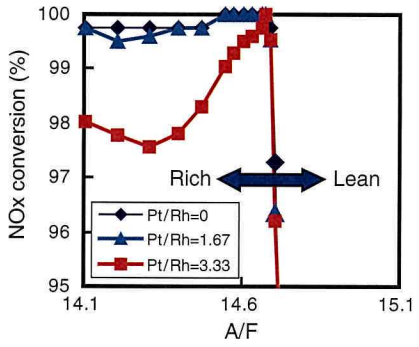


Fig. 3 NOx-A/F Properties

Under conventional use environments of catalysts, alloying has been controlled by supporting Pt and Rh on various supports.(1) From the standpoint of lowering exhaust emissions and enhancing the use efficiency of noble metals, however, a way to fundamentally control alloying is indispensable. Additionally, it has also been pointed out that Rh in the vicinity of CeO_2 is susceptible to being retained in an oxidative state, thereby creating a risk of HC poisoning.(3) This article therefore describes a double-layered catalyst that separates the Pt and Rh layers to maintain the original treatment performance of Pt and Rh even after a durability test. Rh support and Pt grain growth control were also studied in order to improve OSC.

3. Test Method

The conditions of the durability test using the exhaust of an actual engine were as follows: 3UZ-FE engine; floor temperature: 1,000°C×50 h (stoichiometric feedback: 50 seconds; fuel cut: 5 seconds; rich: 5 seconds/cycle). The conditions of the performance evaluation were as follows: 2AZ-FE engine; air/fuel (air-fuel ratio) evaluation: 400°C inlet gas; OSC performance evaluation: 700°C inlet gas.

The Rh support was evaluated using model gas after the durability test under model gas circulation simulating a rich/lean 2-minute cycle after pelletization, with the noble metals loaded onto each support. The OSC performance was gauged from the O_2 discharge volume when switching between the rich and lean gas. The low temperature activity evaluation employed an index set to 50% of the conversion rate when temperature rises using an equal amount of model gas. Pore distribution measurement by the N_2 adsorption method was used for support powder characterization. Fine structure analysis of catalyst was conducted by X-ray diffraction and TEM observation.

Pt grain growth behavior and OSC performance were evaluated by Pt L_3-edge XANES spectrum measurement of in-situ XAFS. For the evaluation, 3% H_2/He and 4% O_2/He gases were introduced alternately in 60 second cycles, and measured for 9,000 seconds heated to 800°C.

4. Results and Discussion

4.1 Study of double catalyst layer

Aiming to control alloying of Pt and Rh in high temperature oxidization conditions, inhibit HC poisoning of Rh, and enhance the use efficiency of Rh, a double-layered catalyst with the Rh catalyst on the top and the Pt catalyst on the bottom was fabricated to study the effect on the durability of catalytic performance. **Fig. 4** shows a SEM image of the fabricated catalyst. **Fig. 5** shows the calculation results of the Pt/Rh alloying rate of the double-layered catalyst from the diffraction angle of Pt and Rh using X-ray diffraction with the exhaust of an actual engine after the durability test.

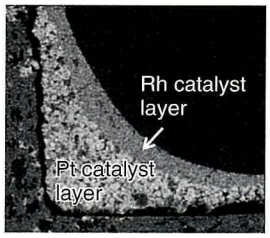


Fig. 4 SEM Image of Double-Layered Catalyst

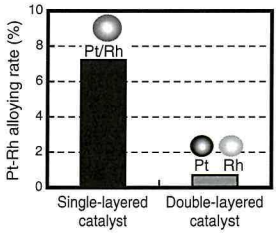


Fig. 5 Catalyst Alloying Rates

The alloying rate drops markedly due to the adoption of a double-layer, which suggests that alloying can be controlled by increasing the distance between Pt and Rh. **Figs. 6a** and **b** show the measurement results of OSC performance and the air/fuel characteristics of the fabricated catalyst.

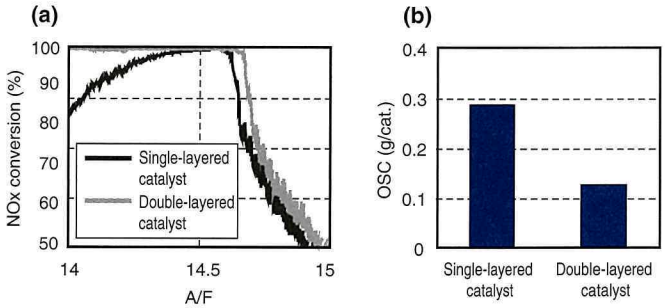


Fig. 6 (a) A/F Properties and (b) OSC Performance of Double-Layered Catalyst

NOx conversion performance in rich conditions, which is adversely affected in a conventional single layered catalyst, is enhanced by using a double-layer. In contrast, OSC performance decreased in the double-layered catalyst due to degeneration of the flow of exhaust to the bottom layer OSC material when using a double-layer. This decrease in OSC performance is thought to be the result of a reduction in the OSC material usage rate as a consequence of the longer gas diffusion distance to the OSC material in the lower layer.

Therefore, using a double-layered catalyst creates a trade-off relationship between the durability of catalytic performance and OSC performance, and the development of a catalyst that can achieve both targets is an important issue. In order to enhance the OSC performance of a double-layered catalyst, a study was conducted as described in the following section, focusing on the following three points.

1) Enhancement of use efficiency of the bottom layer OSC material by improving gas diffusion
2) Providing OSC performance by adding CeO_2 to the top layer Rh support
3) Enhancement of OSC performance by controlling the grain growth of the bottom layer Pt

4.2 Study of Rh support

As part of the development of the top layer Rh support, studies were performed focusing on points 1) and 2) above to improve gas diffusion by pore distribution control and to find a CeO_2/ZrO_2 ratio that enables both favorable OSC performance and Rh activity.

In order to improve the use efficiency of the bottom layer OSC material, it is necessary to improve gas diffusion from the top layer to the bottom layer. It is also necessary to increase the pore diameter and volume of the material powder to provide better gas diffusion. Here, powder was produced by a new method that controls pore structure and then compared with powder produced by the existing method. **Fig. 7a** shows the pore characteristics of the powder fabricated by the new method. Compared with the existing powder, the new method creates larger mesopores of 20 to 50 nm and broader pore characteristics. Subsequently, the gas diffusion of the coating layer was evaluated as diffusion velocity J using Equation 1.

$$J = -D_{eA} \times dC/dx \quad (1)$$

where,
D_{eA}: effective diffusion coefficient
dx: gas diffusion distance
dC: gas concentration

The results in **Fig. 7b** were obtained using this equation. Due to the difference in pore characteristics, the D_{eA} of the developed product is larger and the diffusion velocity increases, thereby improving gas diffusion.

How to provide the Rh support with better OSC performance was then studied. The OSC reaction is based in oxygen adsorption and discharge involved with the reversible reaction between trivalent and tetravalent Ce in CeO_2-ZrO_2 compound oxides. Therefore, OSC performance relies strongly on the ratio of CeO_2 to ZrO_2. **Figs. 8a** and **b** show the evaluation results for the CeO2/ZrO_2 ratio of the Rh support, and the relationship between CeO_2 use efficiency and low temperature activity using the model gas. The use efficiency of CeO_2 is high at CeO_2/ZrO_2=0.25 or less, and further addition of CeO_2 lowers the efficiency. This is because the strain produced at the time of phase transformation is alleviated by the introduction of small ion radius Zr^{4+} into the lattice, thereby enhancing use efficiency when oxygen is discharged.[4][5] Because low temperature activity tends to deteriorate at CeO_2/ZrO_2=0.35 or higher, there is concern that the addition of CeO_2 to the ZrO_2 support of Rh could negatively affect catalytic activity. **Fig. 9** shows the results of TEM observation of Rh after a durability test of Rh/ZrO_2 and Rh/CeO_2 catalysts with the model gas. It is possible to observe the grains of Rh on ZrO_2 clearly. Rh, however, appears as moire stripes on the CeO_2. The surface interval of the two is close and affinity is high. In other words, it is thought that Rh on CeO_2 tends to dissolve on the support to create a state different from the metallic state that exhibits the original activity. Therefore there is a concern that adding excess CeO_2 might cause a drop in catalytic activity.

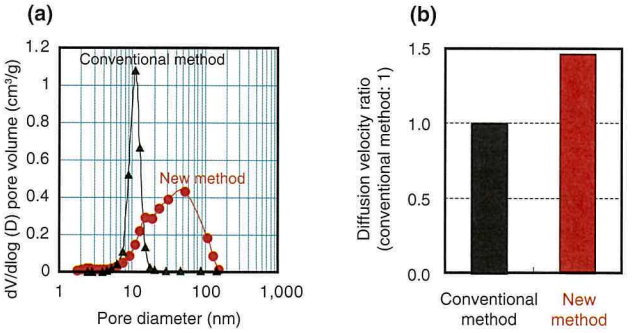


Fig. 7 (a) Pore Properties and (b) Diffusion Velocity Ratio of New Method

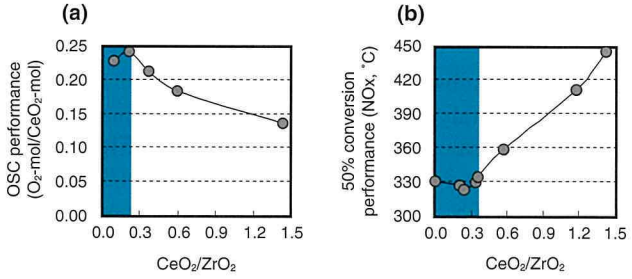


Fig. 8 Relationships Between CeO_2/ZrO_2 Ratio and (a) OSC Performance and (b) 50% Conversion Temperature

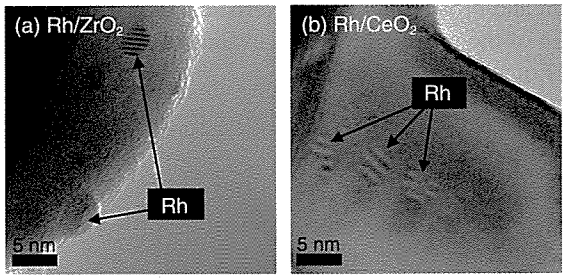


Fig. 9 TEM Images of (a) Rh/ZrO_2 and (b) Rh/CeO_2 Catalysts

Therefore, an Rh support allows both Rh activity and high efficiency OSC performance. In addition, a new ZrO_2-CeO_2 series support with a CeO_2/ZrO_2 ratio that satisfies the required conversion performance for the whole catalyst was adopted.

4.3 Study of Pt grain growth control

Because OSC performance is proportional to the number of active sites of the supported noble metal, control of Pt grain growth and optimal Pt support amount design as part of this control have attracted attention as a means of enhancing OSC performance of the bottom layer Pt support. The strong mutual effect resulting from Pt-O-Ce bonding affects the support and noble metals in the case of Pt on CeO_2. Therefore, it is known that grain growth under high temperatures can be controlled using CeO_2-ZrO_2 compound oxides as the Pt support. Equation 2 has been proposed to determine the Pt support amount to maximize the mutual effect of the Pt and the support.[6][7]

$$X = \frac{(\delta/100) \times S \times M_{pt}}{s \times N} \times 100 \qquad (2)$$

where,

X: anchored Pt amount (g/support: 100 g)
δ: Pt retention site appearance probability (%)
$\delta=(m/100)^5\times100$
m: concentration of Ce in support (mol%)
M_{Pt}: atomic weight of Pt (195.09)
s: positive ion site unit surface area (Å²/each)
N: Avogadro number (units)
S: specific surface area (SSA) of support (m^2/g)

As a result of substituting the conditions of the Pt support in the developed catalyst into Equation 2, the optimal Pt support amount as been calculated to be Pt=0.53wt%. **Fig. 10** shows the measurement results for Pt L_3-edge XANES spectrum using in-situ XAFS, and for Pt grain growth behavior from the oxidized and reduced states of the catalyst and the peak height difference (PHD). In the case of loading a minimum of 1.0wt% of Pt, the dispersibility of Pt decreases with time at a maintained temperature of 800°C. However, in the case of Pt=0.5wt%, no drop in Pt dispersibility is observed. In other words, it is thought that Pt grain growth is controlled because much of the Pt on the support is immobilized by the anchor effect and the support, which backs up the validity of Equation 2. **Fig. 11** shows the results of an evaluation of the deterioration behavior of OSC performance from H_2 consumption on measurement. The behavior related to the time of OSC performance differs according to the Pt support amount. Almost no change in OSC performance is observed at Pt=1.0wt%, but it tends to drop at Pt=2.0wt%, and tends to improve at Pt=0.5wt%.

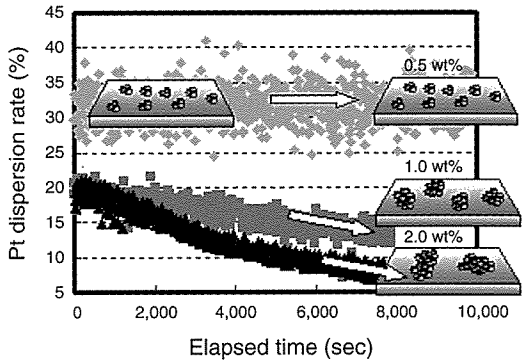


Fig. 10 Changes in Pt Dispersion Behavior Due to Pt Support Amount

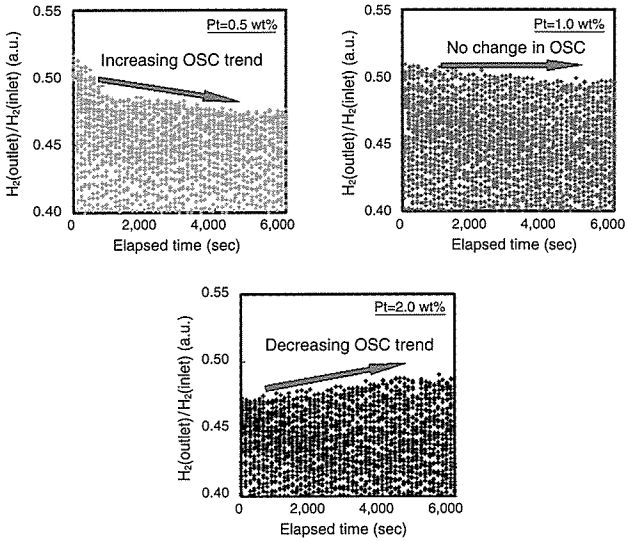


Fig. 11 Changes in OSC Reaction Due to Pt Support Amount

This behavior is similar to the Pt grain growth behavior, and it shows that the durability of OSC performance can be enhanced by controlling Pt grain growth.

Therefore, optimal Pt support amount design that obtains a Pt grain growth control effect was adopted as a means of enhancing OSC performance of the bottom layer of a double-layered catalyst.

4.4 Confirmation of improved catalyst effect

A double-layered catalyst was produced using the new Rh support and optimal Pt support amount obtained from the studies described above. The catalyst was evaluated in a durability test using the exhaust of an actual engine. **Fig. 12** shows the results of evaluation of OSC performance and LA#4 mode NOx emissions. Compared to the conventional catalyst, the developed double-layered catalyst used approximately 40% less noble metals, enabled dramatically lower NOx emissions in excess of the targeted value, and also maintained the same OSC performance.

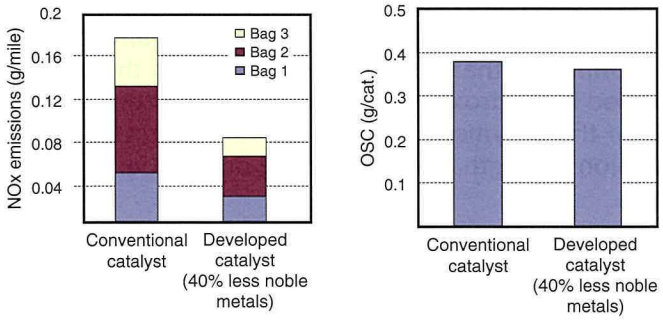


Fig. 12 (a) Emissions and (b) OSC Performance of Developed Catalyst

5. Conclusion

A study of catalytic layer structures, Rh support, and Pt grain growth control that aimed to improve the durability of three-way catalysts revealed the following points.

1) Use of double catalytic layers allows alloying of Pt and Rh to be controlled, and improves treatment performance.
2) Both treatment performance and OSC performance can be achieved through the use of CeO_2-ZrO_2 compound oxides for the Rh support with CeO_2/ZrO_2=0.25.
3) A Pt grain growth control effect can be obtained and the durability of OSC performance can be improved by supporting an optimal amount of Pt on the CeO_2-ZrO_2 compound oxides.

Double-layered catalysts fabricated reflecting these results are capable of lowering the amount of noble metals used by 40% from conventional catalysts. The developed catalysts have been commercialized since August 2008.

Finally, this development is a result of joint research with Toyota Central R&D Labs., Inc. and Cataler Corporation. The authors deeply appreciate the tremendous help from people concerned including the staff of Toyota Central R&D Labs. and Cataler in conducting the research.

References

(1) T. Yoshida et al., "Development of High Performance Three-Way-Catalyst", *SAE Paper 2006-01-1061.*
(2) Y. Murakami et al. *Catalyst Deterioration Mechanism and Prevention Measures* (in Japanese) (1995).
(3) T. Fujiwara et al. "Development of High Performance Three-Way-Catalyst (1)." *JSAE Annual Congress (Autumn)* No. 282-20085659 (2008).
(4) F. Dong et al. "Dynamic Oxygen Mobility and a New Insight into the Role of Zr Atoms in Three-Way Catalysts of Pt/CeO_2-ZrO_2." *Catalyst Today* 93-95 (2004) pp. 827-832.
(5) Y. Nagai et al. "X-Ray Adsorption Fine Structure Analysis of Local Structure of CeO_2-ZrO_2 Mixed Oxides with the Same Composition Ratio (Ce/Zr=1)." *Catalyst Today* 74 (2002) pp. 225-234.
(6) Y. Nagai et al. "Sintering Inhibition Mechanism of Platinum Supported on Ceria-Based Oxide and Pt-Oxide-Support Interaction." *Journal of Catalysis* 242 (2006) p. 103.
(7) M. Hatanaka et al. "Clarification of Pt Sintering Inhibition Mechanism of Pt/Ceria Catalyst (2)"(in Japanese). *Proceedings of 100th Catalyst Congress* 3G27.

Authors


Y. AOKI


T. YOSHIDA


T. TANABE


M. SHIMIZU

Investigation of Novel Metal Plating Process Using Ozone Treatment

Hiroshi Yanagimoto*
Takeshi Bessho*

Abstract

The use of an ozone solution to modify plastic surfaces is being studied as a pretreatment method for metal plating on plastics. Although this method has the merits of reducing substances of environmental concern and allowing metal plating on smooth plastic surfaces, it has yet to enter practical use because it provides lower adhesion strength than conventional methods. When the adhesion strength of metal plating using this method was measured, fractures were located within the plastic layer. Consequently, the mechanism of plastic reformation using ozone solution was identified, and it was confirmed that this treatment reduces the strength of the plastic. It was speculated that this phenomenon is caused by hydroxyl radicals within the ozone solution advancing the oxidation of the plastic, resulting in fractures of the polymer network. Tests confirmed that the use of ozone gas without hydroxyl radicals improved the adhesion strength of metal plating on plastic.

Keywords: *plating, ozone, plastic, adhesion strength, reforming*

1. Introduction

Metal plating on plastics is an inexpensive surface treatment technology in which a metal coating can be evenly applied to a plastic surface with a complicated shape by reducing metal ions that are held in an aqueous solution. Therefore, this process is used on a wide variety of automotive parts, such as trim, electronic components, as well as sliding and wear-resistant parts.

Fig. 1 shows an example of nickel (Ni) metal plating deposited on acrylonitrile butadiene styrene (ABS) plastic. In order to ensure adhesion between the plastic and the metal plating, a roughening treatment has to be applied to the surface of the plastic.(1) The metal plating is deposited along the intricate plastic shapes that result from the treatment to obtain physical adhesion strength (the anchor effect).

However, in order to effectively roughen the surface of the plastic it is necessary to use substances of environmental concern, such as hexavalent chromium acid or permanganic acid. In recent years, trends in environmental regulation have made the elimination of such hazardous substances from the manufacturing process an urgent task. In addition, increasing the roughness of the plastic surface has an adverse effect on a variety of part characteristics. For example, in order to reduce the size of circuit boards it is essential to miniaturize the wiring. However, increasing the roughness of the plastic surface reduces the reliability of the insulation between the wires. To solve this issue it is necessary to develop metal plating that possesses excellent adhesiveness and does not require roughening of the plastic surface.

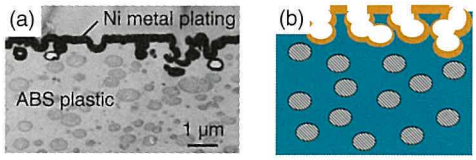


Fig. 1 (a) Cross Section of Metal Plating and (b) Pattern Diagram Obtained by Conventional Method

Therefore, research into a plastic surface treatment method that uses an ozone solution is being promoted as a new metal plating pretreatment technology.(2) In this method, the plastic is immersed in an aqueous solution, into which highly-concentrated ozone has been dissolved, in order to perform an oxidation treatment. After this, the metal coating can be applied to the plastic by existing metal plating treatment processes. This article describes the details of the mechanism of plastic reformation, which was an issue for this method. As a result, it is now possible to improve the adhesion strength of metal plating.

2. Ozone Solution Treatment Method

Ozone has strong oxidizing power and is able to reform a variety of different plastics. Ozone or hydroxyl radicals in an aqueous solution oxidize the plastic surface and generate polar groups as shown in **Fig. 2**. A cross section of Ni metal plating deposited on ABS plastic is shown in **Fig. 3** as an example. The metal plating solution infiltrates into the plastic surface and achieves adhesion strength because the metal coating is deposited within the plastic. Therefore, it is not necessary to apply a conventional roughening treatment to the plastic surface.

* Power Train Material Engineering Div.

In addition, since ozone is easy to decompose, substances of environmental concern are not discharged.

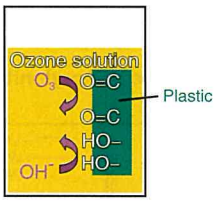


Fig. 2 Outline of Ozone Solution Treatment

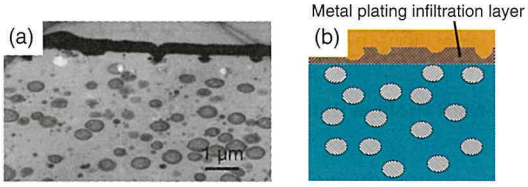


Fig. 3 (a) Cross Section of Metal Plating and (b) Pattern Diagram Obtained by Ozone Solution Treatment Method

The main issue with this method is the lack of adhesion strength of the metal plating. As shown in **Fig. 4**, by adding a heat treatment process after the ozone solution treatment, the adhesion strength is increased, but further improvement is necessary. Therefore, the mechanisms of plastic reformation using ozone solution and heat treatment were identified and methods of increasing the adhesion strength were examined. It should be noted that acrylonitrile styrene (AS) plastic, which is used for trim parts, was used as the plastic for the evaluation.

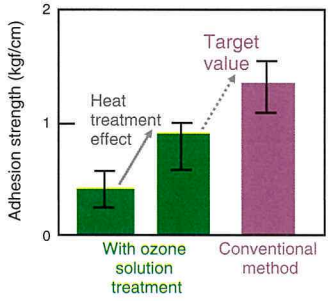


Fig. 4 Adhesion Strength of Metal Plating

3. Mechanism of Plastic Reformation Using Ozone Solution

3.1 Evaluation of AS plastic properties

As shown in **Fig. 5**, fractures were found within the plastic when the adhesion strength was measured. The fractures were located at a depth of approximately 100 to 200 nm from the surface of the plastic.

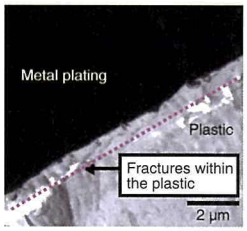


Fig. 5 Cross Section at Time of Adhesion Strength Measurement

The thickness of the plastic layer that was reformed by the ozone solution was verified. From the FT-IR analysis shown in **Fig. 6**, a peak was detected for the carbonyl group, which indicates plastic reformation. A simulation of the thickness of the plastic reformation layer was conducted using the strength of the carbonyl peak that was detected when the IR angle of incidence was changed. As a result, it was found that the thickness of the plastic reformation layer was approximately 200 nm, as shown in **Fig. 7**. This value is almost equal to the depth of the fractures found when the adhesion strength of the metal plating was measured. Therefore, it is believed that there is a correlation between the plastic reformation layer and the decrease in the adhesion strength of the metal plating. Consequently, an evaluation of the plastic strength before and after reformation was conducted.

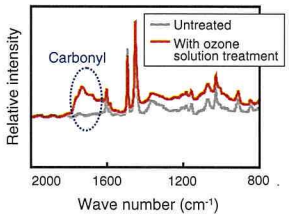


Fig. 6 FT-IR Spectrum Before and After Ozone Solution Treatment

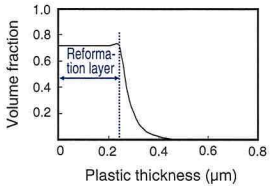


Fig. 7 Thickness of Reformed Plastic due to Ozone Solution

3.1.1 Experimental method

The surface and interfacial cutting analysis system (SAICAS) was used as the evaluation method.[3] An outline of SAICAS is shown in **Fig. 8**. The vertical resistance and horizontal resistance are detected when the cutting blade is inserted into the plastic at a 1° angle of incidence. The vertical resistance signifies the modulus of elasticity and the horizontal resistance signifies the fracture strength. It is known that the angle θ formed between these two resistances is able to track changes in the plastic properties. This means that when θ becomes large, deformation in the vertical direction becomes difficult or fractures in the horizontal direction are produced more easily.

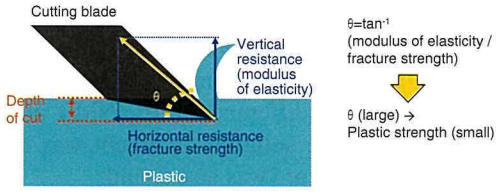


Fig. 8 Outline of SAICAS

In other words, an increase in the angle θ signifies a reduction in the strength of the plastic. Therefore this angle θ can be used to qualitatively evaluate changes in plastic strength.

3.1.2 Results and observations

Fig. 9 shows the SAICAS evaluation results for the samples from before and after the ozone solution treatment. It was confirmed that θ increased in the vicinity of 100 nm in the plastic surface layer due to the use of the ozone solution treatment. This thickness is analogous to the fracture area found when the adhesion strength of the metal plating was measured, as confirmed in **Fig. 5**. Therefore, the cause of the reduction in adhesion strength is considered to be the reduction in plastic strength that results from the plastic reformation by the ozone. An attempt was made to analyze the plastic structure in order to clearly identify the mechanism of plastic strength reduction.

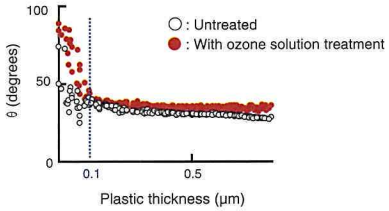


Fig. 9 Plastic Strength Measurement Using SAICAS

3.2 AS plastic structure analysis

3.2.1 Experiment method

The plastic sheet used for the evaluation had a thickness of 3 mm and the thickness of the plastic that was reformed by the ozone solution was 100 to 200 nm. Consequently, the condition of the plastic sheet limited the portion to be analyzed to a minute amount and a detailed analysis was not possible. Therefore, buffing was used to shave off several μm of the AS plastic surface layer and the obtained plastic powder was used to conduct the evaluation.

The following methods were used for the analysis: nuclear magnetic resonance (NMR), gel permeation chromatography (GPC), and electron spin resonance (ESR).

3.2.2 Results and observations

NMR analysis was conducted on the plastic before and after the ozone treatment in order to identify the change in the AS unit structure. The structural formula of the AS unit is shown in **Fig. 10**. Furthermore, the numbers in that figure represent the binding sites that were returned from the NMR analysis shown in **Fig. 11**. However, no difference in the NMR profiles from before and after the ozone solution treatment was recognized. No change in the unit structure was also found.

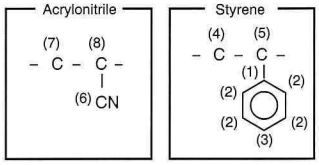


Fig. 10 Structure of Acrylonitrile Styrene Plastic

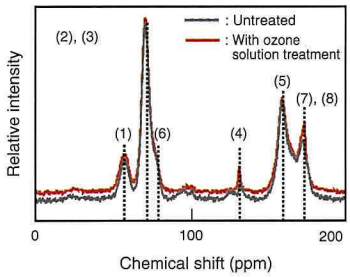


Fig. 11 C^{13}-NMR Profiles Before and After Ozone Solution Treatment

Next, an evaluation was conducted using GPC analysis to determine any change in the molecular weight. As shown in **Fig. 12**, an increase and decrease in molecular weight due to the ozone solution treatment was confirmed. The average molecular weight shown in **Table 1** demonstrates that the majority of changes were increases in the molecular weight. Furthermore, when the samples were dissolved in tetrahydrofuran (THF) solution in preparation for the GPC analysis, only the samples that had received the ozone solution treatment were found to have insoluble matter. The cause of this matter not being dissolved in a good solvent despite the lack of change in the AS unit structure is inferred to be the production of cross-linked matter.

The oxidatively active species in the ozone solution are the ozone or the hydroxyl radicals that are generated by the reaction between ozone and water.[4] These oxidatively active species attack and sever a variety of molecular bonds. When this occurs, an active electron (radical) is produced in the place where the bond is severed. Therefore, the amount of radicals was measured

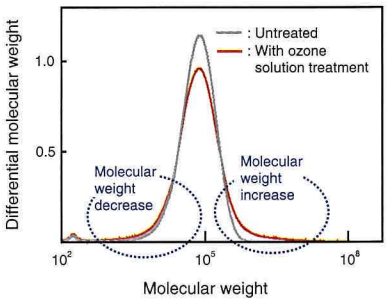


Fig. 12 GPC Profile Before and After Ozone Solution Treatment

Table 1 Change in Average Molecular Weight and Solubility in Good Solvent

	Average molecular weight	THF solubility
Untreated	94,600	Good
With ozone solution treatment	151,000	Poor (insoluble matter)

using ESR analysis and an attempt was made to identify the cause of the change in the molecular weight. **Table 2** shows that carrying out the ozone solution treatment increased both the carbon radicals and oxygen radicals within the plastic. In particular, since carbon radicals increased by approximately four times, it became clear that carbon bonds were being severed. The main chain of AS is composed of chemically stable saturated bonds. Therefore, it is thought that the active species that is capable of severing these types of bonds is the hydroxyl radicals since they possess strong oxidizing power.[4]

The change in the structure of the AS plastic caused by the ozone solution treatment is summarized in **Fig. 13** based on the results described above. The hydroxyl radicals sever the main chain of AS and a recombination reaction (cross-linking reaction) also occurs. Furthermore, it was concluded that the ozone was causing the oxidation of polymer terminals or side chains.

Table 2 Change in Amount of Radicals Before and After Ozone Solution Treatment

	Carbon radicals	Oxygen radicals
Untreated	8.3E+14	1.7E+15
With ozone solution treatment	3.4E+15	4.1E+15

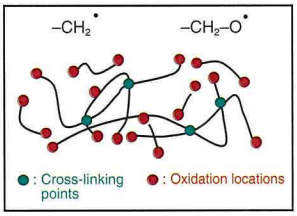


Fig. 13 Changes in Polymer Network due to Ozone Solution Treatment

4. Heat Treatment Mechanism

As is shown in **Fig. 4**, it was confirmed that the adhesion strength of the metal plating was increased by adding a heat treatment process after the ozone solution treatment. Therefore, an idea for further increasing the adhesion strength was obtained by identifying the mechanism of the heat treatment.

4.1 Experiment method

An FT-IR analysis was conducted to examine the change in the plastic structure before and after the heat treatment. Moreover, in order to make a detailed analysis of the change, the spectrum of the sample from before the heat treatment was subtracted from the spectrum of the sample after the heat treatment and any peaks that exhibited change were identified (difference spectrum).

In addition to this, the components of the gas generated during the heat treatment were identified and their quantity determined by gas chromatograph mass spectrometry. The pyrolytic components produced from the untreated plastic and plastic that had received ozone solution treatment were also compared.

4.2 Results and observations

The FT-IR difference spectrum is shown in **Fig. 14**. A peak returned from the RCOOR bonds was confirmed, although it was quite small. This is a bond formed by a dehydrating condensation reaction between the oxidation pole groups. In other words, this means that the heat treatment caused bonds to form between polymers.

The change in the peak strength of the RCOOR bonds with respect to the length of the heat treatment time is shown in **Fig. 15**. It was confirmed that as the time grows longer, strength increase and the dehydrating condensation reaction progress continuously. It is thought that one cause of the increased adhesion strength of the metal plating due to the heat treatment is that the plastic strength increases as new bonding points are formed. This reasoning is supported by data that shows when samples that received heat treatment were dissolved in THF, the amount of insoluble matter increased in comparison to samples that had not received the heat treatment. From this it was determined that the newly formed bonds were functioning as cross-linking points.

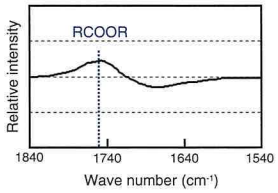


Fig. 14 FT-IR Difference Spectrum Before and After Heat Treatment

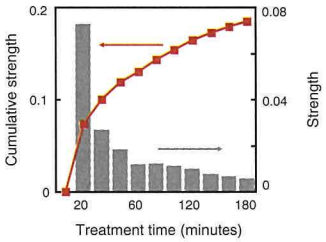


Fig. 15 Change in RCOOR Strength with Respect to Change in Heat Treatment Time

Next, the composition of and amount of components in the gas generated during the heat treatment are shown in **Table 3**. The application of the ozone solution treatment increased the amount of gas produced and formic acid, nitrogen-containing components, and components with a comparatively large molecular weight were also detected from the gas. It is therefore inferred that these components were discharged from the plastic due to the heat decomposition of the low-molecular components confirmed in **Fig. 12**. The coils of low-molecular chains are weak and this leads to a reduction in the plastic strength. Consequently, it is thought that the elimination of low-molecular components via the heat treatment is what causes the increase in the plastic strength.

Based on the explanations above, the mechanism for increased adhesion strength of the metal plating due to the heat treatment

is shown in **Fig. 16**. The dehydrating condensation reaction produced between the active groups by the ozone solution treatment is advanced and cross-linking between polymers is promoted. In addition to this, it was concluded that the polymer density is increased by heat decomposition of low-molecular components and the plastic strength is also increased.

Table 3 Gas Components Generated During Heat Treatment and Amount of Components

	Untreated	With ozone solution treatment
Styrene	11.1	5.1
Formic acid	0	27.1
Unknown component 1 (contains nitrogen)	0.8	23.0
Unknown component 2 (large molecular weight)	3.1	15.0
Total	42.1	101.0

ng/g

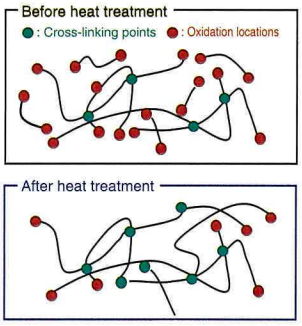


Fig. 16 Change in Polymer Network due to Heat Treatment

5. Measures to Improve Adhesion Strength

From the results of the mechanism analysis conducted up to this point it is thought that the cause of the reduction in adhesion strength of the metal plating is the reduction in the plastic strength caused by hydroxyl radicals in the ozone solution. Therefore, in an attempt to increase the adhesion strength of the metal plating, plastic surface reformation was applied using ozone gas that does not contain hydroxyl radicals. As is shown in **Fig. 17**, a major increase in the adhesion strength of the metal plating through the adoption of ozone gas was confirmed. The values that were obtained are approximately equal to those of the conventional method at 1.3 kg/cm and it was learned that these values satisfy the level necessary to make practical use possible.

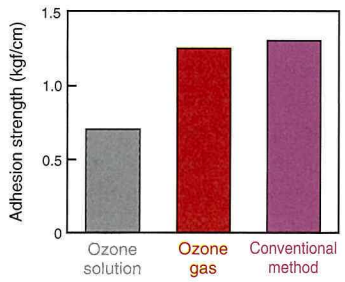


Fig. 17 Peel Strength of Metal Plating Obtained by Each Treatment Method

6. Summary

In order to identify the cause of reduced metal plating adhesion strength, which was an issue for the ozone solution treatment method, the properties of the plastic were evaluated, and detailed examinations were conducted into the mechanisms of plastic reformation using ozone and heat treatment. As a result the following findings were made.

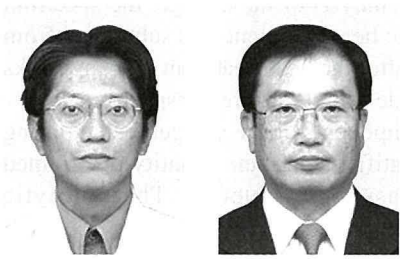
(1) The reduction in adhesion strength was caused by a reduction in plastic strength due to the ozone solution treatment.
(2) Hydroxyl radicals in the ozone solution simultaneously advanced both the fracturing and recombination of polymer main chains. Because of this, the plastic strength was reduced.
(3) Conducting the heat treatment after the ozone solution treatment increased the bonding points between polymers and simultaneously advanced the heat decomposition of low-molecular components. As a result, the plastic strength recovered to a certain extent and the adhesion strength of the metal plating increased.
(4) It was confirmed that conducting plastic reformation using ozone gas that does not contain hydroxyl radicals achieved the target performance. In other words, it resulted in excellent adhesion strength for the metal plating and obtained values that were equal to the current method.

The authors would like to express their gratitude to the following for their assistance with this research: Toyota Central R&D Labs, Inc., for their cooperation with the SAICAS analysis, Kanto Kasei Ltd., for their cooperation with the metal plating treatment, and Kurita Kogyo Inc., for their cooperation with the ozone gas treatment.

References

(1) M. Nakamura. *Journal of The Surface Finishing Society of Japan* Vol. 53 No. 7 (2002) pp. 440-442.
(2) T. Bessho, Yoshinaga, Inoue, Koiwa, Honma. "Pretreatment of Nickel Plating on ASA Resin Using Ozonated Water as Replacement for Chromic Acid Etching." *Journal of the Surface Finishing Society of Japan* Vol. 57 No. 9 (2006) pp. 659-663.
(3) I. Nishiyama. "Evaluating the Adhesion Strength of Adherends Using the SAICAS Method (1) (2)" (in Japanese). *Journal of the Japan Coating Technology Association* Vol. 34 No. 5, p. 129.
(4) I. Somiya. *Ozone Handbook*. Sanyu Publishing (2004), pp. 96-99.

Authors



H. YANAGIMOTO **T. BESSHO**

Development of Power Diode for Hybrid Vehicles

Atsushi Tanida*
Tetsuya Kanata*
Katsuhiko Nishiwaki*
Takahide Sugiyama**

Abstract
Hybrid vehicles (HVs) are seen as an increasingly important measure against recent environmental issues such as global warming. To further enhance the excellent dynamic performance and fuel efficiency of HVs, it is necessary to boost the voltage of the motor drive system. However, the diodes (semiconductor devices) that act as the core parts for driving the motor suffer from a temporary reduction in withstand voltage during operation (called the avalanche phenomenon). This adversely affects the current interruption function and prevents voltage from being increased. This development used atomic level analysis to identify crystalline defects caused by carbon in the diodes as the root cause of the reduction in withstand voltage. Overcoming this issue has contributed to the improvement of HV performance. This article describes the details of this development.

Keywords: *hybrid, diode, dynamic avalanche, carbon, crystalline defect*

1. Introduction

Hybrid and other environmentally friendly vehicles are attracting increasing attention in the face of recent environmental issues such as the depletion of oil resources and global warming caused by CO_2. Hybrid vehicles are provided with an inverter, which converts DC from the battery to AC to drive the motor. As shown in **Table 1**, system voltage has been gradually increased to increase motor power and reduce losses.

As a result of this trend, the power diodes installed in the IGBT module inside the inverter (**Fig. 1**) must be provided with even greater withstand voltage characteristics. However, the desired voltage increase may be prevented by the dynamic avalanche phenomenon, which results in a temporary decrease in withstand voltage during switching.

The performance of Toyota's HVs is positively affected by reductions in diode size and losses. It is therefore imperative to resolve this issue in order to improve the commercial appeal of the vehicle. Additionally, to explain this phenomenon, it was necessary to develop complex technology capable of analyzing elements contained in the diode with a concentration of less than 1 in 100 million compared with the concentration of the base silicon material.

This development used atomic level analysis to identify crystalline defects caused by carbon in the diodes as the root cause of the reduction in withstand voltage. Additionally, controlling the carbon concentration allowed the production of diodes that suppress the dynamic avalanche phenomenon, thereby making a major contribution to the improvement of HV performance.

* Electronics Development Div. 3
** Toyota Central R & D Labs., Inc.

Table 1 HV Motor Power and System Voltage

	'01 Estima	'03 Prius	'05 Harrier	'06 GS
				
Motor power (kW)	13	50	123	147
System voltage (V)	216	500	650	650

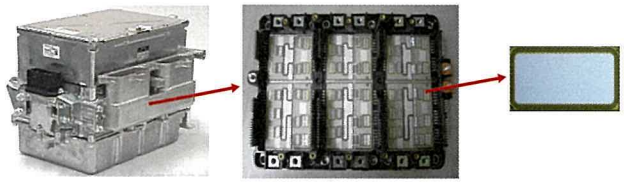


Fig. 1 HV Inverter Diode

2. Development Issues

A diode is a rectifying device that functions to conduct current with low losses when forward-biased, and to interrupt current up to its withstand voltage when reverse biased. Additionally, the diodes in Toyota's HVs use He irradiation to form a crystalline defect layer. This reduces losses during switching and enables high performance operation.

However, if system voltage is increased with conventional diodes, the dynamic avalanche phenomenon occurs. In this phenomenon, the withstand voltage temporarily decreases when the diode switches from forward to reverse bias (**Fig. 2**). This increases switching losses and causes secondary oscillations in voltage and current (i.e., noise).

The aim of this development was to suppress the dynamic avalanche phenomenon that occurs when system voltage is increased.

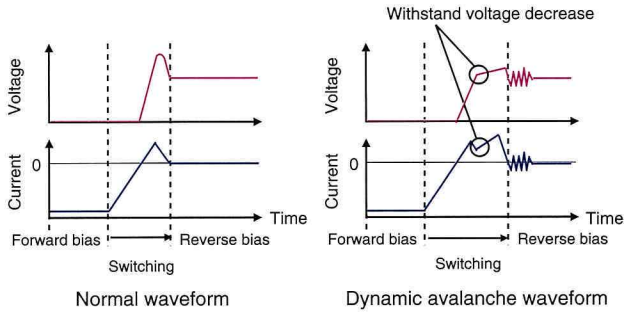


Fig. 2 Voltage and Current Waveforms During Switching Operations

3. Mechanism of Dynamic Avalanche Phenomenon

Fig. 3 shows the principle behind the determination of withstand voltage when the diode switches to reverse bias. As a result of the reverse bias voltage, an electrical field forms in the region (depletion layer) where no carriers are present. Subsequently, this electrical field becomes stronger as the voltage increases.

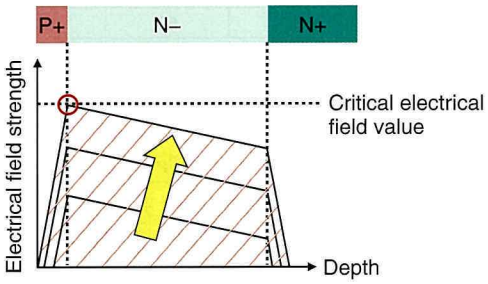


Fig. 3 Principle for Determining Withstand Voltage

When the electrical field reaches the critical value, the voltage cannot be held, and the diode losses its current interrupt function (the avalanche phenomenon). The withstand voltage at this point is the integral of the critical electrical field value, and is represented by the area of the shaded portion in the figure. The gradient of the electrical field can be obtained by the following equation.

$$dE/dx = qN_D/\varepsilon_0\varepsilon_S \quad (1)$$

where,

E: electrical field
x: depth
q: elementary electric charge
N_D: donor concentration in N layer
ε_0: dielectric constant in a vacuum
ε_S: dielectric constant of silicon

As shown in **Fig. 4**, the dynamic avalanche occurs as follows. During switching, holes are trapped by crystalline defects, which results in a temporary rise in positive fixed charge and causes the electrical field in increase.(1)

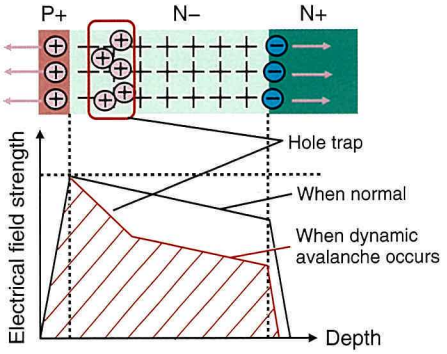


Fig. 4 Electrical Field Distribution when Dynamic Avalanche Occurs

In other words, during switching, the gradient of the electrical field increases by the amount of the trapped holes over the gradient during normal reverse bias operation. This is expressed in Equation 2. Therefore, the withstand voltage decreases because the area of the shaded portion in the figure becomes smaller.

$$dE/dx = q(N_D + N_{hole})/\varepsilon_0\varepsilon_S \quad (2)$$

where,

N_{hole}: hole concentration in N layer

Incidentally, because diodes perform lifetime control, crystalline defects are introduced by high-energy particle (He) radiation into the silicon crystals. As shown in **Fig. 5**, lifetime control refers to the creation of an energy level close to the center of the conduction band containing electrons (E_C) and the valence band containing holes (E_V). This level (called the recombination center) is formed by crystalline defects and it acts to eliminate carriers by re-combining electrons and holes. However, the analysis described above identified that an energy level (called the hole trap level) that traps holes and temporarily generates positive fixed charge is also formed at the same time. To resolve this issue, this development clarified the hole trap level formation mechanism and attempted to suppress its formation.

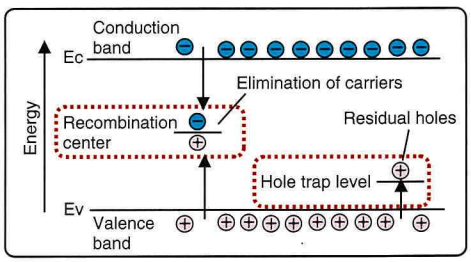


Fig. 5 Residual Holes in Hole Trap Level

4. Identification of Root Cause of Dynamic Avalanche Phenomenon

4.1 Clarification of trap level

It was thought that a test sample in which the dynamic avalanche phenomenon is likely to occur should have many crystalline defects that contribute to hole trapping. As a result, samples A and B were prepared such that the dynamic avalanche phenomenon occurred in sample B, but not in sample A.

The crystalline defects were analyzed by deep level transient spectroscopy (DLTS), which is capable of confirming the trap levels in almost all regions of silicon.

Fig. 6 shows the hole trap measurement results. A comparison of sample A and B showed specific spectrum changes at E_V+0.35eV. The spectrum strength was higher in sample B in which the dynamic avalanche phenomenon occurred. In addition, **Fig. 7** shows the electron trap measurement results. No major differences were found between the samples with respect to electron traps.

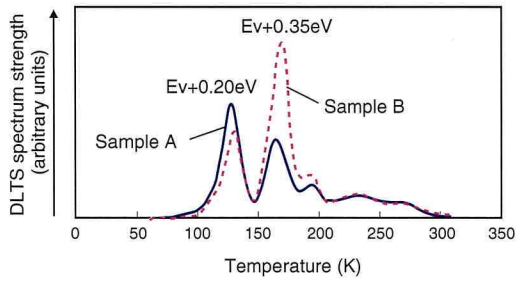


Fig. 6 DLTS Results for Samples A and B (Holes)

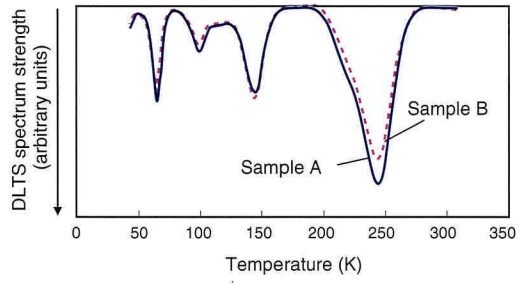


Fig. 7 DLTS Results for Samples A and B (Electrons)

These results indicated that E_V+0.35eV is a hole trap level that affects the dynamic avalanche phenomenon.

4.2 Verification by simulation

The effect of the E_V+0.35eV level on the dynamic avalanche phenomenon was verified by semiconductor device simulation. **Fig. 8** shows the switching waveform calculation results when the E_V+0.35eV trap level density was varied to simulate samples A and B. Simulated sample A with a low trap level had a normal switching mechanism, whereas the waveform for simulated sample B with a high trap level reproduced the double peak of the dynamic avalanche phenomenon. This confirmed that the dynamic avalanche phenomenon was caused by a high E_V+0.35eV level density.

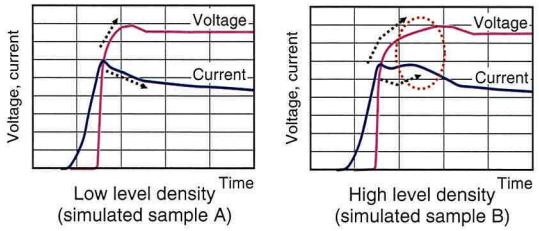


Fig. 8 Waveform Comparison at Various E_V+0.35eV Level Densities

4.3 Clarification of level-generating defects

The defects that generate the E_V+0.35eV hole trap level were identified as shown in **Fig. 9**, focusing on elements that might intrude into the diode as impurities during the diode fabrication process from silicon crystal production.

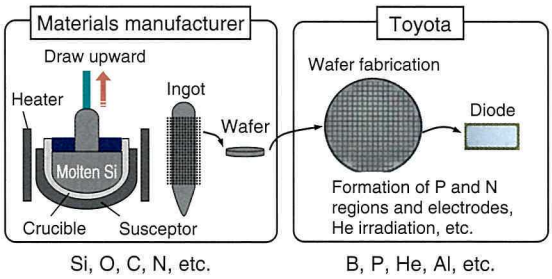


Fig. 9 Impurity Elements in Each Diode Fabrication Step

Cathode luminescence (CL) was selected as the evaluation method as it is capable of detailed investigation of trap levels detected by DLTS. In the same way as the DTLS analysis, samples A (dynamic avalanche not occurring) and B (dynamic avalanche occurring) were prepared. In the evaluation results shown in **Fig. 10**, a C-line (CiOi) and G-line (CsCi) were identified in the CL spectra.[(2)-(5)] Of the two peaks, since the C-line is equivalent to the E_V+0.35eV energy, it was determined that the root cause of the dynamic avalanche phenomenon was C-line CiOi defects.

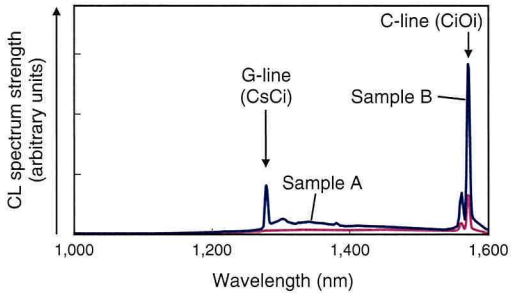


Fig. 10 CL Spectra of Samples A and B

5. Countermeasures and Verification of Effect

The concentration of carbon (1E15 cm^{-3}) in the silicon is significantly lower than that of oxygen (1E18 cm^{-3}). Since CiOi is a composite defect of carbon and oxygen, its formation amount is determined by the carbon concentration. Therefore, samples with different carbon concentrations were fabricated to study the suppression effect on the dynamic avalanche phenomenon.

Fig. 11 shows the switching waveforms for conventional sample B and an improved sample with a lower carbon concentration.

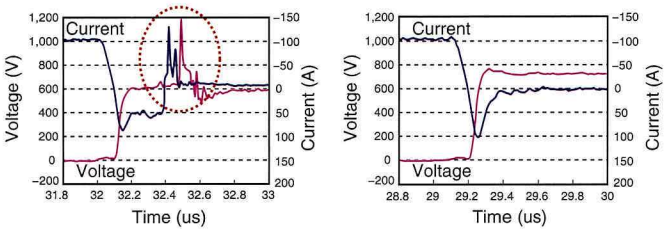


Fig. 11 Comparison of Actual Waveforms of Conventional and Improved Samples

The dynamic avalanche phenomenon occurred in conventional sample B, and the presence of secondary oscillation was confirmed. In contrast, it was verified that the dynamic avalanche phenomenon was suppressed in the improved sample with a lower carbon concentration.

6. Conclusion

This development identified crystalline defects caused by carbon as the root cause of the dynamic avalanche phenomenon that occurs during switching.

The fabrication of high-performance diodes that suppress this phenomenon has helped increase the commercial appeal of HVs and should contribute in the future to further increasing their popularity.

References

(1) T. Misumi Nakagaki, Yamaguchi, Sugiyama, Hirahara. "Analysis of Dynamic Avalanche Phenomenon of PiN Diode Using He Ion Irradiation." *Proceedings of ISPSD '06* (2006) pp. 145-148.

(2) M. Asom, Benton, Sauer, Kimerling. "Interstitial Defects Reaction in Silicon." *Appl. Phys. Lett.* Vol.51 (1987) pp. 256-258.

(3) M. Hüppi. "Proton Irradiation of Silicon: Complete Electrical Characterization of the Induced Recombination Centers." *J. Appl. Phys.* Vol. 68 (1990) pp. 2702-2707.

(4) R. Siemieniec, Lutz, Herzer. "Analysis of Dynamic Impatt Oscillations caused by Radiation Induced Deep Centers." *Proceedings of ISPSD '03* (2003) pp. 283-286.

(5) V. Komarnitskyy, Hazdra. "Identification of Radiation Defect Profiles for Accurate Simulation of Power Devices Irradiated with Proton, Alphas and Low-Energy Electrons." *Proceedings of ISPSD '04* (2004) pp. 177-182.

Authors



A. TANIDA



T. KANATA



K. NISHIWAKI



T. SUGIYAMA

Development of Electrode Structure for High Performance Fuel Cell Using CAE

Joji Tomiyasu*
Takashi Harada*
Makoto Fujiuchi*
Takaji Inamuro**
Shiaki Hyodo***
Toshihisa Munekata***

Abstract

Freeze starting and high temperature operation are current issues in the development of high performance fuel cell electrodes. Although excess water must be removed to improve these aspects of electrode performance, it is also important to adopt a structure that prevents the electrodes from drying up. In the face of this conflicting relationship, it is therefore difficult to design an electrode structure with the required properties. For this reason, using technology jointly developed with Kyoto University and Toyota R&D Labs., Inc., the relationship between structural factors and performance was identified by applying a two-phase flow simulation to the complex microstructure of the gas diffusion layer (GDL) to optimize the electrode structure. As a result, an electrode structure was designed that improves high temperature operation while maintaining freeze starting performance. The simulation results were then validated by experiments.

Keywords: *fuel cell, gas diffusion layer (GDL), lattice Boltzmann method (LBM), water management, diffusivity, structural optimization*

1. Introduction

The fuel cell is attracting attention as an environmentally friendly portable energy source capable of addressing recent energy and environmental issues. Consequently, the fuel cell vehicle (FCV) is recognized as having significant potential for the future due to its exceptionally good environmental performance.

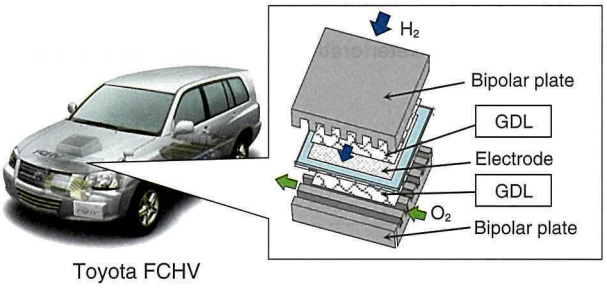


Fig. 1 Basic Fuel Cell Structure

2. Background and Target of Research

2.1 Basic structure and power generation principle of fuel cell

Fig. 1 shows the basic structure of a fuel cell. A gas diffusion layer (GDL) and bipolar plate are placed on each side of a catalyst-coated membrane. Power is generated by an electrochemical reaction by supplying hydrogen to the anode and oxygen to the cathode, resulting in water as a by-product.

A fuel cell stack that produces 90 kW for use in a vehicle consists of several hundred cell layers connected in series. The electrode area (current) and number of cell layers (voltage) are determined in accordance with the required power.

2.2 Issues of fuel cells

High temperature operation is critical for improving fuel cell performance. Achieving operation at high temperatures enables cost and size reduction by boosting system efficiency and simplifying the cooling system.

However, as shown in **Fig. 2**, cell voltage drops rapidly when the cell temperature increases. The reason for this rapid voltage drop is because the polymer electrolyte membrane dries up, which reduces proton (H^+) conductivity (**Fig. 3**). Two approaches are being researched to resolve this issue: the development of a structure that prevents the electrolyte membrane from drying up, and the development of electrolyte membrane materials with lower resistance under dry conditions.

* Fuel Cell Production Engineering Div.
** Graduate School of Engineering, Kyoto University
*** Toyota Central R & D Labs., Inc.

This article focuses on the former structural approach. The concept of the research is to prevent the electrolyte membrane drying up by suppressing diffusion of water vapor generated by the reaction in the GDL. However, a narrow focus on simply suppressing the diffusion of water vapor may produce a dense structure less capable of removing liquid water. This may lead to problems in the cold start process. On start-up, if the amount of generated heat is low, water remaining in the cells will freeze in sub-zero temperatures, hampering the supply of fuel gas, and stopping power generation. Therefore, the GDL structure must also encourage the removal of liquid water to reduce the amount of remaining water. As a result, one issue in developing a diffusion gas layer is to create a structure that both prevents drying of the electrolyte membrane and promotes the removal of liquid water.

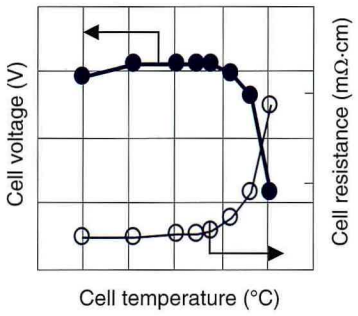


Fig. 2 Performance Deterioration in High Temperature Operation

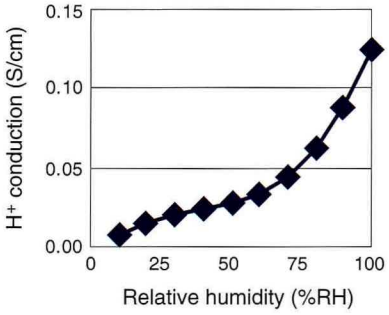


Fig. 3 Relative Humidity and H^+ Conduction

2.3 Target of research

The target of this research is to develop a robust GDL structure that improves high temperature operation while maintaining cold start performance. CAE technology was chosen to achieve optimized solutions within a short period of time and lower investment costs. This article describes new fluid dynamic numerical analysis technology established in this research, structural generator technology utilized to simulate GDL geometry, and statistical quality control (SQC) technology applied to optimize GDL design.

3. Basic Structure of GDL

The functions of the GDL are as follows: the removal of liquid water, electron conductivity, and structural strength expressed as elasticity. To achieve these functions, the GDL consists of a substrate layer with a carbon fiber frame to provide elasticity, and a micro porous layer (MPL) comprising a mixture of conductive carbon and water-repellent material to prevent the generated water coating the electrodes (**Fig. 4**). In addition, each layer has a porous carbon material structure to conduct electrons and diffuse gas.

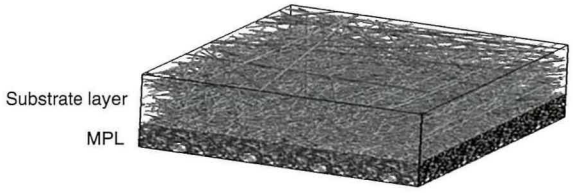


Fig. 4 GDL Structure

4. Development of CAE Technology

4.1 Development of numerical analysis technology for flow inside GDL

To design a robust GDL that enables both high temperature operation and cold start performance, it is necessary to evaluate water vapor diffusivity and liquid water removal. This requires two-phase flow numerical analysis of both gas and liquid. In addition, since the GDL has a complex porous structure, it is not possible to create a mesh structure.

For these reasons, this research focused on the lattice Boltzmann method (LBM),[(1)] the development of which has progressed in recent years. The LBM has the following characteristics, which are suitable for the numerical analysis requirements.

(1) Surface tension and contact angle (wettability) can be considered by tracking the gas-liquid interface as an energy term.

(2) A mesh structure is not required to model the geometry, which enables the modeling of complex structures.

In this research, joint development between Kyoto University and Toyota Central R & D Labs., Inc. achieved the following two points to adapt the LBM to GDL analysis. (i) The contact angle was made more easily adjustable by incorporating a new wall boundary condition using surface free energy. (ii) Numerical analysis of the concentrated gas diffusion phenomenon was enabled by discretizing and integrating the diffusion equations into the LBM.

These developments allowed the analysis of wettability and diffusion even within a complex porous structure. Further details of the LBM can be found in reference (1).

4.2 Technical development of GDL structural generator

As described above, the GDL has a complex porous structure that is impossible to show in drawings. Therefore, for GDL modeling, a structural generator was developed that automatically creates structures using random numbers. Using actual information on the pores, such as the pore size distribution and porosity as inputs, an algorithm was constructed that evenly distributes pores using random numbers. As shown in **Fig. 4**, this has enabled the creation of a virtual structure, making it possible to embody the GDL both quantitatively and qualitatively.

5. Development of Robust GDL Structure

5.1 Flow of structure development

Fig. 5 shows the flow of structure development in this research. Diffusivity and liquid water removal were evaluated in separate cycles featuring design of experiment, numerical analysis, and the application of a response surface method. The knowledge obtained from these cycles was then used to design a robust GDL. The response surface method is a means of optimization by applying functional approximation to properties using certain factors.

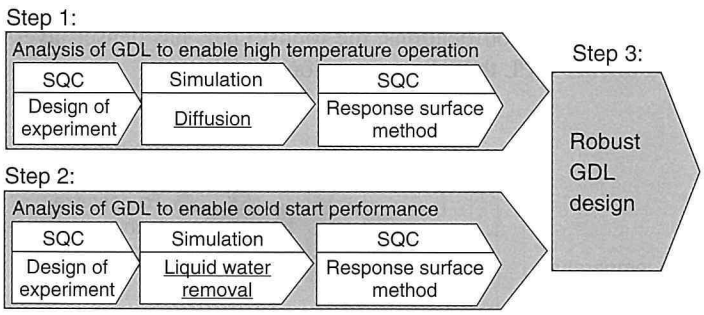


Fig. 5 Flow of GDL Development

5.2 GDL structural factors and conditions

Since water management was the top priority in this research, the structure of the GDL was optimized at the cathode, at which water is generated by electrochemical reaction.

Four structural factors were chosen to optimize the GDL from the standpoints of obtained knowledge, empirical formulas, and manufacturing: substrate layer porosity ($\varepsilon_{substrate}$), MPL porosity (ε_{MPL}), MPL thickness (L_{MPL}), and MPL pore size (ϕ_{MPL}). Three conditions were set for each factor.

5.3 Step 1: Study of GDL structure to optimize high temperature operation

Water vapor diffusion must be suppressed to improve high temperature operation. Diffusion is described by the following diffusion equation.

$$\frac{\partial \phi}{\partial t} = D\nabla^2\phi = D\left(\frac{\partial^2\phi}{\partial x^2} + \frac{\partial^2\phi}{\partial y^2} + \frac{\partial^2\phi}{\partial z^2}\right) \quad (1)$$

where, ϕ is the density and D is the diffusive coefficient. Since the suppression of diffusion increases as the diffusive coefficient decreases, D can be used as an evaluation index for the diffusion of water vapor. Therefore, the target of this study was to reduce D.

Fig. 6 shows quantified results for water vapor diffusion. Diffusion increases at the interface between the substrate and the MPL. This is considered to be the result of sudden diffusion of water vapor as it penetrates from the dense MPL into the large-pore substrate layer. Numerical analysis was performed using the design of experiment method to calculate the diffusive coefficient. The contribution ratio of the four structural factors was analyzed from the obtained calculation results. As shown in **Fig. 7**, the contribution of MPL porosity (ε_{MPL}) is large. In addition, it was also found that diffusion is suppressed when

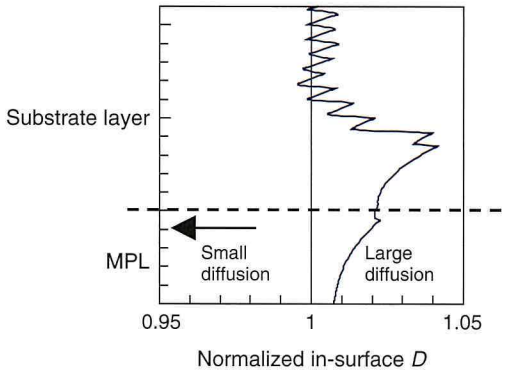


Fig. 6 Evaluation of Diffusivity inside GDL

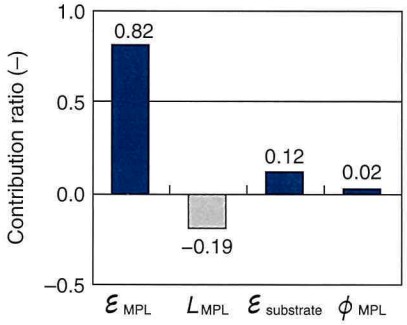


Fig. 7 Evaluation of Contribution Ratio of Structural Factors to Diffusivity

the values for all factors other than MPL thickness (L_{MPL}) are smaller (i.e., the values apart from L_{MPL} have a positive correlation). Subsequently, the response surface method was adopted to optimize the GDL structure for high temperature operation (i.e., to suppress water vapor diffusion). It was found that this could be achieved by decreasing the porosity of each layer by 10%, increasing the MPL thickness by 20%, and reducing the pore size.

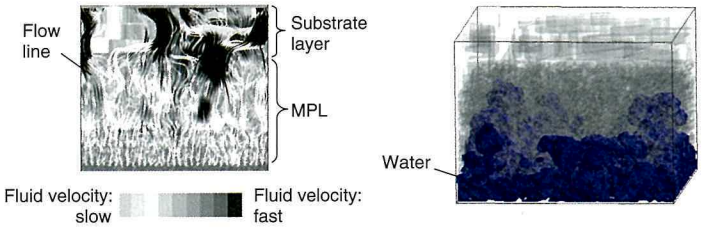
5.4 Step 2: Study of GDL structure to optimize cold start performance

The removal of liquid water must be promoted to improve cold start performance. The movement of water within a porous structure is described by Darcy's equation as shown below.

$$u = \frac{K}{\mu}\frac{\Delta P}{L} \tag{2}$$

where, u is the velocity, μ is the viscosity coefficient, L is the thickness, K is the permeability, which describes the motion resistance through the porous structure, and ΔP is the difference of capillary pressure, which is the driving force of water in a porous medium. Therefore, since $K\Delta P$ is used as an index for the removal of liquid water, the target of this study was to promote the removal of liquid water (increase u) by making $K\Delta P$ larger.

Fig. 8 shows the simulated results for the flow field and water distribution when gas and water flow into the GDL.



(a) Gas flow numerical analysis (b) Liquid water removal numerical analysis

Fig. 8 Results of Numerical Analysis of Flow inside GDL

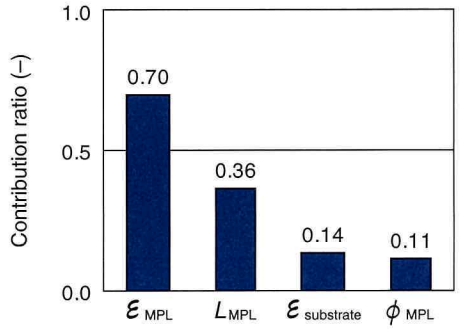


Fig. 9 Evaluation of Contribution Ratio of Structural Factors to Liquid Water Removal

Fig. 9 shows the analysis results for the contribution ratio. The contribution of MPL porosity (ε_{MPL}) and substrate layer porosity ($\varepsilon_{substrate}$) is significant. This shows that the removal of liquid water can be improved by increasing all the structural factor values (i.e., these factors have a positive correlation). Subsequently, the response surface method was adopted to optimize the GDL structure cold start performance (i.e., to promote the removal of liquid water). It was found that this could be achieved by increasing the isolation of each layer by 15%, increasing the MPL thickness by 20%, and enlarging the pore size.

5.5 Step 3: Structural design of robust GDL

A robust GDL structure was developed that enables both high temperature operation and cold start performance. **Fig. 10** shows a summary of the results of the response surface method described in Sections **5.3** and **5.4**. The MPL porosity (ε_{MPL}) and MPL thickness (L_{MPL}) are shown on each axis. The upward direction on the graph indicates improvements in both performance aspects, but improving one has a contradictory effect on the other. In addition, actual production is only possible within a certain range and this acts as a manufacturing restriction. Design was performed within this range, and each structural factor was selected for the following reasons. First, since it has a positive effect on both performance aspects, MPL thickness (L_{MPL}) was increased by 35%. Next, focusing on high temperature operation, the substrate layer porosity ($\varepsilon_{substrate}$) and MPL porosity (ε_{MPL}) were made 5% denser. MPL pore size (ϕ_{MPL}) was not changed because of production restrictions. Based on these modifications, the robust GDL has denser layers and a thicker MPL than the conventional GDL.

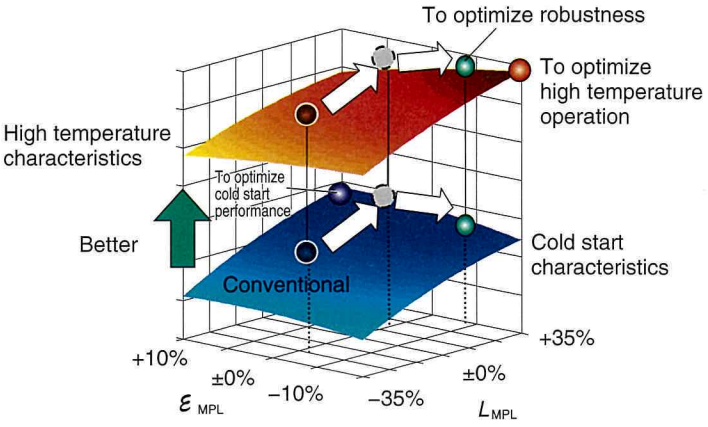


Fig. 10 Results of Response Surface Analysis

6. Validation

6.1 GDL manufacture and predicted performance

GDL prototypes were manufactured based on the structural specifications to optimize robustness, high temperature operation, and cold start performance. Porosity was adjusted by the ratio of mixed hydrophobic material. Thickness was adjusted by the coating amount. When the porosity and coating amount of the substrate and MPL were measured, it was found that the actual GDL prototypes were slightly denser than the conventional GDL. Subsequently, structures were created based on the structural properties of the prototypes, and each value (D and $K\Delta P$) was calculated by another numerical analysis. As shown in **Fig. 11**, it is possible to evaluate relative performance by mapping diffusion (to be suppressed) and liquid water removal on each axis. Compared with the conventional GDL, each property of the robust GDL is improved, and it can be predicted that this GDL will have better performance both under high temperature conditions and in the cold start process.

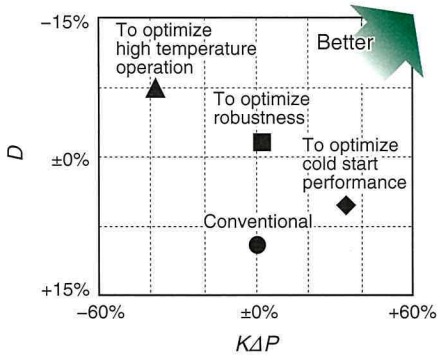


Fig. 11 Performance Prediction by Numerical Analysis

6.2 Performance evaluation

The performance of the GDL was evaluated as follows. High temperature operation was evaluated based on the upper limit temperature at which the cell voltage exceeded 0.5 V. Cold start performance was evaluated based on the amount of liquid water removed from the cell measured when started up at −20°C. In this case, the larger the amount of liquid water removed, the longer continuous power generation is possible without the cell freezing. The evaluation results for a laboratory-scale cell are shown in **Fig. 12** (apart from the GDL, the same conditions were applied in each case). Compared with the predicted results shown in **Fig. 11**, similar trends were obtained for the order of high temperature operation and cold start performance. This indicates the validity of the numerical analysis results as well as the use of diffusivity and liquid water removal to evaluate high temperature operation and cold start performance.

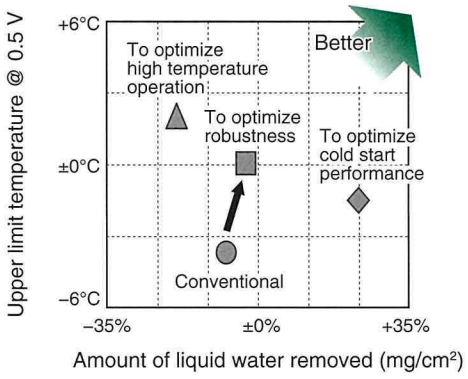


Fig. 12 Evaluation Experiment Results

7. Conclusion

The contribution of structural factors to high temperature operation and cold start performance was quantified to clarify a design policy for creating a robust GDL structure. As a result, a GDL was developed capable of improving high temperature operation while maintaining cold start performance. In addition, unique numerical analysis technology for analyzing flows inside the GDL was established, and the predicted GDL performance obtained by this numerical analysis technology was validated by verification experiments.

Reference

(1) T. Inamuro, Ogata, Tajima, Konishi. "A Lattice Boltzmann Method for Incompressible Two-Phase Flows with Large Density Differences." *Journal of Computational Physics* 198 (2004) pp. 628-644.

Authors


J. TOMIYASU


T. HARADA


M. FUJIUCHI


T. INAMURO


S. HYODO


T. MUNEKATA

Research on Fatigue Mechanism of High-Pressure Tank for Fuel Cell Vehicles

Riki Otsuka*
Nobuyuki Ogami*
Masayoshi Taki*

Abstract
One issue for developing a high-pressure tank for fuel cell vehicles is reducing the amount of carbon fiber reinforced plastic (CFRP) while maintaining sufficient durability. To accomplish this, it is important to understand the phenomenon of fatigue-related breakdowns in order to suppress CFRP fatigue. However, this phenomenon is difficult to identify due to the lack of an evaluation method and because no studies have been reported on the process of fatigue-related breakdowns in high-pressure tanks. This article describes the development of technology for analyzing microscopic damage during tank fatigue tests. This technology has helped to explain the process of fatigue-related breakdowns, thereby allowing the origin of fractures to be identified. Based on the results of this analysis, the fatigue mechanism was estimated and verified, allowing the development of a concept for improving tank fatigue strength.

Keywords: *high-pressure hydrogen tank, CFRP, fatigue, damage process, AE, dry distillation*

1. Background and Aims of Research

1.1 Introduction to high-pressure hydrogen tanks for fuel cell vehicles

The main hydrogen storage method used by current fuel cell vehicles (FCVs) is the high-pressure tank. The use of high-pressure hydrogen tanks for FCVs must consider the following two points: absolute reliability with respect to the storage of flammable hydrogen gas, and vehicle packaging in terms of shape, mass, and cost.

1.2 Basic high-pressure hydrogen tank structure

The basic structure of a high-pressure hydrogen tank consists of a plastic liner to prevent the permeation of hydrogen gas, covered by a strong carbon fiber reinforced plastic (CFRP) layer, which is further covered by an impact-absorbing glass fiber reinforced plastic (GFRP) layer. Aluminum bosses are provided at both ends of the plastic liner for fitting to valves (**Fig. 1**). The laminated structure of the CFRP consists of multiple alternating layers of hoop and helical windings (**Fig. 2**). The hoop winding is wound at virtually 90° to the axial direction to provide strength for the straight sections. The helical winding is wound onto the domes to provide strength in those sections.

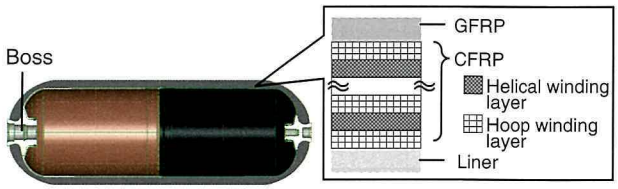


Fig. 1 Structure of High-Pressure Hydrogen Tank



(a) Hoop winding (b) Helical winding

Fig. 2 Winding Patterns

1.3 Issues of high-pressure hydrogen tanks

As described above, high-pressure hydrogen tanks have two main issues: durability, and reduction of cost and mass. However, these issues have a trade-off relationship. In other words, securing durability with the minimum amount of CFRP is a key technical point for developing a high-pressure hydrogen tank.

* Fuel Cell Production Engineering Div.

Currently, high-pressure hydrogen tank durability is designed while factoring in a sufficient safety margin based on the S/N properties of the tank in a fatigue test. The aim is to secure sufficient fatigue strength to withstand 45,000 durability test cycles at a pressure 1.25 times the use pressure. This is the certification criterion for high-pressure containers. However, to make further progress toward limit design, it is necessary to identify the processes related to tank residual strength and fiber breaks in fatigue-related damage, and feedback this information into material selection and the layer structure.

1.4 Aim

The aim of this research was to establish an evaluation technique that contributes to the determination of the design policy for improving CFRP fatigue strength. This article describes how a technique was developed to identify the origin points and initiation timings of fatigue cracks. This technology helped analyze the tank fatigue mechanism and formulate a fatigue strength improvement design policy. The effect of the technology was verified by TP tests.

2. Analysis of CFRP Fatigue Related Damage Process

2.1 Conventional evaluation technology and issues

As shown in **Fig. 3**, CFRP damage is the result of a combination of three types of microscopic damage: plastic cracks, fiber/plastic de-bonding, and fiber breaks.(1)

The origin points of tank fatigue cracks cannot be identified by conventional techniques. X-ray analysis and other non-destructive inspection methods can observe defects with a size of several μm, which is approximately the same as the fiber diameter. For this reason, measurement samples must be several mm square, and such methods are not appropriate for observing actual tank fiber breaks. In addition, since the fracture surface of CFRP does not exhibit any distinct pattern, such as the striations found on metallic fracture surfaces, the origin points of tank fatigue cracks cannot be observed by destructive inspection methods. Therefore, to observe the origin points of tank fatigue cracks, the CFRP must be separated into individual layers when the fiber break of the origin point occurs. Then, the fiber breaks must be observed in each layer.

Acoustic emission (AE) measurement is commonly used in FRP damage process research. Yuyama et al. have published research into the damage propagation process in GFRP laminated sheets by distinguishing microscopic damage(2) and Mizutani et al. have published a report into sound source position determination.(3) However, the accuracy of FRP sound source determination is low. Although it can determine the general position within an FRP surface, it cannot identify the position in the FRP layer direction. There are also no examples of it being used to measure the fatigue damage process in an actual tank.

The research described in this article developed a technique for analyzing the CFRP fatigue mechanism of a tank. This was accomplished through identifying the fatigue origin points by combining a method of separating CFRP layers using dry distillation and AE measurement.

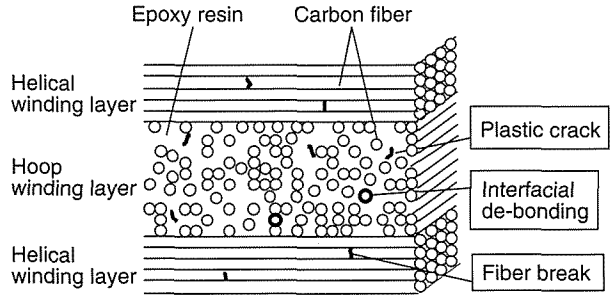


Fig. 3 CFRP Microscopic Damage

2.2 Microscopic damage analysis by AE measurement

2.2.1 Measurement principle

The AE method measures the amplitude, duration, and the like of elastic waves in a frequency band of several kHz to 2 MHz, which are generated in accordance with mechanical damage. Position determination is accomplished through analyzing the difference in time to reach multiple sensors (**Fig. 4**).

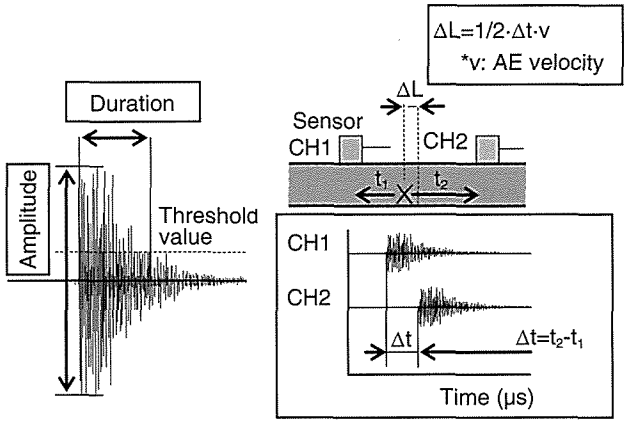


Fig. 4 AE Analysis Method

2.2.2 Distinguishing the microscopic damage mode and position determination

2.2.2.1 TP test of AE measurement performance

Aim

TP tests were performed to verify whether AE signals can distinguish the abovementioned three microscopic damage modes with the material systems used in this research.

Test methods

A TP test was performed for each of the three types of microscopic damage, and AE measurement was performed during the tests (**Fig. 5**). Stand-alone plastic and fiber tests were performed for plastic cracks and fiber breaks, and a CFRP interlaminate shear test was performed for fiber/plastic de-bonding. The interlaminate shear test involved generating shear stress by shortening the distance between the supports in a three-point bending test to cause the CFRP layers to de-bond.

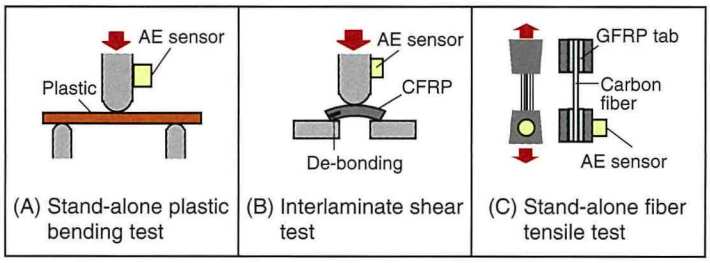


Fig. 5 TP Test Methods

Test results

Fig. 6 shows the AE signals obtained for the three types of microscopic damage. Compared with plastic cracks, the AE signal has a longer duration in the event of fiber/plastic de-bonding, and the amplitude is larger in the event of a fiber break. This indicates that the three types of microscopic damage can be distinguished based on AE signal amplitude and duration.

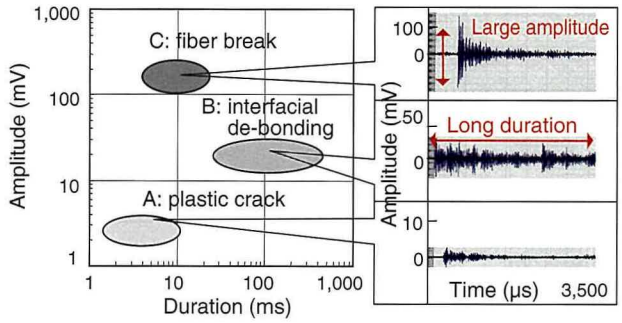


Fig. 6 AE Signals for Microscopic Damage (TP Tests)

2.2.2.2 AE measurement with actual tank

Aim

A test was performed to verify whether the microscopic damage mode could be distinguished and its position identified in an actual tank.

Test method

A tank fatigue test was performed under upper and lower limit pressure conditions of 105 MPa and 1 MPa, respectively (**Fig. 7**). AE measurement was performed by installing 150 kHz resonance type AE sensors at six locations on the tank in order to determine the damage position (**Fig. 8**).

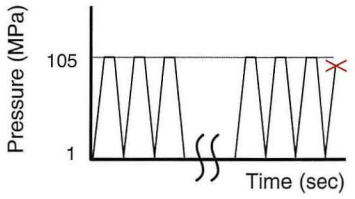


Fig. 7 Pressure Cycle of Tank Fatigue Pressure Test

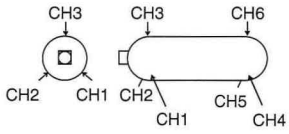


Fig. 8 Locations of AE Sensors

Test result 1: fatigue test results and state of inner tank surface

The fatigue test results showed a leak mode failure after approximately 3,600 cycles. CFRP cracks were observed in the tank inner surface after the test (**Fig. 9**).

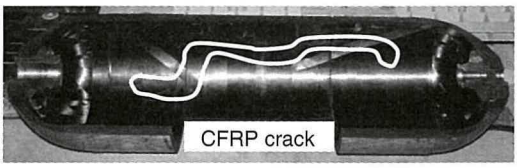


Fig. 9 State of Tank Inner Surface after Durability Test

Test result 2: distinguishing the microscopic damage

Fig. 10 shows the incidence rates of all the AE signals obtained during the fatigue test. The horizontal axis of the graph shows the duration and the vertical axis shows the amplitude. Differences in the incidence rates are expressed by different colors. There were three areas with particularly high cumulative incidence rates, and these are circled. From the TP test results, it can be assumed that area B (long duration) corresponds to fiber/plastic de-bonding, area C (large amplitude) corresponds to fiber breaks, and area A (short duration and small amplitude) corresponds to plastic cracks.

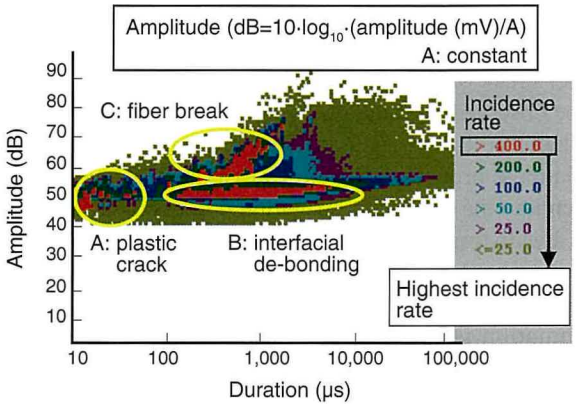


Fig. 10 AE Signals of Microscopic Damage (Tank Test)

Test result 3: microscopic damage process

The AE signals that distinguished the three types of microscopic damage based on threshold values for amplitude and duration were plotted on a graph with elapsed time on the horizontal axis and incidence rate on the vertical axis (**Fig. 11**). As a result, the microscopic damage process was found to have two stages. In the first stage, plastic cracks and fiber/plastic de-bonding occur consecutively, but there is virtually no occurrence of fiber breaks. In the second stage, fiber breaks start to occur and the overall damage incidence rate increases until the tank springs a leak.

In general, the fatigue-related fracture process in a CFRP multi-directional laminated sheet is understood to occur as follows. After transverse cracks and interfacial de-bonding due to overlapping plastic cracks and fiber/plastic de-bonding have accumulated, fiber breaks start to occur, finally leading to fracture.[1] This research found that the fatigue-related fracture process in an actual tank has a similar trend.

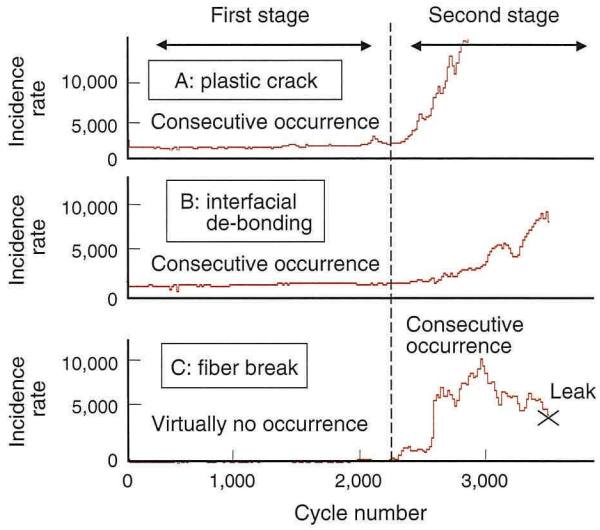


Fig. 11 Proportion of Microscopic Damage Incidence Increase

Test result 4: position of microscopic damage

Fig. 12 shows the AE signal cumulative incidence rate for fiber breaks in the tank straight portion immediately before the leak. The figure indicates that (1) a large number of AE signals were detected at the location of the tank inner surface crack and (2) a large number of AE signals were also detected in locations where no cracks occurred. These locations were then examined by the newly developed fiber crack observation technique (see next section for details). No surface defects were found in the innermost layer, but fiber breaks were confirmed within the layer itself.

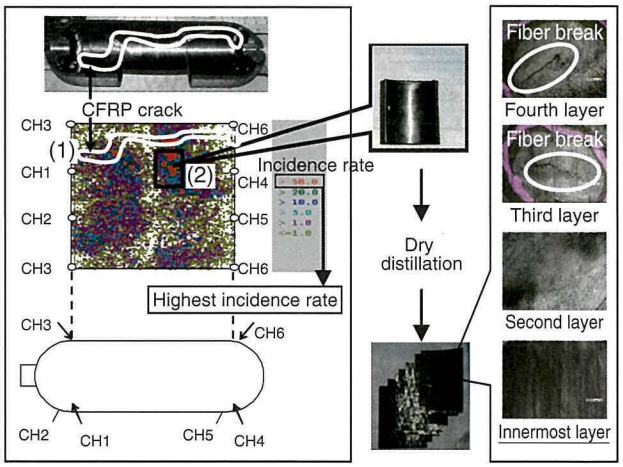


Fig. 12 Observation Results of Fiber Breaks Detected by AE Measurement

2.3 Detailed analysis of fiber break portion

2.3.1 Fiber break observation technique using dry distillation method

It was explained in a previous section that each layer of the CFRP must be separated in order to observe fiber breaks inside the CFRP (**Fig. 13**). However, the plastic used in CFRP for tanks is high adhesive strength epoxy resin. This makes it difficult to separate the individual CFRP layers.

In dry distillation, thermal decomposition is generated in the plastic by heating under oxygen-free conditions, causing evaporation and the extraction of the fiber by itself. This research optimized the temperature and time conditions of the dry distillation method to control the amount of plastic removal. Subsequently, this method is able to separate each CFRP layer while maintaining the layer shape.



Fig. 13 Concept of Fiber Break Observation Technique

2.3.2. Analysis of fiber break origin points

Aim

The aim of this analysis is to identify the fiber break origin points by combining dry distillation and AE measurement.

Test method

A tank fatigue test was performed under upper and lower limit pressure conditions of 105 MPa and 1 MPa, respectively, and AE measurement was performed. The fatigue test was stopped as soon as a fiber break occurred, and the area with a high incidence of fiber break AE signals was cut out (**Fig. 14**). Dry distillation was then used to separate and observe each layer of the sample.

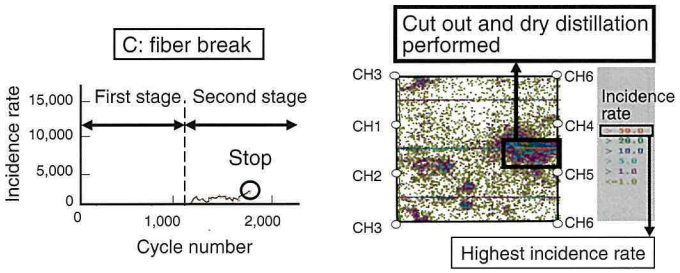


Fig. 14 AE Signal Positions when Fiber Break Occurs

Test result 1: Fiber break occurrence in each layer

Fig. 15 shows three typical examples of fiber break groups in each layer. Each fiber break group penetrates through the layers and a common point for three of the fiber break groups occurred in the third layer. In addition, since some fiber break groups only occurred in the third layer, it was highly likely that the origin points of the fiber breaks were in the third hoop winding layer.

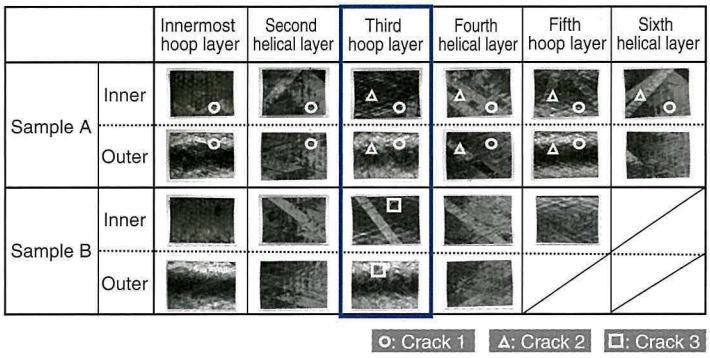


Fig. 15 Fiber Break Occurrence in Each Layer

Test result 2: fiber deflection

The inner states of the third hoop winding layer, in which the fiber break origin point probably occurred, and the innermost hoop winding layer are different. Specifically, the innermost layer is wound against the smooth liner, but the third hoop layer is wound on top of the third helical layer. The effect of this state was investigated by observing the third and innermost hoop winding layers. As a result, it was found that the winding pattern of the second helical layer was transferred onto the third hoop layer. This phenomenon was not observed on the innermost hoop layer. This caused the fibers to deflect by 7° in the third hoop layer (**Fig. 16**).

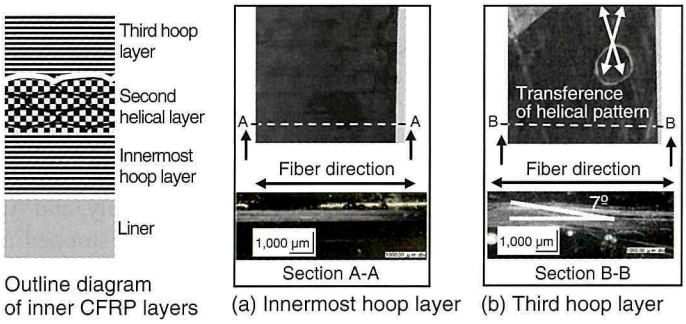


Fig. 16 Fiber Deflection in Third Hoop Winding Layer

3. Estimated Fatigue-Related Fracture Mechanism

Internal pressure is applied to the thick cylindrical portion. The resulting circumferential stress is highest at the inner layers and decreases further toward the outside (**Fig. 17**). Fiber deflection is thought to be a cause of secondary stress (**Fig. 18**). In other words, the following mechanism occurs. (1) Primary tensile stress is applied by the internal pressure. Further tensile stress is then generated due to the fiber deflection, increasing the tensile stress applied to the fibers. (2) The action of shear stress, against which carbon fiber has lower resistance, is observed. These two points are thought to be the cause of the origin point of fiber damage in the (third) hoop winding layer on the outside of the innermost helical winding layer.

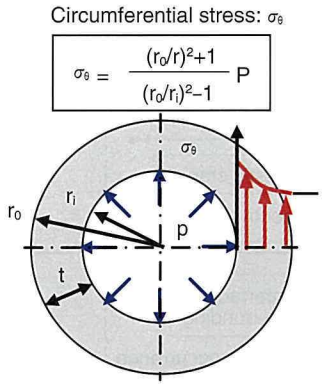


Fig. 17 State of Stress in Thick Cylindrical Portion

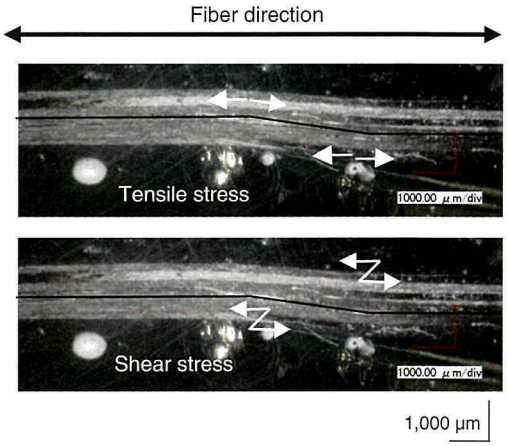


Fig. 18 Stress Modes Caused by Fiber Deflection

4. Verification Test

Test method

To verify the effect of fiber deflection on CFRP fatigue strength, fiber CFRP samples were fabricated with various fiber deflection angles, and a tensile fatigue test was performed (**Fig. 19**). Bending occurred at the portion where the warp and weft threads of the woven material intersected (**Fig. 20**). The fiber deflection angle could be changed by altering the thickness of a single layer.

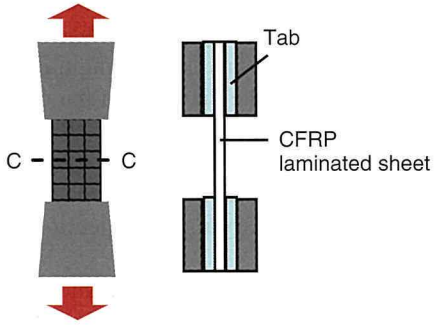


Fig. 19 Tensile Fatigue Test Method

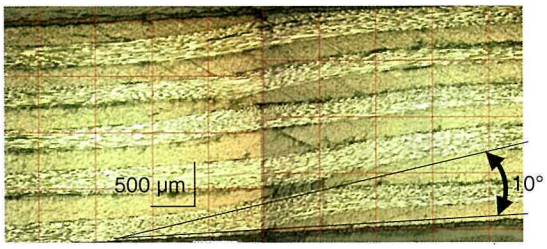


Fig. 20 Section of Plane Weave CFRP Laminated Sheet (Section C-C)

Test results

Fig. 21 shows the fatigue test results of the woven CFRP. The vertical axis shows the normalized maximum stress during the test after taking out the static strength. It indicates that fatigue strength is high when the fiber deflection angle is small, thereby confirming the contribution of the deflection angle on fatigue strength.

This shows that tank fatigue strength can be improved by reducing the fiber deflection angle in the hoop winding layer on the outside of the innermost helical winding layer. It is therefore important to develop a CFRP lamination method that reduces the fiber deflection angle. It is planned to verify this using an actual tank in the future.

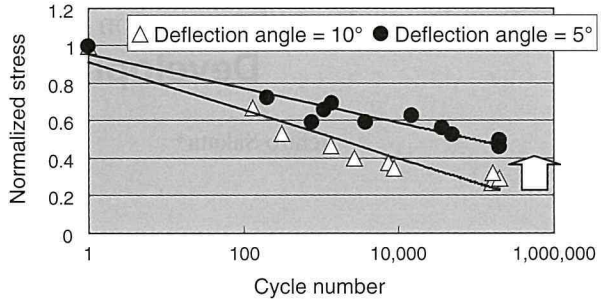


Fig. 21 Fatigue Strength of Plane Weave CFRP Laminated Sheet

5. Conclusions

- An evaluation technique for analyzing the fatigue-related fracture process in tank fatigue tests was developed. The CFRP microscopic damage process and locations of fiber break origin points were identified.
- The fiber break origin points were observed in the hoop winding layer on the outside of the innermost helical winding layer. It was estimated and then verified that fiber deflection affects fatigue strength.
- It was found that tank fatigue strength can be improved by reducing the fiber deflection angle in the hoop winding layer on the outside of the innermost helical winding layer.

References

(1) *Dictionary of Composite Materials Usage* (in Japanese). The Japan Society for Composite Materials.
(2) Yuyama et al. *Journal of the Japanese Society for Non-Destructive Inspection* Vol. 35 No. 10 (1986) p. 720.
(3) Mizutani et al. *Journal of the Society of Materials Science, Japan* Vol. 55 No. 3 (2006) p. 341.

Authors


R. OTSUKA


N. OGAMI


M. TAKI

Best Poster Paper Presentation Award, Society of Automotive Engineers of Japan, Inc.

Development of FTD Fueled Vehicle

Ichiro Sakata* Koji Kitano** Noboru Uchida*** Masaya Umemoto***
Akio Imai**** Nobuhiro Okabe**** Hajime Ishii*****

1. Introduction

The aim of this research was to develop technology for an environmentally friendly heavy-duty diesel vehicle capable of meeting strict future emissions standards by modifying an engine and optimizing exhaust aftertreatment to utilize the merits of Fischer-Tropsch diesel (FTD) fuel. The engine modification strategy was formulated by producing three types of test gas-to-liquids fuels and investigating their effect on diesel combustion. The distillation characteristics of these test fuels were varied primarily within the range where commercial FTD fuel production is possible. The information obtained from this investigation was then used to modify a commercial 7.7-liter diesel engine. For the exhaust aftertreatment system, a NOx storage and reduction catalyst (NSR) was tested in combination with the Diesel Particulate Active Reduction (DPR) system developed by Hino Motors Ltd. This research was performed as part of the Next-Generation Environmentally Friendly Vehicles Development and Commercialization Project headed by the National Traffic Safety and Environment Laboratory, which was commissioned by the Ministry of Land, Infrastructure, Transport and Tourism in 2005.

2. Engine Modifications Assuming Use of FTD Fuel

The following engine modification strategy was implemented to take advantage of the merits of FTD fuel, namely low smoke, low HC, and low noise: (1) low compression ratio, (2) high EGR, (3) optimized pre-injection pattern, and (4) combustion chambers modified to accommodate the lower compression ratio. The final specifications of the 7.7-liter diesel engine were as follows: (a) the compression ratio was lowered from 18 to 16, (b) the injection nozzles were modified to increase flow by 25%, (c) the EGR valve system was changed from a poppet valve to a butterfly valve, (d) the number of EGR coolers was increased from one to two in parallel, and (e) a small turbocharger was adopted.

3. Conclusion

(1) FTD fuels have the merits of reducing smoke, HC, and combustion noise in diesel combustion.
(2) The modification strategy for a dedicated engine capable of utilizing these merits involved combining a low combustion ratio (by increasing the diameter of the combustion chamber) with high EGR/low λ and an optimized pre-injection pattern.
(3) When using an NSR as the exhaust aftertreatment system, the fuel addition to the NSR for NOx reduction can be optimized by increasing and varying the injection pressure (0.7 to 5 MPa).
(4) The target of this research was to achieve the 2009 emissions standards, which was accomplished by modifying a 7.7-liter diesel engine according to points (2) and (3) above without any deterioration in fuel economy.

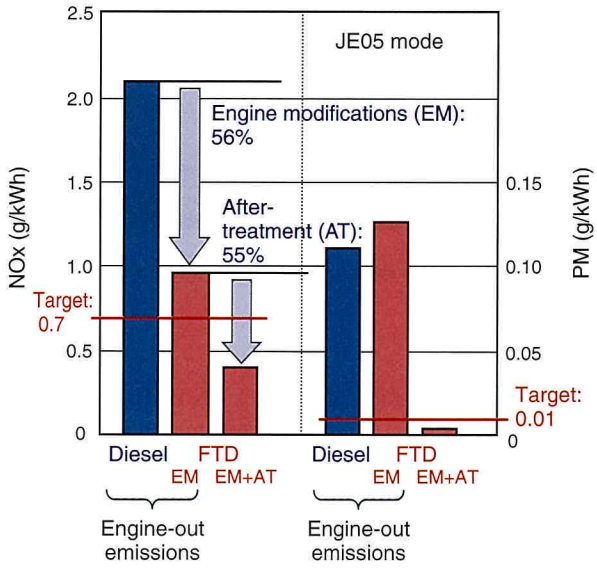


Fig. 1 Reduction in Emissions Using Dedicated FTD Engine

* BR Energy Affairs Dept.
** Advanced Power Train Engineering Div. 1
*** Technical Research Center, Hino Motors Ltd.
**** Showa Shell Sekiyu K.K.
***** National Traffic Safety and Environment Laboratory

2008 JSME Medal for New Technology

The 41st Ichimura Prizes in Industry-Meritorious Achievement Prize, The New Technology Development Foundation

Permanently Engaged Gear Mechanism for Stop & Start System

Toshiaki Asada* Kazuaki Sugimura*
Kazuhito Sakai** Ryosuke Nagata*

1. Introduction

In response to issues such as global warming, the development of idling stop technology to meet the need for lower vehicle fuel consumption and CO_2 emissions began in 1981 with the mass production of a system utilizing a gear pinion shift starter. However, users required such systems to achieve quieter engine starts and improved response to enable the engine to be started at all times. Consequently, this article describes the world's first developed and mass produced permanently engaged gear mechanism.

2. Outline of Developed Technology

The permanently engaged gear mechanism uses a one-way clutch (OWC) and ball bearings to maintain constant engagement between the starter pinion gear and ring gear. As a result, engagement noise between the two gears and the time required for engagement are eliminated. When the engine is started, the OWC engages and the starter drive force is transferred to the crankshaft. After starting, the OWC is released and the ring gear stops.

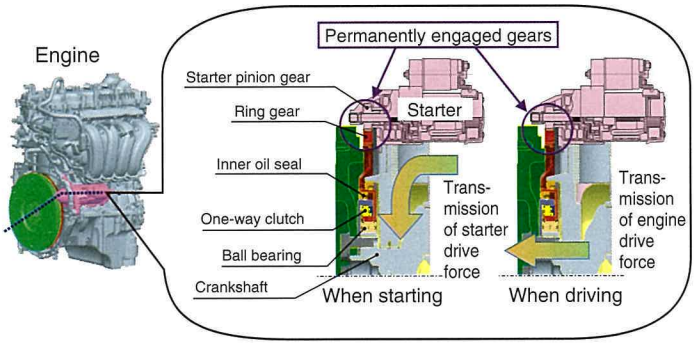


Fig. 1 Outline of Permanently Engaged Gear Mechanism

3. Characteristics and Effect of Developed Technology

By driving the ring gear, which is not affected by variations in the rotation of the crankshaft, engagement noise was eliminated and the starting noise inside the passenger compartment was reduced by 4 dB (**Fig. 2**). This mechanism also achieves rapid engine start response if re-start is demanded during the engine stop process (**Fig. 3**).

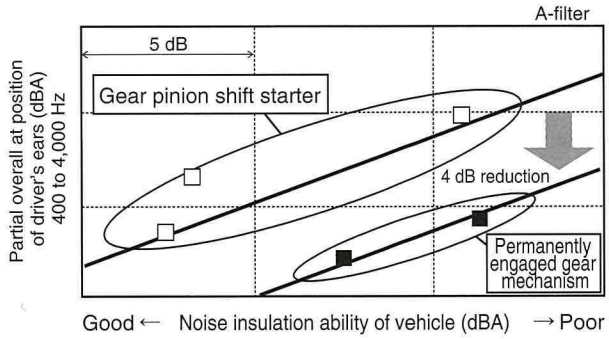


Fig. 2 Comparison of Starting Noise in Passenger Compartment

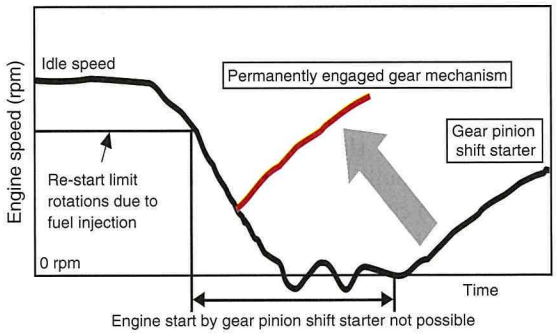


Fig. 3 Comparison of Start Response

4. Conclusion

This system began mass production in 2008. It provides users with comfort (low noise, low vibration, and quick start response), an approximate 10% improvement in fuel efficiency and CO_2 emissions in city driving, and impressive silence while the vehicle is stopped.

The authors would like to extend their gratitude for the cooperation of everyone involved in this development.

* New Engine Development Div.
** Advanced Power Train Engineering Div. 2

Air Model

Japanese Patent No. 3985746

Harufumi Muto* Yuichiro Ido**

1. Background of the Invention

Engine development has been pursuing lower CO_2 and cleaner exhaust emissions. Continuous improvements are being made, such as the adoption of various types of variable systems including intake and exhaust valve timing. In contrast, the growing complexity of systems is causing the number of measurement points and working hours required for calibration to increase dramatically. For example, it might take several months for some engines to measure the static air intake flow into the cylinders (Mc_ta) and static intake manifold pressure (Pm_ta) when the throttle and valve timings are fixed. After a thorough review, a method has been developed to calculate Pm_ta and Mc_ta. This article describes the patent that covers how these calculations are performed.

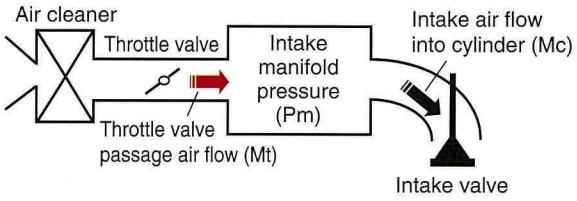


Fig. 1 Structural Diagram of Engine Intake System

2. Overview of the Invention

Fig. 2 shows the throttle valve passage air flow (Mt) calculated by Bernoulli's principle, and the intake air flow into the cylinders (Mc) calculated from the cylinder model. In steady state conditions, the air flow passing into and out of the intake manifold (Mt and Mc) must be the same due to the conservation of mass rule. Therefore, by calculating the intersection of Mc and Mt (point A), it is possible to obtain Mc_ta (Y coordinate) and Pm_ta (X coordinate).

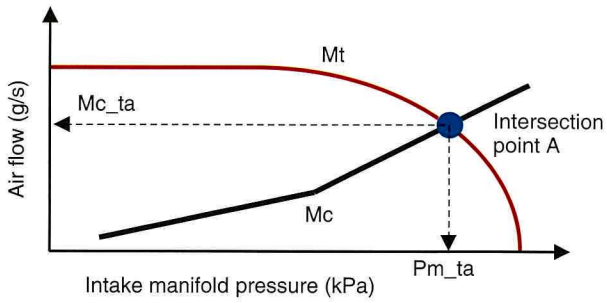


Fig. 2 Mt and Mc Model

3. Effects of the Invention

This invention enables Mc_ta and Pm_ta to be calculated accurately (within an error of 1%), and this has greatly shortened the engine development period. **Fig. 3** shows the transient intake manifold pressure (Pm) values when the throttle is opened suddenly. One line shows the values calculated using this invention and the other shows actual measurement values obtained by a highly responsive pressure sensor. Since the calculation accurately obtained the same Pm as the pressure sensor in both steady state and transient conditions, it is no longer necessary to use an intake manifold pressure sensor for engine control.

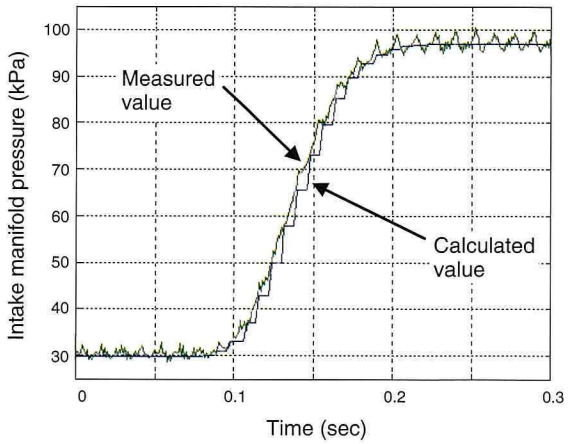


Fig. 3 Intake Manifold Pressure when Throttle Opened Suddenly

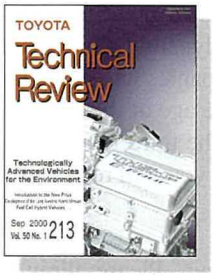
* Engine Engineering Management Div.
** Toyota Technical Development Corporation

TOYOTA Technical Review

Back Number Index



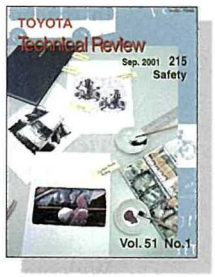
Vol. 49 No. 2
Special Feature: Electronics



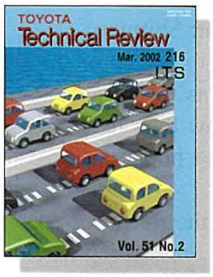
Vol. 50 No. 1
Special Feature: Technologically Advanced Vehicles for the Environment



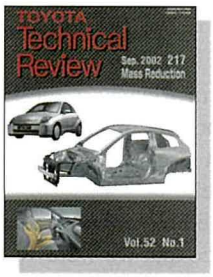
Vol. 50 No. 2
Special Feature: Engine



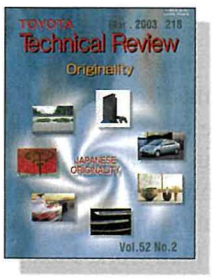
Vol. 51 No. 1
Special Feature: Safety



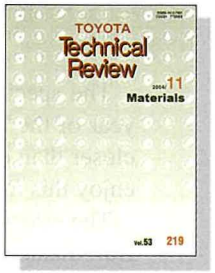
Vol. 51 No. 2
Special Feature: ITS



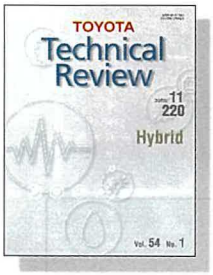
Vol. 52 No. 1
Special Feature: Mass Reduction



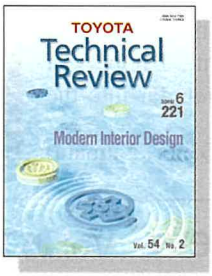
Vol. 52 No. 2
Special Feature: Originality



Vol. 53
Special Feature: Materials



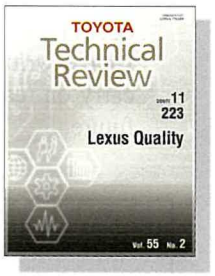
Vol. 54 No. 1
Special Feature: Hybrid



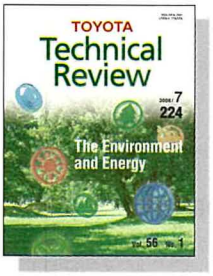
Vol. 54 No. 2
Special Feature: Modern Interior Design



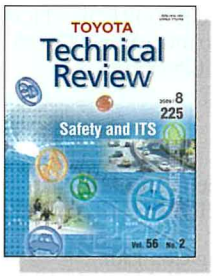
Vol. 55 No. 1
Special Feature: Intuitive Dynamic Design



Vol. 55 No. 2
Special Feature: Lexus Quality



Vol. 56 No. 1
Special Feature: The Environment and Energy



Vol. 56 No. 2
Special Feature: Satety and ITS

¥2,940 (excluding tax: ¥2,800)

Distributor: Ohmsha, Ltd.
Tel: 81-3-3233-0641
http://www.ohmsha.co.jp/information/st/magazine/index.htm

Thank you for reading the *Toyota Technical Review*, Toyota Motor Corporation's only technical journal. Despite the global financial crisis, environmentally conscious businesses are thriving, and twelve years have already passed since Toyota announced the first generation Prius to the world as an environmentally friendly hybrid vehicle.

In the meantime, the tireless efforts of our engineers to meet the needs of the customer have advanced the Prius on all fronts: from fuel economy to dynamic performance, advanced technology, safety, interior space, and design. Furthermore, other companies have followed up with hybrid vehicles of their own, and I truly feel that we have at last entered the age of the hybrid. Amidst these trends, this *Review* describes a full range of the technology found in the third generation Prius, information that is not available in any other catalog or magazine. I hope that you will read it with interest and inspiration.

(Publisher: Tsutsuki)

Welcome to edition 226 of the *Toyota Technical Review*. Please allow me to express my deepest gratitude here to all our regular readers and the authors for their tremendous contributions. This issue's special feature is the third generation Prius, which was released after a model change in May 2009.

The *Review* is Toyota's only technical journal for introducing our latest technologies. As such, we are always seeking ways to improve the *Review* and expand our readership, and we welcome any comments from readers.

(Editor: Shimizu)

The special feature of this issue of the *Toyota Technical Review* is the Prius. 2009 was truly the year of the hybrid. In the past, I could only think of hybrids with distant longing, but now they feel closer than ever. The Prius has already been featured in a large number of magazines, but I hope you enjoy this *Review* as a publication with a truly different feel.

The effects of the global financial crisis briefly threatened the continuing publication of the *Review*. But, thanks to everyone's hard work, I am glad to announce that we were able to bring this issue out. We even took the chance to make various minor changes to the cover design, and introduce a universal design font that is easy on the eye. I hope that these changes will make this *Review* easier to read for our loyal subscribers. Advanced technology opens doors for our dreams. This is my last edition in charge of the *Review* and I have written these words brimming with this sentiment. I hope you carry on reading and enjoying the *Toyota Technical Review* far into the future.



(Editor: Numata)

TOYOTA Technical Review Vol. 57 No. 1

©2010 TOYOTA MOTOR CORPORATION, Printed in Japan
(All rights reserved)

Publisher's Office	Technical Administration Div. TOYOTA MOTOR CORPORATION 1 Toyota-cho, Toyota, Aichi, 471-8572 Japan 81-565-28-2121 (Operator)
Publisher	Misao Tsutsuki
Editor	Eri Numata Intellectual Property Business Management. Div. TOYOTA TECHNICAL DEVELOPMENT CORPORATION
Printer	Sasatoku Printing Co., Ltd. Owaki 7, Sakae-cho, Toyoake, Aichi, 470-1196 Japan
Distributor	Ohmsha, Ltd. 81-3-3233-0641 (Operator) http://www.ohmsha.co.jp/
Printed	July 23, 2010

Printed on recycled paper.



ECO.

TOYOTA



TOYOTA
Technical Review

2010/7
Vol.57 No.1 226

発売元　株式会社 オーム社
定価 2,940円（本体2,800円）
Distributor: Ohmsha, Ltd.
￥2,940 (excluding tax: ¥2,800)